University of South-Eastern Norway
Faculty of Technology, Natural Sciences and Maritime Studies
—
Doctoral dissertation no. 109
2021

Mathias Henriksen

A study of premixed combustion of gas vented from failed Li-ion batteries

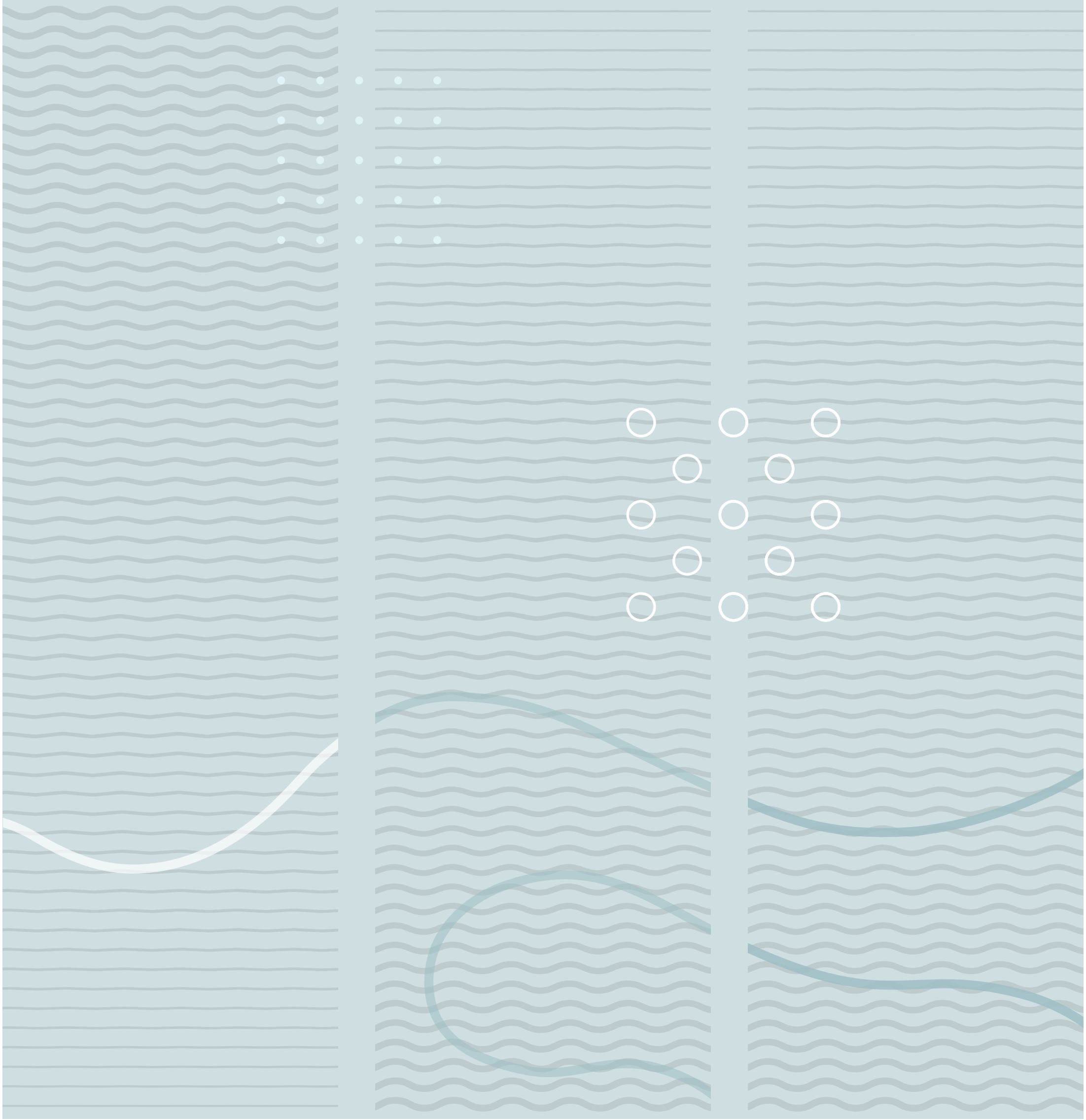

Mathias Henriksen

A study of premixed combustion of gas vented from failed Li-ion batteries

A PhD dissertation in

Process, Energy and Automation Engineering

Faculty of Technology, Natural Sciences and Maritime Studies
University of South-Eastern Norway
Porsgrunn, 2021

Doctoral dissertations at the University of South-Eastern Norway no. 109

ISSN: 2535-5244 (print)
ISSN: 2535-5252 (online)

ISBN: 978-82-7206-6WUõW (print)
ISBN: 978-82-7206-6WVõT (online)

Print: University of South-Eastern
Norway

Dedication

To Eva and Anton

and to my loving and supporting friends and family

Preface

This dissertation was submitted as part of the requirement for a Ph.D. degree within the Process, Energy, and Automation Engineering program at the Faculty of Technology, Natural Sciences, and Maritime Sciences. The thesis presents my doctoral research work, including a collection of journal articles. The research work was carried out between 2017 and 2021 at the University of South-Eastern Norway Campus Porsgrunn. This project has been part of the Norwegian research center for environmentally friendly energy *MoZEES* (Mobility Zero Energy Emission Systems), which provided the financial support for this project, for which I am most thankful.

A special thanks to my supervisor Dag Bjerketvedt, for the expert guidance, for pushing me when needed, and for supporting me throughout this project. I am also truly grateful for all the support and guidance from my three co-supervisors, Knut Vågsæther, Joachim Lundberg, and Sissel Forseth. Thanks to the rest of the research group, Andre Gaathaug, Ola Marius Lysaker, Agnieszka Lach, and Raghav Sikka, for helpful discussions and valuable advice.

To the past and present technical personnel Eivind Fjelddalen, Per Kristian Fylkesnes, Øyvind Johansen, Fredrik Hansen, and Bjørn Vegard Tveraaen, thank you for the technical support and assistance in developing the experimental setups.

Finally, I am sincerely grateful to my patient wife Eva and my family and friends, who have supported and encouraged me throughout this period of my life.

Porsgrunn, August 2021

Mathias Henriksen

Acknowledgments

This work was performed within MoZEES, a Norwegian Centre for Environment-friendly Energy Research (FME), co-sponsored by the Research Council of Norway (project number 257653) and 40 partners from research, industry, and public sector.

Abstract

As the world moves towards more clean and suitable energy sources such as wind and solar, there is an increasing demand for energy storage systems. Lithium-ion batteries (LIBs) are today the leading electrical energy storage system due to high energy density, high specific energy, and low maintenance requirement compared to other traditional batteries. However, the combination of flammable organic electrolytes and the release of oxygen at elevated temperatures in LIBs presents a potential hazard, with numerous fires and explosions reported in the last decades, where failing LIBs were the cause. This study focuses on the explosion hazards by experimentally and numerically studying the premixed combustion of various gas compositions vented from failing LIBs.

In this study, two experimental setups have been used, a 20-liter explosion sphere and a 1-meter explosion channel. In the 20-liter explosion sphere, the maximum explosion pressure, the maximum rate of explosion pressure rise, and the laminar burning velocity (LBV) have been determined for three electrolyte solvents and three Li-ion vent gas compositions. The results showed that the three electrolyte solvents had very similar explosion characteristics, which were also similar to the propane characteristics. Furthermore, the LBV for all gas compositions analyzed ranged from 0.3 m/s to 1.1 m/s, illustrating the influence of certain vented species and their concentrations on the LBV.

The experimental results obtained from the 1-meter explosion channel were used to evaluate model performance a computational fluid dynamic (CFD) method for simulating an explosion from gases vented from failing LIBs using only open-source software. Three different gas compositions and three different channel geometries have been experimentally and numerically studied. In addition, a code for generating the required CFD parameters for combustion, thermodynamic, and transport properties is presented. Finally, the CFD method gave an overall acceptable model performance when comparing the experimental and numerical temporal evolution of the pressure, maximum pressure, positive impulse, and spatial evolution of the flame front velocity.

Keywords: Lithium-ion battery safety; Gas explosion; Li-ion vent gas composition; Laminar burning velocity; Explosion characteristics; XiFoam CFD simulations; Flame Acceleration; Vented deflagration; Hydrogen; Hydrocarbons; Electrolyte solvents

List of Articles

Article A

Henriksen M., Vaagsaether K., Lundberg, J, Forseth S., Bjerketvedt D. *Explosion characteristics for Li-ion battery electrolytes at elevated temperatures*. Journal of Hazardous Materials, Volume 371, 5 June 2019, Pages 1-7, doi: https://doi.org/10.1016/j.jhazmat.2019.02.108

Article B

Henriksen M., Vaagsaether K., Gaathaug A.V., Lundberg, J, Forseth S., Bjerketvedt D. *Laminar Burning Velocity of the Dimethyl Carbonate-Air Mixture Formed by the Li-Ion Electrolyte Solvent,* Journal of Combustion, Explosion, and Shock Waves, Volume 56, 2020, pages 383-393, doi: https://doi.org/10.1134/S0010508220040024

Article C

Henriksen M., Vaagsaether K., Lundberg, J, Forseth S., Bjerketvedt D. *Laminar Burning Velocity of Gases Vented from Failed Li-Ion Batteries*. Journal of Power Sources, Volume 506, 2021, doi: https://doi.org/10.1016/j.jpowsour.2021.230141

Article D

Henriksen M., Vaagsaether K., Lundberg, J, Forseth S., Bjerketvedt D. *Simulation of a Premixed Explosion of Gas Vented During Li-Ion Battery Failure*. It was submitted to the Fire Safety Journal on the 07 of April 2021.

Article E

Henriksen M., Vaagsaether K., Lundberg, J, Forseth S., Bjerketvedt D. *Numerical Study of Premixed Gas Explosion in a 1-meter Channel Partly Filled with 18650 Cell-like Cylinders with Experiments*. It was submitted to the Journal of Loss Prevention in the Process Industries on the 19 of August 2021.

List of Conference Proceedings

Proceeding A

Henriksen M., Vaagseather K., Gaathaug A.V., Lundberg J., Forseth S., Bjerketvedt D. *Laminar burning velocity measurements for an outwardly propagating flame of dimethyl carbonate and air mixtures*. 9th International Seminar on Fire and Explosion Hazards, April 21-26, 2019, Saint-Petersburg

List of Published Supplementary Data

Supplementary Data A

Henriksen, M. and Bjerketvedt D. (2021): *Generating thermodynamic and combustion properties for CFD, mech2Foam*. The University of South-Eastern Norway. Software, doi: https://doi.org/10.23642/usn.13721134.v4

Supplementary Data B

Henriksen, M. and Bjerketvedt D. (2021): *Experimental data of gas explosions in a 1-meter open-ended channel*. The University of South-Eastern Norway. Dataset, doi: https://doi.org/10.23642/usn.13796108.v3

Supplementary Data C

Henriksen, M. and Bjerketvedt D. (2021): *Experimental data of gas explosions in a 1-meter channel partly filled with 18650 Cell-like geometry*. The University of South-Eastern Norway. Dataset, doi: https://doi.org/10.23642/usn.15134442.v1

List of Co-authorship

Co-Proceeding A

Johnsplass J., Henriksen M., Vaagsaether K., Lundberg J., Bjerketvedt D. *Simulation of burning velocities in gases vented from thermal run-a-way lithium ion batteries*. Linköping University Electronic Press, Sep. 2017, pp. 157–161.

Report A

Espen Åkervik, Hannibal E. Fossum, Mathias Henriksen Dag, Bjerketvedt. *Measurements of hydrocarbon flame propagation in a channel.* Norwegian Defence Research Establishment, FFI report: 21/00790, PN: 1600.

Abbreviations

AC	Alternating Current
ARC	Accelerating Rate Calorimeter
BESS	Battery Energy Storage System
BMS	Battery Management System
CAD	Computer-aided design
CID	Charge Interruption Device
CFD	Computational Fluid Dynamics
CT	X-ray Computer Tomography
DES	Detached eddy simulations
DSC	Differential Scanning Calorimeter
DEC	Diethyl Carbonate
DMC	Dimethyl Carbonate
DNS	Direct Numerical Simulation
EC	Ethyl Carbonate
EMC	Ethyl Methyl Carbonate
FID	Flame Ionization Detector
FTIR	Fourier-transform Infrared Spectroscopy
GC	Gas Chromatograph
Ka	Karlovitz Number
LBV	Laminar burning velocity
ICE	Internal Combustion Engine
LCM	Lithium cobalt manganese oxide
LCO	Lithium cobalt oxide
Le	Lewis Number
LFL	Lower Flammability Limit
LES	Large Eddy Simulation
LFP	Lithium iron phosphate
LIB	Lithium-Ion Battery

LMO	Lithium manganese oxide
Ma	Markstein Number
MS	Mass Spectrometer
NDIR	Nondispersive infrared
NCA	Lithium Nickel Cobalt Aluminate
NMC	Lithium Nickel Cobalt Manganese Oxide
OPF	Outwardly Propagating Spherical Flame
PC	Propylene Carbonate
RANS	Reynolds averaging Navier-Stokes
RMS	Root Mean Square
SDE	Standard Deviation of the Error
SEM	Scanning Electron Microscopy
SOC	State of Charge
STL	Stereolithography
TCD	Thermal Conductivity Detector
THC	Total Hydrocarbon
TR	Thermal Runaway
UFL	Upper Flammability Limit

Nomenclature

Roman Symbol	**Description**	**Units**
A	Area	m^2
C_P	Heat Capacity as constant pressure	$J\cdot(g\ K)^{-1}$
D_m	Mass Diffusivity	$m^2\cdot s^{-1}$
J	Diffusive mass flux	$m^2\cdot s^{-1}$
K_G	Deflagration Index	$bar\cdot m^3\cdot s^{-1}$
L	Length	m
R^2	Coefficient of Determination	None
R_u	Universal Gas Constant	$J\cdot(g\cdot K)^{-1}$

Roman Symbol	Description	Units
W	Mole weight	g·mole^{-1}
S	Flame speed	m·s^{-1}
T	Temperature	K
Y	Mass Fraction	None
l	Markstein Length	M
h	Enthalpy	J·g^{-1}
$\dot{m}$	Mass flow	g·s^{-1}
p	Pressure	Pa, bar
r	Radius	m
s	Entropy	J·(g·K)$^{-1}$
t	time	s
u	velocity	m·s^{-1}
u'	Subgrid turbulence intensity	m·s^{-1}

Greek	Description	Units
α	Thermal Diffusivity	m^2·s^{-1}
$\mathcal{D}$	Sub-grid diffusion coefficient	m^2·s^{-1}
κ	Stretch Rate	s^{-1}
ℓ	Turbulent length scale	m
λ	Thermal Conductivity	W·(m·K)$^{-1}$
μ	Viscosity	Pa·s
ρ	Density	kg m^{-3}
$\mathcal{R}_\eta$	Kolmogorov Reynolds number	None
ϕ	Fuel-Air Equivalence Ratio	None
ω	Molar reaction rate	mole·s^{-1}
Ξ	Subgrid wrinkling factor	None

Subscript	**Description**
0	Integral length scale
D	Diffusive Zone / Flame Thickness
K	Kolmogorov length scale
L	Laminar
R	Reaction Zone
T	Turbulent
b	Burnt
ex	explosion pressure in an experiment
f	Flame front
max	maximum pressure in a series of experiments
u	Unburnt
i	Specie, index

Superscript	**Description**
0	Planar

Table of contents

1 Introduction

The world is constantly searching for technology and products that can reduce the dependency on fossil fuels and reduce carbon (CO_2, CH_4) emissions, which most researchers believe is the main contributor to global warming and climate change. Greenhouse gas emissions from the transport sector contribute significantly to worldwide gas emissions [1–4]. In addition, smog, soot, and other air pollution from the transport sector reduce the local air quality in dense urban areas, which is a considerable threat for cities [5].

Several milestones have been set in Norway, and incentives made to meet a low emission society/nation in 2050 [6]. In 2016, the Research Council of Norway founded eight new centers for environmental-friendly energy research (FME). One of these research centers was the Mobility Zero Emission Energy System (MoZEES). MoZEES focuses on battery and hydrogen research within the transport sector [7]. Electric and hydrogen vehicles can reduce greenhouse gas emissions and improve air quality in urban areas [5].

Lithium ion (Li-ion) batteries (LIBs) are the leading energy storage system. LIBs have a high energy density, high specific energy, and low maintenance compared to other traditional batteries such as lead-acid, alkaline, and other batteries [8,9]. There are many different types of LIBs. The different types of LIBs are usually named after the cathode material. The name can be written in whole or as an abbreviation of the chemical composition such as lithium cobalt oxide (LCO), lithium iron phosphate (LFP), lithium manganese oxide (LMO), and more [10].

One of the challenges with LIBs is that they can violently fail if stressed outside their design limits. To ensure safety, every LIB must have a protection circuit. In addition, the combination of a flammable organic electrolyte in contact with highly energetic materials presents a potential hazard [8]. The probability of a single Li-ion cell failure is considered very low. However, a single cell failure could have severe consequences for large LIB applications containing several thousand cells, such as grid storage, electric vehicles, and ferries. The heat released during a single cell failure can lead to cell-to-cell propagation and cause more and more cells to release/vent toxic and flammable gas [11].

There have been reported numerous incidents where LIBs have started fires and explosions in the last decades [8,12–16]. For example, in Texas, USA, in April 2017, a train car carrying LIBs for recycling caused an explosion, which shattered windows 350 feet from the incident [17]. In Arizona, USA, in April 2019, a battery energy storage system (BESS) using Li-ion cells caught fire, likely from a single cell failure. Several hours after the fire had started, an explosion occurred inside the BESS. The BESS was severely damaged, and several firefighters were injured [18]. In July 2019, a parked electrical car caused an explosion in a private garage in Montreal, Canada. The strength of the explosion was enough to throw the garage door across the street and create a hole in the garage ceiling [19]. In October 2019, a hybrid car ferry in Norway caught fire. The cooling system for the LIB is suspected to be the cause of the fire. After the fire was extinguished, an explosion occurred in the switchboard room next to the battery room. The explosion occurred due to accumulated flammable gases vented from the damaged LIB [20]. In April 2021, a fire occurred in a solar panel installation with 25 MWh of LFP LIBs on the rooftop of a shopping mall in Beijing, China. While the firefighters tried to extinguish the fire, an explosion occurred. The explosion led to the death of two firefighters [21].

The underlying cause for a LIB catastrophic failure can be complicated and challenging to determine, but it is usually triggered by an internal or external short-circuit. For example, a short-circuit may internally heat the LIB and cause it to vent the flammable electrolyte and experience a thermal event. During a thermal event, gases and materials may be vented from the battery, creating a combustible mixture when mixed with air [22–24]. Figure 1 shows potential factors that make a LIB unstable and cause thermal runaway (TR), gas release, fire, and explosion.

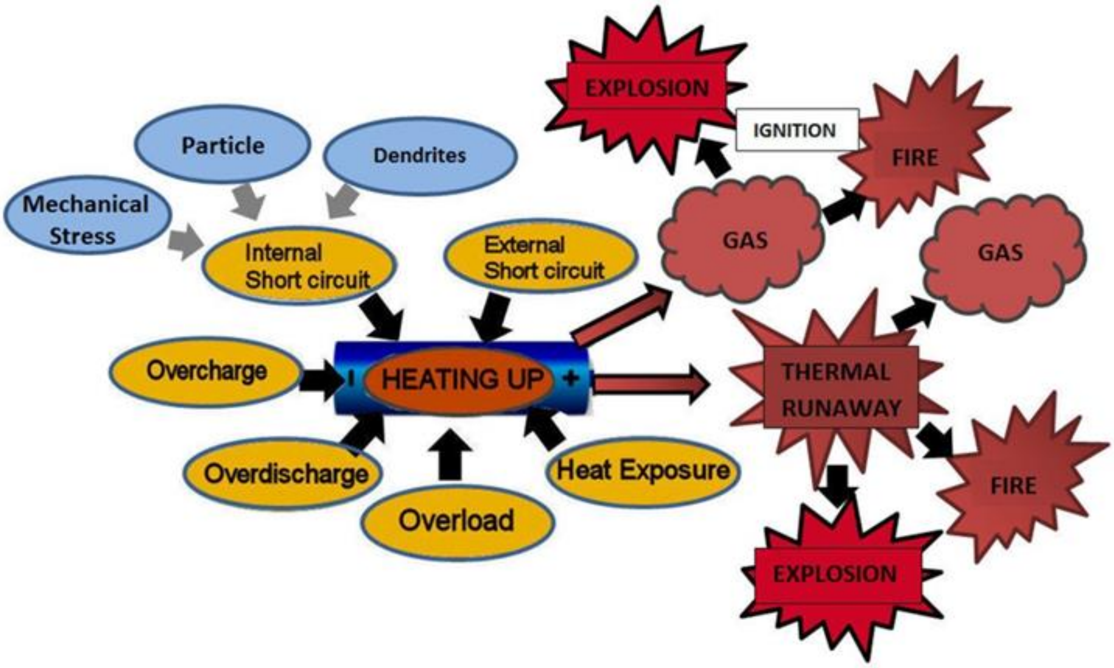

Figure 1. Overview of different factors that could affect the stability of a LIB and lead to thermal runaway, gas release fire, and explosion [25].

There are many studies published on LIBs and TR. A standard experimental method is the Accelerating Rate Calorimeter (ARC). An ARC slowly heats a cell under adiabatic conditions with precise temperature measurements. Since the experiments are performed adiabatically, the onset temperature of self-heating can be detected [22,23,26]. Furthermore, the vented gas composition can be determined by connecting the ARC or a heated vessel to a gas detection instrument, e.g., gas chromatograph, spectrometer [27,28].

Puncture and crush tests are experimental methods to initiate a TR by initiating an internal short-circuit externally. The deformation or needle puncture causes the cell to short circuits and into TR. These mechanical abuse tests can analyze the capability to withstand impact or deformation and cell-to-cell propagation [23,29].

Earlier studies mainly focus on the LIB during a thermal event and determining the gas composition vented. However, when flammable gases are vented and mixed with air, a combustible mixture is formed that can lead to severe external explosions, especially in confined areas [30]. The severity of such an explosion will be a function of the combustion properties of the gas composition and the surrounding geometry. To understand more about the severity and possibly predict the behavior of these explosions, this Ph.D. study focuses on premixed combustion of the flammable gas mixture released from failed LIBs.

1.1 Scope of thesis and objectives

This Ph.D. study is part of the MoZEES research center that focuses on LIB and hydrogen fuel cell systems and applications (RA3). More specifically, the safety and risk management associated with LIB technology. The results obtained in this study are intended for future consequences and risk assessments to assist in the safe integration of LIB installations. As an end objective, develop a computational fluid dynamic (CFD) method to predict explosions characteristics of vented gases from LIBs. To limit the scope of the thesis, the cause, type of failure, the venting process, and the thermal event was not included in the study. Furthermore, combustion, including particles, aerosols, and toxic species, has also been excluded to limit the scope. Therefore, the focus of this study is the characteristics of premixed combustion of the flammable gases vented from failed LIBs.

One of the most fundamental properties in homogeneous premixed combustion is the laminar burning velocity (LBV). LBV gives insight into the distinctive property of reactivity and exothermicity in a given diffusive medium [31]. It is also used in turbulent combustion modeling and as a parameter in CFD methods [32,33]. There is minimal published data on experimentally measured LBVs or other combustion properties for gas compositions vented from LIBs. Therefore, the first objective is to experimentally determine the LBV, the explosion pressure, and the rate of explosion pressure rise for the gases vented, which can be used as CFD input parameters and in safety engineering models.

The XiFoam model/solver, part of the open-source CFD toolbox OpenFOAM [34,35], was used as the basis for developing the CFD method. OpenFOAM was chosen since it is open-source and a free CFD toolbox that is available for all. For large-scale and laboratory-scale cases, the XiFoam combustion model/solver was considered the most accommodating method. XiFoam requires combustion, transport, and thermodynamic model coefficients that are dependent on the gas composition studied. These properties can be determined using reaction mechanisms/ chemical-kinetics models. However, the reaction mechanisms prediction accuracy for determining combustion properties of various Li-ion vent gas compositions is uncertain. Therefore, the prediction accuracy of reaction mechanisms will be studied by comparing the numerical calculation with experimentally obtained LBV for different gas compositions. In addition, the CFD simulation results are compared to laboratory-scale experiments to review the CFD method. The points below summarize the main objectives of this thesis.

- Experimentally measure combustion properties of vented gas compositions from failed LIBs.
- Review the combustion property prediction accuracy of reaction mechanisms by comparing numerical calculations with experimental results
- Develop a CFD method for modeling premixed combustion for gas compositions vented from failed LIBs.
- Review the CFD method by comparing simulated results with laboratory-scale experiments.

Five journal articles document the fulfillment of the four objectives above. Articles A, B, and C address the first two objectives, while articles D and E addresses the last two objectives.

1.2 Outline of thesis

Following this introductory chapter are the literature review and relevant combustion theory in Chapter 2. The literature review presents general information and research concerning LIBs. Chapter 2 also gives the reader an introduction to relevant combustion theory. Detailed descriptions of the experimental setups and numerical tools used in this study are given in Chapter 3. Finally, a summary of each journal article is presented in Chapter 4, followed by a summary and conclusion in Chapter 5. The submitted and published articles are in Part 2 of the thesis.

2 Literature Review and Relevant Theory

This chapter is divided into two main sections, the Li-ion cell/battery and combustion theory. The first section introduces LIB technology, followed by a literature study related to LIB safety research. Relevant premixed combustion theory is presented in the second section. Thus, this chapter targets both readers from the battery and combustion "community."

2.1 Lithium-ion Battery

Lithium electrochemical cells can be divided into two main categories, primary and secondary. A primary lithium cell or lithium-metal cell is a non-rechargeable battery that is disposable after use. The Li-ion cell, a secondary cell, is the more common rechargeable cell found in most consumer electronic devices. Both cells have the same basic structure, with a cathode, anode, and electrolyte. The main difference between the two cells is that the primary lithium cells use pure lithium as an anode, hence the name lithium-metal. Most Li-ion cells have a graphite anode where lithium ions are intercalated to store energy. Only secondary Li-ion cells will be discussed further in this thesis since it is the most widely used battery.

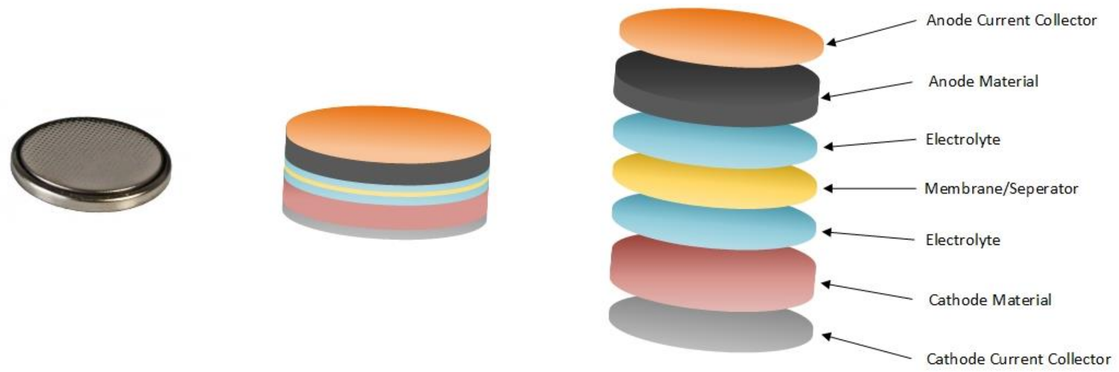

Figure 2. An illustration of a simplified structure of a Li-ion cell from a typical coin cell battery.

Figure 2 shows an illustration of a simplified Li-ion cell structure. The anode electrode consists of the anode material bonded to a current collector. The anode current collector is often made of cobber and is where the electrical charge is released or received. The active material is often pure graphite for the anode, but other materials and hybrids are being researched [36,37]. By intercalating lithium ions in the anode stores energy. An electrolyte solution is needed to enable the transport of the lithium ions between the two electrodes. The most common type of electrolyte is a lithium salt, e.g., $LiPF_6$, dissolved in an organic solvent. The organic solvent can consist of a pure organic carbonate or a mixture of different organic carbonates. In addition, there can be other additives in the electrolyte to improve lifetime, performance, and safety [8,23,38]. Between the anode and the cathode, there is a thin microplastic film/membrane. The membrane allows for the transport of ions between the electrodes but not electrons. In Li-ion cells, there are several different active cathode materials used. Most active cathode material consists of lithium, oxygen, and metals, such as cobalt, iron, and manganese. When differentiating various Li-ion cell chemistries, it is often the active cathode material that gives the cells its name, e.g., lithium cobalt oxide (LCO), lithium iron phosphate (LFP), and lithium manganese oxide (LMO)[10]. Bonded to the cathode is the second current collector, typically made of aluminum.

An electrical current can be applied (charging) or drawn (discharging) from a cell by connecting the two current collectors in an electrical circuit. During discharge, the lithium ions on the anode will de-intercalate, which will create an electrical current that flows from the current collector on the anode to the current collector on the cathode. The current can then power an electrical unit in an external circuit. On the cathode, a free lithium ion in the electrolyte will then intercalate to the cathode. The following equations show the chemical redox reactions for a graphite anode and a cobalt cathode [23,39].

Oxidation - Anode - $LiC_6 \leftrightarrow Li^+ + e^- + C_6$

Reduction - Cathode - $CoO_2 + Li^+ + e^- \leftrightarrow LiCoO_2$

When charging a Li-ion cell, the reactions above are reversed by applying an electrical current to the circuit. Figure 3 show a simple illustration of a discharge and a charging process for a Li-ion cell

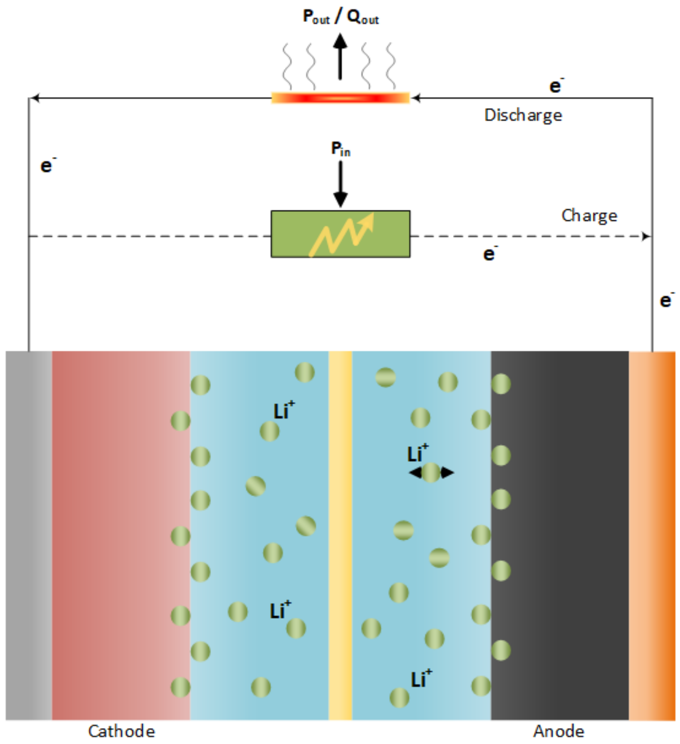

Figure 3. An illustration of a Li-Ion cell during a charge or discharge process [14]

Depending on the application, Li-ion cells can have different shapes, usually either cylindrical or prismatic. For example, the battery in cellular phones will mostly use prismatic cells because they are thin compared to cylindrical cells. A LIB can consist of a single cell but usually consists of several cells stacked together to achieve the desired voltage and capacity. The cells can be stacked into modules, and the sum of all the modules is the battery. Figure 4 shows the different levels, from cell to battery [14,40,41].

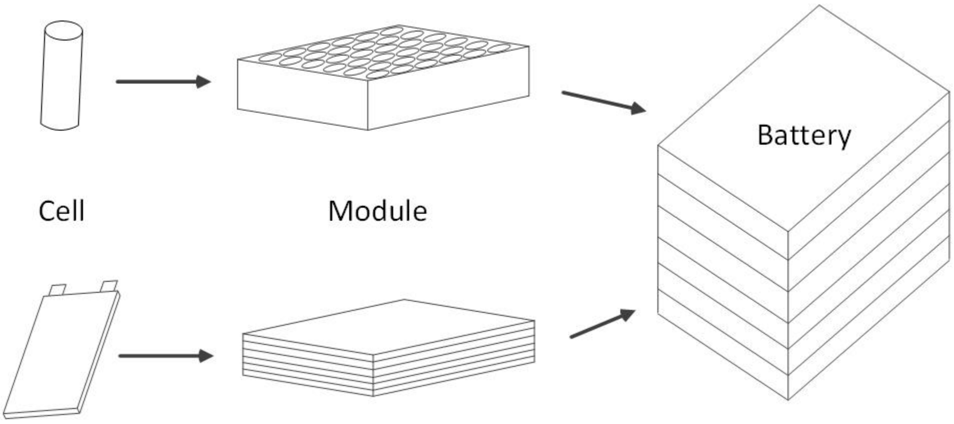

Figure 4. An illustration of the simplified process from the single cell to the battery pack [14]

All units with a LIB have a battery management system (BMS). For some LIBs, the BMS will also be considered part of the complete battery pack. One of the main tasks of the BMS is to protect the cells from abuse, may it be overcharge, over-discharge, and high temperatures [42]. Abuse and manufacturing defects may lead to a catastrophic failure of the LIB.

2.1.1 Energetic and Non-Energetic Battery Failure

LIB failure can be divided into two modes, non-energetic and energetic failure. A non-energetic failure is when the battery loses its function to store or discharge energy without releasing the already stored internal electrical energy. A Non-energetic failure is typically associated with cell aging; however, it can be triggered by internal safety features such as a charge interruption device (CID), a shutdown separator, or a fuse [23]. Most non-energetic failures will not present any fire or explosion hazards.

Loss of the electrolyte due to leakages is a non-energetic failure. A dry cell cannot transport lithium ions, which results in a dead cell. However, the leaked electrolyte may pose a fire and explosion hazard. The organic solvents used in the electrolyte are flammable and may cause fires and explosions when mixed with air. Some of these organic solvents also have a low flashpoint in the temperature range of 18-30^{o}C [43] and thus have the potential to create a combustible mixture at room temperatures. The amount of solvent varies for different cell sizes. In general, smaller cells contain less free liquid compared to large cells. Leaks may occur due to tears or damage done to the cell casing or corrosion.

Li-ion cells contain energy in the form of electrochemical energy and chemical energy in the electrolyte organic solvent, cathode, and anode. The electrical and chemical energy combination causes a Li-ion cell to fail more violently than most water-based electrolyte batteries [13,23]. A violent or catastrophic failure of a Li-ion cell can be referred to as an energetic failure. An energetic failure is a thermal event caused by internal self-heating or external heating of the cell, which causes the internal temperature in the cell to rise. The self-heating occurs because of exothermic reactions in the cathode, anode, and electrolyte. The onset temperature for these reactions depends on the chemistry in the Li-ion cell, additives, and SOC [22,23]. A thermal event may lead to the venting of gases, particles, and aerosols, and TR. The rise in temperature causes the internal pressure to increase and causes the cell to vent, reducing internal cell pressure. The reduction in pressure may stop or reduce the internal self-heating, so the cell does not reach the onset temperature for TR. However, if self-heating or external heating is sufficient, a TR will occur. A TR is defined as a thermal event with rapid and accelerating self-heating, which causes the cell to violently release particles, gases, and vapors that can cause fires and explosions [12,14]. Figure 5 shows an experiment where a pouch cell was externally heated until catastrophic failure. The cell in Figure 5 has swelled and consequently ruptured, venting flammable gas/mist, which most likely was ignited by the external heat source.

Figure 5. A photo of a pouch cell externally heated by a bunsen burner

There are several ways of initiating an energetic failure of a Li-ion cell. Thermal and mechanical abuse have been briefly mentioned, but there is also electrical abuse, poor cell design, and cell flaws from manufacturing. Figure 1 presented by Lian et al. [25] in the introduction shows a schematic overview of causes leading to a thermal event and possibly TR.

2.1.1.1 Thermal abuse

Exposing Li-ion cells to an external heat source is referred to as thermal abuse [22]. The external heat source can be an adjacent cell or cells experiencing a thermal event or fire. A cell has a thermal stability temperature limit in the range of 373 K [23]. Above the thermal stability limit, internal exothermic reactions will occur and initiate self-heating. The self-heating rate and onset temperature depend on the cell chemistry, SOC, and additives [22,23]. If external heating stops and the heat loss from the cell is less or equal to the heat generated, thermal runaway will not occur. However, if external heating continues or self-heating is larger than the heat loss from the cell, TR is inevitable.

Two typical experimental setups for analyzing thermal stability are the accelerated rate calorimeter (ARC) and the differential scanning calorimeter (DSC). The ARC slowly heats the cell in an adiabatic environment while monitoring the outer temperature of the cell. When the cell begins to self-heat, the ARC will equilibrate to the temperature of the cell. The DSC is a similar experimental setup as the ARC but can test individual components of the cell. By heating the components separately, one can identify where the exothermic reaction first starts.

2.1.1.2 Mechanical Abuse

Mechanical abuse of cells is referred to physical damage that punctures (i.e., nail penetration test) or deforms the cell, which causes internal damage. Internal damage may cause a local short-circuit that leads to self-heating. The thermal event can be an instant TR or progress slowly over several charge-discharge cycles until an energetic or non-energetic failure occurs. Crush, puncture, and drop tests are common to perform on cell and battery pack levels [23,44].

2.1.1.3 Electrical Abuse

Overcharge, over-discharge, and external short circuits are some examples of electrical abuse of Li-ion cells. Overcharging a cell to a high voltage (above 100% SOC) or over-discharging to low voltage (below 0% SOC) can permanently alter the cell by causing lithium plating and metallic dendrites [23,45–47]. These changes in the cell may lead to exothermal reactions, short circuits, and immediate TR. Furthermore, an external short circuit can lead to charging and discharging rates beyond the limits of the cell. High discharge and charging rates will heat the cell internally, which may cause its temperature to exceed the thermal stability limit.

Investigating internal damage and alterations due to overcharge and over-discharge can require complex instrumentation such as scanning electron microscopy (SEM) and X-ray computer tomography (CT) [46,48]. These imaging techniques can give a deeper understanding of triggering components and the onset of a thermal event.

Studying internal short-circuits is challenging to achieve in a controlled and repeatable setup compared to overcharge abuse testing. A nail penetration test is a method to initiate an internal short-circuit. However, the results show dependencies on nail speed, size, and point of impact [49]. There are methods to achieve internal shorts without penetrating or crushing the cell. For example, Fang et al. [44] remove parts of the separator, reassemble the cell, and pinch the location missing the separator. It still needed some mechanical pressure, but much less than the nail penetration or the crush tests. Finegan et al. [50] constructed a cell with a small section of the separator that would melt at a temperature of 333 K and cause a localized internal short-circuit. Both studies showed that internal short-circuits between the aluminum current collector and the anode resulted in an energetic event and imidate TR.

2.1.1.4 Manufacturing Defects

Manufacturing defects that can cause an energetic failure can take place in almost any step of production. Some examples are defects and impurities in cell raw materials, contaminations, misplaced, misaligned and misapplied, or damage to components [23]. An estimated failure rate for manufacturing defects for 18650 Li-ion cells is 1 in 40 million [44]. A thermal event from manufacturing defects usually results in an internal short, triggering self-heating, internal hotspots, or cause TR instantaneously.

2.1.2 Gas vented from failed Li-ion batteries

The previous section presented various failure modes and experimental setups used to understand and describe a thermal event. Gases vented during these types of thermal events pose an explosion and toxic hazard. This section presents studies that focus on the gas released during a thermal event.

Toxic fluorinated gases such as hydrogen fluoride (HF) and phosphoryl fluoride (POF_3) can be produced during thermal events from reactions with the lithium salt in the electrolyte, e.g., $LiPF_6$. Other toxic species, such as hydrogen chloride (HCl), sulfur dioxide (SO_2), carbonyl sulfide (COS), carbon monoxide (CO), can be attributed to reactions with the plastic separator/membrane, packaging, electrolyte, and additives [51,52].

However, most of the gas volume fraction vented from failed LIBs is flammable if the inert species carbon dioxide (CO_2) is ignored. The flammable gas is generated due to the decomposition of electrolyte solvents, which typically consist of organic carbonates, such as ethyl methyl carbonate (EMC), dimethyl carbonate (DMC), diethyl carbonate (DEC), ethylene carbonate (EC), and propylene carbonate (PC) [41]. During a thermal event, the solvents can decompose into hydrogen (H_2), carbon monoxide (CO), methane (CH_4), and other hydrocarbons [53]. Table 1 shows a summary of studies concerning abuse testing coupled with gas analysis from the last decade.

Table 1. A summary of published studies combing abuse/failure testing and gas analysis of Li-ion and lithium batteries from the last decade

Reference	**Cell shape**	**Cathode chemistry**	**Electrolyte solvents**	**SOC**	**Major Species detected**	**Test atmosphere**	**Failure test apparatus**	**Gas analysis instrument**
Gachot et al. [53]	Coin 2035	LCrO	EC, DMC	N/A	CO_2, CO, hydro-carbons	vacuum	Heated in vessel	GC-MS
Ribiere et al. [51]	Cylindrical 18650	LMO	EC, DEC, DMC	0 to 100%	CO, CO_2 HF, SO_2, HCl, NO	air	Fire Calorimeter	FTIR, GC-FID Paramagnetic (O_2)
Golubkov et al. [54]	Cylindrical 18650	LCO/NMC, NMC LFP	DMC, EMC, EC DMC, EMC, EC, PC DMC, EMC, EC, PC	100%	H_2, CO_2, CO, hydro-carbons	inert	Heated in vessel	GC-TCD

Reference	Cell shape	Cathode chemistry	Electrolyte solvents	SOC	Major Species detected	Test atmosphere	Failure test apparatus	Gas analysis instrument
Somandepalli et al. [55]	Pouch	LCO	EC-DEC	50 to 150%	H_2, CO_2, CO, hydrocarbons	inert	Heated in vessel	GC-MS
Larsson et al. [56]	Pouch, Battery assembly	LFP	N/A	0 to 100%	HF	air	Combustion Chamber (Open flame)	NDIR, FTIR Paramagnetic (O_2)
Golubkov et al. [28]	Cylindrical 18650	NCA	EC, DMC, EMC, MPC	0 to 143%	H_2, CO_2, CO, hydrocarbons	inert	Heated in vessel	GC-TCD
		LFP	EC, DMC, EMC, PC	From 0% to 130%				
Berström et al. [57]	Pouch	LFP, NMC	N/A	N/A	Various toxic gases	inert	Heated in vessel	GC-MS, FTIR
Spinner et al. [58]	Cylindrical 18650	LCO	DMC, EC, PC	N/A	CO_2, CO, CH_4, O_2, SO_2	air	Overcharge and heating in a vessel	ZRE IR FT-IR
Fu et al. [59]	Cylindrical 18650	LCO	N/A	From 0 to 100%	CO, CO_2, O_2	air	Cone Calorimeter	N/A
Yuan et al. [60]	Prismatic	NMC	EC, DEC, EMC	From 100 to 200%	CO_2, CO, hydrocarbons	air	Overcharge	GC-MS
Sun et al. [61]	Cylindrical 18650	NMC LMO LCO LFP	N/A	From 0% to 150%	CO, SO_2, toxic hydrocarbons	air	Combustion chamber (open flame)	GC-MS, M40, and IC
	Pouch	NMC LMO						
Zheng et al. [62]	Pouch	LFP	EC, DMC, EMC	0%	H_2, C_2H_6, CH_4	Inert	Over-discharge	GC
Maloney (FAA) [63]	Cylindrical	LCO, LMO, LFP, LCM	N/A	From 0% to 100%	H_2, CO_2, CO, hydrocarbons	inert	Heat controlled vessel	GC-TCD/FID, NDIR, THC, Paramagnetic, H2scan
Nedjalkov et al. [52]	Pouch	NMC	EMC, EC	above 100%	HF, H_2 CO, toxic hydrocarbons	air	Nail Penetration	GC-MS, QMS, QEPAS, IC
Larsson et al. [64]	Cylindrical, Prismatic, Pouch, Battery pack	LCO, LFP, NCA	N/A	From 0% to 100%	HF, POF_6	air	Combustion Chamber (Open flame)	SBI, FTIR
Lammer et al. [65]	Cylindrical 18650	NCA	N/A	100%	H_2, CO_2, CO, hydrocarbons	inert	Heated in vessel	GC
Fernandes et al. [27]	Cylindrical 26650	LFP	DMC, EMC, EC, PC	above 100%	H_2, CO_2, DMC, EMC¤, hydrocarbons	air	Overcharge	GC-MS/TCD, FTIR
Koch et al. [66]	Pouch	NMC	DMC, EMC, DEC, EC	100%	H_2, CO_2, CO, hydrocarbons	air	Heated in vessel	GC-WLD, GC-FID
Sturk et al. [67]	Pouch	LFP, NMC/LMO	N/A	100%	HF, CO_2, POF_6, hydrocarbons,	inert	Heated in vessel	GC-MS, GC-FID, FTIR

2.1.3 Explosion hazard

As Table 1 shows, several studies have determined that LIBs release combustible species. However, only a few studies investigate the explosion hazard related to these vented gas compositions. This section presents studies related to the explosion hazard from the gases vented from failed LIBs.

Harris et al. [68] identified and analyzed (numerically) the combustion properties for electrolyte solvents and compared the results with hydrocarbons with an equal number of carbon atoms. The three main observations from this study are summarized below.

- A lower heat release per unit volume for the electrolyte solvents compared to hydrocarbons.
- There is a significant difference in the heat of combustion and heat of vaporization amongst the electrolyte solvents. Combustion properties of electrolyte solvents should be considered if flammability is of concern.
- Heat release rates are more valuable than temperature profiles concerning cell to cell propagation.

Somandepalli et al. [55] experimentally determined the gas composition of commercial LCO cells. In addition, the vented gas was injected at various concentrations into a 20-liter explosion sphere to determine the explosion pressure and rate of explosion pressure rise. The results were compared to the explosion characteristics of methane, propane, ethane, and hydrogen. Furthermore, the comparison showed that the explosion pressure and rate of explosion pressure rise for the vent gas compositions were in the same range as the common hydrocarbons.

In his master thesis, Jonathan Johnsplass [24] studied the combustion properties of DMC and various vent gas compositions numerically, which were compared to methane, propane, and hydrogen. Similar to the study by Somandepalli et al. [55], the combustion properties were in the same range as the hydrocarbons. Additionally, Johnsplass externally heated 18650 cells until the safety mechanism ruptured and vented gas. The cells did not experience an energetic failure, and thus only evaporated electrolyte and mist were assumed vented. The gas was vented into a 0.45-meter explosion channel and ignited. Figure 6 shows two still images of the inhomogeneous propagating flame from these experiments.

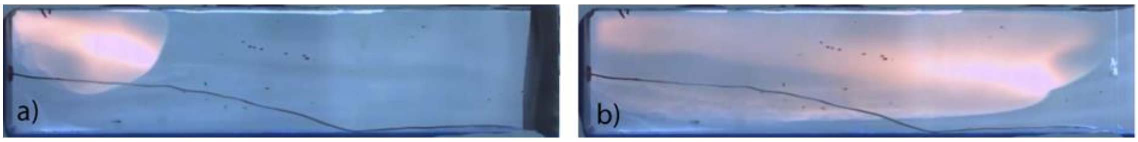

Figure 6 Two still images of an inhomogeneous flame propagating inside a 0.45x0.10x0.10 explosion channel. A 18650 Li-ion cell was externally heated until the combustible gas/mist was vented. a) Short after the ignition. b) Image when the flame has reached the end of the channel [69]

Fernandes et al. [27] analyzed the gas vented from LFP cells from overcharge abuse testing. Combustion properties were numerically calculated for the determined vented gas composition and compared to that of pure DMC. One of the critical observations regarding the explosion hazards was that over 50% of the vent gas consisted of flammable organic solvents. Moreover, the vent gas and pure DMC had similar combustion properties, probably due to the high concentration of DMC in the vent gas composition.

In 2020, Baird et al. [15] published a study comparing the combustion properties of several published gas compositions from thermal and overcharge abuse testing. The combustion properties were numerically determined using the reaction mechanism GRI-Mech 3.0 [70]. The results showed that the nickel cobalt aluminate (NCA) and LCO cell chemistries produced gas with higher laminar burning velocities and maximum explosion pressures than LFP cell chemistries. However, Baird et al. stated that more laminar burning velocity and maximum explosion pressure experiments are needed to validate the models used in these calculations.

2.2 Premixed Combustion Theory

This section presents relevant premixed combustion theory, aiming to introduce readers outside the field of combustion to premixed flames, laminar burning velocity (LBV), and mechanisms related to flame propagation. Readers with a background within the field of combustion will likely be familiar with the material presented.

2.2.1 Laminar Premixed Flames

In combustion, flames can be divided into two main categories, diffusion flames or non-premixed flames and premixed flames. A non-premixed flame will position itself between fuel and oxidizer based on the diffusivity and stoichiometry. For example, the conventional household lighter or candle are good examples of a non-premixed flame. Figure 7 shows a photo of a non-premixed flame with a simple one-dimensional flame structure.

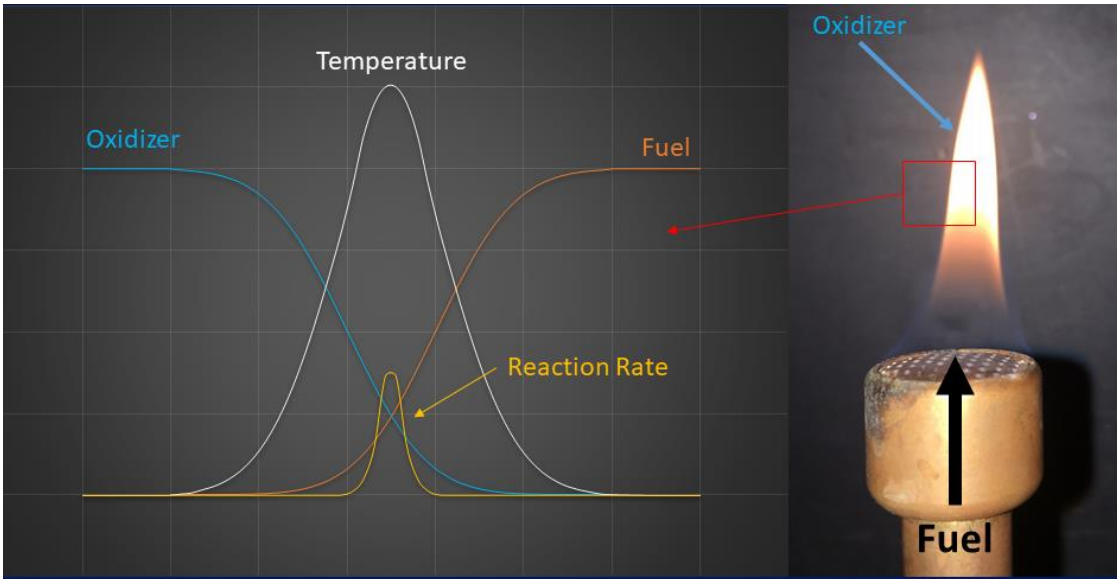

Figure 7. An example of a non-premixed flame/diffusion flame with fuel and oxidizer concentration, temperature, and reaction rate profiles.

Conversely, premixed flames will move into and consume the unburnt mixture as a wave phenomenon. Figure 8 shows a photo of a premixed flame with a simple one-dimensional flame structure.

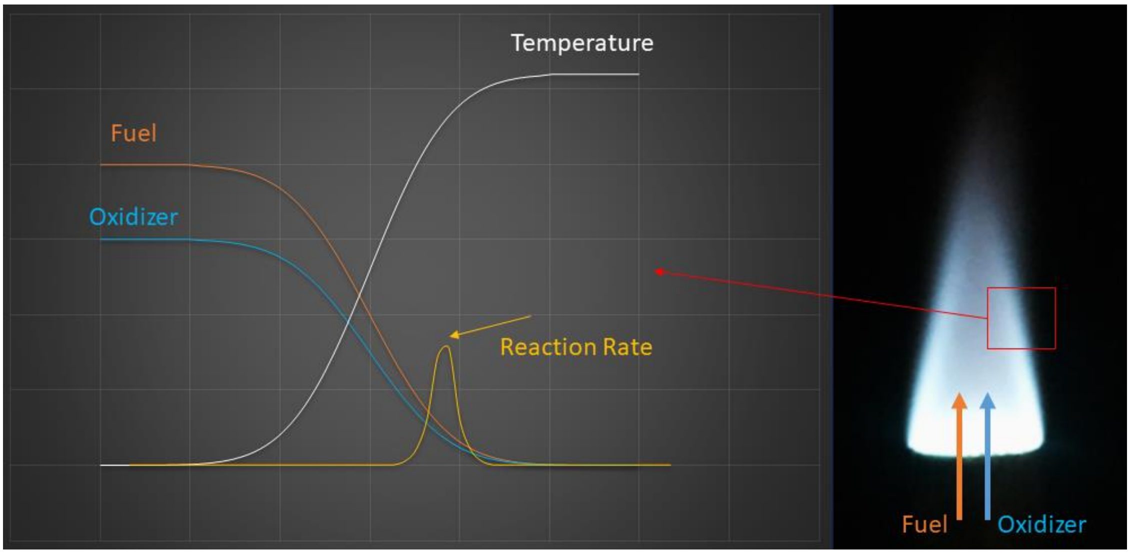

Figure 8. An example of a premixed flame (Bunsen burner) with fuel and oxidizer concentration, temperature, and reaction rate profiles.

Combustion waves with subsonic propagation speed (relative to the unburnt mixture) are referred to as deflagrations, commonly called premixed flames. However, if the combustion wave propagates at supersonic speed (relative to the unburnt mixture), it is called a detonation. This subsection introduces laminar premixed flames in different levels of detail and its fundamental property, laminar burning velocity (LBV). For a comprehensive review and analysis of these topics, the book by C.K Law, Combustion Physics [31], is recommended.

2.2.1.1 *Flame sheet structure*

One of the simplest models to describe a premixed flame phenomenon is the flame sheet structure illustrated in Figure 9. The flame sheet structure describes the flame as one-dimensional and planar, with a stationary, infinitely thin flame. Furthermore, the flame is assumed infinitely thin and discontinuously separates the unburnt and burnt state, where mass and species are conserved and at thermodynamic equilibrium. With this consideration, the flame sheet structure can be mathematically expressed by the Rankine-Hugoniot relations.

Moreover, by considering the flame stationary, the gas of the unburnt mixture approaches the flame sheet with velocity u_u^0 and exits the flame with velocity u_b^0. Subscripts *u* and *b* refer to the unburnt and burnt gas, respectively. Superscript *0* indicates that velocity is planar. S_u is often referred to both as the burning velocity and flame speed. In this study, however, the burning velocity refers to the combustion property of the mixture and the flame speed to the flame's displacement speed. In simpler terms, burning velocity is relative to the unburnt state, and flame speed is relative to the burnt state.

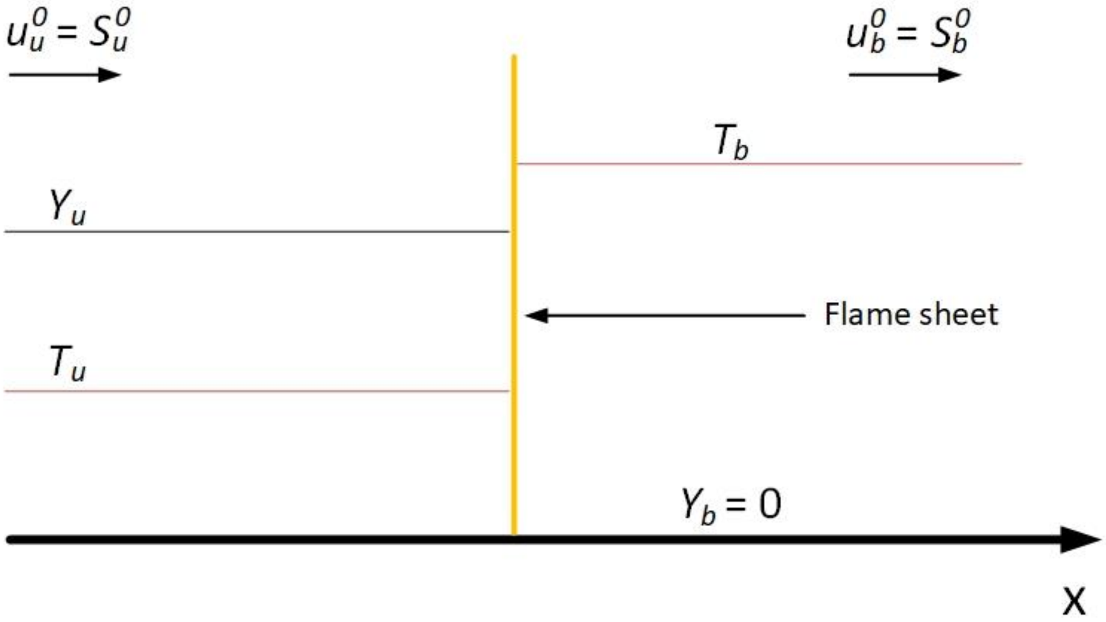

Figure 9. The flame sheet structure of a stationary premixed flame [31]

2.2.1.2 Flame sheet structure with transport

Including transport in the flame sheet structure gives a more detailed explanation of a premixed flame. The mass and thermal transport reveal a preheat zone with characteristic thickness L_D. As the reactants approach the reaction sheet, they will gradually get heat from the chemical heat release. The reactants will heat up continuously until reaching the temperature T_b. Due to the large activation energy consideration, no reaction occurs until reaching a temperature close to the adiabatic temperature. Once the reaction starts, deficient reactants will be rapidly consumed and ending combustion. Thus, the reaction sheet will act as an interface that serves as a heat source and a sink for reactants. Figure 10 shows an illustration of the flame sheet structure, including mass and thermal transport.

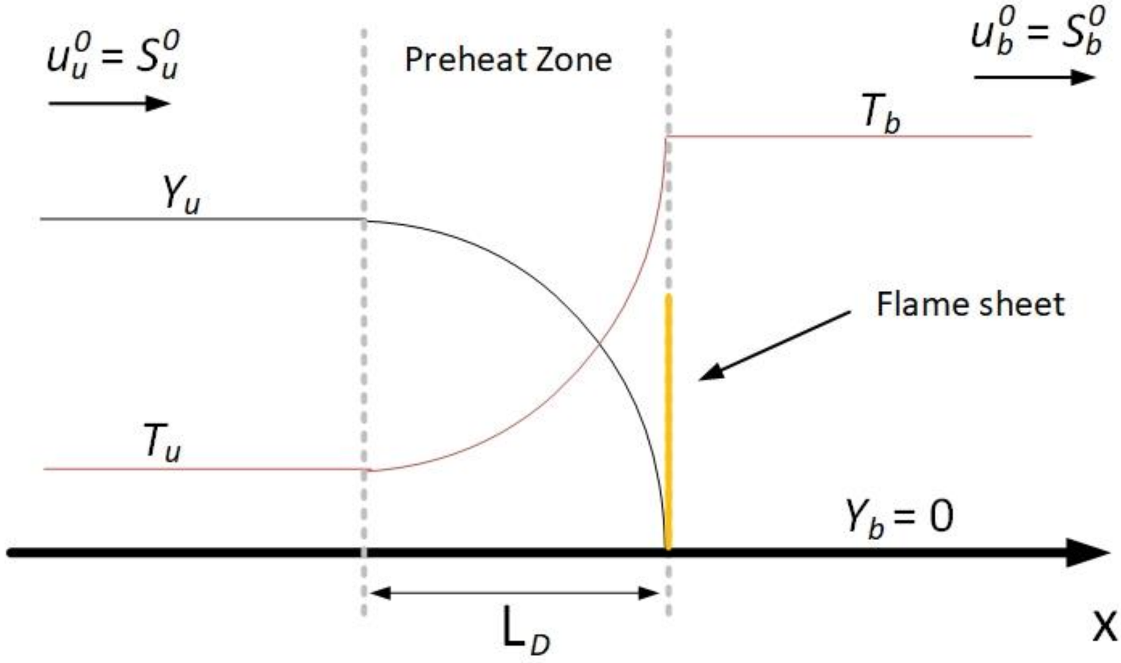

Figure 10. A stationary premixed flame structure with transport and a flame sheet level of detail [31]

2.2.1.3 The detailed structure of a premixed flame

By expanding the reaction zone, reveals the detailed structure of a premixed flame illustrated in Figure 11. This expansion reveals the reaction rate profile with a characteristics length of L_R. The reaction rate will rapidly increase when the reaction reaches its onset (activation energy) and rapidly decrease as the deficient reactants deplete. Consequently, the length of L_R will be much shorter than L_D ($L_R << L_D$). The preheat zone is convection and diffusion dominated, while the reaction zone is diffusion and reaction dominated.

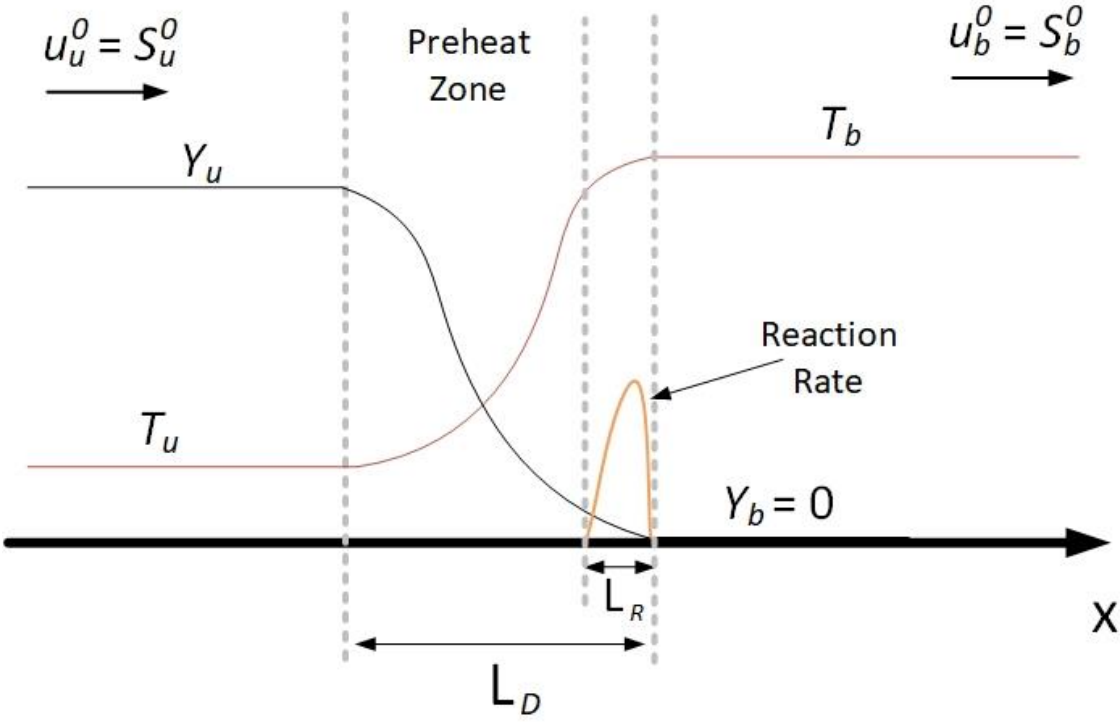

Figure 11 Detailed structure of a stationary premixed flame [31]

2.2.1.4 Laminar burning velocity (LBV)

The last structure shows that a premixed flame is governed by aerodynamics through the following relation: convention, diffusion, and chemistry. Furthermore, the analytical solutions to the governing equations for the three presented flame structures give insight into the behavior, dependencies, and the fundamental significance of LBV [31]. The LBV is a distinctive mixture property and a function of reactivity, exothermicity, and transport properties. The LBV is defined as one-dimensional, planar, stationary, and adiabatic like the premixed flame structures.

Analytical solution for the detailed structure of laminar premixed flame can only be obtained with simple combustion chemistry and therefore confined to a region inside the flame due to the large activation energy. In reality, however, most combustion processes consist of several hundred to thousands of elementary reactions, which may occur throughout the entire length of the flame due to the back diffusion of radicals. For numerous chemical reactions, analytical solutions are not feasible. Therefore, only numerical solutions exist for a detailed chemistry structure of a premixed flame. Figure 12 shows an example of the chemical structure of a stoichiometric hydrogen-air premixed flame. Section 3.3 gives additional information regarding the numerical approach to premixed flames.

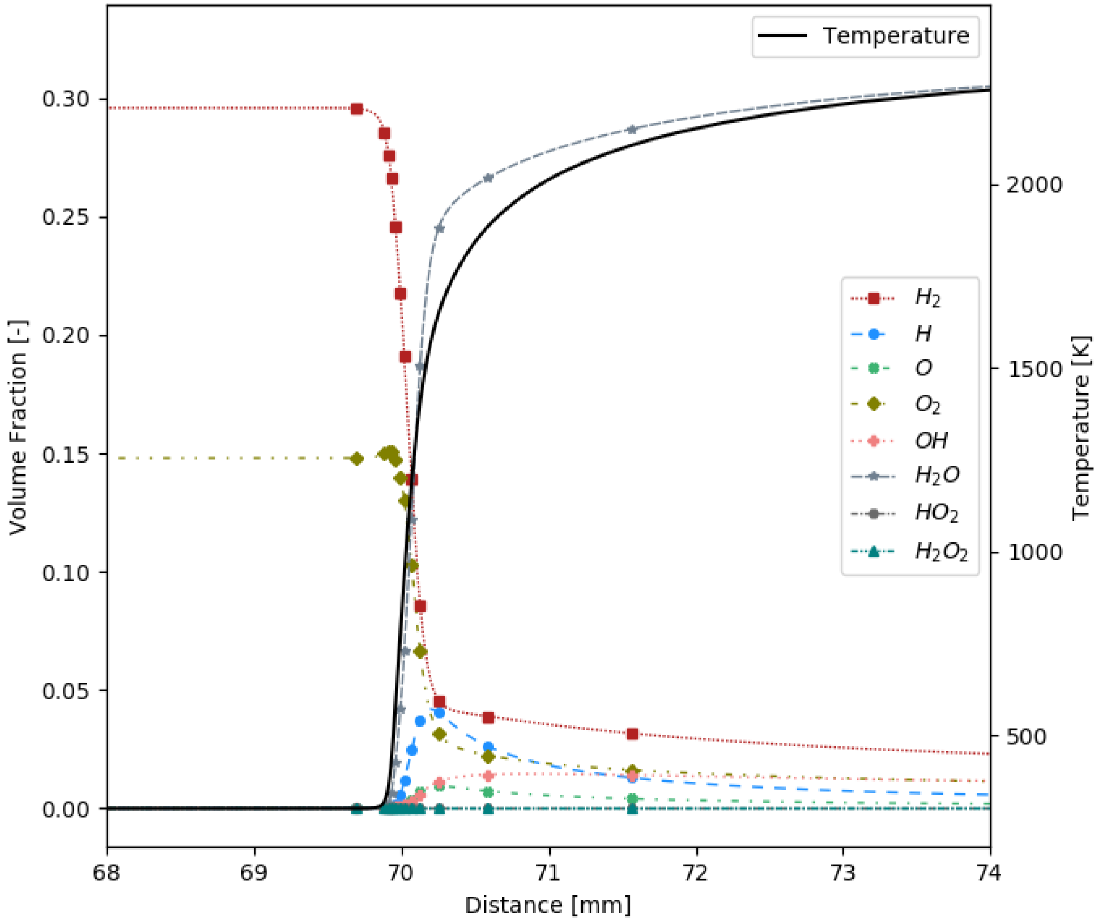

Figure 12. The chemical structure of a stoichiometric premixed hydrogen-air flame

2.2.1.5 Experimentally determining the laminar burning velocity

As mentioned, the LBV is defined as one-dimensional, planar, stationary, and adiabatic. Today, however, no experimental setup can produce a flame that is both planar and considered adiabatic. For example, the flat-flame burner (McKenna burner) can produce a planar or flat flame but will have a noticeable heat loss to the burner head. Therefore, the LBV must be determined while measuring the heat loss and extrapolating the LBV measurements to zero heat loss. Moreover, in the outwardly propagating spherical flame (OPF) method and the stagnation flame method (counterflow flame), the flame will experience stretch/curvature effects, which must be accounted for when determining the LBV.

In this study, the LBV is only determined experimentally by the OPF method; therefore, it only addresses this method. The following references are recommended for a comprehensive review of different methods of determining the LBV experimentally: Combustion Physics by Law 2006 [31], Egolfopoulos et al. 2014 [71], and Konnov et al. 2018 [72].

The OPF experimental setup consists of a chamber, typically a spherical chamber, and a device to record the flame propagation. The chamber is filled with combustible gas, which is then ignited in the vessel's center, creating a spherical flame propagating outwards with the laminar flame speed. Typically, the flame propagation is recorded with a high-speed camera combined with an optical technique such as schlieren or shadowgraph. From Eq. 1 below, the flame speed can be calculated by considering the flame stationary in the laboratory frame, as depicted in Figure 13.

$$S_b(t) = \frac{dr_f(t)}{dt} = \frac{r_{f,2} - r_{f,1}}{t_2 - t_1} \qquad \textit{Eq. 1.}$$

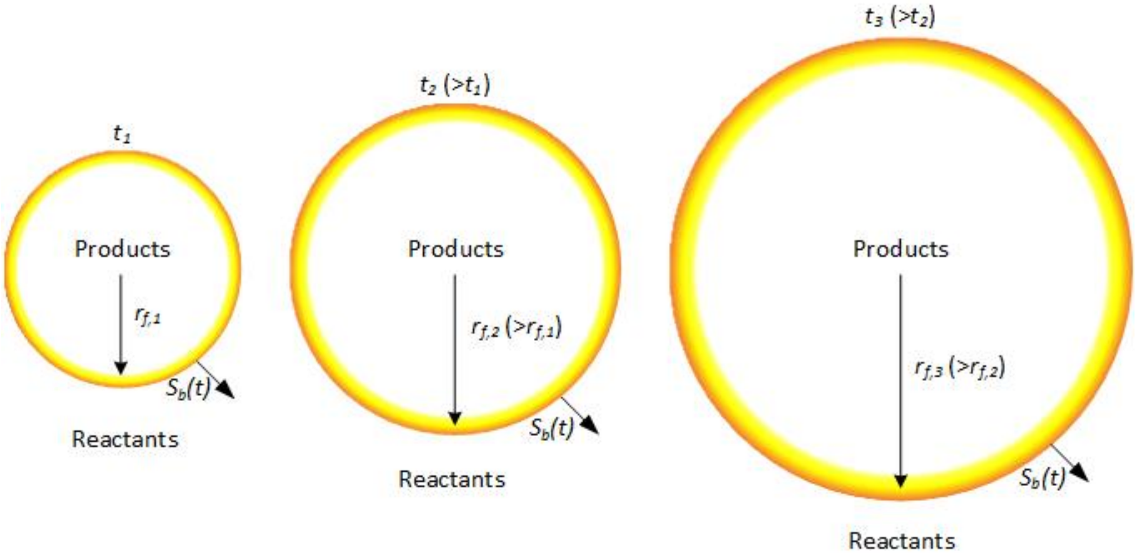

Figure 13. Illustration of an outwardly propagating spherical flame.

Since the propagating flame front is spherical/curved, it does not conform to the planar laminar flame speed. Therefore, the stretch needs to be evaluated to determine the unstretched/planar laminar flame speed. The flame stretch rate can be defined by the equation below for spherical symmetric flames [73].

$$\kappa = \frac{1}{A_f} \cdot \frac{dA_f}{dt} = \frac{2S_b}{r_f}$$ Eq. 2.

To obtained the laminar flame speed and the Markstein length, the calculated flame speed data must be extrapolated to a zero stretch rate. The Markstein length is related to the stretch rate influence on the flame speed. Furthermore, the Markstein length is also closely linked to the thermal-diffusive instabilities discussed in section 2.2.2 [31]. Table 2 summarizes the most common stretch extrapolation models used in this study to evaluate the laminar flame speed.

Table 2. Stretch extrapolation models[74]

Model name/description	**Expression**	**Ref.**
Linear stretch (LS) model	$S_b = S_b^0 - \frac{2L_b \cdot S_b}{r_f}$	[31,73]
Linear curvature (LC) model	$S_b = S_b^0 \left(1 - \frac{2L_b}{r_f}\right)$	[67] [68]
Non-linear model with 3 fitting parameters (N3P)	$S_b = S_b^0 \left(1 - \frac{2L_b}{r_f} + \frac{c}{r_f^2}\right)$	[77]
Non-linear (NQ) model in expansion form	$S_b^0 t + c = r_f + 2L_b \ln(r_f) - \frac{4L_b^2}{r_f} - \frac{8L_b^3}{3r_f^2}$	[78]
Quasi-steady (NE) non-linear model	$\left(\frac{S_b}{S_b^0}\right)^2 \cdot \ln\left(\frac{S_b}{S_b^0}\right) = -\frac{4L_b \cdot S_b}{S_b^0 \cdot r_f}$	[79,80]

The LBV can be evaluated from the continuity equation shown in Eq. 3, assuming equilibrium between the unburnt and burnt states. However, for nitro-methane and air mixtures at 432 K, Nauclér et al. [81] found that spherical flames with radii between 6.5 to 20 mm had not reached equilibrium. Therefore, the assumption of equilibrium may cause errors in the estimation of the LBV.

$$S_u \rho_u = S_b \rho_b$$ Eq. 3.

The pressure will increase as the flame propagates in a closed/constant volume vessel and heat the reactants and products due to the compression. However, if the vessel is sufficiently large, the temperature and pressure during the radii measurements can be considered quasi-steady and therefore neglected. The temporal evolution of the temperature and pressure must be recorded together with the radii for smaller vessels.

With the dual/double-chambered vessel developed by Tse, Zhu & Law [31,82], near-constant pressure measurements of the LBV have been achieved up to 60 atm. The outer chamber is filled with an inert gas balanced with the combustible gas in the inner chamber. The pressure build-up is therefore only generated by the inner chamber.

2.2.2 Flame Acceleration

When a quiescent combustible mixture is ignited, the flame initially propagates as a laminar burning flame. However, flames are inherently unstable, and at some point, the smooth flame surface will be distorted and wrinkled [30]. By distorting and wrinkling the flame surface, the flame area increases and thus accelerates the flame. The flame surface distortion and wrinkling can be caused by instabilities, turbulence, and interaction with geometry. In this section, an introduction to flame front instabilities and reacting turbulent flow is given. Flame front instabilities have not been addressed in detail to limit the scope of this study. However, due to their significant influence on flame acceleration, a brief review is given. For a more comprehensive review of flame front instability, the work by C.K Law in Combustion Physics [31], G. Searby and S. Candel in Combustion Phenomena [83], and S.B. Dorofeev [84], is recommended.

2.2.2.1 Hydrodynamic instability

Hydrodynamic instability, also referred to as Darrieus-Landau instability, is caused by the expansion of the gas through the flame. Consider an infinitely thin flame (flame sheet structure) where the far upstream and downstream states are at constant density (ρ_u and $\rho_{b)}$, as shown in Figure 14. With the flame as the frame of reference, where the streamlines are perpendicular to the flame surface, the streamlines will accelerate thru the flame without deviating. However, the streamlines alter their trajectory where the flame's surface is curved due to density and minor pressure gradients. Thus, the upstream flow must accelerate and deaccelerate at the concave and convex regions, respectively, to conserve mass. Therefore, a perturbation to a flat flame surface will grow due to hydrodynamic instabilities.

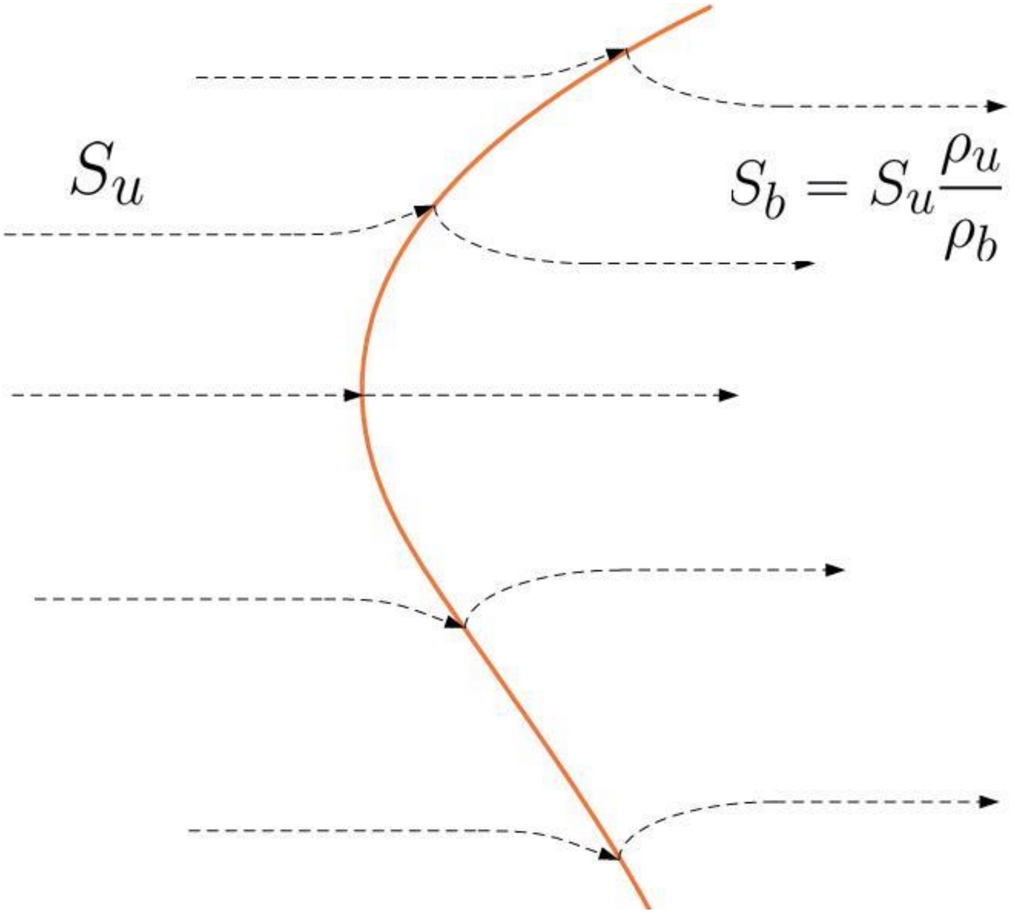

Figure 14. Hydrodynamic instability is illustrated by the diverging streamlines in a curve flame front [83]

2.2.2.2 Thermal-diffusive instability

Figure 10 shows the flame sheet structure with an expanded preheat zone (also called the diffusion zone), with a characteristic length L_D. With the flame as a frame of reference, mass diffuses downstream in the preheat zone, and heat diffuses upstream. The ratio of this diffusion is called the Lewis number and is defined by Eq. 4.

$$Le = \frac{\alpha}{D_m} = \frac{\lambda}{\rho D_m C_p} \qquad \text{Eq. 4.}$$

Mixtures with a Lewis number less than unity may experience thermal-diffusive instabilities. Conversely, mixtures with a Lewis number equal or greater than unity are considered thermal-diffusive stable. Furthermore, an additional stabilizing effect arises for a curved flame surface independent of the Lewis number. For example, consider the curved flame surface in Figure 15. The flame speed is reduced in the convex (unburnt side) part of the flame and increased in the concave section of the flame. Over time, this will smooth out the curvature [31].

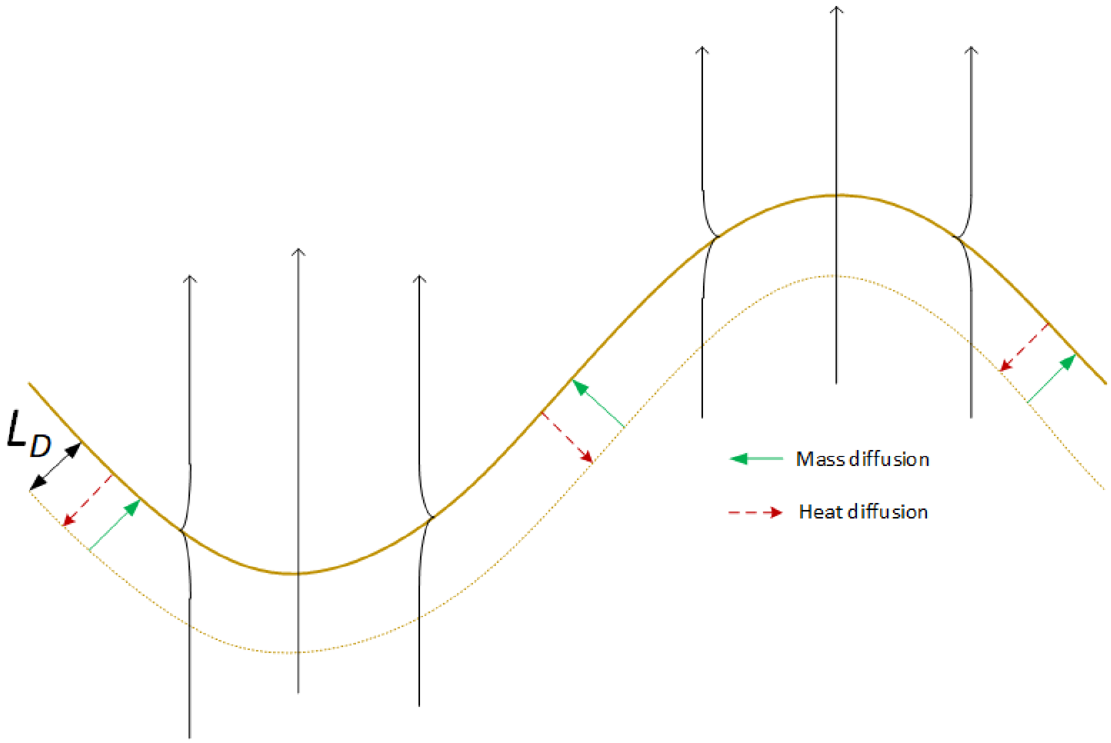

Figure 15. Illustration showing the mechanism of thermal-diffusive instability [83]

2.2.2.3 Rayleigh-Taylor instability

Rayleigh-Taylor instabilities can occur naturally in freely propagating flames as buoyancy-driven instabilities. For example, Rayleigh-Taylor instabilities may occur for an upwardly propagating flame due to the negative density stratification between the burnt and unburnt gas. Hence, Rayleigh-Taylor instabilities occur when a lighter fluid is accelerated into a heavier fluid [31]. Although Rayleigh-Taylor instabilities occur for freely propagating flames, the contribution to flame acceleration is usually relatively low. However, for confined flames and vented explosions, the Rayleigh-Taylor instabilities can cause significantly flame acceleration [85]. In addition, the Rayleigh-Taylor instabilities can be a source for turbulence by producing vorticity when pressure and density gradients are oblique to the interface [86].

Furthermore, the Richtmyer-Meshkov instability can be triggered when a shock passes over an interface separating two fluids with different densities, such as reactants and products. The Richtmyer-Meshkov instability corresponds to the Rayleigh-Taylor instability for compressible flow. For example, as a shock passes through a curved or corrugated flame front, the transmitted shock will alter its shape (compared to the incident shock) and generate pressure and density gradients, disturbing the flame front.

2.2.2.4 Kelvin-Helmholtz instability

Kelvin-Helmholtz instabilities occur at the interface separating two fluids flows with different densities in shear flow. Initially, the interface will start to be slightly rippled. However, as the Kelvin-Helmholtz instability grows, larger vortices can cause the interface to "roll-up," and ripples will turn into waves. A typical example is the formation of ripples and waves in the ocean due to the wind. Moreover, this instability will increase the flame surface area and mixing, thus, accelerate the flame propagation.

2.2.2.5 Acoustically induced instability

Instabilities caused by acoustic waves can occur when the radiated sound from combustion resonance with the surrounding system [83]. Sound and pressure waves cause small perturbations in the flame front, making it unstable. Thermo-acoustic instabilities significantly impact the stability of high-performance combustion systems, such as gas turbines and jet engines. These instabilities can cause fluctuations in heat release and heightened vibrations, increasing the fatigue of the system.

2.2.2.6 Premixed turbulent flames

As discussed, a planar laminar premixed flame is inherently unstable. However, the discussed instabilities consider only a flame propagation into a quiescent or laminar flow of unburnt mixture, which is rarely the case. However, the unburnt mixture ahead of the flame can be accelerated in confined explosions and may become turbulent depending on the velocity and the surrounding geometry. For example, in internal combustion engines (ICE) and gas turbines, the unburnt mixture ahead of the flame is already turbulent. As the premixed flame propagates into the turbulent unburnt mixture, the flame front will be stretched and wrinkled and thus affect the propagation speed.

Turbulence can have a tremendous influence on flame acceleration, and for specific turbulent flows, the flame can even lead to extinction. However, before categorizing the different turbulent flame regimes shown in Figure 16, it is helpful to establish two characteristic turbulent length scales.

- The integral length scale (ℓ_0) is the macroscopic turbulent length scale. The integral scale eddies are in the order of the confinement or phenomena of study. A characteristic velocity fluctuation (u_0') can be identified at the integral scale.
- Kolmogorov length scale (ℓ_K) is the turbulent microscale. In this turbulent scale, the turbulent kinetic energy dissipates into internal energy.

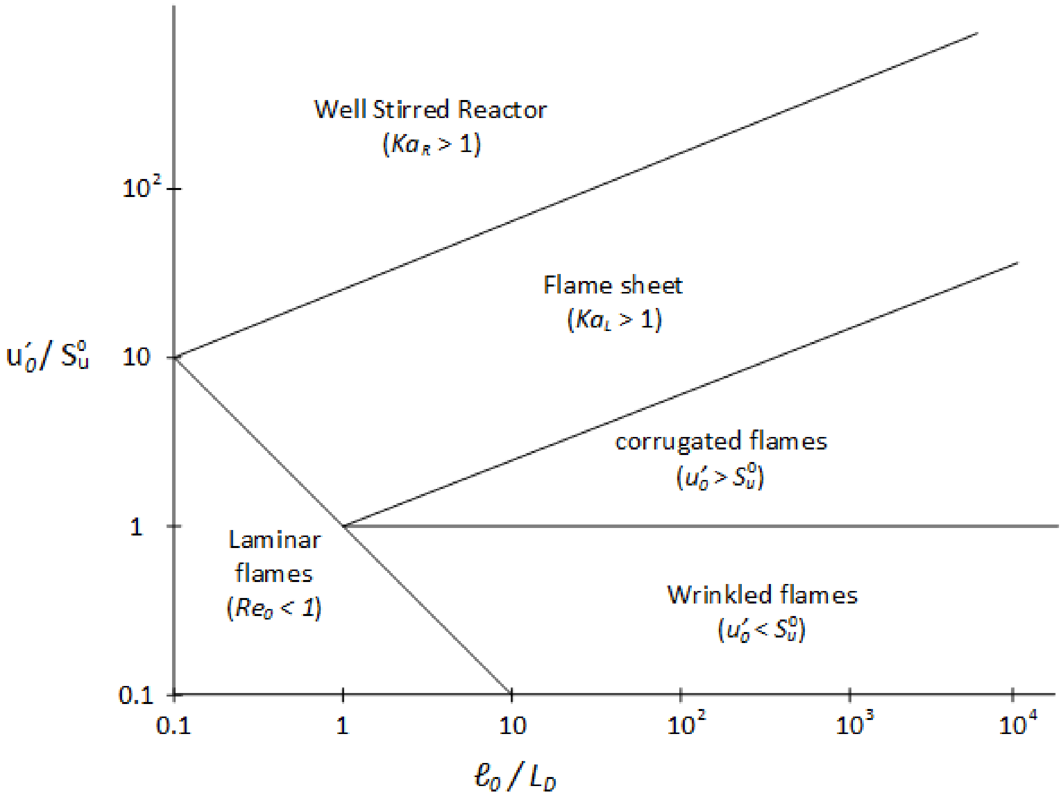

Figure 16. Phase diagram of different regimes of premixed turbulent combustion [31]

Laminar flames Regime: In this regime, there is little to no turbulence, and the flame propagates with the laminar flame structure shown in Figure 11, with a minimum of flame wrinkling.

Wrinkled flame regime: In this regime, the characteristic velocity fluctuation (u_0') is less than the laminar burning velocity (S_u^0). Since u_0' is less than $S_{u,}^0$ the eddies will only have a weak interaction with the flame front and make it slightly wrinkled. However, the flame will still maintain the laminar flame structure.

Corrugated flame regime: When u_0' is larger than S_u^0, there will be a strong flame-vortex interaction, which means the flame can become highly convoluted. Although the flame is highly convoluted, the flame will still have a laminar flame structure because Ka_L ($Ka_L=(L_D/\ell_K)^2$) is smaller than 1.

Flame sheet regime: For regimes where Ka_L is larger than one, the smaller eddies can penetrate the preheat zone (L_D), enhancing the heat and mass transfer in the flame. However, since Ka_R ($Ka_R=(L_R/\ell_K)^2$) is less than one, the eddies will not penetrate the reaction zone. Thus, the flame will still have the laminar flame structure but with an expanded preheat zone.

Well stirred Reactor regime: When Ka_R is larger than one, the eddies can penetrate the reaction zone (L_R) since they are smaller than L_R. As a result, the flame no longer has a distinct structure and can be considered more like a well-stirred reactor. In this regime, the flame can extinguish due to increased heat and mass transfer in the reaction zone, lowering the flame temperature.

For all regimes where Ka_L is smaller than 1, the flame retains its local laminar structure and is called a laminar flamelet. Therefore, the relationship between the laminar and turbulent burning velocity in the laminar flamelet approach can be related to the difference in flame surface area. Thus, the turbulent burning velocity can be expressed by Eq. 5 [87,88]. In Eq. 5, the ratio between the turbulent and laminar surface area (A_T and A_L, respectively) reports the increase in flame surface area due to the turbulence.

$$S_T = S_L \frac{A_T}{A_L} \tag*{Eq. 5.}$$

2.2.3 Detonations

If a combustion wave keeps accelerating, it will eventually reach a point when the propagation suddenly transitions from deflagration to detonation (DDT). A detonation is defined as a supersonic combustion wave relative to the unburnt gas. This study has not investigated detonations or DDT of LIB vent gases to limit the focus. Furthermore, DDT was not observed in the flame acceleration experiment nor the numerical simulations. However, a short introduction is given so readers can distinguish deflagration from detonations. For more information on detonation and DDT, the studies by J.H.S. Lee (1977) [89], Shepherd and Lee (1992) [90], and J.E. Shepherd (2009) [91], is recommended.

In the ZND model, the detonation is considered one-dimensional and described as a wave with a reaction zone with a leading shock [31]. The leading shock heats the unburnt reactants and initiates the reactions. A thermal explosion in the reaction zone emits a compression wave, which maintains the leading shock. However, the 1-dimensional ZND theory is a simplification of an actual detonation, which is a more complex and highly 3-dimensional phenomenon.

Detonations can have severe consequences in accidental explosions. As mentioned, the detonation wave propagates above the speed of sound, which causes the unburnt gas ahead to be undisturbed. Supersonic propagation makes explosion mitigation methods such as deflagration panels and vent areas with little to no success [84]. In addition, a detonation wave initiated at ambient pressures can generate maximum pressures close to 2000 kPa (gauge), which can cause massive destruction of equipment and structures [30].

Finally, although a deflagration is a subsonic combustion wave relative to the unburnt gas ahead, it can still seem supersonic relative to the stationary observer (laboratory reference frame). The distinction between burning velocity and displacement speed causes some confusion.

3 Experimental Setup and Computational tools

This chapter presents the experimental setups and computational tools used in this thesis. The chapter is divided into four sections, the 20-liter explosion sphere, the 1-meter explosion channel, numerical methods used in Cantera, and the computational fluid dynamic (CFD) model/solver XiFoam in OpenFOAM.

3.1 20-liter Explosion Sphere

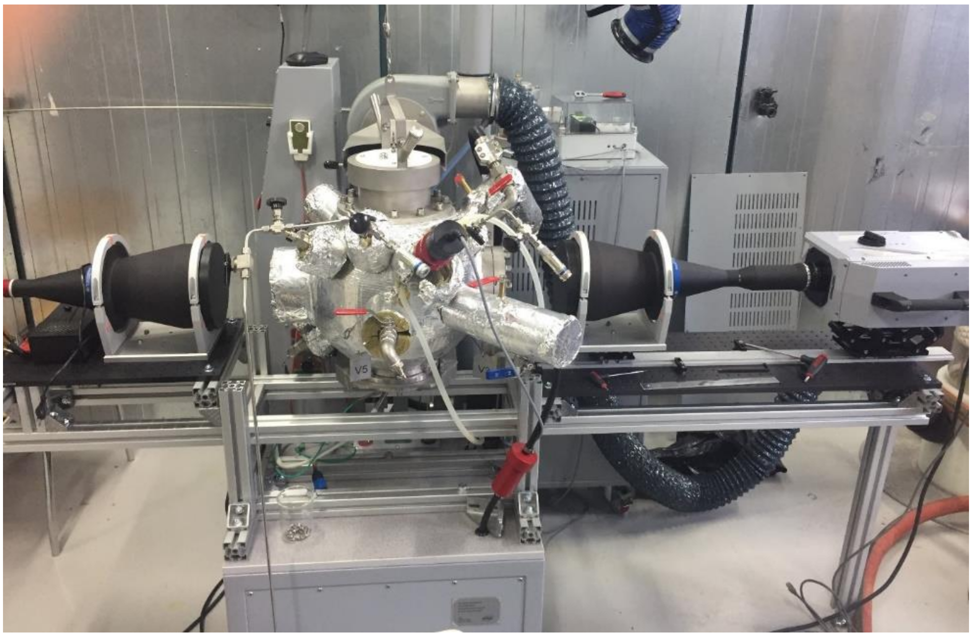

Figure 17. Photo of the 20-liter explosion sphere[74]

The explosion sphere in Figure 17 has an internal volume of 20.4 dm^3. Surrounding the sphere is a heating jacket, which controls the internal/ambient gas temperature. At the bottom of the vessel, there is a heating plate with a separate temperature controller for evaporating liquids. There are three filling ports, each dedicated for either liquid fuel, gaseous fuel, or oxidizer. A Keller PAA-33X pressure transducer records the pressure during the filling process to get the partial pressures for each component added. An internal fan mixes the ambient gas to ensure a homogeneous mixture is achieved before ignition.

Two types of ignition systems have been used, ignition/exploding wire and electrical spark. The ignition wire was used when studying the explosive limits because of its high-energy release. For all other experiments, the spark ignition system was used. An ignition coil was used as the ignition system when measuring the LBV. The ignition coil had a primary inductance of 8.0 mH and was charged with 12 V to 15 V. Two metal wires with a diameter of 1 mm and a variable spark gap between 0.5 and 2 mm were connected to the ignition coil. A single spark with an energy of approximately 100 mJ and 30 kV was used to ignite the gas mixture. Two Kistler 601CAA pressure transducers measured the temporal evolution of the explosion pressure.

There are two circular windows with a diameter of 100 mm on opposite sides, providing optical access to the chamber. The flame propagation was recorded using the focused shadowgraph imaging technique and a Photron SA-Z high-speed camera operating at 20 000 frames per second (fps). The focused shadowgraph imaging technique is achieved using a lamp that emits collimated light and a camera with a telecentric lens [92]. Figure 18 shows a schematic illustration of the 20-liter explosion sphere experimental setup.

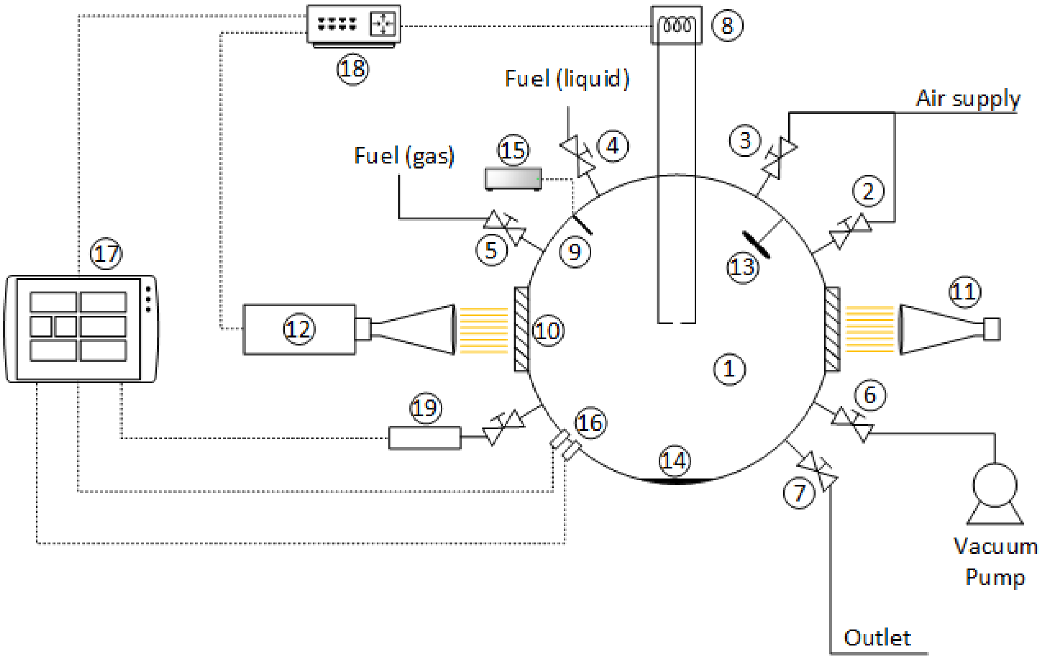

Figure 18. Schematic of the experimental setup [28]. 1: explosion chamber; 2: oxidizer inlet; 3: flush inlet; 4: fuel (liquid) injection port; 5: fuel (gas) inlet; 6: vacuum port; 7: gas outlet; 8: ignition system; 9: thermocouple; 10: glass windows (100 mm); 11: LED light source; 12: high-speed camera; 13: stirrer; 14: heating plate; 15: ambient temperature display; 16: dual explosion pressure sensors; 17: data acquisition system; 18: control/trigger unit and 19: ambient pressure sensor

3.1.1 General Experimental Procedure

The explosion sphere was purged with compressed and oil-free air for a minimum of five minutes before each experiment. Purging for five minutes resulted in approximately 40 volume exchanges. The explosion sphere was evacuated after purging. Fuel was filled to the desired partial pressure, and then the sphere was filled with air to 100 kPa (±0.5 kPa, absolute). Air and fuel were actively mixed for three and a half minutes to ensure a homogeneous mixture. After mixing, the temperature in the local display was manually registered. The ignition was delayed for one and a half minutes after mixing to ensure that the mixture was quiescent.

3.1.2 Determining the laminar burning velocity

The first step was determining the laminar flame speed using the outwardly propagating spherical flame method. From the high-speed video, the temporal evolution of the radius was measured using an in-house developed method coded in Python to analyze the digital images. The following points summarize the algorithm used for each image to extract the flame radius.

- Subtract background from the image and set all negative pixel values to zero
- Set threshold to distinguish the flame from the background in the image
- Store all pixels that are above the set threshold
- Find the outer perimeter and remove outliers in stored data.
- Curve fit outer perimeter to a circle and store the radius
- Print and store the control images (Figure 19).

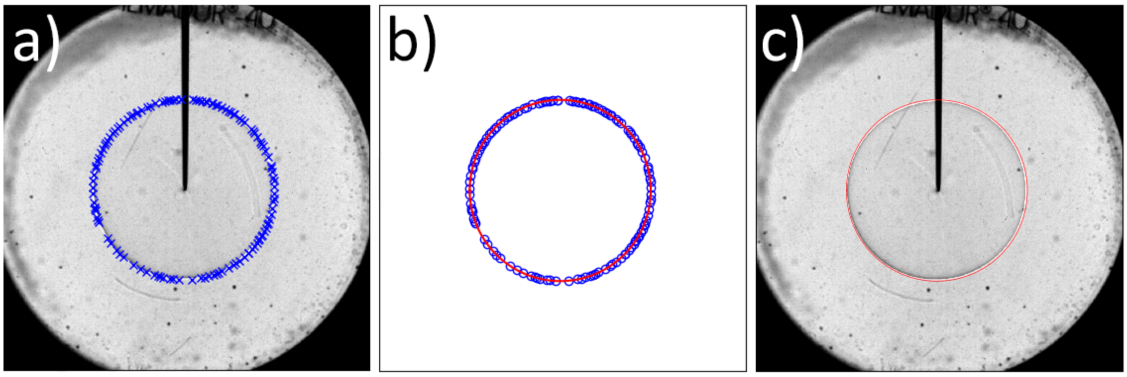

Figure 19. An example of the post-processed control images. a): High-speed image with the detected outer perimeter marked; b): The marked outer perimeter with the curve fitted circle; c): High-speed image with the outer perimeter curve fitted circle.

The calculated rate of change in flame radius (*dr/dt*) can be defined as the flame speed. By curve fitting the calculated flame speed and the radius to any of the equations in Table 2 gives the Markstein length (L_b) and the laminar flame speed (S_b^0). The LBV is calculated by assuming equilibrium between the unburnt and burnt state (Eq. 3). The linear stretch (LS) model in Table 2 was used to calculate the laminar flame speed and Markstein length in Proceeding A, *Laminar burning velocity measurements for an outwardly propagating flame of dimethyl carbonate and air mixtures* [90].

Article B, *Laminar Burning Velocity of the Dimethyl Carbonate-Air Mixture Formed by the Li-Ion Electrolyte Solvent* [74], presents another approach for calculating the Markstein length and the laminar flame speed. The stretch extrapolation models in Table 2 were converted to differential equations by substituting the flame speed (S_b) with *dr/dt*. These differential equations can be analytically solved, which gives equations that are implicit functions of radius and time (except the non-linear model). In Table 3, the solved implicit equations for all stretch extrapolation models in Table 2, except the non-linear model NQ. This approach was used in Articles B and C.

Table 3. Implicit functions of radius derived from the flame stretch model equations found in Table 2[74]

Model name	**The implicit function of $r_f(t)$**
Linear stretch (LS) model	$r_f = S_b^0 t - 2L_b \ln r_f + Cst$
Linear curvature (LC) model	$r_f = S_b^0 t - 2L_b \ln\left(r_f - 2L_b\right) + Cst$
Non-linear model with 3 fitting parameters (N3P, A > 0)	$r_f = S_b^0 t - L_b\left(r_f^2 - 2L_b r_f + c\right) - \frac{2L_b^2 - c}{2\sqrt{A}} \ln\left(-\frac{r_f + \sqrt{A} + L_b}{r_f + \sqrt{A} - L_b}\right) + Cst$
Non-linear model with 3 fitting parameters (N3P, A < 0)	$r_f = S_b^0 t - L_b\left(r_f^2 - 2L_b r_f + c\right) - \frac{2A}{\sqrt{-A}} \operatorname{atan}\left(\frac{r - L_b}{\sqrt{-A}}\right) + Cst$
	$A = L_b^2 - c$
Non-linear (NQ) model in expansion form	$r_f = S_b^0 t + c - 2L_b \ln\left(r_f\right) + \frac{4L_b^2}{r_f} + \frac{8L_b^3}{3r_f^2}$

3.2 The 1-meter Explosion Channel

Figure 20. Photo of the 1-meter explosion channel

The premixed flame acceleration experiments were conducted in a 1-meter-long rectangular open-ended channel, with a height of 116.5 mm and a width of 65 mm. Separate rotameters for fuel and air controls the volume flow to the channel. All rotameters were calibrated with a Ritter drum-type gas meter for each gas analyzed. The premixed gas inlet was located 50 mm from the back end/wall of the channel, with the flow controlled by a pneumatic on/off valve. There was a porous lid at the open end of the channel during filling to avoid gravity currents and stratification. The lid was released slightly before ignition. A 230 V AC transformer with an output voltage of 10 kV RMS and a current of 20 mA generated the high voltage spark. A maximum of two sparks (in atmospheric conditions) was generated within a total duration of 20 ms. The spark duration was controlled by switching on/off the power to the transformer. Four Kistler 7001 pressure transducers measured the explosion pressure. The first pressure transducer was located 250 mm from the back end of the channel, with the rest of the transducers separated with an equal interval of 200 mm. A Photron SA1.1 high-speed camera recorded the flame propagation with frame rates between 2000 and 20 000 fps. Figure 21 shows a schematic illustration of the experimental setup used in Article D and Article E.

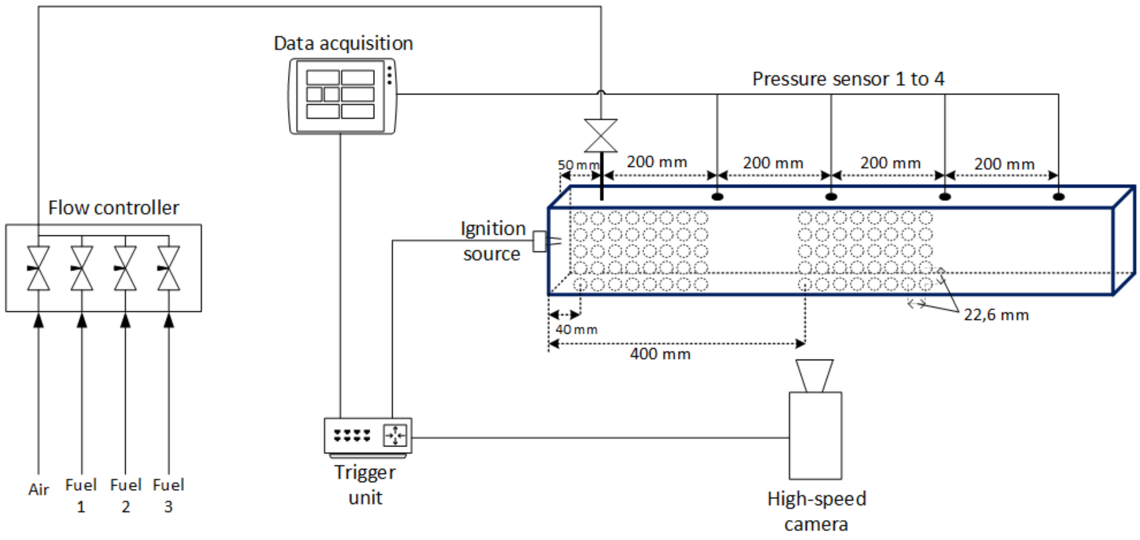

Figure 21 Schematic illustration of the experimental setup with dimensions

3.2.1 General Experimental Procedure

Before each experiment, the channel was purged with air for 5 minutes, resulting in a volume exchange of approximately ten times. A porous lid was attached at the open end before filling premixed fuel and air. After the lid was attached, the rotameters were adjusted accordingly to give the desired fuel-air equivalence ratio for the experiment. The premixed gas was flushed to achieve a minimum of 8 volume exchanges before the gas inlet was closed. There was a 1-minute delay before ignition to reduce the convective flow in the channel. After the 1-minute ignition delay, the porous lid was released, immediately followed by ignition.

3.2.2 Determining the flame front position and velocity

The method for tracking the flame front is based on the algorithm presented in section 3.2.2. The following points summarize the algorithm used for each image in the high-speed video to extract the flame front position. Figure 22 shows an example of the generated images after the image-processing.

- Subtract background from the image and set all negative pixel values to zero
- Set threshold to distinguish the flame from the background in the image
- Remove noise in the image and store all pixels that are above the threshold
- From stored data, find the outer perimeter of the flame.

- Find the rightmost position in the outer flame perimeter data
- Store flame front position and control images (Figure 22)

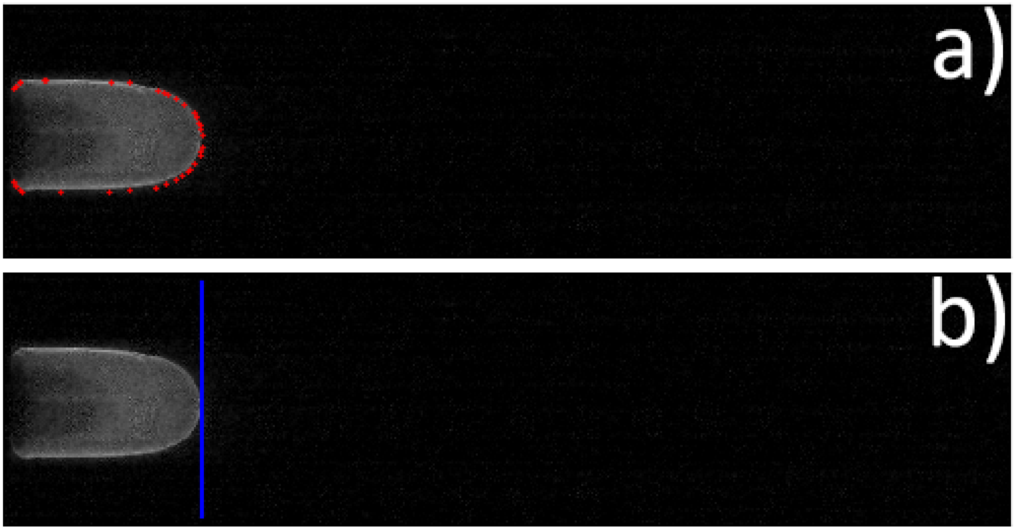

Figure 22. An example of the post-processed control images generated for each high-speed image in an experiment. a): High-speed image with outer flame contour; b): High-speed image with flame front position marked with a vertical line.

The flame front position was filtered with a Savitzky-Golay filter [93] before calculating the flame front velocity using a second-order accurate central differencing equation. Figure 23 shows an example of the output data from one experiment, including the recorded explosion pressure from the four pressure sensors and the temporal evolution of the flame front position and velocity.

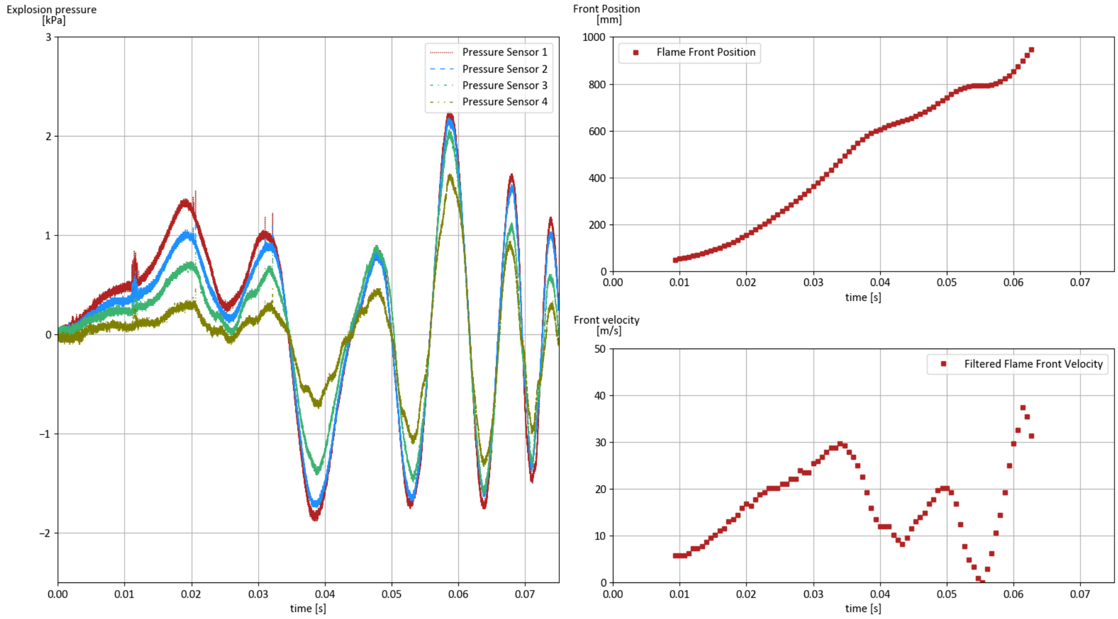

Figure 23. Example of the experimental results from a single experiment

Figure 24 shows the three different configurations of the 1-meter channel studied. The empty channel was studied in Article D, *Simulation of a Premixed Explosion of Gas Vented During Li-Ion Battery Failure*. The obstructed channels were studied in Article E, *Numerical Study of Premixed Gas Explosion in a 1-meter Channel Partly Filled with 18650 Cell-like Cylinders with experiments*. The obstructions consisted of 40 cylinders, where each cylinder had a diameter of 18 mm and a length of 650 mm and had an equal distance of 4.6 mm from each other. In one experimental series, the cylinders were near the back end of the channel. In the other experimental series, the cylinders were placed approximately in the center of the channel.

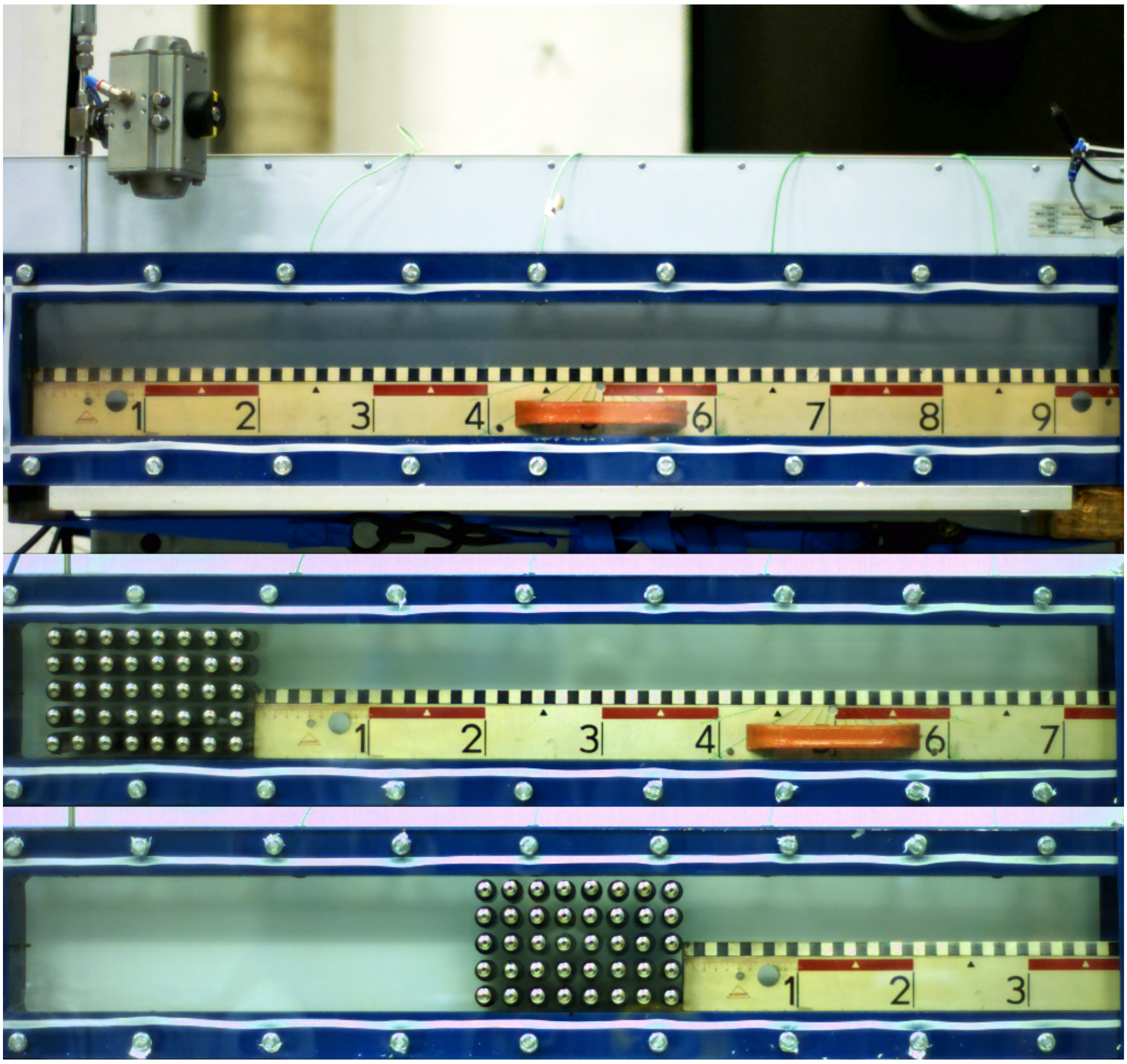

Figure 24. Calibration photos of the three different channel geometries

3.3 Cantera – Predicting Combustion Properties

Cantera is an open-source set of routines for solving problems of thermodynamics, chemical kinetics, and transport processes [94]. It has a broad specter of applications, including combustion, detonations, electrochemical energy, fuel cells, batteries, and more. Cantera can run on multiple interfaces, most commonly Python and Matlab, and applications written in C/C++ and Fortran 90. In this study, Cantera version 2.3.0 and 2.4.0 were used exclusively in a Python environment.

3.3.1 Closed volume explosion pressure calculation

To predict the closed volume explosion pressure, the thermodynamic equilibrium solver *equilibrate* was used. Equilibrate solves for the composition with minimum Gibbs free energy at constant internal energy and volume.

3.3.2 Laminar burning velocity calculations

In Cantera, the FreeFlame routine was used to predict LBVs. The FreeFlame routine solves the governing equations (Eq. 6., Eq. 7., and Eq. 8.) for a steady-state solution of 1-D freely propagating, planar, and adiabatic flame.

Continuity equation,

$$\dot{m} = \rho u A = constant$$

Eq. 6.

Conservation of species,

$$\rho u \frac{\delta Y_i}{\delta x} + \frac{\delta J_i}{\delta x} = \dot{\omega}_i W_i$$

Eq. 7.

Conservation of energy,

$$\rho u C_p \frac{\delta T}{\delta x} = \frac{\delta}{\delta x}\left(\lambda \frac{\delta T}{\delta x}\right) - \sum_i h_i \dot{\omega}_i W_i - \sum_i J_i C_{p,i} \frac{\delta T}{\delta x}$$

Eq. 8.

Where, $\dot{m}$ is the mass flow; ρ is the density; u is the velocity; A is the area; Y_i is the mass fraction of specie *I*; J_i is the diffusive mass flux of specie *i*; ω_i is the molar reaction rate of specie *i*; W_i is the mole weight of specie *i*; C_p is heat capacity; T is temperature; λ is thermal conductivity; h is the enthalpy of specie *I*; $C_{p,i}$ is the heat capacity of specie *i.*

Two boundary conditions are needed to solve the equations above. The cold boundary conditions are the initial temperature and gas composition (T, Y_i, respectively), with their derivatives equal to zero. An equilibrium calculation determines the temperature and gas composition at constant pressure and enthalpy for the hot boundary conditions.

The temperature and species mass fraction derivatives are set equal to zero at the hot boundary. Finally, the mass flow or the velocity is solved as an eigenvalue of the governing equations.

3.3.3 Reaction mechanisms

A reaction mechanism/model (also referred to as a chemical kinetics model) is required to calculate the combustion properties with detailed chemistry for a combustible mixture. A reaction mechanism contains elementary reactions and the corresponding chemical kinetics, thermodynamic, and transport properties for the included species and reactions. The NASA polynomials usually express the thermodynamic properties for heat capacity (C_P), enthalpy (h), and entropy (s) [95]. The transport properties, viscosity, diffusion, and heat conduction are evaluated using the Leonard-Jones parameters [96].

Five different reaction mechanisms have been used to predict combustion properties in this thesis. The points below give a short description of each mechanism and in which articles they were used.

- Glaude et al. [97] developed a reaction mechanism for the dimethyl carbonate (DMC) oxidation process to study DMC as an oxygenate additive to diesel. The mechanism contains 102 species and 257 reactions, with ethane (C_2H_6) being the largest alkane. The reaction mechanism was used in articles A, B, and C and can be found at the Lawrence Livermore National Laboratory Combustion website, https://combustion.llnl.gov/

- Nakamura et al. [98] developed a reaction mechanism for an oxidation process of diethyl carbonate (DEC) to study DEC as a biofuel additive to petroleum-derived diesel. The mechanism contains 355 species and 2163 reactions, with n-pentane (nC_5H_{12}) being the largest alkane. This reaction mechanism was only used in article A to predict the closed volume explosion pressure.

- GRI-Mech 3.0 [70] is designed for natural gas combustion; it contains 53 species and 325 reactions, with propane (C_3H_8) being the largest alkane. The reaction mechanism was used in articles A, C, and E, and can be found at the GRI-Mech homepage, http://combustion.berkeley.edu/gri-mech/

- Sun et al. [99] developed a reaction mechanism to study the combustion and pyrolysis process of dimethyl carbonate (DMC). The mechanism contains 257 species and 1563 reactions, with butane (C_4H_{10}) being the largest alkane. The reaction mechanism was used in articles B and C and can be found under supplementary materials to the original publication [99].

- The San Diego reaction mechanism [100] is designed to suit a wide range of combustion and detonation processes. It includes 57 species and 268 reactions, with butane (C_4H_{10}) being the largest alkane. The reaction mechanism was used in articles C and D and can be found on the homepage of Combustion Research at UC San Diego http://web.eng.ucsd.edu/mae/groups/combustion/index.html.

3.4 OpenFOAM - Computational Fluid Dynamic

The computational fluid dynamics (CFD) toolbox OpenFOAM is an open-source software containing extensive features to solve problems such as fluid flows, turbulence, heat transfer, and combustion [34]. This study used the XiFoam model/solver for combustion simulations exclusively from versions 6 and 7 of OpenFOAM [35].

3.4.1 Pre-processing

Pre-processing consists of mesh generation, defining the boundary conditions and the initial conditions. SnappyHexMesh in the OpenFOAM software package was used to generate the mesh from stereolithography (STL) computer-aided design (CAD) drawing created in Onshape, the online CAD tool [101]. Articles D and E document the geometry, computational mesh, boundary conditions, and initial values used for each simulation case.

3.4.2 XiFoam – Combustion modeling

In XiFoam, the flame modeling is based upon the laminar-flamelet approach [88], which assumes that the turbulent premixed flame comprises a group of laminar flamelets. For premixed combustion, the flame can be expressed as a progress variable or a regress variable. XiFoam uses a regress variable (b) connected to progress variable (c) by Eq. 10, where b equals 1.0 is unburnt, and burnt is b equals 0. Progress variable c can be calculated by Eq. 9.

$$c = \frac{Y_F - Y_{F,u}}{Y_{F,b} - Y_{F,u}} \qquad \text{Eq. 9.}$$

$$b = 1 - c \qquad \text{Eq. 10.}$$

Where: c is the combustion progress variable; Y_F is the fuel mass fraction; $Y_{F,u}$ is the unburnt fuel mass fraction; $Y_{F,b}$ is the burnt fuel mass fraction; b is the combustion regress variable.

The flame propagation is modeled by solving the transport equation for the regress variable *b*. The equations below show the combustion model proposed by Weller et al. [102,103] and the transport equation implemented in XiFoam.

$$\frac{\partial}{\partial t}(\rho b) + \nabla \cdot (\rho \boldsymbol{u} b) - \nabla \cdot (\rho \mathcal{D} \nabla b) = -\rho S_c \qquad \textit{Eq. 11.}$$

$$\rho S_c = \rho_u S_u \Xi |\nabla b| \qquad \textit{Eq. 12.}$$

$$\frac{\partial}{\partial t}(\rho b) + \nabla \cdot (\rho U b) - \nabla \cdot (\nabla \cdot \rho \mathcal{D} b) = -\rho_u S_u \Xi |\nabla b| \qquad \textit{Eq. 13.}$$

Where: ρ is the density; *b* is the combustion regress variable; ***u*** is the velocity vector, $\mathcal{D}$ is the subgrid thermal diffusion coefficient; S_C is the combustion source term; ρ_u is the unburnt density; S_u is the laminar burning velocity; Ξ is the subgrid wrinkling factor.

Part of the source term is the flame subgrid wrinkling factor, Ξ, which can be regarded as the ratio between the turbulent and laminar burning velocity (Eq. 5). Ξ can be evaluated by three methods, constant, algebraic, and transport. The equations below show the different methods, where Eq. 14 is the transport equation, and Eq. 15 and Eq. 16, as the algebraic equations. For more information about Ξ equations and how to evaluate the terms in Eq. 14, see the original publications by Weller et al. [102,103].

$$\frac{\partial \Xi}{\partial t} + \hat{\tilde{U}}_s \cdot \nabla \Xi = \mathrm{G}\Xi - \mathrm{R}(\Xi - 1) + (\sigma_s - \sigma_t)\Xi \qquad \textit{Eq. 14.}$$

$$\Xi_{eq}^{*} = 1 + 0.62\sqrt{\left(\frac{u'}{S_u}\right)\mathcal{R}_\eta} \qquad \textit{Eq. 15.}$$

$$\Xi_{\mathrm{eq}} = 1 + 2(1-b)\left(\Xi_{eq}^{*} - 1\right) \qquad \textit{Eq. 16.}$$

Where: U_s is the surface filter velocity; *G* is the turbulence generation rate; *R* is the turbulence removal rate; σ_s is the surface-filtered strain rate; σ_t is the resolved strain rate; *u'* is the subgrid turbulence intensity; S_u is the laminar burning velocity; $\mathcal{R}_\eta$ is the Kolmogorov Reynolds number.

The LBV (S_u in Eq. 13) is calculated using the Gülder flame speed correlation proposed by Ömer L. Gülder [104], shown in Eq. 17. The Gülder equation consists of six model coefficients, where five must be determined for a fuel and oxidizer composition. A detailed description of the fitting process and the complete code is given in supplementary data A [105].

$$S_L(\phi, T, p) = \omega\phi^{\eta}e^{\xi(\phi-1.075)} \cdot \left(\frac{T}{T_{ref}}\right)^{\alpha} \cdot \left(\frac{p}{p_{ref}}\right)^{\beta} \cdot \left(1 - X_f \cdot f\right) \quad \text{Eq. 17.}$$

Where: S_L is laminar burning velocity; ϕ is the fuel-air equivalence ratio; T is the temperature; p is the pressure; ω is a model coefficient; η is a model coefficient; ξ is a model coefficient; T_{ref} is the reference temperature; α is a model coefficient; p_{ref} is the reference pressure; β is a model coefficient; X_f is the mole fraction of inert that is not part of the fuel and oxidizer mixture, f is a model constant.

3.4.3 Thermodynamic modeling

The gas was modeled as an ideal gas with the heat capacity (C_P), enthalpy (h), and entropy (s) evaluated by the NASA polynomials [95] shown in the equations Eq. 18, Eq. 19, and Eq. 20. The NASA polynomials consist of 7 polynomial coefficients which are specific for the composition.

$$\frac{C_p(T)}{R_u} = a_0 + a_1T + a_2T^2 + a_3T^3 + a_4T^4 \quad \text{Eq. 18}$$

$$\frac{h(T)}{R_u} = a_0T + \frac{a_1T^2}{2} + \frac{a_2T^3}{3} + \frac{a_3T^4}{4} + \frac{a_4T^5}{5} + a_5 \quad \text{Eq. 19}$$

$$\frac{s(T)}{R_u} = a_0 \ln T + a_1T + \frac{a_2T^2}{2} + \frac{a_3T^3}{3} + \frac{a_4T^4}{4} + a_6 \quad \text{Eq. 20}$$

The Sutherland equation was chosen as the transport model to calculate the dynamic gas viscosity (μ) [106]. In the Sutherland equation below, two composition-specific coefficients (As and Ts) must be evaluated.

$$\mu = \frac{A_s\sqrt{T}}{1 + \frac{T_s}{T}} \quad \text{Eq. 21}$$

A detailed description of the determination of the NASA polynomials and the fitting procedure of the Sutherland equation is given in supplementary data A [105].

3.4.4 Turbulence modeling

In OpenFOAM, there are four main categories for handling turbulent flow, Reynolds-averaged Navier-Stokes (RANS) equations, Large eddy simulations (LES), Detached eddy simulations (DES), and Direct numerical simulations (DNS). Furthermore, there are several sub-models below the main turbulence approaches.

The turbulence is related to the mean flow and its properties for RANS simulations and is modeled by solving the time-averaged Navier-Stokes equations. In LES, the mean flow and the larger eddies are resolved. Before computations, the Navier-Stokes equations are spatially filtered to set the threshold between large and smaller eddies. Next, a sub-grid scale model computes the effect of the smaller eddies on the resolved flow. However, LES requires a higher resolution grid than RANS to resolve the larger eddies and thus more computationally demanding. The third turbulence model is the detached eddy simulation (DES), which combines LES and RANS modeling. The larger eddies in a free turbulent flow (detached eddies) are resolved, but eddies near a wall are modeled similarly to RANS simulations. DES does not require as fine a grid as LES and thus reduces the computational requirements. In DNS, there are no turbulence models, and thus all turbulent length scales must be resolved, requiring a grid with very high resolution.

Only the LES approach was used in this study. The simulations in Article D used the LES sub-grid stress model WALE proposed by Nicoud and Ducros [107], suited for unstructured meshes, complex geometries, and laminar to turbulent transition. The WALE model is based on the square of the velocity gradient tensor and has a near-wall scaling function without requiring a dynamic procedure.

Furthermore, in Article E, a turbulence model for compressible turbulent shear flows developed by Akira Yoshizawa [108] was used.

3.4.5 Post-Processing

For Post-processing, the open-source software ParaView was used. It is one of the most common post-processing software used with OpenFOAM and is integrated into the OpenFOAM software package.

4 Summary of Articles

This section contains summaries of each of the journal articles published in this study. For the complete manuscript for each article, see Part 2 of this thesis.

4.1 Article A: *Explosion characteristics for Li-ion battery electrolytes at elevated temperatures.*

4.1.1 Introduction

In this study, the explosion characteristics for the three electrolyte solvents, dimethyl carbonate (DMC), ethyl methyl carbonate (EMC), and diethyl carbonate (DEC), were analyzed in a 20-liter explosion sphere at 373 K and 100 kPa (absolute). The explosion characteristics determined were the explosion pressure (P_{ex}), the rate of explosion pressure rise ($(dp/dt)_{ex}$), and upper and lower explosive limits (UEL and LEL, respectively), which are critical parameters for consequence and risk assessments [30,89,109]. In addition, the results were compared with three common combustible gases, hydrogen (H_2), methane (CH_4), and propane (C_3H_8), and with theoretical calculations.

4.1.2 Methods and materials

The 20-liter explosion sphere and the procedure described in section 3.1 were used to obtain the experimental results. Due to the relatively low vapor pressure for DEC at 298 K, a temperature of 373 K was used. Two experiments (parallels) were conducted for each target concentration to determine the P_{ex} and $(dp/dt)_{ex}$ using a spark ignition system. Five experiments with no ignition using the exploding wire ignition method were performed to determine the UEL and LEL. All species analyzed had a purity of 99% or higher. For the theoretical calculations of P_{ex}, the equilibrate solver in Cantera was used to find the equilibrium state at constant volume and internal energy. The reaction mechanism used for DMC was published by Glaude et al. [97] and for DEC published by Nakamura et al. [98]. For hydrogen, methane, and propane calculations, GRI-Mech 3.0

[70] was used. No reaction mechanism for EMC was found, and thus no theoretical calculation of explosion pressure was performed.

4.1.3 Results and Discussion

Table 4 summarizes the experimental results for the electrolyte solvents. The three carbonates have similar explosion pressure and rate of explosion pressure rise, giving a minimal difference in the calculated vent area [89,109]. Since the results from all three carbonates are within the same range, the preliminary risk assessment may be simplified. However, carbonates will decompose into other species during a TR, such as hydrogen, carbon monoxide, carbon dioxide, and other hydrocarbons. The vent gas composition is dependent on the state of charge (SOC), electrolyte mixture, and more [22,51,110,111]. Therefore, the explosion characteristics for these vented gas compositions may differ from the results in this study.

Table 4 Summary of the primary results from the dimethyl carbonate (DMC), ethyl methyl carbonate (EMC), and diethyl carbonate (DEC) experiments with initial conditions at 373 K and 100 kPa (absolute)

Variables/ Parameters	Materials					
	DMC		EMC		DEC	
P_{ex} ($\phi \approx 1$)	ϕ=0.95	720 kPa	ϕ=1.02	744 kPa	ϕ=1.00	731 kPa
P_{max}	ϕ=1.28	763 kPa	ϕ=1.22	768 kPa	ϕ=1.34	757 kPa
$(dp/dt)_{max}$	ϕ=1.23	34.8 $MPa \cdot s^{-1}$	ϕ=1.13	41.4 $MPa \cdot s^{-1}$	ϕ=1.33	38.9 $MPa \cdot s^{-1}$
$K_{G,\ max}$	94.5 $bar \cdot m \cdot s^{-1}$		112.4 $bar \cdot m \cdot s^{-1}$		105.7 $bar \cdot m \cdot s^{-1}$	
LEL	3.2%		2.1%		1.6%	
UEL	18.0%		15.8%		11.3%	

Table 5 shows the theoretically predicted explosion pressure results and the LEL and UEL found in the literature for the electrolyte solvent. The discrepancy between experimental and calculated explosion pressure is attributed to heat loss. Radiative and convective heat losses will occur in the experiments. Similar discrepancies were found for the methane and propane explosion pressures. DMC had the highest discrepancy in LEL and UEL compared with previously published data [112]. The corresponding temperature and pressure for the explosive limits are not reported in the IPCS safety chemical database for DMC and may differ from this study, explaining the discrepancy.

Table 5. Theoretical calculation of the maximum explosion pressure and the literature values for the lower and upper explosive limit for dimethyl carbonate and diethyl carbonate.

Variables/Parameters	Materials	
	DMC	DEC
P_{ex} (ϕ=1, theoretical)	788 kPa	778 kPa
P_{max} (theoretical)	ϕ=1.25 818 kPa	ϕ=1.23 807 kPa
LEL [112,113]	4.22%	1.4%
UEL [112,113]	12.87%	11.0%

Figure 25 and Figure 26 compare the P_{ex} and the $(dp/dt)_{ex}$ for all experiments with spark ignition, respectively. Propane has a very similar P_{ex} and $(dp/dt)_{ex}$ profile as the carbonates; thus, explosion characteristics of a Li-ion electrolyte solvent (a mixture of carbonates) are comparable to that of propane. Therefore, when estimating the consequence for LIBs with unknown electrolyte solvents, the explosion characteristics of propane may be initially assumed.

4.1.4 Conclusion

- Explosion pressure, rate of explosion pressure rise, UEL, and LEL were determined for three common carbonates used for electrolyte solvent in LIBs.
- All three carbonates have similar explosion pressure and rate of explosion pressure rise, which may simplify preliminary risk assessments.
- Discrepancies in explosion pressure between theoretical calculation and experiments are likely caused by heat loss in the experiments.
- Comparing the carbonates to the three common fuels, hydrogen, methane, and propane, showed that the explosion characteristics of propane were very similar to that of the three carbonates.

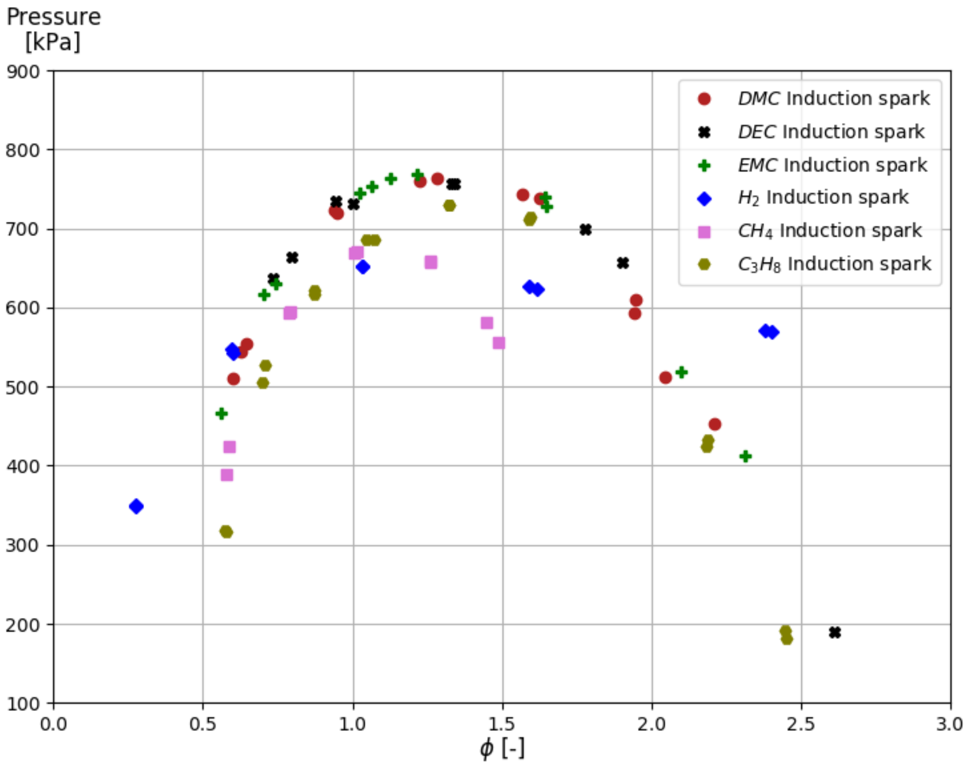

Figure 25. Explosion pressure for all experiments. The initial absolute pressure and temperature were 100 kPa (absolute) and 373 K, respectively [69].

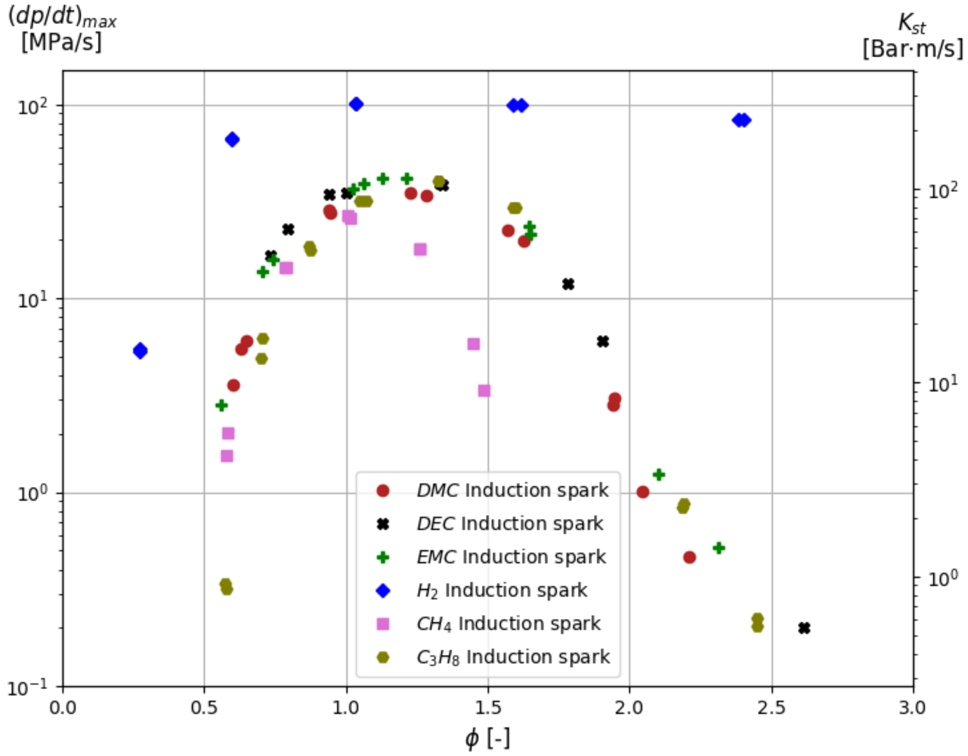

Figure 26. The rate of explosion pressure rise for all experiments. The initial absolute pressure and temperature were 100 kPa (absolute) and 373 K, respectively [69].

4.2 Article B: Laminar burning velocity of the dimethyl carbonate-air mixture formed by the Li-ion electrolyte solvent

4.2.1 Introduction

In this study, the LBV, laminar flame speed, and the Markstein length were determined for dimethyl carbonate (DMC) and propane at 300 K and 100 kPa (absolute). The Experimental results are compared with previously published studies and with theoretical calculations.

4.2.2 Materials and Methods

The 20-liter explosion sphere and the procedure described in section 3.1 were used to obtain the experimental results. For determining the LBV, the detailed procedure can be found in section 3.1.2. DMC had a purity above 99% and propane a purity above 99.95%.

For validating the experimental method, the measured LBVs of propane were compared to several previously published studies. Furthermore, the LBV for DMC was compared to a study by Bardin et al. [114] and predicted LBVs using Cantera (see section 3.3) with reaction mechanisms proposed by Glaude et al. [97] and Sun et al. [99].

4.2.3 Results and Discussion

Thermal diffusion, hydrodynamic instabilities, and buoyancy can cause instabilities and may influence the propagation of the flame [71,72]. However, no buoyancy instabilities or hydrodynamic instabilities caused by pressure changes were observed. Although ignition-induced instabilities were detected, experiments with non-spherical flame propagation were rejected. Several stretch extrapolations models were used; however, for experiments with a Markstein times Karlovitz number within -0.05 and 0.15, the unstretched flame propagation speed is practically independent of the stretch extrapolation model.

Moreover, the measured LBV of propane compared well with previously published results, indicating that the experimental setup and method produce acceptable results, as shown in the left plot in Figure 27. Table 6 summarizes the experimental results for DMC using the derived linear stretch extrapolation model.

Table 6. Summary of dimethyl carbonate results. The unstretched flame propagation speed Markstein length, laminar burning velocity, coefficient of determination at 300 K, and 100 kPa (absolute)

Fuel-air equivalence ratio	**Laminar flame speed (S_b^0) [mm s^{-1}]**	**Markstein length (L_b) [mm]**	**Laminar burning velocity (S_u^0) [mm s^{-1}]**
0.84	1895	2.84	251
1.01	2436	1.74	294
1.04	2492	1.57	300
1.13	2494	0.98	297
1.16	2522	1.10	301
1.32	2145	0.41	261

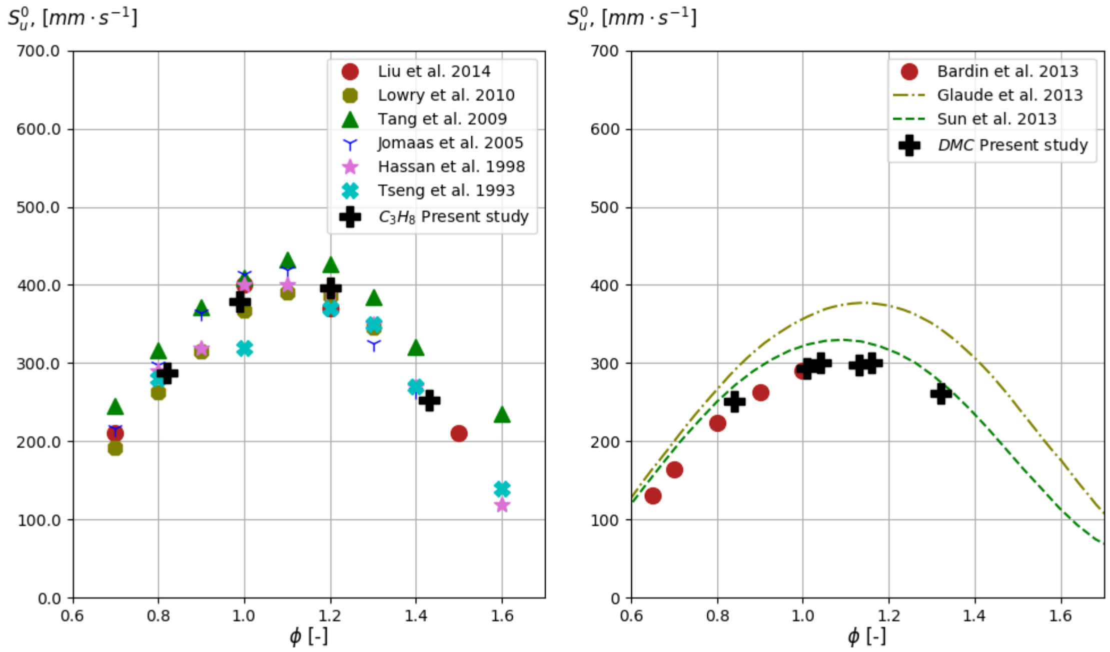

Figure 27. Laminar burning velocity as a function of equivalence ratio; left – measurements for propane compared to previously published results; right – measurements for dimethyl carbonate compared to previously published results and predictions with two reaction mechanisms. Initial conditions: temperature 300 K, absolute pressure 100 kPa (absolute) [74].

Figure 27 shows that the LBV of DMC in this study match reasonably well with the LBV measured by Bardin et al. [114]. Although only a few points from the two studies overlap, Figure 27 shows that the trend from the two datasets fits quite well. Of the two reaction mechanisms, the model proposed by Sun et al. [99] had the lowest discrepancy compared to the measured LBV. The reason for the discrepancy between predicted and measured LBV is uncertain. However, the radiative heat loss could be contributing to the discrepancy between simulations and experiments [115].

For the LBV at ϕ equal to 1.32, the partial pressure for that experiment (8.5 kPa at 302 K) was close to the estimated DMC vapor pressure of 8.8 kPa [116]. This slight pressure difference may cause some uncertainties concerning the concentration in this experiment. It is crucial to notice that at 300 K, the upper explosive limit for DMC will not be reached.

4.2.4 Conclusion

- The laminar flame speed, Markstein length, and the LBV were experimentally measured for DMC at 300 K and 100 kPa (absolute).
- The experimental method was validated by comparing the measured LBVs of propane with previously published studies.
- Experiments with a Markstein times Karlovitz number within -0.05 and 0.15 show that the calculated LBV is practically independent of the stretch extrapolation model used.
- For DMC, the highest LBV of 300 $mm \cdot s^{-1}$ was measured at a ϕ of 1.04. At 302 K, near the saturated vapor pressure, the LBV is 261 $mm \cdot s^{-1}$.
- Of the two DMC reaction mechanisms analyzed, the one proposed by Sun et al. had the lowest discrepancy compared to the measured LBV.

4.3 Article C: Laminar Burning Velocity of Gases Vented from Failed Li-Ion Batteries

4.3.1 Introduction

This study presents the LBV, laminar flame speed, and the Markstein length for three gas compositions vented from failed LIBs and a pseudo/simplified gas mixture at 300 K and 100 kPa (absolute). Two of the vent gas compositions were taken from literature, which represents the upper and the lower LBV range, based on the study done by Baird et al. [15]. Furthermore, the third Li-ion vent gas composition (the Generic Li-ion gas) was determined by a research partner in the research center MoZEES [7].

Additionally, a simplified gas composition was generated to resemble the combustion properties of the Generic Li-ion gas composition. The measured LBVs were compared to predicted LBVs from four different reaction mechanisms using Cantera. Table 7 presents the four gas compositions studied.

Table 7. Gas compositions of the three potential gases vented from a failing Li-ion battery and the generated simplified gas [117].

Fuel mixture	**H_2 [%]**	**CO [%]**	**CO_2 [%]**	**CH_4 [%]**	**C_2H_4 [%]**	**C_2H_6 [%]**
High LBV Li-ion gas	42.8	37.1	10.0	7.1	3.0	[-]
Low LBV Li-ion gas	29.5	9.0	48.4	5.6	7.0	0.5
Generic Li-ion gas	34.9	25.0	20.1	15.0	5.0	[-]
Simplified gas	35.0	[-]	[-]	65.0	[-]	[-]

4.3.2 Methods and Materials

The 20-liter explosion sphere and the procedure described in section 3.1 were used to obtain the experimental results. For determining the LBV, the detailed procedure can be found in section 3.1.2.

With Cantera version 2.4, the routines *FreeFlame* and *equilibrate* calculated the LBVs and closed volume explosion pressure, respectively. These methods are described in section 3.3. Four reaction mechanisms were used in this study, GRI-Mech 3.0 [70], San Diego Mech [100], a reaction mechanism propose by Glaude et al. [97], and Sun et al. [99] (hereafter referred to as the Glaude model and Sun model, respectively). GRI-Mech 3.0 and San Diego Mech were chosen due to their versatility in various combustion processes, while the Glaude and Sun models were selected because they include the electrolyte solvent, DMC.

The Simplified gas composition was determined by matching the LBVs and the explosion pressures to that of the Generic Li-ion gas for fuel-air equivalence ratios between 0.5 and 1.7 (ϕ), using the GRI-Mech 3.0. At 35 vol% of H_2 and 65 vol% of CH_4, an acceptable resembles was found.

4.3.3 Results and Discussion

Thermal diffusion and hydrodynamic instabilities that could have caused errors in the measurements were not observed. All experiments that had ignition-induced instabilities that caused the flame to propagate non-spherical were rejected. Parallel experiments for each concentration only gave minor differences in LBV, which are barely noticeable, as illustrated in Figure 28.

Certain species influence the LBV significantly, as illustrated by the wide range of LBVs observed in Figure 28. For example, the maximum LBV of the Low LBV Li-ion gas composition is 351 mm·s^{-1}, whereas the LBV for the High LBV Li-ion gas composition is approximately three times higher at 1056 mm·s^{-1}. As the High LBV Li-ion gas comprises approximately 80% H_2 and CO, a high LBV is expected. On the other hand, the Low LBV Li-ion gas contains approximately 50% CO_2, which is inert; thus, a lower LBV is expected.

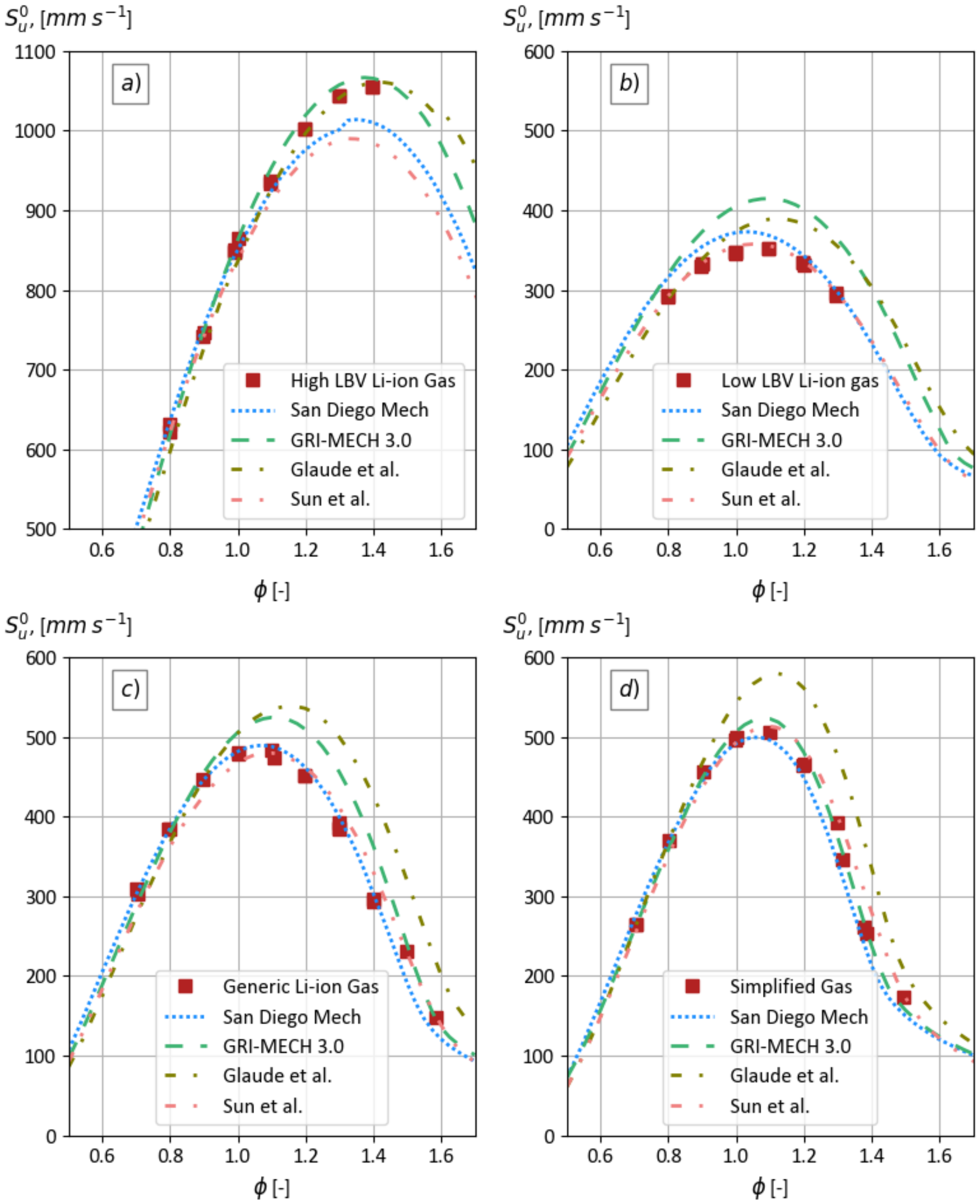

Figure 28 Comparison of the predicted laminar burning velocity (LBV) using the four reaction mechanisms and the measured LBVs of a) the high LBV Li-ion gas mixture, b) the low LBV Li-ion gas mixture, c) the generic Li-ion gas mixture, and d) the simplified gas mixture. [117]

4.3.3.1 LBV prediction accuracy of the reaction models

The prediction accuracy of the four reaction mechanisms was compared by computing the coefficient of determination (R^2) and the standard deviation of the error (*SDE*), commonly used in statistical analysis. Furthermore, the Sun model had the most consistently high R^2 values, above 0.95 for all mixtures. However, the Sun model exhibits issues predicting the LBV for High LBV Li-ion gas, as shown in Figure 28 a). Similarly, the San Diego mech has a high R^2 value (0.97) for the High LBV Li-ion gas but has a peak difference of 55 mm·s^{-1} and under-estimates the LBV at the fuel-rich side, as shown in Figure 28 a). Although the San Diego mech had a low R^2 value (0.72) for the Low LBV Li-ion gas, the peak discrepancy (25 mm·s^{-1}) and *SDE* (20.4 mm·s^{-1}) was lower than for the High LBV Li-ion gas.

Of all reaction mechanisms, the Glaude model had the lowest prediction accuracy and overestimated the LBVs. Previous studies have reported that the Glaude model deviates from experimentally obtained LBVs [74,99,114,118]. However, the Glaude model estimated the LBV of the High LBV Li-ion gas relatively accurately (R^2 = 0.99 and *SDE* = 20 mm·s^{-1}) as shown in Figure 28 a), which may be attributed to that mixture composition.

The GRI-Mech 3.0 model most accurately predicted the LBV for the High LBV Li-ion gas (R^2 = 0.997 and *SDE* = 11.6 mm·s^{-1}) and the Simplified gas (R^2 = 0.99 and *SDE* = 12.1 mm·s^{-1}), which predominantly comprises H_2, CO, and CH_4. Previous studies have shown that the GRI-Mech 3.0 model accurately predicts the LBVs of similar gas composition [119], [120], [82], [121]. However, for gas compositions that have a higher CO_2 concentration, such as the Low LBV Li-ion gas (R^2 = 0.547 and *SDE* = 61 mm·s^{-1}) and the Generic Li-ion gas (R^2 = 0.86 and *SDE* = 47.7 mm·s^{-1}), the GRI-Mech 3.0 model tends to over-predict the LBVs. Zahedi et al. [117] reported that GRI-Mech 3.0 predicted slightly higher LBVs for CH_4 diluted in 10% and 20% CO_2.

The reaction mechanisms studied have different LBV prediction accuracy and thus may produce different results when used in safety engineering models and as input to CFD simulations. However, the uncertainties in these models and CFD simulations can be substantially more significant than the deviations between these reaction mechanisms.

4.3.3.2 Ideal reaction mechanisms for different gas compositions

Studies have shown that different SOC and chemistry can yield different gas compositions during a LIB failure (Table 1). Therefore, based on the results in this study, selecting a reaction model based on the CO_2 concentration in the gas composition can improve the accuracy of the predicted LBVs. Table 8 presents a method of choosing a reaction mechanism to predict LBVs considering the CO_2 concentration in the gas compositions as a criterion. However, this criteria may be valid only for the gas compositions listed in Table 7. If conservative estimations of LBV are essential, GRI-Mech 3.0 can be considered the ideal choice and not the presented criteria in Table 8.

Table 8 Recommendation for choosing a reaction mechanism to predict laminar burning velocities of the gases vented from Li-ion batteries based on the carbon dioxide (CO_2) concentration in gas compositions [117].

Reaction mechanism	**CO_2 concentration**	**Gas mixture**
GRI-Mech 3.0	Less than 15%	Simplified, High LBV
San Diego Mech	Between 15% and 40%	Generic
Sun model	Above 40%	Low LBV

4.3.3.3 Challenges in generating a simplified Li-ion gas

GRI Mech 3.0 was used to determine the gas composition of the Simplified gas by matching the combustion properties of the Generic Li-ion gas. However, as presented in Figure 28 c), GRI Mech 3.0 overpredicts the LBVs for the Generic Li-ion gas. Based on the experimental results, the San Diego mech should have been used to predict the combustion properties more accurately for the Generic Li-ion gas. Although the accuracy of the predicted LBVs would have improved by using the San Diego Model, the composition of the Simplified gas would remain the same. For example, reducing the H_2 concentration to lower the LBV would increase the explosion pressure due to increased CH_4 concentration, further increasing the closed volume explosion pressure discrepancy. A higher level of resemblance requires a third inert species such as CO_2.

Furthermore, the Simplified gas generated resembles the Generic Li-ion gas only in terms of combustion properties. However, in actual experiments, gas dispersion and mixing with air are essential factors. As the Simplified gas is lighter than the Generic Li-ion gas, the dispersion will differ. If the vented Li-ion gas temperature exceeds 300 K used in this study, it will reduce its density and alter the combustion properties. Therefore, matching both density and combustion properties of vented Li-ion gas compositions requires the knowledge of release temperature and species composition. Based on the results of this study, a non-toxic “pseudo” or “simplified” gas that reproduces the required properties can be designed using theoretical calculations.

4.3.4 Conclusions

- To address the explosion hazards related to gases vented from failed LIBs, the Markstein length, laminar flame speed, LBV, maximum explosion pressure, and maximum rate of explosion pressure rise for three gas compositions and one pseudo (simplified) Li-ion gas has been determined at various ϕ.
- Certain species influence the LBV of a gas composition significantly. Gas composition with a high concentration of H_2 and CO has a higher LBV; whereas, gas compositions with a high CO_2 concentration tend to have a lower LBV.
- The LBV prediction accuracy of four reaction mechanisms, namely the GRI-Mech 3.0, San Diego Mech, Glaude model, and Sun model, were compared to experimental results. Among these, the Sun model had the most consistent high coefficient of determination (R^2).
- GRI-Mech 3.0 predicted the LBV with the highest accuracy for gas compositions with low CO_2 content. However, over predicted the LBV when the CO_2 content was more than 20%.
- Based on the compositions carbon dioxide (CO_2) concentration in the LIBs vent gas composition, a method for choosing a reaction mechanism to predict the LBVs is recommended.
- This study shows that a non-toxic “pseudo” or “simplified” gas that reproduces the required properties can be designed using theoretical calculations. However, matching density, explosion pressure, and LBV can be challenging for a wide range of ϕ. Moreover, for accurate reproduction of these properties requires the knowledge of release temperature and species composition.
- The experimental and numerical results of combustion properties are considered novel and can be used as input for CFD modeling, safety engineering models for risk assessments of battery installations.

4.4 Article D: Simulation of a Premixed Explosion of Gas Vented During Li-Ion Battery Failure

4.4.1 Introduction

This study presents a CFD method and its prediction accuracy for simulating explosions of gases vented from failed LIBs. The CFD method includes a code for generating combustion, transport, and thermodynamics properties, required for CFD simulations using the XiFoam model/solver. As method verification, the required input parameters generated by the proposed method are compared to results from theoretical calculations. The input parameters are also used in several CFD simulations of an explosion in a 1-meter rectangular channel, which are compared with experimental results.

4.4.2 Materials and Method

4.4.2.1 Experimental setup

The 1-meter explosion channel and the procedure described in section 3.2 were used to obtain the experimental results. Two parallel experiments were conducted for each target concentration. A research partner determined the gas composition used by analyzing the vented gas from thermally abused commercial cells with cell chemistry based upon LFP with 100% SOC. Table 9 shows the fuel gas composition, which was purchased premixed from AGA Linde.

Table 9. The gas composition of the Generic Li-ion gas in volume percentage.

Name of fuel mixture	**H_2 [%]**	**CO [%]**	**CO_2 [%]**	**CH_4 [%]**	**C_2H_4 [%]**
Generic Li-ion gas	34.9	25.0	20.1	15.0	5.0

4.4.2.2 CFD Simulation - XiFoam

For the CFD simulations, the XiFoam solver/model described in detail in section 3.4 was used. The first-order forward Euler scheme was used for the time integration. For the gradient and diffusion terms, the second-order linear scheme was used. A blend of the first-order upwind and second-order limited linear and linear scheme was used for the convective terms. The LES sub-grid model WALE proposed by Nicoud and Ducros [107] was used to evaluate the sub-grid turbulence. The WALE model is based on the square of the velocity gradient tensor and has a near-wall scaling function without requiring a dynamic procedure. Moreover, the model is suited for complex geometries and flow that experience laminar to turbulent transition.

SnappyHexMesh was used to generate the computational mesh from a computer-aided design (CAD) geometry drawn in Onshape, the online CAD tool [101]. At the open end of the channel, the cell size expands linearly in all directions to twice the initial cell size, creating a rectangular frustum shape with a length of 500 mm. Three initial cell sizes, 2, 4, 8, and 16 mm, were analyzed to investigate the mesh sensitivity. The final mesh shown in Figure 29 was based on the background mesh with a cell size of 4 mm and consist of 426 026 cells.

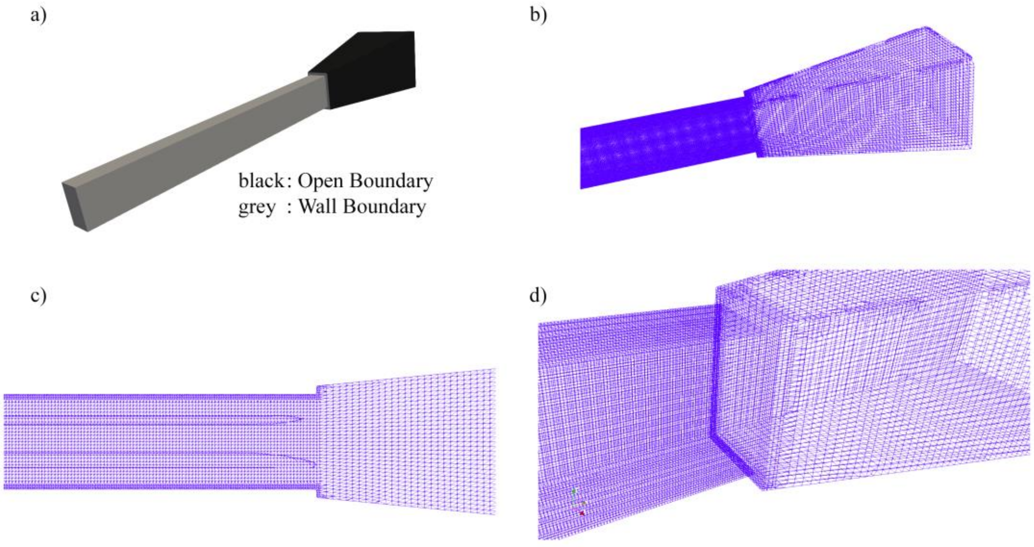

Figure 29. The geometry and computational mesh for most of the numeric simulations. a): Side view of the entire CAD geometry with boundary conditions. b): Side view of the computational mesh front part. c) Horizontal cross-section view of the computational mesh center. d): Side view close-up of the computational mesh intersection between the channel and open geometry.

In the channel (the grey part of Figure 29a)), typical wall boundary conditions were used as non-slip (zero velocity), isothermal (fixed temperature), and zero gradients (all other variables). For the outer domain (the black part of Figure 29a)), open boundary conditions as inlet-outlet (fixed value inlet, zero gradient outlet) and constant total pressure were used. The atmospheric conditions were set to 293 K and 101.3 kPa (absolute), similar to the overall experimental conditions.

4.4.2.3 mech2Foam – the method for generating input parameters

An inhomogeneous mixture in XiFoam requires three species: oxidizer (air), fuel, and burntProducts; hereafter referred to as the XiFoam species. These XiFoam species require three parameters: mole weight, NASA polynomial coefficients [95], and Sutherland Coefficients [106]. The Generic Li-ion gas in Table 9 was used for the fuel species, and air (21 vol% O_2 and 79 vol% N_2) was used as the oxidizer species. Using the set fuel and oxidizer as inputs, the required transport, combustion, and thermodynamic model coefficients for XiFoam were calculated using the *mech2Foam* code and the San Diego reaction mechanism [100].

A detailed description of *mech2Foam* foam can be found in part 2 of this thesis under Supplementary Data A – mech2Foam documentation [105].

4.4.3 Results and Discussion

The NASA polynomial coefficient generated for the XiFoam species gave nearly identical thermodynamic values as those calculated by Cantera. A statical comparison showed that the coefficient of determination (R^2) was approximately 1.0, and the standard deviation of the error (*SDE*) was approximately zero. This accuracy was obtained because all species in the XiFoam species had the same common reference temperature. However, different common reference temperatures for these species may reduce the accuracy. Therefore, for mixtures with different reference temperatures, the generated NASA polynomial coefficients should be validated. Comparing the dynamic viscosity from Cantera and the fitted Sutherland coefficients gave a maximum *SDE* and minimum R^2 of $1.547 \cdot 10^{-6}$ Pa·s and 0.997, respectively.

The fitted Gülder coefficients calculated the LBVs reasonably well compared to those numerically calculated using Cantera, with the lowest R^2 of 0.98, for LBV as a function of pressure (at constant φ and temperature). However, by estimating LBVs outside of fitted data, the accuracy is reduced. For example, at 751.3 kPa (absolute), the *SDE* was 35 $mm \cdot s^{-1}$ and R^2 of 0.70. Therefore, when using the Gülder equation for LBV estimations, the expected temperature and pressure range should be considered.

The background mesh comparison showed some discrepancies in minimum and maximum values but had similar temporal profiles. Based on the cell size comparison, the 4 mm case gave acceptable results compared to the 2 mm case. A cell size of 4 mm is also favorable concerning computational time and requirements for larger geometries.

Figure 30 shows the maximum recorded explosion pressure in the experiments and the simulation cases. Although the CFD simulations predicted the maximum explosion pressure with only minor differences compared to experimental results, a considerable difference was found by comparing the temporal evolution of the pressure, flame front, flame front velocity, as shown in Figure 31. The CFD simulation predicted the initial stages of the flame propagation; however, it did not predict the pressure and velocity oscillations as the flame approached the end of the channel. As the gauge pressure in the channel becomes negative, the flame front in the simulations stretches significantly, which could dampen the pressure oscillations observed in the experiments. Thus, for these experimental conditions, the XiFoam solver accurately predicts the maximum pressure, the initial pressure peaks, initial front velocity development, and flame front position for an open-ended channel.

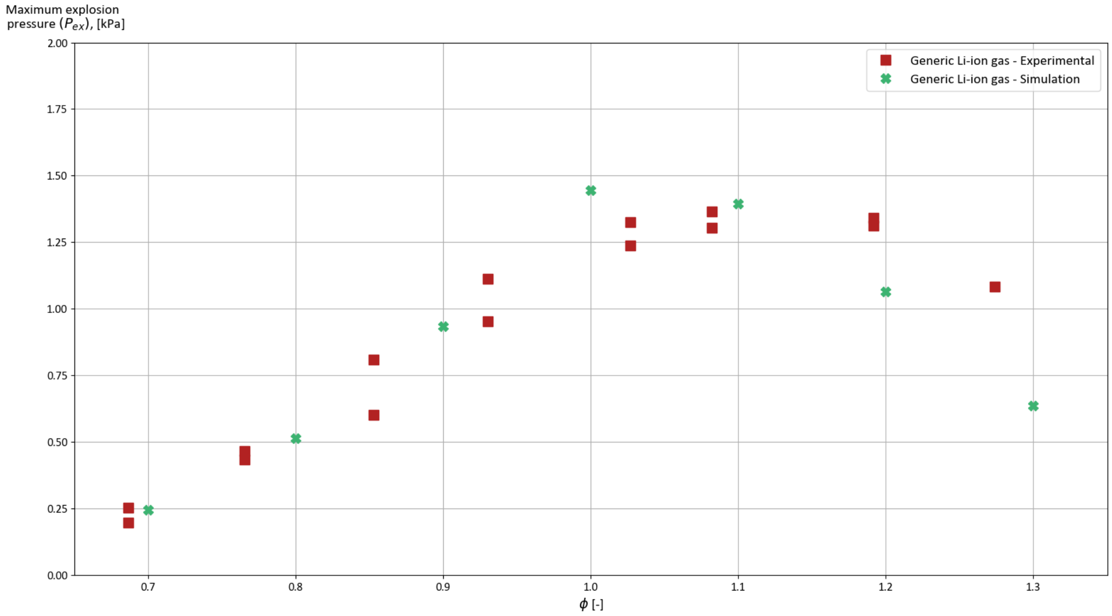

Figure 30. Maximum explosion pressure from the generic Li-ion gas experiments, recorded in the 1-meter explosion channel [REF].

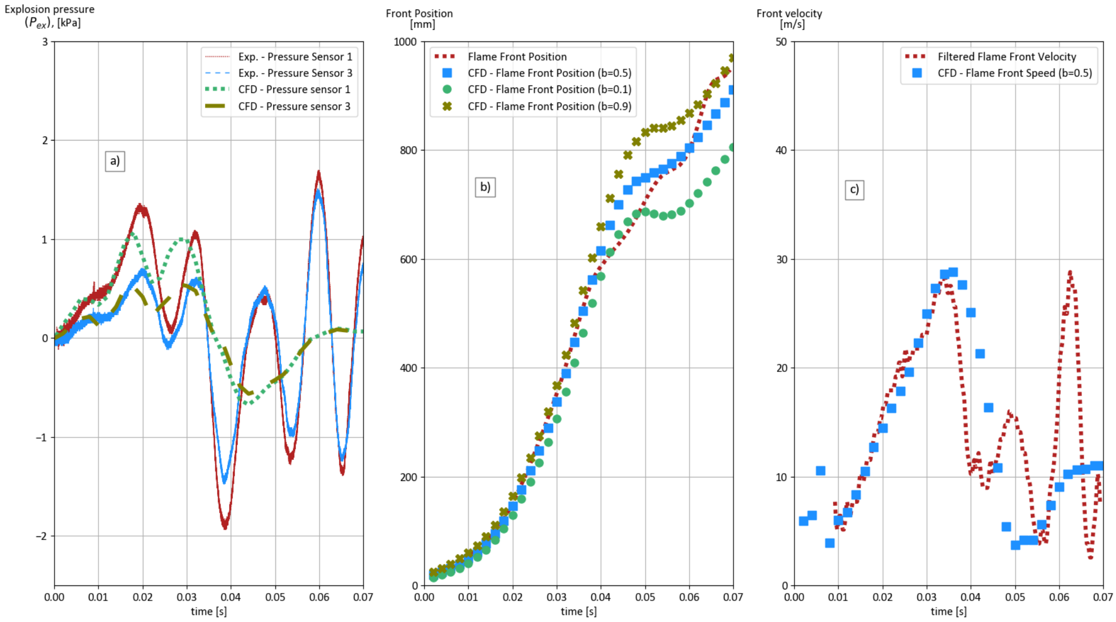

Figure 31. Comparison of the CFD simulated and the experimental results at fuel-air equivalence ratio 1.2. a) Comparison of the temporal evolution of the pressure; b) Comparison of the temporal evolution of the flame front position; c) Comparison of the temporal evolution of the flame front velocity

4.4.4 Conclusion

- This study presents a CFD method for simulating explosions of gases vented from failed LIBs, including the generation of the required combustion, transport, and thermodynamic model coefficients (*mech2Foam*) for the CFD XiFoam model/solver in OpenFOAM, using only open-source software.
- The comparison between generated NASA polynomials and thermodynamic values calculated using Cantera and the San Diego reaction mechanism was neglectable. Furthermore, the curve-fitted Sutherland equation had only minimal differences compared to values calculated using Cantera.
- The curve-fitted Gülder equation had only minor deviations from the values used in the regression. However, comparing to values outside the regression data, the deviation significantly increases. The temperature and pressure range should be considered when using the Gülder equation for LBV correlation.
- Although the CFD method *mech2Foam* is designed for the XiFoam CFD solver, the method can be used for other CFD tools that require similar input parameters.
- CFD simulations predicted the maximum explosion pressure and flame front position with only minor discrepancies. The highest maximum explosion pressure was 1.36 kPa (gauge) and 1.45 kPa (gauge) in the experiments and simulations, respectively.
- The predicted initial temporal evolution of the pressure and flame front velocity also agreed well with experiments. However, pressure and flame front velocity oscillations, which occurred as the flame approached the channel opening, were not accurately predicted.
- The method is intended for evaluating the risk and consequences related to LIB applications and installations.

4.5 Article E: Numerical Study of Premixed Gas Explosion in a 1-meter Channel Partly Filled with 18650 Cell-like Cylinders with Experiments

4.5.1 Introduction

This study investigates the prediction accuracy of the CFD method XiFoam. More specifically, the XiFoam prediction accuracy of the temporal pressure evolution, maximum pressure peak, positive impulse, and the spatial evolution of the flame front velocity for premixed gas explosions in a 1-meter-long explosion channel partly filled with 18650 cell-like cylinders. Two gas compositions and two different geometries were studied. The difference in the two channels geometries was the location of the arrangement of 40 18650 cell-like cylinders. Finally, the experiments were compared at three different fuel-air equivalence ratios (ϕ) 0.8, 1.0, and 1.2, resulting in a total of 12 simulation cases, at typical atmospheric conditions, 293 K and 101.3 kPa (absolute).

4.5.2 Materials and Methods

4.5.2.1 Experimental Setup

The 1-meter explosion channel and the procedure described in section 3.2 were used to obtain the experimental results. Figure 21 shows the dimensions of the two geometries, hereafter referred to as the inner channel geometry and the center channel geometry, with the names referring to the location of the cylinders in the channel. Both geometries had a 0.5 void ratio and maximum blockage ratio of 0.77 in the obstructed part of the channel. The two gas compositions have been previously studied by Henriksen et al. [117]; one has a high LBV compared to other Li-ion ion vent gases and is referred to as the High LBV Li-ion gas, while the other gas is a pseudo/simplified Li-ion vent gas. The pseudo/simplified Li-ion vent gas has an LBV and explosion pressure in the same range as many other Li-ion vent gas compositions and is referred to as the Simplified Li-ion gas. Table 10 shows the two fuel gas compositions.

Table 10. The gas compositions analyzed numerically and experimentally in this study in volume percentage.

Name of fuel mixture	**H_2 [%]**	**CO [%]**	**CO_2 [%]**	**CH_4 [%]**	**C_2H_4 [%]**
High LBV Li-ion gas	42.8	37.1	10.0	7.1	3.0
Simplified Li-ion gas	35.0	[-]	[-]	65.0	[-]

4.5.2.2 CFD Simulation

The XiFoam solver/model described in detail in section 3.4 was used for the CFD simulations. Several simulation results were compared with an experiment (case 38 in Table 11) to determine the numerical scheme and models for the remaining CFD simulations. The focus of the comparison was on the explosion pressure at pressure sensor one and the flame propagation.

The second-order Crank-Nicolson scheme, with a ratio of 0.6 forward Euler and 0.4 Crank-Nicolson, was used for the time integration. For the gradient and diffusion terms, the second-order linear scheme was used. Moreover, the gradient and diffusion terms were discretized using the second-order linear scheme. Three different second-order schemes were used for the divergence terms, linear, linear-upwind, and limited linear. The species model coefficients for the transport and thermodynamic models and the Gülder coefficients were generated using *mech2Foam* [105].

LES was used for the turbulence approach, with the sub-grid model proposed by Akira Yoshizawa [108] for compressible turbulent shear flows. The Van-Driest dampening function was used for wall turbulence treatment, with the A^+ coefficient and ΔC equal 26 and 0.158, respectively.

The two geometries and computational meshes were generated using Onshape, the online CAD tool [101], blockMesh, and SnappyHexMesh. The initial cell size was 4 mm in the channel, which was refined to have three layers of half the initial cell size at the outer walls. At the 18650 cell/cylinder walls, the first three layers were a fourth of the initial cell size, followed by an additional three layers with half the initial cell size. At the open end of the channel, the cell size expands linearly from 4 mm to 8 mm in all directions, creating a rectangular frustum with a length of 500 mm outside the channel.

For the inner and center channel geometries, the total amount of cells were 944 849 and 945 843, respectively.

Typical wall boundary conditions were applied as non-slip (zero velocity), isothermal (fixed temperature), and zero gradients on the wall boundaries. The open boundary conditions were applied on the outer domain, such as inlet-outlet (fixed value inlet and zero gradient outlet), constant total pressure, and zero gradients. The atmospheric conditions were 293 K and 101.3 kPa (absolute), similar to the overall experimental conditions.

Table 11. List of all experiments that were compared to CFD simulations.

Experimental Case Number	Gas Composition	Fuel-Air Equivalence ratio	Channel Geometry	Corresponding CFD Case Name
Case 01.	High LBV Li-ion gas	0.79	Inner	High CFD 0.8 Inner
Case 03.	High LBV Li-ion gas	1.00	Inner	High CFD 1.0 Inner
Case 05.	High LBV Li-ion gas	1.18	Inner	High CFD 1.2 Inner
Case 06.	High LBV Li-ion gas	1.18	Inner	High CFD 1.2 Inner
Case 15.	Simplified Li-ion gas	0.79	Inner	Simple CFD 0.8 Inner
Case 16.	Simplified Li-ion gas	0.79	Inner	Simple CFD 0.8 Inner
Case 20.	Simplified Li-ion gas	0.97	Inner	Simple CFD 1.0 Inner
Case 21	Simplified Li-ion gas	0.97	Inner	Simple CFD 1.0 Inner
Case 22.	Simplified Li-ion gas	1.01	Inner	Simple CFD 1.0 Inner
Case 23.	Simplified Li-ion gas	1.01	Inner	Simple CFD 1.0 Inner
Case 27.	Simplified Li-ion gas	1.19	Inner	Simple CFD 1.2 Inner
Case 28.	Simplified Li-ion gas	1.19	Inner	Simple CFD 1.2 Inner
Case 33.	High LBV Li-ion gas	0.79	Center	High CFD 0.8 Center
Case 36.	High LBV Li-ion gas	0.97	Center	High CFD 1.0 Center
Case 37.	High LBV Li-ion gas	0.98	Center	High CFD 1.0 Center
Case 38.	High LBV Li-ion gas	0.98	Center	High CFD 1.0 Center
Case 42.	High LBV Li-ion gas	1.18	Center	High CFD 1.2 Center
Case 43.	High LBV Li-ion gas	1.18	Center	High CFD 1.2 Center
Case 52.	Simplified Li-ion gas	0.79	Center	Simple CFD 0.8 Center
Case 53.	Simplified Li-ion gas	0.79	Center	Simple CFD 0.8 Center
Case 54.	Simplified Li-ion gas	0.79	Center	Simple CFD 0.8 Center
Case 57.	Simplified Li-ion gas	1.01	Center	Simple CFD 1.0 Center
Case 58.	Simplified Li-ion gas	1.01	Center	Simple CFD 1.0 Center
Case 62.	Simplified Li-ion gas	1.19	Center	Simple CFD 1.2 Center

4.5.3 Results and Discussion

The comparison of experimental Case 38 and the High CFD 1.0 center simulation case showed that the XiFoam predicted the explosion pressure for pressure sensor one and flame front position. However, there were significant discrepancies in maximum explosion pressure at pressure sensors 3 and 4 and the flame acceleration predictions.

There was a significant difference in the maximum explosion pressure between parallel experiments, especially for the High LBV Li-ion gas experiments. Some parallel experiments had a maximum explosion pressure difference of 60 to 70 kPa, which is the same range as the deviation between simulation and experimental results. Explosion pressure may not be an ideal comparable parameter due to potential variance between parallel experiments as observed in this study.

The model evaluation protocol proposed for the HySEA project [122], which is based on the MEGGE protocol [123], was used for a statistical quantification of the model performance. Table 12 shows the model performance criteria for the mean geometric bias (MG) and the mean geometric variance (VG).

Table 12. Criteria for evaluating model performance for a specific variable from the model evaluation protocol proposed for the HySEA project [122].

The scale of Model Performance	MG and VG Limits
Excellent	$0.7 < MG < 1.3$ [Solid red line] $VG < 1.6$ [Solid black line]
Acceptable	$0.5 < MG < 2.0$ [Dashed red line] $VG < 3.3$ [Dashed black line]
Poor	$2.0 < MG > 0.5$ $VG > 3.3$

Figure 32 and Figure 33 show that the MG and VG for all High LBV Li-ion gas cases were within the criteria for acceptable model performance. XiFoam had an overall better model performance for the center geometry cases, which was expected since the numerical scheme and model parameters were adjusted to this geometry. In the simulation cases, all the maximum pressure peaks were at pressure sensor one; however, in the center channel geometry experiments, the maximum pressure peaks were observed on the two outer pressure sensors (PS3 and PS4). In the simulation, as the flame propagated through the geometry, the modeled flame thickness grows, which most likely dampens the pressure peaks. Although the model did not predict the maximum pressure peaks at these sensors (PS3 and PS4), the positive impulses were predicated with significantly less deviation. For the inner channel geometry, the overall averaged MG and VG were 0.96 and 1.26, respectively, whereas, for the center channel geometry, the overall averaged MG and VG were 1.10 and 1.14, respectively.

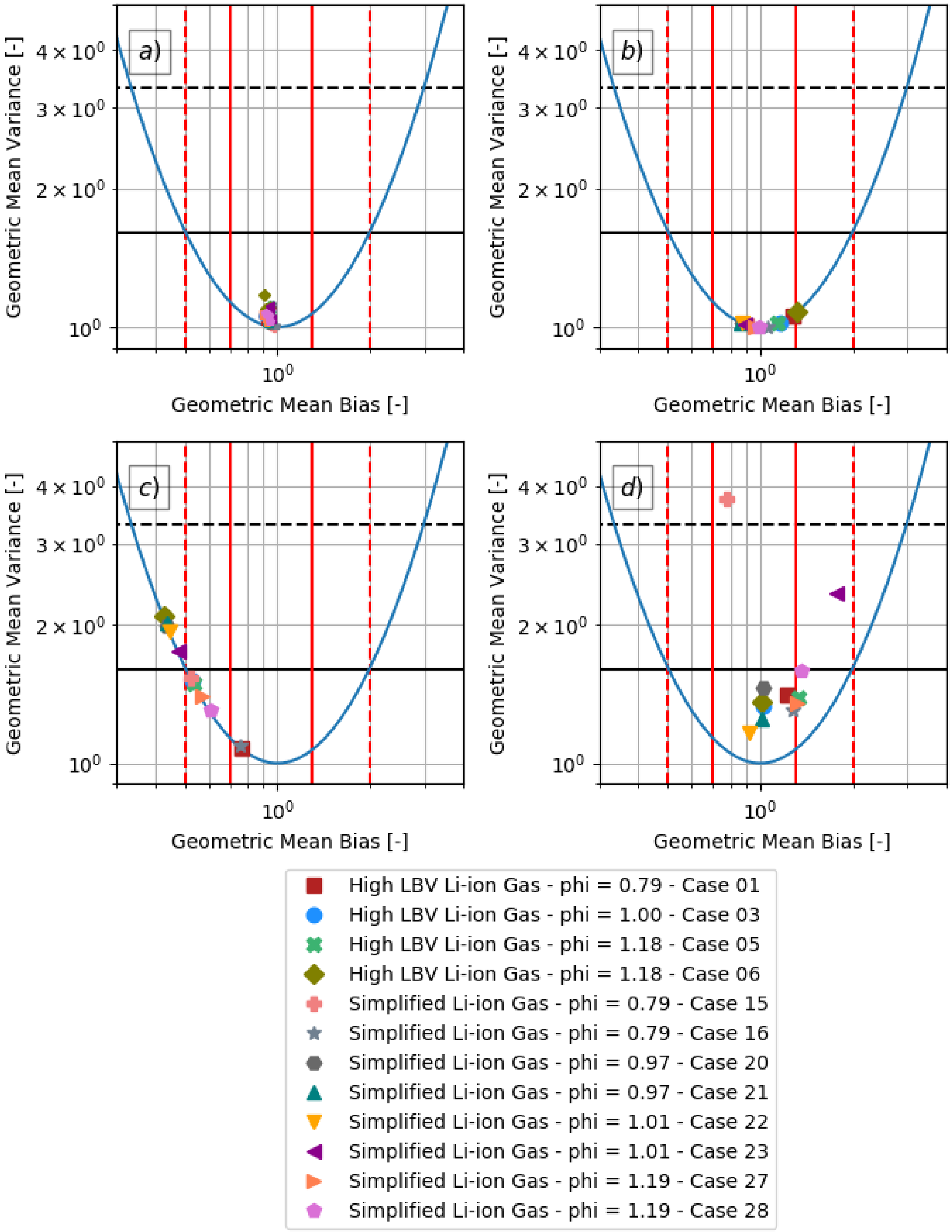

Figure 32. The mean geometric bias and the mean geometric variance for the inner channel geometry High LBV Li-ion gas and the Simplified Li-ion gas cases. a): Temporal pressure evolution; b): Maximum pressure; c): Positive impulse; d): Spatial flame front velocity.

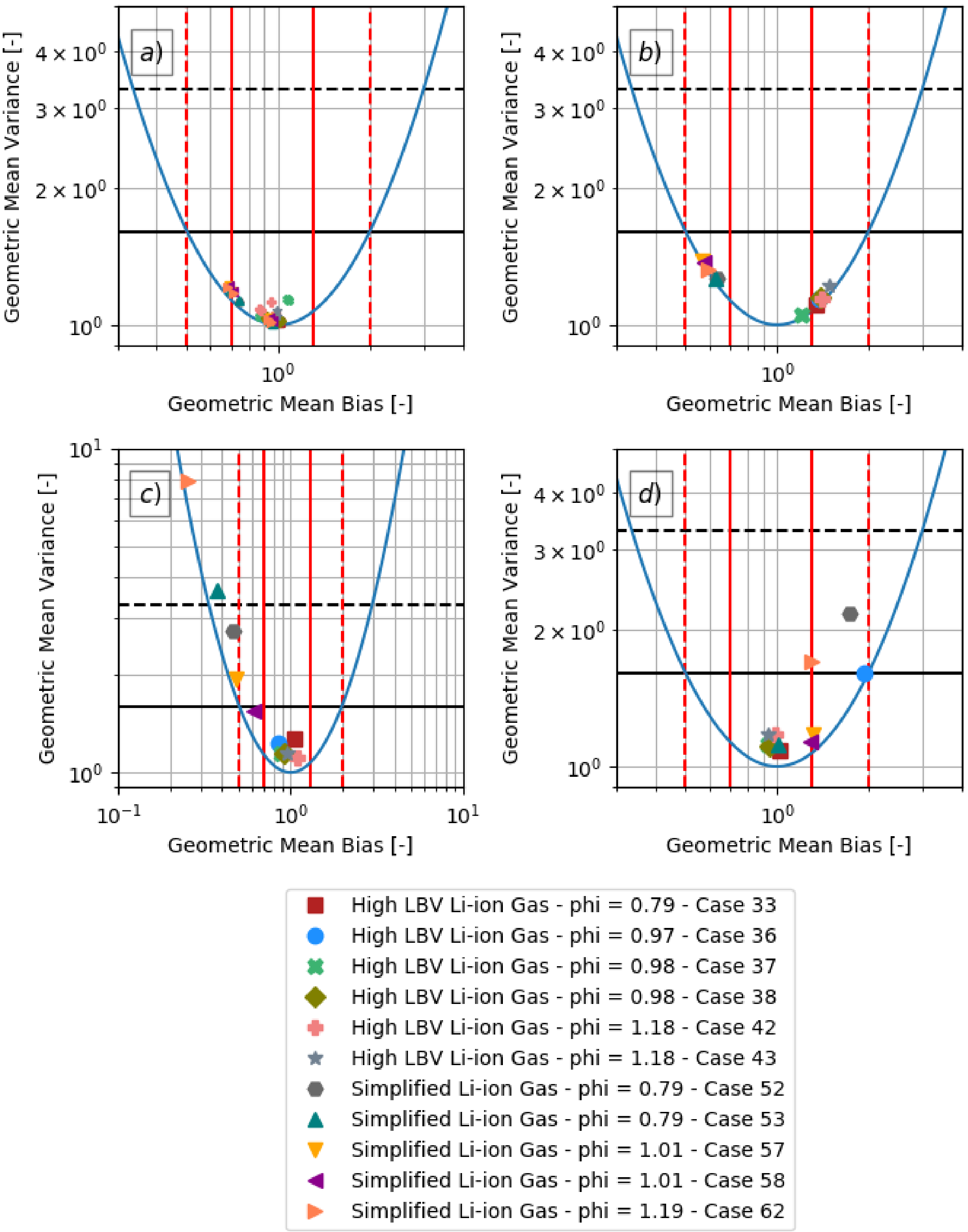

Figure 33. The mean geometric bias and the mean geometric variance for the High LBV Li-ion gas and the Simplified Li-ion gas in the center channel geometry; a) Temporal pressure evolution; b) Maximum pressure; c) Positive impulse; d) Spatial flame front velocity

The XiFoam model performance of the temporal pressure evolution, maximum pressure peak, and spatial evolution of the flame front velocity for the Simplified Li-ion gas cases were within the acceptable criteria for all but case 15. However, only five of thirteen cases were within the acceptable model performance criteria for the positive impulse. A significant discrepancy was found when comparing the flame front position for the Simplified Li-ion gas, center channel geometry cases. In the simulations, the flame propagates faster, causing a more significant pressure increase and, thus, a higher positive impulse. There is less disagreement in flame acceleration in the inner channel geometry cases, resulting in better model performance for the maximum explosion pressure and slightly better for the positive impulse. For the inner channel geometry, the overall averaged MG and VG were 0.89 and 1.36, respectively, whereas, for the center channel geometry, the overall averaged MG and VG were 0.80 and 1.86, respectively.

Changing the value of the combustion model parameter *uPrimeCoef* and the Crank-Nicolson coefficient greatly influenced the simulation results. The *uPrimeCoef* affects the sub-grid turbulence kinetic energy influence on the variable Ξ, which affects the flame propagation speed. For the center channel geometry, High LBV Li-ion gas cases, a *uPrimeCoef* of 0.6 fitted reasonably well with the experiments. However, for the center channel geometry, Simplified Li-ion gas cases, a lower *uPrimeCoef* would have resulted in a better prediction of the flame propagation and, thus, better maximum pressure prediction.

Increasing the Crank-Nicolson coefficient usually resulted in a higher flame acceleration and thus higher maximum pressures. Increasing this coefficient from 0.4 to 0.6 for the High CFD 1.0 center simulation case resulted in a maximum pressure of 450 kPa (gauge), 300 kPa higher than when using a coefficient value of 0.4. Numerical instabilities were encountered as the Crank-Nicolson coefficient increased.

It is possible to accurately predict the maximum explosion peak, positive impulse, and the spatial evolution of the flame front velocity by adjusting the *uPrimeCoef* and the Crank-Nicolson coefficient. However, accurately predicting these three simulation results in the same simulation is challenging with XiFoam. One of the reasons this is difficult is caused by the broadening of the flame thickness in the simulations.

Finally, the center channel geometry, Simplified Li-ion gas cases with a ϕ above 1.19, except case 62, would quench while propagating through the cylinder geometry. Some cases, however, reignited, but after a considerably long time. The quenching may be caused by a highly turbulent flow, which may be violating the XiFoam laminar flamelet assumption. Further investigation is needed to explain this phenomenon, which is beyond the scope of this study.

4.5.4 Conclusion

- This study examined the XiFoam model performance by comparing the experimental and the CFD simulated temporal pressure evolution, maximum pressure peak, positive impulse, and spatial evolution of the flame front velocity for two different channel geometries and two gas compositions for several ϕ.
- The XiFoam model performance for the temporal pressure evolution, maximum pressure peak, positive impulse, and spatial evolution of the flame front velocity for the High LBV Li-ion gas cases was all within the acceptable criterion shown in Table 12.
- For the Simplified Li-ion gas cases, the temporal pressure evolution, maximum pressure peak, and spatial flame front speed evolution were within the acceptable model performance criteria for all cases, except case 15. However, for the positive impulse, only five of thirteen cases were within the acceptable model criteria.
- Both gas compositions in both geometries have an overall averaged MG and VG within the acceptable model performance criteria.
- Adjusting the combustion parameter *uPrimeCoef* and the Crank-Nicolson coefficient can impact the flame propagation significantly, thus the simulation results.
- Accurately predicting the maximum peak pressure and positive impulse in the same simulation is difficult with the CFD method XiFoam.

5 Summary and Conclusion

This Ph.D. thesis presents a study of premixed combustion of flammable gas vented from failed LIBs. Premixed combustion is an extensive topic with numerous research areas; therefore, the four research goals/objectives listed in section 1.1 were set to focus and limit the study. These research goals were set in accordance with the research center MoZEES. This section summarizes each research goal, ending with recommended future research that can improve on the work done in this thesis.

5.1 Combustion properties determined in explosion sphere

A total of seven different compositions have been studied in the explosion sphere, three different electrolyte solvents, three gas compositions related to failed LIBs, and a pseudo/simplified Li-ion vent gas. In Article A, the explosion pressure, the rate of explosion pressure rise, and the explosive limits, for the electrolyte solvents DMC, EMC and DEC were determined at 373 K and 100 kPa (absolute). Furthermore, in Article B, the explosion pressure, the rate of explosion pressure rise, and the LBV for DMC at 300 K and 100 kPa (absolute) were determined. Finally, in Article C, the explosion pressure, the rate of explosion pressure rise, and the LBV for the three gas compositions related to failed LIBs and a pseudo/simplified Li-ion vent gas were determined at 300 K and 100 kPa (absolute). The point below summarizes the key observations and conclusions in these articles.

- The electrolyte solvents, DMC, EMC, and DEC, have similar explosion pressure and rate of explosion pressure rise, which may simplify preliminary risk assessments. (Article A)
- Comparing the electrolyte solvents to H_2, CH_4, and C_3H_8 showed that the explosion characteristics of C_3H_8 were very similar to that of the three carbonates at 373 K and 100 kPa (absolute). (Article A)
- For DMC at 300 K and 100 kPa (absolute), the maximum measured LBV was 300 $mm \cdot s^{-1}$ at a fuel-air equivalence ratio of 1.04. Additionally, at 302 K, near the saturated vapor pressure, the LBV is 261 $mm \cdot s^{-1}$. (Article B)

- Of the three Li-ion vent gas compositions, the minimum and maximum LBV ranges from 351 mm·s^{-1} and 1056 mm·s^{-1}, respectively. This range of LBV illustrates the significance of particular species in the gas compositions. Gas compositions with a high concentration of H_2 and CO, as a higher LBV, whereas gas compositions with a high CO_2 concentration tend to have a lower LBV. (Article C)

In addition to the point above, the experimental results of the explosion characteristics and LBVs presented in Table 4, Figure 25, Figure 26, Table 6, and Figure 28 are considered novel and one of the scientific contributions from this study.

5.2 Comparison of predicted and measured combustion properties

To experimentally determine combustion properties for the vast variation of vent gas compositions published would not be feasible, at least not within the time frame of this Ph.D. thesis. Moreover, the 20-liter explosion sphere has temperature and pressure limitations, which restricts the experimental range. However, explosion pressure and LBV can be determined numerically using solvers in tools such as Cantera with the appropriate reaction mechanisms (chemical kinetics model). Therefore, in this thesis, statistical analysis and visual (qualitative) comparison have been done to evaluate the LBV prediction accuracy of four different reaction mechanisms.

In Article B, the reaction mechanisms by Glaude et al. [97] and Sun et al. [99] were compared to the measure LBV of DMC. Moreover, in Article C, the reaction mechanisms GRI-Mech 3.0, San Diego Mech, and those proposed by Glaude et al. and Sun et al. were compared to four different gas compositions. The point below summarizes the key observations and conclusions in these articles.

- Compared to the measured LBV for DMC, the reaction mechanism proposed by Sun et al. had the lowest discrepancy. The mechanisms by Glaude et al. significantly over predicts the LBVs. (Article B)

- GRI-Mech 3.0 predicted the LBV with the highest accuracy for gas compositions with low CO_2 content. However, over predicted the LBV when the CO_2 content was more than 20%. (Article C)
- The reaction mechanism by Sun et al. had a consistently high coefficient of determination (R^2), which was above 0.95 for all gas compositions. Although under predicted the LBV for the High LBV Li-ion gas on the fuel-rich side. Article C)
- Recommended criteria for choosing a reaction mechanism to predict LBV for gases vented from LIBs based on the composition's carbon dioxide (CO_2) concentration. (Article C)

Within LIB safety research, a few studies use reaction mechanisms to predict combustion properties for Li-ion vent gas compositions, with the study performed by Baird et al. [15] being probably the most comprehensive. However, in this thesis, the prediction accuracy of several reaction mechanisms have been compared with experimental results of LIB vent gas compositions, which has not been previously published, and one of the scientific contribution from this study.

5.3 CFD method

The third objective was to develop a CFD method to simulate premixed combustion of gases vented from failed LIBs, with the XiFoam model/solver in OpenFOAM as the basis CFD tool. XiFoam required a set of coefficients for modeling transport, combustion, and thermodynamic properties, which are gas composition dependent. The code *mech2Foam* was created to calculate these model coefficients.

Mech2Foam generates all the required model coefficients for an inhomogeneous combustion simulation in XiFoam, from a specified fuel and air gas composition. The code is written in the Python programming language and utilizes the Cantera functions described in section 3.3. The m*ech2Foam* code/method and the comparison result in article D are summarized in the points below.

- The NASA polynomial coefficients are generated for the XiFoam species, oxidant, fuel, and burntProducts, by mole-weighted NASA coefficients gathered from a reaction mechanism. (Supplementary Data A)
- The Sutherland coefficients are determined for the XiFoam species by curve fitting the Sutherland equation (dynamic viscosity) to data generated using Cantera and a reaction mechanism. (Supplementary Data A)
- Determines the Gülder coefficients required for LBV correlation by curve fitting to data generated using Cantera and a reaction mechanism. (Supplementary Data A)
- The comparison between generated NASA polynomials and thermodynamic values calculated using Cantera and the San Diego reaction mechanism was neglectable. Furthermore, the curve-fitted Sutherland equation had a low discrepancy compared to values calculated using Cantera. (Article D)
- The curve-fitted Gülder equation had only minor deviations from the values used in the regression. However, comparing to values outside the regression data, the deviation significantly increases. The temperature and pressure range should be considered when using the Gülder equation for LBV correlation. (Article D)
- Although *mech2Foam* is designed for XiFoam, any CFD model utilizing the same input parameters could use this method.

As mentioned, mech2Foam is an openly available tool written in Python, which generates the necessary combustion, thermodynamic, and transport properties for a CFD simulation of inhomogeneous combustion of Li-ion vent gases. Hopefully, the *mech2Foam* tool can contribute to more CFD simulations of battery installations, thus potentially improving the safety of such installations.

5.4 CFD modeling

The final research goal was to review the CFD method by comparing simulated results with laboratory-scale experiments. Section 3.2 describes the experimental setup of the 1-meter explosion channel used for this comparison. Furthermore, the CFD method XiFoam is described in section 3.4, and the *mech2Foam* code is described and demonstrated in supplementary data A and article D, respectively.

In total, three different channel geometries and three different gas compositions have been analyzed. Article D is a numerical and experimental study of a premixed gas explosion with the Generic Li-ion gas in an empty channel. In Article E, a premixed gas explosion of two gas compositions with two explosion channel configurations with 18650 cell-like cylinders was experimentally and numerically studied. The articles D and E results were determined at standard atmospheric conditions, 293 K and 101.3 kPa (absolute). The point below summarizes the key observations and conclusions in these articles.

- The CFD simulations predicted the maximum explosion pressure and flame front position for an empty channel with only minor discrepancies. The highest maximum explosion pressure was 1.36 kPa (gauge) and 1.45 kPa (gauge) in the experiments and simulations, respectively. (Article D)
- The initial temporal evolution of the pressure and flame front velocity in the empty channel simulations agreed well with the experiment. However, pressure and flame front velocity oscillations, which occurred as the flame approached the channel opening, were not predicted. (Article D)
- The XiFoam model performance for the temporal pressure evolution, maximum pressure peak, positive impulse, and spatial evolution of the flame front velocity for the two channels with the 18650 cell-like cylinders with the High LBV Li-ion gas cases were all within the acceptable criteria shown in Table 12. (Article E)
- For the two channels with the 18650 cell-like cylinders with the Simplified Li-ion gas composition, the XiFoam model performance for the temporal pressure evolution, maximum pressure peak, and spatial evolution of the flame front

velocity was within acceptable model performance criteria in Table 12, for all except one case. However, for the positive impulse, only five of thirteen cases were within the acceptable model criteria.

- The combustion parameter *uPrimeCoef* and the Crank-Nicolson coefficient used in the time discretization can significantly change the flame propagation and thus the CFD simulation results.
- Accurately predicting the maximum peak pressure and positive impulse in the same simulation is difficult with the CFD method XiFoam, due to the increase in flame thickness during simulation.

Most CFD simulations related to LIBs focus on single-cell failure, thermal runaway, and cell-to-cell propagation, which does not directly address the explosion hazard. In a report by DNV [124], CFD simulations of gas dispersion and explosion in maritime LIB installations were investigated. However, the explosion simulations were never compared or validated with experiments. This thesis presents a CFD method for simulating explosions related to LIB failure and the model performance of this CFD method. Hopefully, this CFD method, which has been compared several to laboratory-scale experiments, will contribute to future risk and consequences analysis of LIB applications and installations.

5.5 Future work

Below are some research goals that can improve upon the scientific work presented in this thesis.

- Some studies in Table 1 show that both toxic species and electrolyte solvents are released, in addition to the combustible and inert species studied in this thesis. As more detailed gas compositions are published, which contain electrolyte solvents, toxic, inert, and combustible species, the combustion properties of such gas mixtures should be studied further.
- The Simplified Li-ion gas composition was generated to resemble the combustion properties of the Generic Li-ion gas composition. Although these gas

compositions have similar combustion properties in the 20-liter explosion sphere, it is uncertain how similar a vented gas explosion is. Experimentally investigating the flame propagation would improve on the simplified gas assumption.

- In this study, homogeneous premixed gas explosions have been studied. In an actual LIB event, it is improbable that the ignited combustible cloud is homogeneous. An analysis of inhomogeneous gas explosions could provide valuable insight into more realistic LIB explosions.
- List with suggested improvements to the XiFoam model/solvers.
    - Implement a function for *uPrimeCoef*, instead of a constant. A variable *uPrimeCoef* value may improve the flame propagation speed during the transition from laminar to turbulent.
    - Improve the thermodynamic evaluation of rich combustion. The highest heat of combustion will always be at a fuel-air equivalence ratio of 1.0 for an inhomogeneous mixture in XiFoam. However, for most fuels, the maximum heat release is usually found slightly on the rich side.
    - Reduce the growth of the simulated flame thickness. As the two CFD studies have shown, the increase in simulated flame thickness can significantly impact the results.
- The prediction accuracy of the XiFoam model/solver has been evaluated for laboratory-scale experiments only. Comparing XiFoam simulations to experiments with larger geometries would give further insight into to prediction accuracy of XiFoam.

References

[1] J.J. Corbett, J.J. Winebrake, E.H. Green, P. Kasibhatla, V. Eyring, A. Lauer, Mortality from Ship Emissions: A Global Assessment, Environmental Science & Technology. 41 (2007) 8512–8518. https://doi.org/10.1021/es071686z.

[2] B. Lin, C. Xie, Reduction potential of CO2 emissions in China's transport industry, Renewable and Sustainable Energy Reviews. 33 (2014) 689–700. https://doi.org/10.1016/j.rser.2014.02.017.

[3] M. Viana, P. Hammingh, A. Colette, X. Querol, B. Degraeuwe, I. de Vlieger, J. van Aardenne, Impact of maritime transport emissions on coastal air quality in Europe, Atmospheric Environment. 90 (2014) 96–105. https://doi.org/10.1016/j.atmosenv.2014.03.046.

[4] L. Zhang, R. Long, H. Chen, J. Geng, A review of China's road traffic carbon emissions, Journal of Cleaner Production. 207 (2019) 569–581. https://doi.org/10.1016/j.jclepro.2018.10.003.

[5] H. Shi, Y. Wang, J. Chen, D. Huisingh, Preventing smog crises in China and globally, Journal of Cleaner Production. 112 (2016) 1261–1271. https://doi.org/10.1016/j.jclepro.2015.10.068.

[6] Ministry of Climate and Environment, Act relating to Norway's climate targets (Climate Change Act), 2018. https://lovdata.no/dokument/NLE/lov/2017-06-16-60 (accessed August 20, 2019).

[7] MOZEES, MOZEES, Mobility Zero Emission Energy Systems. (2017). https://www.mozees.no/ (accessed August 20, 2019).

[8] P.G. Balakrishnan, R. Ramesh, T. Prem Kumar, Safety mechanisms in lithium-ion batteries, Journal of Power Sources. 155 (2006) 401–414. https://doi.org/10.1016/j.jpowsour.2005.12.002.

[9] Battery University, What's the Best Battery?, Battery University. (2017). http://batteryuniversity.com/learn/archive/whats_the_best_battery.

[10] Battery University, Types of Lithium-ion, Battery University. (2019). https://batteryuniversity.com/learn/article/types_of_lithium_ion (accessed August 21, 2019).

[11] D.P. Finegan, E. Darcy, M. Keyser, B. Tjaden, T.M.M. Heenan, R. Jervis, J.J. Bailey, N.T. Vo, O.V. Magdysyuk, M. Drakopoulos, M. Di Michiel, A. Rack, G. Hinds, D.J.L. Brett, P.R. Shearing, Identifying the Cause of Rupture of Li-Ion Batteries during Thermal Runaway, Advanced Science. 5 (2018) 1700369. https://doi.org/10.1002/advs.201700369.

[12] D. Lisbona, T. Snee, A review of hazards associated with primary lithium and lithium-ion batteries, Process Safety and Environmental Protection. 89 (2011) 434–442. https://doi.org/10.1016/j.psep.2011.06.022.

[13] S. Abada, G. Marlair, A. Lecocq, M. Petit, V. Sauvant-Moynot, F. Huet, Safety focused modeling of lithium-ion batteries: A review, Journal of Power Sources. 306 (2016) 178–192. https://doi.org/10.1016/j.jpowsour.2015.11.100.

[14] Q. Wang, P. Ping, X. Zhao, G. Chu, J. Sun, C. Chen, Thermal runaway caused fire and explosion of lithium ion battery, Journal of Power Sources. 208 (2012) 210–224. https://doi.org/10.1016/j.jpowsour.2012.02.038.

[15] A.R. Baird, E.J. Archibald, K.C. Marr, O.A. Ezekoye, Explosion hazards from lithium-ion battery vent gas, Journal of Power Sources. 446 (2020) 227257. https://doi.org/10.1016/j.jpowsour.2019.227257.

[16] L. Kong, C. Li, J. Jiang, M. Pecht, Li-Ion Battery Fire Hazards and Safety Strategies, Energies. 11 (2018) 2191. https://doi.org/10.3390/en11092191.

[17] Sophia Beausoleil, Lithium batteries causes train car explosion in NE Houston, KPRC, Click2Houston. (2017). https://www.click2houston.com/news/2017/04/24/lithium-batteries-causes-train-car-explosion-in-ne-houston/.

[18] D. Hill, McMicken Battery Energy Storage System Event Technical Analysis and Recommendations, DNV-GL, 2020. https://www.aps.com/-/media/APS/APSCOM-PDFs/About/Our-Company/Newsroom/McMickenFinalTechnicalReport.ashx?la=en&hash=50335FB5098D9858BFD276C40FA54FCE.

[19] A. Reid, Exploding Kona EV in Montreal prompts investigation from Hyundai, Exploding Kona EV in Montreal Prompts Investigation from Hyundai. (2019). https://driving.ca/hyundai/auto-news/news/exploding-kona-ev-in-montreal-prompts-investigation-from-hyundai.

[20] Corvus Energy, Fire onboard the car-ferry Ytterøyningen: Preliminary investigation results, Fire Onboard the Car-Ferry Ytterøyningen: Preliminary Investigation Results. (2020). https://corvusenergy.com/fire-onboard-the-car-ferry-ytteroyningen-preliminary-investigation-results/.

[21] CTIF - International Association of Fire and Rescue Services, Accident analysis of the Beijing lithium battery explosion which killed two firefighters, (2021). https://www.ctif.org/news/accident-analysis-beijing-lithium-battery-explosion-which-killed-two-firefighters.

[22] E.P. Roth, C.C. Crafts, D.H. Doughty, James. McBreen, Advanced technology development program for lithium-ion batteries : thermal abuse performance of 18650 Li-ion cells., 2004. https://doi.org/10.2172/918751.

[23] C. Mikolajczak, M. Kahn, K. White, R.T. Long, Lithium-Ion Batteries Hazard and Use Assessment, Springer US, Boston, MA, 2011. https://doi.org/10.1007/978-1-4614-3486-3.

[24] J. Johnsplass, Lithium-ion battery safety, University of South-Eastern Norway, 2017.

[25] Torleif Lian, Preben J. S. Vie, Martin Gilljam, Sissel Forseth, Safety Aspects of Cyclic Aged Commercial Lithium-ion Cells, in: n.d.

[26] R. Spotnitz, J. Franklin, Abuse behavior of high-power, lithium-ion cells, Journal of Power Sources. 113 (2003) 81–100. https://doi.org/10.1016/S0378-7753(02)00488-3.

[27] Y. Fernandes, A. Bry, S. de Persis, Identification and quantification of gases emitted during abuse tests by overcharge of a commercial Li-ion battery, Journal of Power Sources. 389 (2018) 106–119. https://doi.org/10.1016/j.jpowsour.2018.03.034.

[28] A.W. Golubkov, S. Scheikl, R. Planteu, G. Voitic, H. Wiltsche, C. Stangl, G. Fauler, A. Thaler, V. Hacker, Thermal runaway of commercial 18650 Li-ion batteries with

LFP and NCA cathodes – impact of state of charge and overcharge, RSC Advances. 5 (2015) 57171–57186. https://doi.org/10.1039/C5RA05897J.

[29] V. Ruiz, A. Pfrang, A. Kriston, N. Omar, P. Van den Bossche, L. Boon-Brett, A review of international abuse testing standards and regulations for lithium ion batteries in electric and hybrid electric vehicles, Renewable and Sustainable Energy Reviews. 81 (2018) 1427–1452. https://doi.org/10.1016/j.rser.2017.05.195.

[30] D. Bjerketvedt, J.R. Bakke, K. Van Wingerden, Gas explosion handbook, Journal of Hazardous Materials. 52 (1997) 1–150.

[31] C.K. Law, Combustion physics, Cambridge University Press, Cambridge ; New York, 2006.

[32] E. Varea, J. Beeckmann, H. Pitsch, Z. Chen, B. Renou, Determination of burning velocities from spherically expanding H 2 /air flames, Proceedings of the Combustion Institute. 35 (2015) 711–719. https://doi.org/10.1016/j.proci.2014.05.137.

[33] J. Beeckmann, R. Hesse, J. Schaback, H. Pitsch, E. Varea, N. Chaumeix, Flame propagation speed and Markstein length of spherically expanding flames: Assessment of extrapolation and measurement techniques, Proceedings of the Combustion Institute. 37 (2019) 1521–1528. https://doi.org/10.1016/j.proci.2018.08.047.

[34] H.G. Weller, G. Tabor, H. Jasak, C. Fureby, A tensorial approach to computational continuum mechanics using object-oriented techniques, Comput. Phys. 12 (1998) 620. https://doi.org/10.1063/1.168744.

[35] CFD Direct, OpenFOAM v7 User Guide, OpenFOAM v7 User Guide. (2021). https://cfd.direct/openfoam/user-guide-v7/.

[36] S. Goriparti, Review on recent progress of nanostructured anode materials for Li-ion batteries, Journal of Power Sources. (2014) 23.

[37] V. Etacheri, R. Marom, R. Elazari, G. Salitra, D. Aurbach, Challenges in the development of advanced Li-ion batteries: a review, Energy & Environmental Science. 4 (2011) 3243. https://doi.org/10.1039/c1ee01598b.

[38] S.S. Zhang, A review on electrolyte additives for lithium-ion batteries, Journal of Power Sources. 162 (2006) 1379–1394. https://doi.org/10.1016/j.jpowsour.2006.07.074.

[39] H. Maleki, J.N. Howard, Role of the cathode and anode in heat generation of Li-ion cells as a function of state of charge, Journal of Power Sources. 137 (2004) 117–127. https://doi.org/10.1016/j.jpowsour.2004.05.053.

[40] R. Schröder, M. Aydemir, G. Seliger, Comparatively Assessing different Shapes of Lithium-ion Battery Cells, Procedia Manufacturing. 8 (2017) 104–111. https://doi.org/10.1016/j.promfg.2017.02.013.

[41] Q. Wang, B. Mao, S.I. Stoliarov, J. Sun, A review of lithium ion battery failure mechanisms and fire prevention strategies, Progress in Energy and Combustion Science. 73 (2019) 95–131. https://doi.org/10.1016/j.pecs.2019.03.002.

[42] L. Lu, X. Han, J. Li, J. Hua, M. Ouyang, A review on the key issues for lithium-ion battery management in electric vehicles, Journal of Power Sources. 226 (2013) 272–288. https://doi.org/10.1016/j.jpowsour.2012.10.060.

[43] S. Hess, M. Wohlfahrt-Mehrens, M. Wachtler, Flammability of Li-Ion Battery Electrolytes: Flash Point and Self-Extinguishing Time Measurements, Journal of The Electrochemical Society. 162 (2015) A3084–A3097. https://doi.org/10.1149/2.0121502jes.

[44] D.H. Doughty, Vehicle Battery Safety Roadmap Guidance, 2012. https://doi.org/10.2172/1055366.

[45] D. Ouyang, M. Chen, J. Liu, R. Wei, J. Weng, J. Wang, Investigation of a commercial lithium-ion battery under overcharge/over-discharge failure conditions, RSC Adv. 8 (2018) 33414–33424. https://doi.org/10.1039/C8RA05564E.

[46] D. Belov, M.-H. Yang, Investigation of the kinetic mechanism in overcharge process for Li-ion battery, Solid State Ionics. 179 (2008) 1816–1821. https://doi.org/10.1016/j.ssi.2008.04.031.

[47] F. Xu, H. He, Y. Liu, C. Dun, Y. Ren, Q. Liu, M. Wang, J. Xie, Failure Investigation of $LiFePO_4$ Cells under Overcharge Conditions, J. Electrochem. Soc. 159 (2012) A678–A687. https://doi.org/10.1149/2.024206jes.

[48] D.P. Finegan, M. Scheel, J.B. Robinson, B. Tjaden, M. Di Michiel, G. Hinds, D.J.L. Brett, P.R. Shearing, Investigating lithium-ion battery materials during overcharge-induced thermal runaway: an operando and multi-scale X-ray CT study, Physical Chemistry Chemical Physics. 18 (2016) 30912–30919. https://doi.org/10.1039/C6CP04251A.

[49] T. Ma, L. Chen, S. Liu, Z. Zhang, S. Xiao, B. Fan, L. Liu, C. Lin, S. Ren, F. Wang, Mechanics-morphologic coupling studies of commercialized lithium-ion batteries under nail penetration test, Journal of Power Sources. 437 (2019) 226928. https://doi.org/10.1016/j.jpowsour.2019.226928.

[50] D.P. Finegan, E. Darcy, M. Keyser, B. Tjaden, T.M.M. Heenan, R. Jervis, J.J. Bailey, R. Malik, N.T. Vo, O.V. Magdysyuk, R. Atwood, M. Drakopoulos, M. DiMichiel, A. Rack, G. Hinds, D.J.L. Brett, P.R. Shearing, Characterising thermal runaway within lithium-ion cells by inducing and monitoring internal short circuits, Energy & Environmental Science. 10 (2017) 1377–1388. https://doi.org/10.1039/C7EE00385D.

[51] P. Ribière, S. Grugeon, M. Morcrette, S. Boyanov, S. Laruelle, G. Marlair, Investigation on the fire-induced hazards of Li-ion battery cells by fire calorimetry, Energy Environ. Sci. 5 (2012) 5271–5280. https://doi.org/10.1039/C1EE02218K.

[52] A. Nedjalkov, J. Meyer, M. Köhring, A. Doering, M. Angelmahr, S. Dahle, A. Sander, A. Fischer, W. Schade, Toxic Gas Emissions from Damaged Lithium Ion Batteries—Analysis and Safety Enhancement Solution, Batteries. 2 (2016) 5. https://doi.org/10.3390/batteries2010005.

[53] G. Gachot, P. Ribière, D. Mathiron, S. Grugeon, M. Armand, J.-B. Leriche, S. Pilard, S. Laruelle, Gas Chromatography/Mass Spectrometry As a Suitable Tool for the Li-Ion Battery Electrolyte Degradation Mechanisms Study, Anal. Chem. 83 (2011) 478–485. https://doi.org/10.1021/ac101948u.

[54] A.W. Golubkov, D. Fuchs, J. Wagner, H. Wiltsche, C. Stangl, G. Fauler, G. Voitic, A. Thaler, V. Hacker, Thermal-runaway experiments on consumer Li-ion batteries with metal-oxide and olivin-type cathodes, RSC Adv. 4 (2014) 3633–3642. https://doi.org/10.1039/C3RA45748F.

[55] V. Somandepalli, K. Marr, Q. Horn, Quantification of Combustion Hazards of Thermal Runaway Failures in Lithium-Ion Batteries, SAE International Journal of Alternative Powertrains. 3 (2014) 98–104. https://doi.org/10.4271/2014-01-1857.

[56] F. Larsson, P. Andersson, P. Blomqvist, A. Lorén, B.-E. Mellander, Characteristics of lithium-ion batteries during fire tests, Journal of Power Sources. 271 (2014) 414–420. https://doi.org/10.1016/j.jpowsour.2014.08.027.

[57] U. Bergström, Å. Gustafsson, C. Lejon, D. Sturk, T. Tengel, Screening of Vented Gases and Aerosols from Li-Ion LFP & NMC Batteries under Nitrogen atmosphere, 2015.

[58] N.S. Spinner, C.R. Field, M.H. Hammond, B.A. Williams, K.M. Myers, A.L. Lubrano, S.L. Rose-Pehrsson, S.G. Tuttle, Physical and chemical analysis of lithium-ion battery cell-to-cell failure events inside custom fire chamber, Journal of Power Sources. 279 (2015) 713–721. https://doi.org/10.1016/j.jpowsour.2015.01.068.

[59] Y. Fu, S. Lu, K. Li, C. Liu, X. Cheng, H. Zhang, An experimental study on burning behaviors of 18650 lithium ion batteries using a cone calorimeter, Journal of Power Sources. 273 (2015) 216–222. https://doi.org/10.1016/j.jpowsour.2014.09.039.

[60] Q. Yuan, F. Zhao, W. Wang, Y. Zhao, Z. Liang, D. Yan, Overcharge failure investigation of lithium-ion batteries, Electrochimica Acta. 178 (2015) 682–688. https://doi.org/10.1016/j.electacta.2015.07.147.

[61] J. Sun, J. Li, T. Zhou, K. Yang, S. Wei, N. Tang, N. Dang, H. Li, X. Qiu, L. Chen, Toxicity, a serious concern of thermal runaway from commercial Li-ion battery, Nano Energy. 27 (2016) 313–319. https://doi.org/10.1016/j.nanoen.2016.06.031.

[62] Y. Zheng, K. Qian, D. Luo, Y. Li, Q. Lu, B. Li, Y.-B. He, X. Wang, J. Li, F. Kang, Influence of over-discharge on the lifetime and performance of $LiFePO_4$ /graphite batteries, RSC Adv. 6 (2016) 30474–30483. https://doi.org/10.1039/C6RA01677D.

[63] T. (FAA) Maloney, Lithium Battery Thermal Runaway Vent Gas Analysis, U.S. Department of Transportation William J. Hughes Technical Center, 2016. https://www.fire.tc.faa.gov/pdf/TC-15-59.pdf.

[64] F. Larsson, P. Andersson, P. Blomqvist, B.-E. Mellander, Toxic fluoride gas emissions from lithium-ion battery fires, Scientific Reports. 7 (2017). https://doi.org/10.1038/s41598-017-09784-z.

[65] M. Lammer, A. Königseder, V. Hacker, Holistic methodology for characterisation of the thermally induced failure of commercially available 18650 lithium ion cells, RSC Advances. 7 (2017) 24425–24429. https://doi.org/10.1039/C7RA02635H.

[66] S. Koch, A. Fill, K.P. Birke, Comprehensive gas analysis on large scale automotive lithium-ion cells in thermal runaway, Journal of Power Sources. 398 (2018) 106–112. https://doi.org/10.1016/j.jpowsour.2018.07.051.

[67] D. Sturk, L. Rosell, P. Blomqvist, A. Ahlberg Tidblad, Analysis of Li-Ion Battery Gases Vented in an Inert Atmosphere Thermal Test Chamber, Batteries. 5 (2019) 61. https://doi.org/10.3390/batteries5030061.

[68] S.J. Harris, A. Timmons, W.J. Pitz, A combustion chemistry analysis of carbonate solvents used in Li-ion batteries, Journal of Power Sources. 193 (2009) 855–858. https://doi.org/10.1016/j.jpowsour.2009.04.030.

[69] M. Henriksen, K. Vaagsaether, J. Lundberg, S. Forseth, D. Bjerketvedt, Explosion characteristics for Li-ion battery electrolytes at elevated temperatures, Journal of Hazardous Materials. 371 (2019) 1–7. https://doi.org/10.1016/j.jhazmat.2019.02.108.

[70] G.P. Smith, D.M. Golden, M. Frenklach, N.W. Moriarty, B. Eiteneer, M. Goldenberg, C.T. Bowman, R.K. Hanson, S. Song, W.C.G. Jr, V.V. Lissianski, Z. Qin, GRI-MECH 3.0, (1999). http://combustion.berkeley.edu/gri-mech/version30/text30.html#cite (accessed March 18, 2018).

[71] F.N. Egolfopoulos, N. Hansen, Y. Ju, K. Kohse-Höinghaus, C.K. Law, F. Qi, Advances and challenges in laminar flame experiments and implications for combustion chemistry, Progress in Energy and Combustion Science. 43 (2014) 36–67. https://doi.org/10.1016/j.pecs.2014.04.004.

[72] A.A. Konnov, A. Mohammad, V.R. Kishore, N.I. Kim, C. Prathap, S. Kumar, A comprehensive review of measurements and data analysis of laminar burning velocities for various fuel+air mixtures, Progress in Energy and Combustion Science. 68 (2018) 197–267. https://doi.org/10.1016/j.pecs.2018.05.003.

[73] F.A. Williams, Combustion Theory., Chapman and Hall/CRC, Boulder, 1975. http://public.eblib.com/choice/publicfullrecord.aspx?p=5320077 (accessed September 7, 2018).

[74] M. Henriksen, A.V. Gaathaug, K. Vaagsaether, J. Lundberg, S. Forseth, D. Bjerketvedt, Laminar Burning Velocity of the Dimethyl Carbonate-Air Mixture Formed by the Li-Ion Electrolyte Solvent, Combustion, Explosion, and Shock Waves. 56 (2020) 383–393. https://doi.org/10.1134/S0010508220040024.

[75] G.H. Markstein, Nonsteady Flame Propagation, Elsevier Science, Burlington, 2014. http://public.eblib.com/choice/publicfullrecord.aspx?p=1880008 (accessed August 13, 2019).

[76] Z. Chen, On the extraction of laminar flame speed and Markstein length from outwardly propagating spherical flames, Combustion and Flame. 158 (2011) 291–300. https://doi.org/10.1016/j.combustflame.2010.09.001.

[77] F. Wu, W. Liang, Z. Chen, Y. Ju, C.K. Law, Uncertainty in stretch extrapolation of laminar flame speed from expanding spherical flames, Proceedings of the Combustion Institute. 35 (2015) 663–670. https://doi.org/10.1016/j.proci.2014.05.065.

[78] A.P. Kelley, J.K. Bechtold, C.K. Law, Premixed flame propagation in a confining vessel with weak pressure rise, Journal of Fluid Mechanics. 691 (2012) 26–51. https://doi.org/10.1017/jfm.2011.439.

[79] A.P. Kelley, C.K. Law, Nonlinear effects in the extraction of laminar flame speeds from expanding spherical flames, Combustion and Flame. 156 (2009) 1844–1851. https://doi.org/10.1016/j.combustflame.2009.04.004.

[80] Q. Liu, X. Chen, Y. Shen, Y. Zhang, Parameter extraction from spherically expanding flames propagated in hydrogen/air mixtures, International Journal of Hydrogen Energy. 44 (2019) 1227–1238. https://doi.org/10.1016/j.ijhydene.2018.11.004.

[81] J.D. Nauclér, E.J.K. Nilsson, A.A. Konnov, Laminar burning velocity of nitromethane + air flames: A comparison of flat and spherical flames, Combustion

and Flame. 162 (2015) 3803–3809. https://doi.org/10.1016/j.combustflame.2015.07.017.

[82] G. Rozenchan, D.L. Zhu, C.K. Law, S.D. Tse, Outward propagation, burning velocities, and chemical effects of methane flames up to 60 ATM, Proceedings of the Combustion Institute. 29 (2002) 1461–1470. https://doi.org/10.1016/S1540-7489(02)80179-1.

[83] J. Jarosinski, B. Veyssiere, eds., Combustion phenomena: selected mechanisms of flame formation, propagation, and extinction, CRC Press, Boca Raton, 2009.

[84] S.B. Dorofeev, Flame acceleration and explosion safety applications, Proceedings of the Combustion Institute. 33 (2011) 2161–2175. https://doi.org/10.1016/j.proci.2010.09.008.

[85] G. Ciccarelli, S. Dorofeev, Flame acceleration and transition to detonation in ducts, Progress in Energy and Combustion Science. 34 (2008) 499–550. https://doi.org/10.1016/j.pecs.2007.11.002.

[86] K. Vaagsaether, Modelling of gas explosions, Telemark University College, 2010.

[87] P. Clavin, F.A. Williams, Theory of premixed-flame propagation in large-scale turbulence, J. Fluid Mech. 90 (1979) 589–604. https://doi.org/10.1017/S002211207900241X.

[88] N. Peters, Laminar flamelet concepts in turbulent combustion, Symposium (International) on Combustion. 21 (1988) 1231–1250. https://doi.org/10.1016/S0082-0784(88)80355-2.

[89] F.P. Lees, Loss prevention in the process industries: hazard identification, assessment and control, 2. ed, Butterworth-Heinemann, Oxford, 1996.

[90] J.E. Shepherd, J.H.S. Lee, ON THE TRANSITION FROM DEFLAGRATION TO DETONATION, Major Research Topics in Combustion. (1992) 2.

[91] J.E. Shepherd, Detonation in gases, Proceedings of the Combustion Institute. 32 (2009) 83–98. https://doi.org/10.1016/j.proci.2008.08.006.

[92] G.S. Settles, Schlieren and shadowgraph techniques: visualizing phenomena in transparent media, Springer, Berlin ; New York, 2001.

[93] A. Savitzky, M.J.E. Golay, Smoothing and Differentiation of Data by Simplified Least Squares Procedures., Analytical Chemistry. 36 (1964) 1627–1639. https://doi.org/10.1021/ac60214a047.

[94] D.G. Goodwin, H.K. Moffat, R.L. Speth, Cantera: An Object-Oriented Software Toolkit For Chemical Kinetics, Thermodynamics, And Transport Processes, Zenodo, 2017. https://doi.org/10.5281/zenodo.170284.

[95] B.J. McBride, S. Gordon, M.A. Reno, Coefficients for Calculating Thermodynamic and Transport Properties of Individual Species, NASA, 1993. https://ntrs.nasa.gov/api/citations/19940013151/downloads/19940013151.pdf.

[96] B.E. Poling, J.M. Prausnitz, J.P. O'Connell, The properties of gases and liquids, 5. ed., internat. ed, McGraw-Hill, Boston, IL., 2007.

[97] P.A. Glaude, W.J. Pitz, M.J. Thomson, Chemical kinetic modeling of dimethyl carbonate in an opposed-flow diffusion flame, Proceedings of the Combustion Institute. 30 (2005) 1111–1118. https://doi.org/10.1016/j.proci.2004.08.096.

[98] H. Nakamura, H.J. Curran, A. Polo Córdoba, W.J. Pitz, P. Dagaut, C. Togbé, S.M. Sarathy, M. Mehl, J.R. Agudelo, F. Bustamante, An experimental and modeling

study of diethyl carbonate oxidation, Combustion and Flame. 162 (2015) 1395–1405. https://doi.org/10.1016/j.combustflame.2014.11.002.

[99] W. Sun, B. Yang, N. Hansen, C.K. Westbrook, F. Zhang, G. Wang, K. Moshammer, C.K. Law, An experimental and kinetic modeling study on dimethyl carbonate (DMC) pyrolysis and combustion, Combustion and Flame. 164 (2016) 224–238. https://doi.org/10.1016/j.combustflame.2015.11.019.

[100] UCSD, "Chemical-Kinetic Mechanisms for Combustion Applications", San Diego Mechanism web page, Mechanical and Aerospace Engineering (Combustion Research), University of California at San Diego, The San Diego Mechanism. (2016). http://combustion.ucsd.edu.

[101] Onshape, Onshape. (2014). https://www.onshape.com/en/.

[102] H.G. Weller, G. Tabor, A.D. Gosman, C. Fureby, Application of a flame-wrinkling les combustion model to a turbulent mixing layer, Symposium (International) on Combustion. 27 (1998) 899–907. https://doi.org/10.1016/S0082-0784(98)80487-6.

[103] H.G. Weller, C.J. Marooney, A.D. Gosman, A new spectral method for calculation of the time-varying area of a laminar flame in homogeneous turbulence, Symposium (International) on Combustion. 23 (1991) 629–636. https://doi.org/10.1016/S0082-0784(06)80310-3.

[104] Ö.L. Gülder, Correlations of Laminar Combustion Data for Alternative S.I. Engine Fuels, in: 1984. https://doi.org/10.4271/841000.

[105] M. Henriksen, D. Bjerketvedt, mech2Foam - Generating transport, combustion, and thermodynamic properties for the CFD solver XiFoam V3, University of South-Eastern Norway, 2021. https://doi.org/10.23642/USN.13721134.V3.

[106] W. Sutherland, LII. *The viscosity of gases and molecular force*, The London, Edinburgh, and Dublin Philosophical Magazine and Journal of Science. 36 (1893) 507–531. https://doi.org/10.1080/14786449308620508.

[107] F. Nicoud, F. Ducros, Subgrid-Scale Stress Modelling Based on the Square of the Velocity Gradient Tensor, Flow, Turbulence and Combustion. 62 (1999) 18.

[108] A. Yoshizawa, Statistical theory for compressible turbulent shear flows, with the application to subgrid modeling, Phys. Fluids. 29 (1986) 2152. https://doi.org/10.1063/1.865552.

[109] D.A. Crowl, J.F. Louvar, Chemical process safety: fundamentals with applications, 2nd ed, Prentice Hall PTR, Upper Saddle River, N.J, 2002.

[110] B. Lei, W. Zhao, C. Ziebert, N. Uhlmann, M. Rohde, H. Seifert, Experimental Analysis of Thermal Runaway in 18650 Cylindrical Li-Ion Cells Using an Accelerating Rate Calorimeter, Batteries. 3 (2017) 14. https://doi.org/10.3390/batteries3020014.

[111] T. Inoue, K. Mukai, Roles of positive or negative electrodes in the thermal runaway of lithium-ion batteries: Accelerating rate calorimetry analyses with an all-inclusive microcell, Electrochemistry Communications. 77 (2017) 28–31. https://doi.org/10.1016/j.elecom.2017.02.008.

[112] IPCS INCHEM, Dimethyl carbonate, International Programme on Chemical Safety INCHEM. (2005). http://www.inchem.org/documents/icsc/icsc/eics1080.htm (accessed December 21, 2018).

[113] IPCS INCHEM, Diethyl carbonate, International Programme on Chemical Safety INCHEM. (2000). http://www.inchem.org/documents/icsc/icsc/eics1080.htm (accessed December 21, 2018).

[114] M.E. Bardin, E.V. Ivanov, E.J.K. Nilsson, V.A. Vinokurov, A.A. Konnov, Laminar Burning Velocities of Dimethyl Carbonate with Air, Energy & Fuels. 27 (2013) 5513–5517. https://doi.org/10.1021/ef401108a.

[115] Z. Chen, On the accuracy of laminar flame speeds measured from outwardly propagating spherical flames: Methane/air at normal temperature and pressure, Combustion and Flame. 162 (2015) 2442–2453. https://doi.org/10.1016/j.combustflame.2015.02.012.

[116] V. Pokorný, V. Štejfa, M. Fulem, C. Červinka, K. Růžička, Vapor Pressures and Thermophysical Properties of Dimethyl Carbonate, Diethyl Carbonate, and Dipropyl Carbonate, Journal of Chemical & Engineering Data. 62 (2017) 3206–3215. https://doi.org/10.1021/acs.jced.7b00295.

[117] M. Henriksen, K. Vaagsaether, J. Lundberg, S. Forseth, D. Bjerketvedt, Laminar burning velocity of gases vented from failed Li-ion batteries, Journal of Power Sources. 506 (2021) 230141. https://doi.org/10.1016/j.jpowsour.2021.230141.

[118] S. de Persis, N. Chaumeix, Y. Fernandes, A. Bry, A. Comandini, Experimental and theoretical determination of DMC/air flame velocities, in: 11th International Conference on Chemical Kinetics, Orleans, 2019: p. Poster. https://icck2019.sciencesconf.org/data/pages/ICCK_Proc_final.pdf (accessed August 13, 2019).

[119] Z.H. Wang, W.B. Weng, Y. He, Z.S. Li, K.F. Cen, Effect of H2/CO ratio and N2/CO2 dilution rate on laminar burning velocity of syngas investigated by direct measurement and simulation, Fuel. 141 (2015) 285–292. https://doi.org/10.1016/j.fuel.2014.10.040.

[120] I.C. McLean, D.B. Smith, S.C. Taylor, The use of carbon monoxide/hydrogen burning velocities to examine the rate of the CO+OH reaction, Symposium (International) on Combustion. 25 (1994) 749–757. https://doi.org/10.1016/S0082-0784(06)80707-1.

[121] T. Boushaki, Y. Dhué, L. Selle, B. Ferret, T. Poinsot, Effects of hydrogen and steam addition on laminar burning velocity of methane–air premixed flame: Experimental and numerical analysis, International Journal of Hydrogen Energy. 37 (2012) 9412–9422. https://doi.org/10.1016/j.ijhydene.2012.03.037.

[122] H. Hisken, S. Lakshmipathy, G. Atanga, T. Skjold, Model evaluation protocol for HySEA, Gexcon AS, 2020.

[123] Model Evaluation Group Gas Explosion, Gas Explosion Model Evaluation Protocol, 1996.

[124] H. Helgesen, Technical Reference for Li-ion Battery Explosion Risk and Fire Suppression, DNV GL, Norway, 2019.

Part 2.

Published and Submitted Articles

Article A

Explosion characteristics for Li-ion battery electrolytes at elevated temperatures.

Published in the Journal of Hazardous Materials, Volume 371, 5 June 2019, doi: https://doi.org/10.1016/j.jhazmat.2019.02.108

Journal of Hazardous Materials 371 (2019) 1–7

Contents lists available at ScienceDirect

Journal of Hazardous Materials

journal homepage: www.elsevier.com/locate/jhazmat

Explosion characteristics for Li-ion battery electrolytes at elevated temperatures

M. Henriksen[a,*], K. Vaagsaether[a], J. Lundberg[a], S. Forseth[b], D. Bjerketvedt[a]

[a] *Faculty of Technology, Natural Sciences and Maritime Sciences, University of South-Eastern Norway, Kjølnes Ring 56, Porsgrunn, 3901, Norway*
[b] *Norwegian Defence Research Establishment (FFI), Instituttveien 20, 2007, Kjeller, Norway*

ARTICLE INFO

Keywords:
Dimethyl carbonate
Diethyl carbonate
Ethyl methyl carbonate
Maximum explosion pressure
The maximum rate of explosion pressure rise

ABSTRACT

Li-ion batteries are used in electronic devices and electric cars, yet they create safety concerns due to the possibility of the release of combustible materials. The electrolyte, one of the main components in a Li-ion cell, consists of organic carbonates. Venting and thermal runaway release organic carbonates and when mixed with air, it can result in fires and explosions. A 20-liter explosion sphere was used to determine the explosion characteristics for three typical carbonates used in electrolytes, at 373 K, and 100 kPa absolute pressure. The explosion pressure and the maximum rate of explosion pressure rise are presented for the carbonates and for hydrogen, methane, and propane, and the explosive limits for the carbonates are also identified at the same conditions. This allowed a comparison of the explosion characteristics for the carbonates with those for hydrogen, methane, and propane. Theoretical calculations gave a higher explosion pressure than that from the experimental results most likely due to losses in the hydrocarbon experiments. The carbonates analyzed have very similar explosion pressures and rate of explosion pressure rise as propane. The explosion characteristics found for the three carbonates can be used in future consequence and risk assessments for Li-ion battery installations.

1. Introduction

A wide range of products uses Li-ion batteries, from cellular phones and computers to hybrid, fuel cell, and electric vehicles. A high energy density, low self-discharge, and low maintenance are advantages that distinguish Li-ion batteries from traditional batteries [1]. One of the main components of a Li-ion battery/cell is the electrolyte. The electrolyte consists of one or a mixture of organic carbonates together with a Li-ion salt, i.e., $LiPF_6$. The flammable electrolyte is a potential hazard [2,3] and in the last two decades, there have been several reports of fire and explosion related incidents caused by Li-ion battery failure [4]. Li-ion battery failure can be caused by several different events, such as mechanical abuse, overcharge, heat exposure, over-discharge, external and internal short-circuit [5]. Battery failure can lead to the release of a combustible mixture and under certain conditions, thermal runaway can occur [6–8]. The combustible mixture that is release can consist of organic carbonates and other combustible gases such as hydrogen, methane, and propane in addition to particulate matter [5,9]. It is this release of combustible materials mixed with air that can cause fires and explosions [4–6,9–11]. Fig. 1 shows two still images of an inhomogeneous propagating flame caused by from the released gas/mist vented from an externally heated 18,650 Li-ion cell.

Explosion characteristics such as the explosion pressure, the rate of explosion pressure rise, and upper and lower explosive limits (UEL and LEL, respectively) are critical parameters for consequence and risk assessment [12–14]. Explosion pressure and the rate of explosion pressure rise are also used to verify computational models. Essential explosion characteristic data for dimethyl carbonate (DMC), ethyl methyl carbonate (EMC), and diethyl carbonate (DEC) are missing in the literature. Only the explosive limits for DMC and DEC have been reported but without a description of the experimental conditions [15,16].

In this study, the explosion characteristics for DMC, EMC, and DEC were analyzed in a 20-liter explosion sphere. The initial conditions for all experiments were 100 kPa absolute and 373 K. Hydrogen, methane, and propane are also analyzed and compared with previously published results [17–22].

2. Materials and method

The vessel used in the experiments was a standard 20-liter Anko explosion sphere, which is in accordance with standards EN-1839 [23] and EN-13673-1 [24]. Fig. 2 shows a photo and a schematic drawing of

---

[*] Corresponding author at: University of South-Eastern Norway, PEM, Kjølnes Ring 56, Porsgrunn, 3901, Norway.
E-mail address: mathias.henriksen@usn.no (M. Henriksen).

https://doi.org/10.1016/j.jhazmat.2019.02.108
Received 12 April 2018; Received in revised form 26 February 2019; Accepted 27 February 2019

Nomenclature

Variables/Parameters

P_{ex}	Maximum explosion pressure from experiment
P_{max}	Maximum explosion pressure from a series of experiments
$(dp/dt)_{ex}$	Maximum rate of explosion pressure rise from an experiment
$(dp/dt)_{max}$	Maximum rate of explosion pressure rise from a series of experiments
K_G	Deflagration index for an experiment
LEL	Lower explosive limit
UEL	Upper explosive limit
ϕ	Fuel-air equivalence ratio

the explosion sphere used. Two Kistler 601CAA pressure transducers measured the explosion pressure at 100 kHz. A Keller PAA-33X pressure transducer recorded the pressure during the filling process to get the partial pressures for each component. Separate injection ports for all materials were used to reduce uncertainties in the fuel-air concentration. There were two types of ignition systems used. The wire ignition system, used to determine LEL and UEL, causes a metal wire to melt and evaporate, which then ignites the mixture. The ignition energy is approximately 10 J according to the supplier. The spark ignition system was used to achieve the explosion pressure (P_{ex}) and the maximum rate of explosion pressure rise ($(dp/dt)_{ex}$). The spark ignition is a series of electrical sparks between two electrodes that has a total duration of 0.5 s. The temperature set point for the apparatus was chosen to be 373 K instead of the typical value of 298 K due to a relatively low vapor pressure for DEC at 298 K A Photron high-speed camera recorded each experiment that was conducted with the spark ignition for visual in-

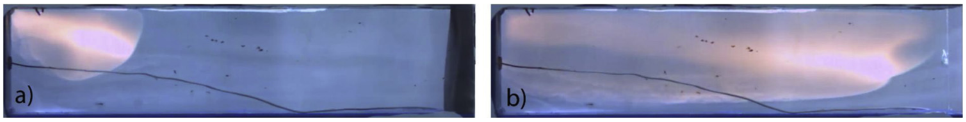

Fig. 1. Two still images of an inhomogeneous flame propagating inside a 0.45 × 0.10 × 0.10 explosion channel. A 18650 Li-ion cell was externally heated until the combustible gas/mist vented. a) Short after the ignition. b) Image when the flame has reached the end of the channel.

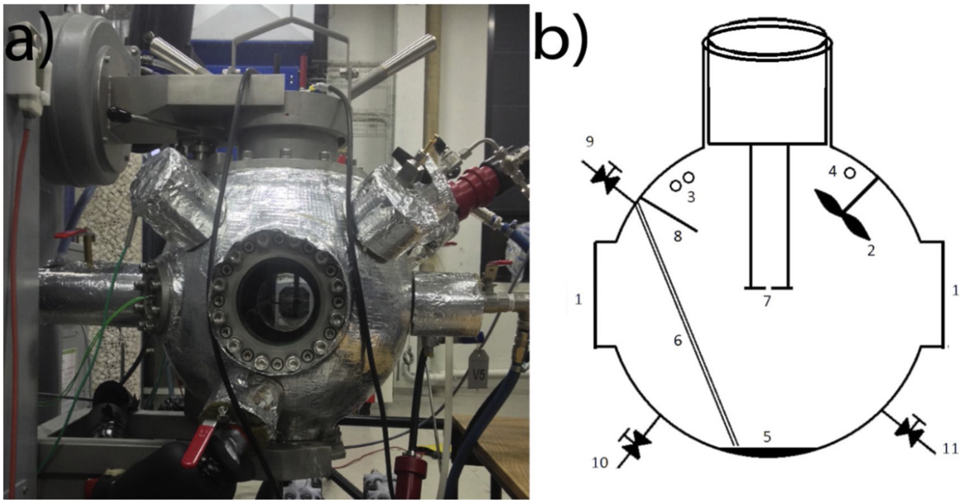

Fig. 2. (a) Photo of the 20-liter explosion sphere. (b) Illustration of the 20-liter explosion sphere. 1: 0.1 m windows; 2: mixing propeller; 3: Kistler pressure transducers; 4: Keller pressure transducer; 5: liquid evaporator; 6: liquid sample tube; 7: spark igniter; 8: ambient temperature probe; 9: liquid injection port; 10: fuel (gas) injection port; 11: air injection port.

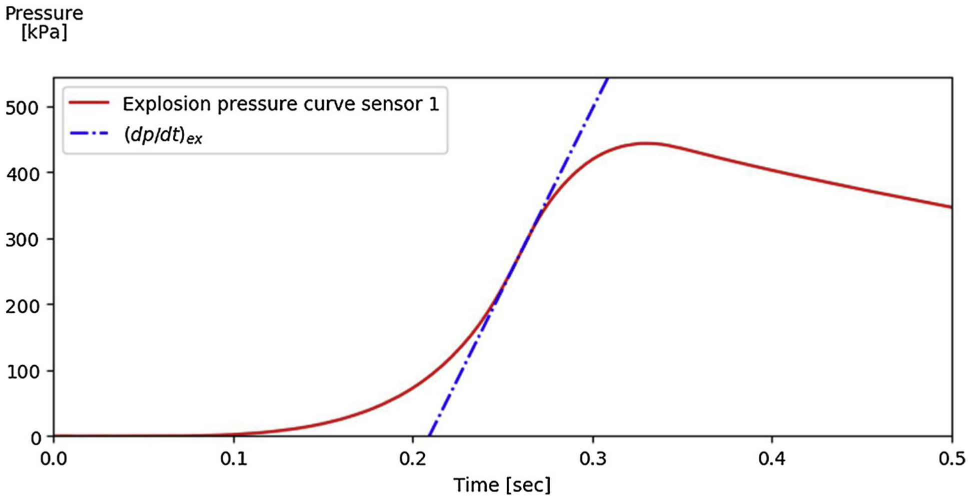

Fig. 3. The filtered explosion pressure measurement, with the calculated $(dp/dt)_{ex}$ line, for the 4.2% dimethyl carbonate experiment. This plot was used to validate the linear regression of the rate of explosion pressure rise.

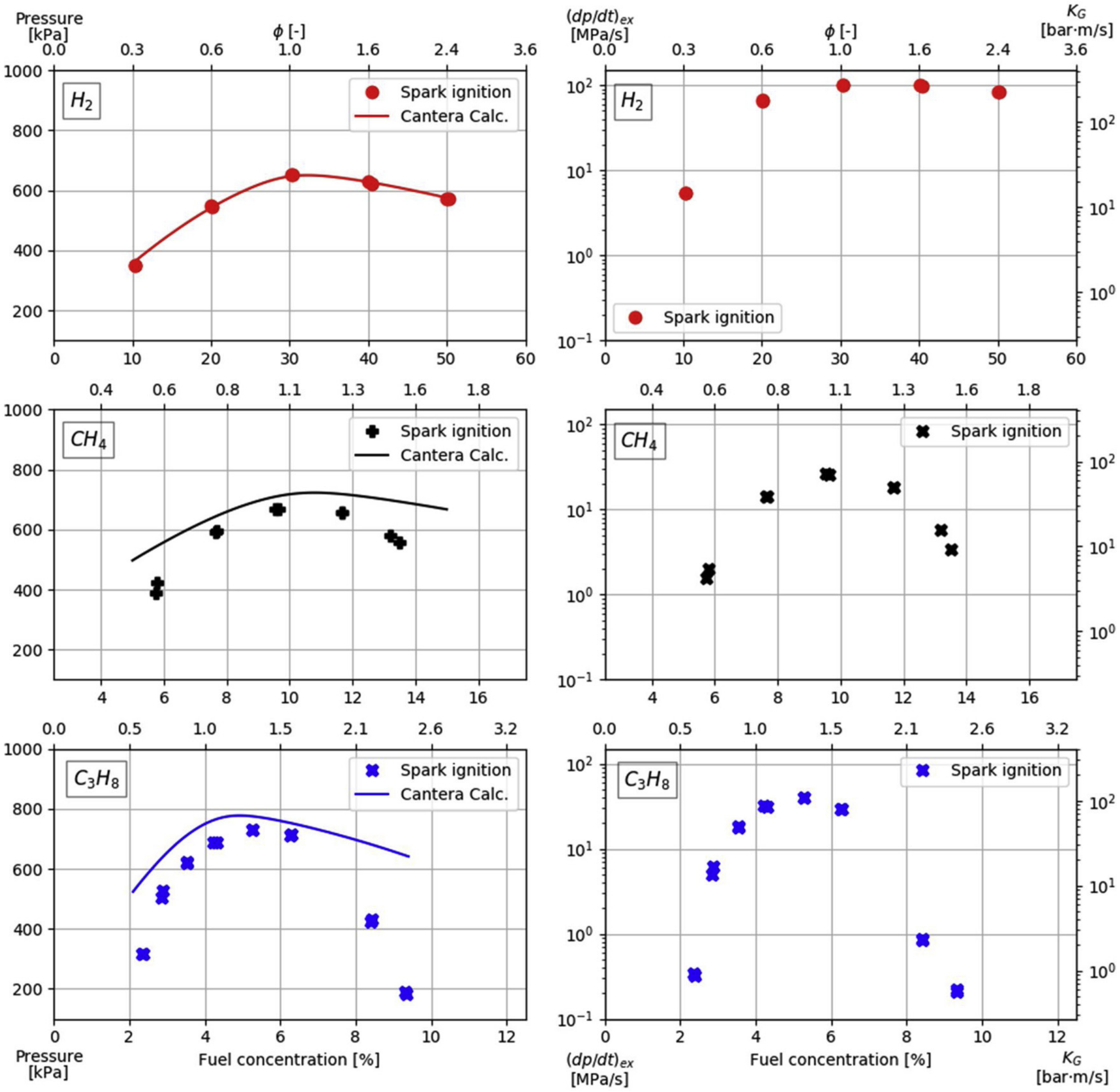

Fig. 4. Left: The maximum explosion pressure (P_{ex}) from each experiment. Right: The maximum rate of explosion pressure rise ($(dp/dt)_{ex}$) from each experiment. The initial absolute pressure and temperature was 100 kPa and 373 K, respectively.

Table 1
Summary of the primary results from the hydrogen, methane, and propane experiments at 373 K and 100 kPa.

Variables/Parameters	Materials					
	Hydrogen		Methane		Propane	
P_{ex} ($\phi \approx 1$)	$\phi = 1.04$	653 kPa	$\phi = 1.00$	670 kPa	$\phi = 1.05$	687 kPa
P_{max}	$\phi = 1.04$	653 kPa	$\phi = 1.02$	670 kPa	$\phi = 1.32$	729 kPa
$(dp/dt)_{max}$	$\phi = 1.04$	101.9 MPa/s	$\phi = 1.02$	26.8 MPa/s	$\phi = 1.32$	40.6 MPa/s
$K_{G,max}$	276.6 (bar·m)/s		72.7 (bar·m)/s		110.3 (bar·m)/s	

spection.

The explosion sphere was purged with compressed and oil-free air for a minimum of five minutes, exchange the total volume in the sphere approximately 40 times, before each experiment. The explosion sphere was evacuated to an absolute pressure of 10 kPa or less, after purging. Fuel was filled to the desired partial pressure, and then the sphere was filled with air to 100 kPa (± 0.5 kPa). Air and fuel were actively mixed for three and a half minutes to ensure a homogenous mixture. After mixing, the temperature was recorded. The temperature difference between experiments was within ± 2.5 K. The ignition was delayed for one and a half minutes after mixing to ensure that the mixture was quiescent. For P_{ex} and $(dp/dt)_{ex}$, two parallel experiments were conducted for each target concentration. Five parallel experiments with no ignition were performed to determine the explosive limits.

Alfa Aesar was the supplier for EMC and Sigma-Aldrich the supplier for DMC and DEC. All three carbonate solutions had 99% purity or higher and bought from Sigma Aldrich Norway. AGA Linde Norway supplied the hydrogen, methane, and propane with a purity of 99.95% or higher.

The explosion pressure measurement was post-filtered with a Savitzky-Golay smoothing algorithm [25]. All experiments had identical smoothing-filter parameters at 999 data points and a second-order polynomial fit. For each experiment, the average maximum pressure for the two filtered data sets determined P_{ex}. The algorithm below was used

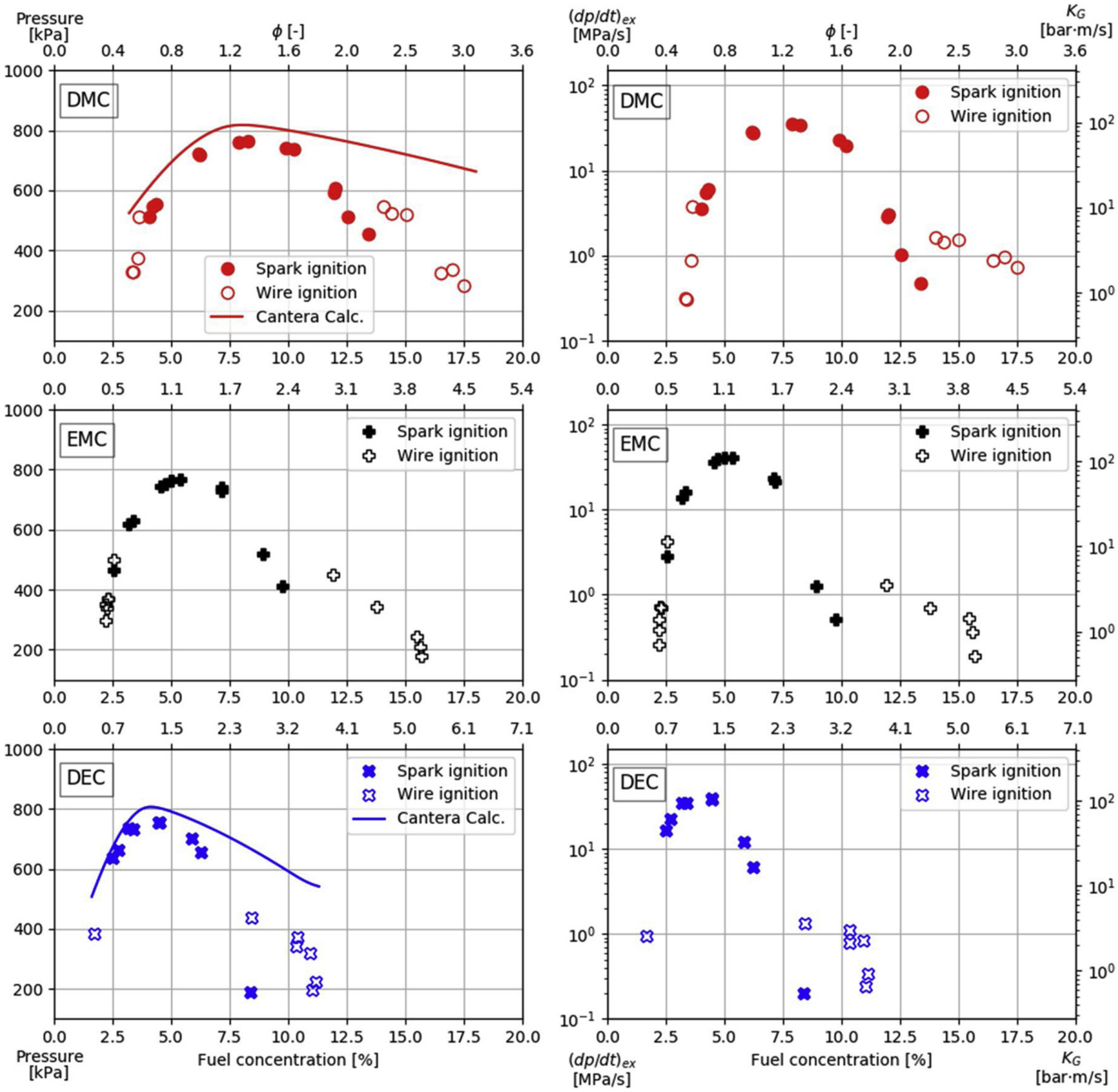

Fig. 5. Left: The maximum explosion pressure (P_{ex}) from each experiment. Right: The maximum rate of explosion pressure rise ($(dp/dt)_{ex}$) from each experiment. The initial absolute pressure and temperature was 100 kPa and 373 K, respectively.

Table 2
Summary of the primary results from the dimethyl carbonate (DMC), ethyl methyl carbonate (EMC), and diethyl carbonate (DEC) experiments with initial conditions at 373 K and 100 kPa.

Variables/Parameters	Materials					
	DMC		EMC		DEC	
P_{ex} ($\phi \approx 1$)	$\phi = 0.95$	720 kPa	$\phi = 1.02$	744 kPa	$\phi = 1.00$	731 kPa
P_{max}	$\phi = 1.28$	763 kPa	$\phi = 1.22$	768 kPa	$\phi = 1.34$	757 kPa
$(dp/dt)_{max}$	$\phi = 1.23$	34.8 MPa/s	$\phi = 1.13$	41.4 MPa/s	$\phi = 1.33$	38.9 MPa/s
$K_{G,max}$	94.5 bar m/s		112.4 bar m/s		105.7 bar m/s	
LEL	3.2%		2.1%		1.6%	
UEL	18.0%		15.8%		11.3%	

to calculate $(dp/dt)_{ex}$:

- Find gradients in the filtered pressure data
- Filter gradient data to remove noise
- Use the largest gradient as the starting point for the $(dp/dt)_{ex}$ calculation
- Conduct a 150-data-point regression to find the maximum gradient, $(dp/dt)_{ex}$

Fig. 3 shows one of the control images produced to validate the $(dp/dt)_{ex}$ algorithm. The highest maximum rate of explosion pressure rise for a series of experiments ($(dp/dt)_{max}$) was used to calculate the deflagration index (K_G) for one material. Eq. (1) is used to calculate the deflagration index. The standard unit for K_G is (bar·m)/s, which was therefore used in this study.

$$K_G = \left(\frac{dp}{dt}\right)_{max} \cdot V^{\frac{1}{3}} \qquad (1)$$

where K_G is the deflagration index for gases [(bar·m)/s], $(dp/dt)_{max}$ is the maximum rate explosion pressure rise from a series of experiments [bar/s], and V is the volume of the explosion sphere [m^3].

The chemical kinetics, thermodynamics, and transport process simulation tool Cantera (version 2.3.0) [26] was used to calculate P_{ex} theoretically. To calculate the P_{ex}, the standard equilibrium solver was used with constant internal energy, constant volume, and the same initial conditions as in the experiments. This theoretical calculation was also referred to as closed volume combustion or adiabatic isochoric complete combustion (AICC). The reaction mechanism for DMC was taken from Glaude et al. [27]; that for DEC was from Nakamura et al. [28]; and the Gri3.0 reaction mechanism for hydrogen, methane, and propane was from Smith et al. [29]. The established reaction mechanism for the different fuels provided the equilibrium constants and reaction sets for the calculation. No reaction mechanism for EMC was found and thus no theoretical calculation of explosion pressure.

3. Results

Fig. 4 shows the experimental results for hydrogen, methane, and propane with the P_{ex} on the left and $(dp/dt)_{ex}$ on the right. Propane had the highest maximum explosion pressure (P_{max}) at 729 kPa, and hydrogen had the highest $(dp/dt)_{max}$ at 101.9 MPa/s. Of the three fuels, hydrogen had the smallest discrepancy between the experimental results and the theoretical calculations. For methane and propane, the disagreement between these results was approximately 40 kPa for a fuel-air equivalence ratio (ϕ) between 0.75 and 1.5. The average difference between all parallels was 3 kPa for the three fuels. Table 1 summarizes the primary results in Fig. 4.

Fig. 5 shows the results from the DMC, EMC, and DEC experiments. EMC has the highest P_{max} and $(dp/dt)_{max}$, at 768 kPa and 41.4 MPa/s, respectively. DMC and EMC have a slightly lower P_{max}, with the small difference of 11 kPa. There is disagreement in P_{ex} between the experimental and theoretical results for both DMC and DEC. For $0.65 \leq \phi \geq 1.6$, the discrepancy is approximately 50 kPa. For $\phi > 1.6$, the gap between the results and calculations increases significantly. The average difference between parallels for all experiments and all three fuels was calculated to be 8 kPa.

The open symbols in Fig. 5 show the experiments where ignition occurred when iterating toward the explosive limits. The explosive limits for both DMC [15] and DEC [16] were found on the International Programme on Chemical Safety (IPCS) INCHEM database. Table 2 summarizes the results from the experiments with DMC, EMC, and DEC. Table 3 summarizes the calculated pressures and explosive limits found in literature.

4. Discussion

To validate the procedure and experimental setup and to quantify the variation between experiments, two parallel experiments were performed at each target concentration. A comparison of the spark ignition experiments (solid symbols) in Figs. 4 and 5 show that there is only a small difference in P_{ex} and $(dp/dt)_{ex}$ for two parallels. DMC, EMC, and DEC have greater differences in P_{ex} than hydrogen, methane, and propane: 8 kPa and 3 kPa, respectively. This difference is likely caused by the variation in concentration for the two liquid parallels. The syringe used to inject the liquid made it hard to obtain an exact concentration for each parallel. The experimental results were also compared with a theoretical calculation performed using Cantera. Figs. 4 and 5 and Tables 2 and 3 show that there is a discrepancy between the results and calculations in all cases except for hydrogen. The difference is within 50 kPa for $0.65 \leq \phi \leq 1.6$. For methane and propane, the disagreement between the theoretical calculation and experiments is in the same range as previously published results [18,19,21]. The experimental results for hydrogen, methane, and propane at 298 K and 373 K was in good agreement with previously published experimental results at similar conditions [17–22]. Spark ignition was chosen for the P_{ex} and $(dp/dt)_{ex}$ experiments since it resulted in a lower variation between two parallels: 0.44 MPa/s, and 1.38 MPa/s, respectively. The procedure and experimental setup provided reproducible results with little variation between parallels.

The differences between the theoretical and experimental results are most likely due to heat loss in the experiments. Since the calculations are adiabatic and reach chemical equilibrium, they are ideal with no losses. The experimental setups have radiative heat loss, especially for the hydrocarbon materials. Bradly [30] estimated a heat loss of 5% for spherically shaped combustion with a radius of 0.5 m in methane and propane experiments. The radiative heat loss for hydrogen is less than that for hydrocarbons. Since hydrogen has a low radiative flux and high $(dp/dt)_{ex}$ (short combustion time), the experimental results are very close to the theoretical results. For ϕ above 1.6, the disagreement between calculation and experiments increases for hydrocarbons, as shown in Figs. 4 and 5. The discrepancy is not only due to heat losses from radiation, but also due to other effects, as buoyancy causing a non-spherical flame and soot formation. Dahoe [31] reported that buoyancy would have a more significant effect on the experiments when concentrations approached the explosive limits. The flame front would be mushroom shaped instead of spherical. Heat loss would then occur in the upper part of the vessel due to the direct contact between the combustion products and the walls before the flame reaches the lower walls. Heat loss at the top from convection will influences the explosion pressure. The high-speed video for mixtures close to the explosive limits clearly shows a mushroom-shaped flame front. At rich conditions, soot also forms for hydrocarbons. Soot residue was found inside the explosion sphere for experiments that were close to the explosive limits for most of the hydrocarbon experiments. None of the reaction mechanisms used in the theoretical calculations included the formation or reaction of soot. The radiative heat loss will also increase due to the high radiative properties of soot and increased combustion time.

The three carbonates have very similar P_{ex} and $(dp/dt)_{ex}$. Only 11 kPa separates the highest and lowest P_{max}, which is close to the variation between parallels at 8 kPa. The difference of 6.6 MPa/s in $(dp/dt)_{max}$ is regarded as relatively small and will only give a minimal difference in vent areas [12,13]. Since the results from all three carbonates are within the same range, the preliminary risk assessment is simplified. In the course of a thermal runaway, carbonates will decompose into other materials, such as hydrogen, carbon monoxide, carbon dioxide, and ethylene, among others. The composition of the vented gas is dependent on the state of charge (SOC) and electrolyte mixture [5,7,9,32]. The explosion characteristics for this gas mixture may differ from the results of this study. Further study in dispersion rates, vented material concentration, and total vented mass from known Li-ion cell compositions are needed to improve the consequence and risk assessment of Li-ion batteries further.

DMC showed the most significant discrepancy in LEL and UEL compared with previous data [15]. The absolute difference is -1% for LEL and +5.1% for UEL when comparing the results in Table 2 and the literature values in Table 3. In the IPCS safety chemical database for DMC, the temperature and pressure for the explosive limits are not

Table 3
Theoretical calculation of the maximum explosion pressure and the literature values for the lower and upper explosive limit for dimethyl carbonate and diethyl carbonate.

Variables/Parameters	Materials			
	DMC		DEC	
P_{ex} (ϕ = 1, theoretical)	ϕ = 1.00	788 kPa	ϕ = 1.00	778 kPa
P_{max} (theoretical)	ϕ = 1.25	818 kPa	ϕ = 1.23	807 kPa
LEL [15,16]	4.22%		1.4%	
UEL [15,16]	12.87%		11.0%	

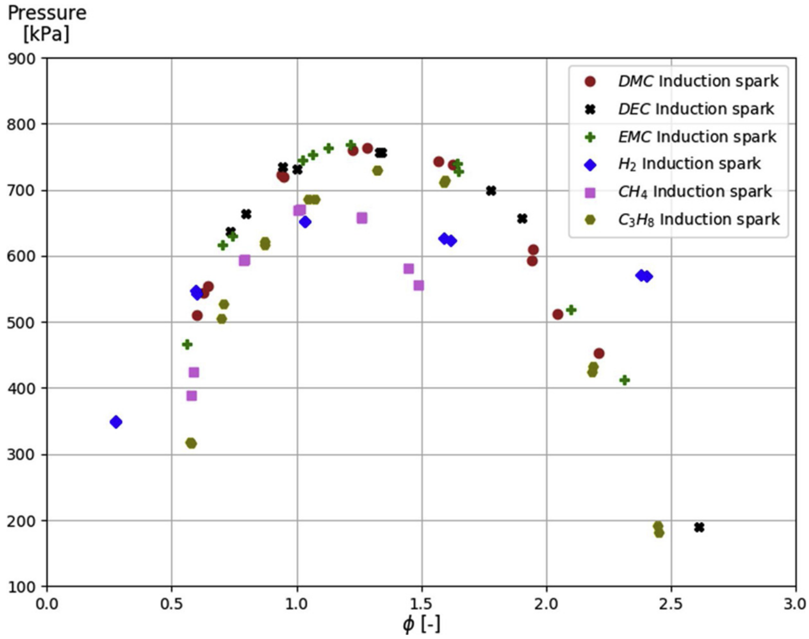

Fig. 6. Explosion pressure for all experiments. The initial absolute pressure and temperature were 100 kPa and 373 K, respectively.

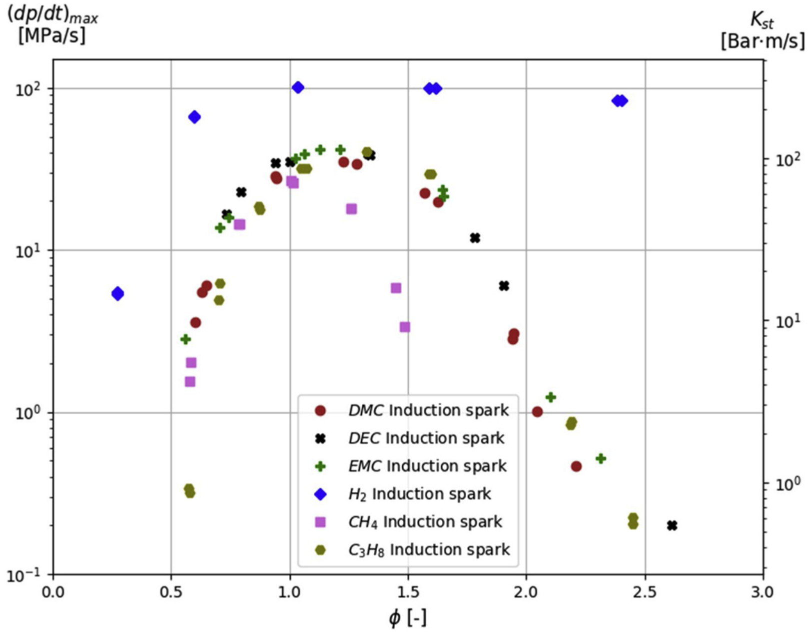

Fig. 7. The rate of explosion pressure rise for all experiments. The initial absolute pressure and temperature were 100 kPa and 373 K, respectively.

reported. The initial conditions for the explosive limits may differ from the 373 K and 100 kPa conditions used in this study. This may be the cause of the relatively large gap in explosive limits. The difference in explosive limits in this study and the IPSC database [16] was less for DEC than for DMC. The small discrepancy between reported explosive limits is not unexpected if there were differences in the experimental setups [17].

Figs. 6 and 7 compare P_{ex} and $(dp/dt)_{ex}$ for all experiments with spark ignition. Fig. 6 shows that there is little difference in the P_{ex} for the carbonate experiments. Hydrogen and methane have a lower P_{ex} compared with the carbonates. Propane has a very similar P_{ex} and $(dp/dt)_{ex}$ profile as the carbonates. Fig. 7 shows that, of all experiments, hydrogen has the highest $(dp/dt)_{ex}$. Considering hydrogen's high laminar burning velocity relative to the other materials, this is expected [10]. Since all the experiments are performed in the same explosion vessel volume, the $(dp/dt)_{max}$ and K_G are linearly related. Therefore, K_G is not discussed any further. The explosion characteristics of a Li-ion electrolyte (a different mixture of carbonates) are comparable to the explosion characteristics of propane. When estimating the consequence for Li-ion batteries with an unknown electrolyte, it may be useful to assume propane explosion characteristics initially.

5. Conclusion

A 20-liter explosion sphere was used to determine the explosion pressure, the rate of explosion pressure rise, and the lower and upper explosive limit for dimethyl carbonate, diethyl carbonate, and ethyl methyl carbonate at different concentrations, with the initial condition at 373 K and 100 kPa. The procedure and experimental setup gave reproducible results and is considered a suitable method for determining explosion characteristics. All three carbonates have similar explosion pressure and rate of explosion pressure rise.

An adiabatic and chemical equilibrium calculation performed using Cantera gave higher explosion pressures compared to experiments for all materials expect hydrogen. This disagreement is reported in other publications and is typical for hydrocarbons [18,19,21]. The difference in explosion pressure between the theoretical calculation and experiments increases for a fuel-air equivalence ratio above 1.7, due to heat loss, non-spherical-shaped combustion, and soot formation.

The explosion characteristics for the three carbonates were compared to experiments with hydrogen, methane, and propane. Propane has very similar explosion characteristics as the carbonates. The results obtained from the experiments with the three carbonates are considered novel and can be of use in future consequence and risk assessments for Li-ion battery installations.

Acknowledgments

This work was performed within MoZEES, a Norwegian Centre for Environment-friendly Energy Research (FME), co-sponsored by the Research Council of Norway (project number 257653) and 40 partners from research, industry and public sector.

References

[1] Battery University, What's the Best Battery? Battery Univ., 2017, http://batteryuniversity.com/learn/archive/whats_the_best_battery.

[2] S.J. Harris, A. Timmons, W.J. Pitz, A combustion chemistry analysis of carbonate solvents used in Li-ion batteries, J. Power Sources 193 (2009) 855–858, https://doi.org/10.1016/j.jpowsour.2009.04.030.

[3] S. Hess, M. Wohlfahrt-Mehrens, M. Wachtler, Flammability of Li-Ion battery electrolytes: flash point and self-extinguishing time measurements, J. Electrochem. Soc. 162 (2015) A3084–A3097, https://doi.org/10.1149/2.0121502jes.

[4] D. Lisbona, T. Snee, A review of hazards associated with primary lithium and lithium-ion batteries, Process Saf. Environ. Prot. 89 (2011) 434–442, https://doi.org/10.1016/j.psep.2011.06.022.

[5] C.C. Crafts, D.H. Doughty, J. McBreen, E.P. Roth, Advanced Technology Development Program for Lithium-ion Batteries : Thermal Abuse Performance of 18650 Li-ion Cells, (2004), https://doi.org/10.2172/918751.

[6] Q. Wang, P. Ping, X. Zhao, G. Chu, J. Sun, C. Chen, Thermal runaway caused fire and explosion of lithium ion battery, J. Power Sources 208 (2012) 210–224, https://doi.org/10.1016/j.jpowsour.2012.02.038.

[7] B. Lei, W. Zhao, C. Ziebert, N. Uhlmann, M. Rohde, H. Seifert, Experimental analysis of thermal runaway in 18650 cylindrical Li-Ion cells using an accelerating rate calorimeter, Batteries 3 (2017) 14, https://doi.org/10.3390/batteries3020014.

[8] F. Jiang, K. Liu, Z. Wang, X. Tong, L. Guo, Theoretical analysis of lithium-ion battery failure characteristics under different states of charge, Fire Mater. 42 (2018) 680–686, https://doi.org/10.1002/fam.2522.

[9] P. Ribière, S. Grugeon, M. Morcrette, S. Boyanov, S. Laruelle, G. Marlair, Investigation on the fire-induced hazards of Li-ion battery cells by fire calorimetry, Synth. Lect. Energy Environ. Technol. Sci. Soc. 5 (2012) 5271–5280, https://doi.org/10.1039/C1EE02218K.

[10] J. Johnsplass, M. Henriksen, K. Vaagsaether, J. Lundberg, D. Bjerketvedt, Simulation of Burning Velocities in Gases Vented From Thermal run-a-way Lithium Ion Batteries, (2017), pp. 157–161, https://doi.org/10.3384/ecp17138157.

[11] C. Mikolajczak, M. Kahn, K. White, R.T. Long, Lithium-Ion Batteries Hazard and Use Assessment, Springer US, Boston, MA, 2011, https://doi.org/10.1007/978-1-4614-3486-3.

[12] D.A. Crowl, J.F. Louvar, Chemical Process Safety: Fundamentals With Applications, 2nd ed., Prentice Hall PTR, Upper Saddle River, N.J, 2002.

[13] F.P. Lees, Loss Prevention in the Process Industries: Hazard Identification, Assessment and Control, 2. Ed., Butterworth-Heinemann, Oxford, 1996.

[14] D. Bjerketvedt, J.R. Bakke, K. Van Wingerden, Gas explosion handbook, J. Hazard. Mater. 52 (1997) 1–150.

[15] IPCS INCHEM, Dimethyl carbonate, Int. Programme Chem. Saf. INCHEM, (2005) (Accessed 21 December 2018), http://www.inchem.org/documents/icsc/icsc/eics1080.htm.

[16] IPCS INCHEM, Diethyl carbonate, Int. Programme Chem. Saf. INCHEM, (2000) (Accessed 21 December 2018), http://www.inchem.org/documents/icsc/icsc/eics1080.htm.

[17] Safe and Efficient Hydrocarbon Oxidation Processes by Kinetics and Explosion Expertise, Report on the Experimentally Determined Explosion Limits, Explosion Pressures and Rates of Explosion Pressure Rise – Part1: Methane, Hydrogen and Propylene, (2019) n.d. http://www.morechemistry.com/SAFEKINEX/deliverables/44.Del.%20No.%208.pdf (Accessed 18 March 2018).

[18] A.A. Pekalski, H.P. Schildberg, P.S.D. Smallegange, S.M. Lemkowitz, J.F. Zevenbergen, M. Braithwaite, H.J. Pasman, Determination of the explosion behaviour of methane and propene in air or oxygen at standard and elevated conditions, Process Saf. Environ. Prot. 83 (2005) 421–429, https://doi.org/10.1205/psep.04211.

[19] D. Razus, V. Brinzea, M. Mitu, D. Oancea, Temperature and pressure influence on explosion pressures of closed vessel propane–air deflagrations, J. Hazard. Mater. 174 (2010) 548–555, https://doi.org/10.1016/j.jhazmat.2009.09.086.

[20] D. Razus, V. Brinzea, M. Mitu, C. Movileanu, D. Oancea, Temperature and pressure influence on maximum rates of pressure rise during explosions of propane–air mixtures in a spherical vessel, J. Hazard. Mater. 190 (2011) 891–896, https://doi.org/10.1016/j.jhazmat.2011.04.018.

[21] M. Mitu, V. Giurcan, D. Razus, M. Prodan, D. Oancea, Propagation indices of methane-air explosions in closed vessels, J. Loss Prev. Process Ind. 47 (2017) 110–119, https://doi.org/10.1016/j.jlp.2017.03.001.

[22] A.E. Dahoe, L.P.H. de Goey, On the determination of the laminar burning velocity from closed vessel gas explosions, J. Loss Prev. Process Ind. 16 (2003) 457–478, https://doi.org/10.1016/S0950-4230(03)00073-1.

[23] European standard, EN 1839, Determination of Explosion Limits of Gases and Vapours, (2012).

[24] European standard, EN 13673-1, Determination of the Maximum Explosion Pressure and the Maximum Rate of Pressure Rise of Gases and Vapours - Part 1: Determination of the Maximum Explosion Pressure, (2003).

[25] W.H. Press (Ed.), FORTRAN Numerical Recipes, 2nd ed, Cambridge University Press, Cambridge; New York, 1996.

[26] D.G. Goodwin, H.K. Moffat, R.L. Speth, Cantera: An Object-Oriented Software Toolkit For Chemical Kinetics, Thermodynamics, And Transport Processes. Version 2.3.0, (2017), https://doi.org/10.5281/zenodo.170284.

[27] P.A. Glaude, W.J. Pitz, M.J. Thomson, Chemical kinetic modeling of dimethyl carbonate in an opposed-flow diffusion flame, Proc. Combust. Inst. 30 (2005) 1111–1118, https://doi.org/10.1016/j.proci.2004.08.096.

[28] H. Nakamura, H.J. Curran, A. Polo Córdoba, W.J. Pitz, P. Dagaut, C. Togbé, S.M. Sarathy, M. Mehl, J.R. Agudelo, F. Bustamante, An experimental and modeling study of diethyl carbonate oxidation, Combust. Flame 162 (2015) 1395–1405, https://doi.org/10.1016/j.combustflame.2014.11.002.

[29] G.P. Smith, D.M. Golden, M. Frenklach, N.W. Moriarty, B. Eiteneer, M. Goldenberg, C.T. Bowman, R.K. Hanson, S. Song, W.C.G Jr, V.V. Lissianski, Z. Qin, GRI-MECH 3.0 (n.d.), (2019) (Accessed 18 March 2018), http://www.me.berkeley.edu/gri_mech/.

[30] D. Bradley, T.M. Cresswell, J.S. Puttock, Flame acceleration due to flame-induced instabilities in large-scale explosions, Combust. Flame 124 (2001) 551–559, https://doi.org/10.1016/S0010-2180(00)00208-X.

[31] A.E. Dahoe, Laminar burning velocities of hydrogen–air mixtures from closed vessel gas explosions, J. Loss Prev. Process Ind. 18 (2005) 152–166, https://doi.org/10.1016/j.jlp.2005.03.007.

[32] T. Inoue, K. Mukai, Roles of positive or negative electrodes in the thermal runaway of lithium-ion batteries: accelerating rate calorimetry analyses with an all-inclusive microcell, Electrochem. Commun. 77 (2017) 28–31, https://doi.org/10.1016/j.elecom.2017.02.008.

Article B

Laminar Burning Velocity of the Dimethyl Carbonate-Air Mixture Formed by the Li-Ion Electrolyte Solvent

Published in Journal of Combustion, Explosion, and Shock Waves, Volume 56, 2020, doi: https://doi.org/10.1134/S0010508220040024

ISSN 0010-5082, Combustion, Explosion, and Shock Waves, 2020, Vol. 56, No. 4, pp. 383–393. © Pleiades Publishing, Ltd., 2020.
Original Russian Text © M. Henriksen, K. Vaagseather, A.V. Gaathaug, J. Lundberg, S. Forseth, D. Bjerketvedt.

Laminar Burning Velocity of the Dimethyl Carbonate–Air Mixture Formed by the Li-Ion Electrolyte Solvent

M. Henriksen[a], K. Vaagseather[a], A. V. Gaathaug[a], J. Lundberg[a], S. Forseth[a], and D. Bjerketvedt[a]

UDC 536.46

Published in *Fizika Goreniya i Vzryva*, Vol. 56, No. 4, pp. 14–25, July–August, 2020.
Original article submitted December 23, 2019; revision submitted February 19, 2020; accepted for publication February 19, 2020.

Abstract: If a Li-ion cell fails and the electrolyte leaks out into air, a flammable premixed gas cloud can be formed. The electrolyte combustion energy is 65–70% of the total energy content of the cell. The main objective of this study is to determine the laminar burning velocity and the Markstein length for dimethyl carbonate and propane in a 20-liter explosion sphere with initial conditions at 100 kPa and 300 K. Five different stretch extrapolation models for the laminar burning velocity give practically the same result. The experimental results agree well with the previously published data and are slightly lower than the theoretical predictions. The laminar burning velocity for dimethyl carbonate is measured close to the saturation point under the initial conditions, which has not been previously reported.

Keywords: laminar burning velocity, dimethyl carbonate, Li-ion battery electrolyte, gas explosion.

DOI: 10.1134/S0010508220040024

INTRODUCTION

With the increasing need for clean and sustainable energy, Li-ion batteries (LIBs) have become a popular choice for energy storage. They are characterized by a high energy density and power compared to other rechargeable batteries. A challenge with the Li-ion technology is that it must have a protection circuit to ensure safety [1–3]. A combination of a flammable organic electrolyte with highly energetic materials present a potential for an accident [4]. In the last two decades, there have been several reports of fire- and explosion-related incidents caused by LIB failure [3–6].

The electrolyte is one of the main components in the Li-Ion cell/battery and consists of one or several organic carbonates (e.g., dimethyl carbonate) together with a Li-ion salt. Typical electrolytes are flammable. Mikolajczak et al. [7] estimated that the heat of combustion of the organic carbonates contributes 65–70% of the total energy content in the 18650 Li-ion cell, depending on the state of the charge.

In the Li-ion battery/cell, a thermal incident can be initiated by an internal or external short circuit, heat exposure, overload, over-discharge, overcharge, and mechanical abuse [7]. Such an incident can lead to the release of the electrolyte, hydrogen, carbon monoxide, methane, and other flammable species [6–12]. If these species mix with air, a flammable premixed gas cloud can be formed. If such a cloud is ignited, a gas explosion can occur.

Johnsplass [13] documented gas explosions in clouds of a vented electrolyte from the 18650 Li-ion cell that was externally heated to 425 K. The flame velocity observed on the high-speed video was up to 10 m/s. Figure 1 shows two still images from one of the exper-

---

[a] University of South-Eastern Norway, Porsgrunn, Telemark, Norway; mathias.henriksen@usn.no.
[b] Norwegian Defence Research Establishment, Oslo, Norway.

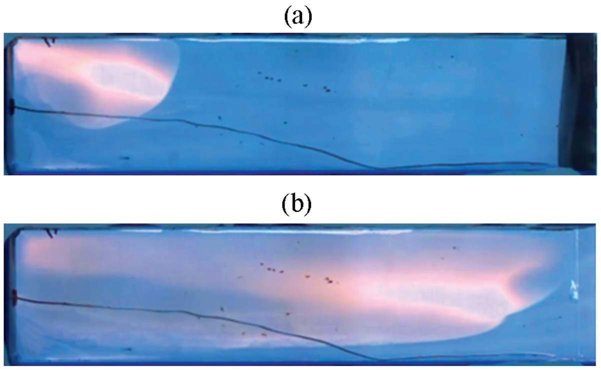

Fig. 1. Still images of an inhomogeneous flame propagating in a 0.45 × 0.10 × 0.10 m explosion channel; the 18650 Li-ion cell was externally heated until the combustible gas/mist vented; (a) image taken soon after ignition; (b) image taken when the flame reached the end of the channel.

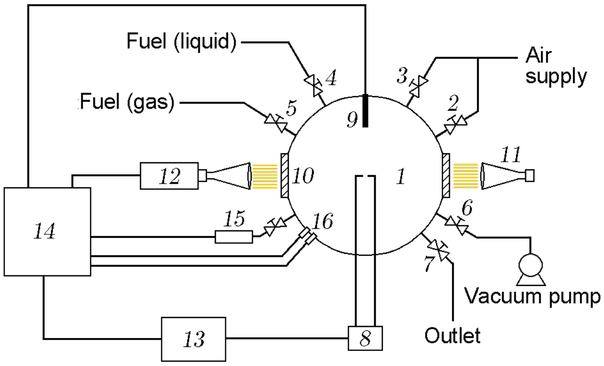

Fig. 2. Experimental setup: (*1*) explosion chamber; (*2*) oxidizer inlet; (*3*) flush inlet; (*4*) fuel (liquid) injection port; (*5*) fuel (gas) inlet; (*6*) vacuum port; (*7*) gas outlet; (*8*) ignition system; (*9*) thermocouple; (*10*) glass window (100 mm); (*11*) LED light source; (*12*) high-speed camera; (*13*) control/trigger unit; (*14*) data acquisition system; (*15*) ambient pressure transducer; (*16*) dual explosion pressure transducers.

iments. The cell lost roughly 2 g, which was assumed to be mostly the electrolyte. With an ambient temperature of 300 K and assuming a homogenous mixture in the channel, the concentration of dimethyl carbonate (DMC) in air would be approximately 8%. A closed volume combustion calculation shows that the explosion pressure can reach almost 1 MPa [14].

When studying flame propagation, the laminar burning velocity (LBV) is one of the essential parameters. At the beginning, the flame is usually slow and laminar with a flame speed in the order of 3–4 m/s. It propagates faster as the flame is affected by turbulence generated due to concentration differences, obstacles, self-generated turbulence, etc. [15]. The LBV is often a key parameter in modeling the turbulent flame speed and can be used to validate chemical kinetics [16–18]. Two previous studies on the LBV of DMC have been published. Bardin et al. [19] measured the LBV of DMC using a heat flux burner at different conditions. Persis et al. [20] measured the LBV of DMC in an explosion sphere with the initial conditions at 318 K and 1 atm.

In this study, a typical 20-liter explosion sphere is used to determine the laminar burning velocity and Markstein length for DMC and propane. The experiments are performed in a typical manner, as described in other studies [21–26]. The experimental results are compared with previously published studies and with theoretical calculations. The initial conditions for all experiments were the absolute pressure of 100 kPa and temperature of 300 K. This paper is an extended version of the work presented at the 9th International Seminar on Fire and Explosion Hazards in April 2019 [27].

MATERIALS AND METHODS

The experimental setup (20-liter explosion sphere) is schematically shown in Fig. 2. A detailed description of the setup and the procedure has been previously published [27]. A heating jacket controls the ambient temperature in the sphere. In the bottom of the sphere, there is a heated plate for evaporating liquids. Two identical pressure transducers measure the explosion pressure, and a separate pressure transducer records the ambient pressure during sphere evacuation and filling. Dedicated inlets are used for the oxidizer, liquid fuel, and gaseous fuel to reduce uncertainties in the fuel–air concentration. DMC has a purity above 99% and propane has a purity above 99.95%. An ignition coil generates a spark between two metal wires with a variable gap.

A focused shadowgraphy technique [28] was used to enhance the visibility of the propagating flame, which was recorded with a high-speed camera operating at 20 000 fps. Image processing and data analysis were undertaken using the tool/code generated in Python.

Image background subtraction was used to remove noise that could potentially influence flame front detection. As the shadowgraphy technique was used, the images contain two intensity gradients corresponding to the inner and outer perimeter of the flame. The outer perimeter was chosen because it is closer to the unburnt mixture. In each image, the threshold that separates the flame from the background is set individually. The perimeter of the flame is then fitted to a circle using the least square minimization to obtain the overall radius.

Table 1. Stretch extrapolation models

Model name/description	Expression	Reference
Linear stretch model (LS)	$S_b = S_b^0 - L_b\kappa$	[30, 31]
Linear curvature model (LC)	$S_b = S_b^0\left(1 - \dfrac{2L_b}{r_f}\right)$	[32, 33]
Nonlinear model with three fitting parameters (N3P)	$S_b = S_b^0\left(1 - \dfrac{2L_b}{r_f} + \dfrac{c}{r_f^2}\right)$	[29]
Nonlinear model in the expansion form (NQ)	$S_b^0 + c = r_f + 2L_b \ln(r_f) - \dfrac{4L_b^2}{r_f} - \dfrac{8L}{3r}$	[34]
Quasi-steady nonlinear model (NE)	$\left(\dfrac{S_b}{S_b^0}\right)^2 \ln\left(\dfrac{S_b}{S_b^0}\right) = -\dfrac{2L_b\kappa}{S_b^0}$	[35, 36]

Table 2. Implicit functions of the flame radius derived from the expressions in Table 1

Model name	Implicit dependence $r_f(t)$
LS	$r_f = S_b^0 t - 2L_b \ln r_f + C_{\rm st}$
LC	$r_f - S_b^0 t - 2L_b \ln(r_f - 2L_b) + C_{\rm st}$
N3P $(A > 0)$	$r_f = S_b^0 t - L_b(r_f^2 - 2L_b r_f + c) - \dfrac{2L_b^2 - c}{2\sqrt{A}} \ln\left(-\dfrac{r_f + \sqrt{A} + L_b}{r_f + \sqrt{A} - L_b}\right) + C_{\rm st}$
N3P $(A < 0)$	$r_f = S_b^0 t - L_b(r_f^2 - 2L_b r_f + c) - \dfrac{2A}{\sqrt{-A}} \arctan\left(\dfrac{r - L_b}{\sqrt{-A}}\right) + C_{\rm st}$
	$A - L_b^2 - c$
NQ	$r_f = S_b^0 t + c - 2L_b \ln(r_f) + \dfrac{4L_b^2}{r_f} + \dfrac{8L_b^3}{3r_f^2}$

The code saves the set of the images together with the temporal evolution of the radius.

The first step in the post-processing tool/code is to set the radius range to be considered in the calculations. The lowest radius is set to 10 mm but may be changed to fit the product of the Markstein number Ma and Karlovitz number Ka (Ma · Ka) in the interval from −0.05 to 0.15 [29]. The radius above 37.5 mm is removed due to an increase in the variation in the data. From the conditioned radii, the laminar flame speed and the Markstein length are calculated. Table 1 shows the stretch extrapolation models used in this study.

By representing the flame speed S_b as the derivative $\dfrac{dr_f}{dt}$, the expressions in Table 1 can be written as differential equations. In particular, the equation below shows the differential equation for the linear stretch model:

$$\frac{dr_f}{dt}\left(1 + \frac{2L_b}{r_f}\right) = S_b^0.$$

Here r_f [m] is the flame radius, t [s] is the time, and L_b [m] is the Markstein length for the burnt gas. The solution to the differential equation above yields an implicit function of the flame radius. This function can be fitted to the measured variation of the radius in time with the least square minimization method. Chen [16] and Liu et al. [26] previously published a similar method for the LS model. Table 2 shows the implicit functions for the expressions in Table 1, except for the NE model.

The NQ model in the expansion form (see Table 1) is already expressed as an implicit function of the flame radius. An analytical solution to the differential equation of the NE model could not be found. Liu et al. [36] proposed a method for solving the NE model, but the regression is on the flame speed and stretch rate relation. This method is represented by the equations

$$\kappa = AS_b - BS_b^2 \ln(S_b^2),$$

$$A = \ln(S_b^0)/L_b S_b^0, \quad B = (1/2)L_b S_b^0,$$

$$S_b^0 = \exp(A/2B), \quad L_b = (1/2)BS_b^0,$$

where κ [s^{-1}] is the stretch rate and A [m^2] is the area. To reduce noise from the image processing, the flame radius and flame speed were post-filtered with the Savitzky–Golay smoothing algorithm [37] and used in the NE method by Liu et al. [36]. All other models were fitted using the raw data from the image processing.

The equilibrium states and the LBV for constant-pressure combustion were calculated in the chemical kinetics, thermodynamics, and transport process simulation tool Cantera (version 2.3.0) [38]. For a one-dimensional freely propagating planar flame, the Cantera routine called FreeFlame was used to calculate the LBV. Two different reaction mechanisms for DMC oxidation were used for comparison: those of Glaude et al. [39] and Sun et al. [40]. A constant-pressure equilibrium solver was used to determine the density ratio for DMC and propane. The reaction mechanism of Glaude et al. [39] and the GRI-Mech 3.0 mechanism [41] were used in the equilibrium calculations.

RESULTS

Tables 3 and 4 summarize the results for propane and DMC, respectively. Propane has the highest measured LBV and flame speed at the equivalence ratio $\phi = 1.2$ of the four different concentrations. Comparing the DMC results, the highest LBV and flame speed were obtained at $\phi = 1.04$. The LBV of DMC is nearly constant in the concentration range $1.0 \leqslant \phi \leqslant 1.2$. For both fuels, the highest LBV values are located near stoichiometric concentrations, with the highest values slightly on the rich side, which could be expected.

For propane, there is only a small difference in the laminar flame speed between different models. By comparing the average value for each concentration, the variation is between ±41 mm/s for $\phi = 0.82$ and ±18 mm/s for $\phi = 1.2$. For DMC, the variation is somewhat larger, from ±90 mm/s for $\phi = 0.84$ to ±2.4 mm/s for $\phi = 1.43$. For the relatively high variation at $\phi = 0.84$ for DMC, the $\mathrm{Ma} \cdot \mathrm{Ka}$ value is equal to 0.24, which is above the recommended value of 0.15. It was not possible to reduce the $\mathrm{Ma} \cdot \mathrm{Ka}$ value by simply removing the smaller radii. The result from the experiment was still kept because the variation in the LBV between the models was not significant (see Table 4).

There is a larger variation in the Markstein length between all models compared to the variation in the laminar burning velocity. By comparing the average L_b value for each concentration, the variation for propane is between ±0.4 mm for $\phi = 0.82$ and ±0.1 mm for $\phi = 1.2$. DMC had a higher variation compared to propane: from ±1.0 mm for $\phi = 0.84$ to ±0.02 mm for $\phi = 1.43$. The maximum and minimum variations of the Markstein length corresponds to the same experiments with the maximum and minimum variations in the laminar flame speed.

The coefficient of determination R^2 is almost identical for the four stretch models used to fit the dependence of the flame radius on time. At the same time, the NE method proposed by Liu et al. [26] yields smaller R^2 values in all experiments. As the models are fitted based on different parameters, it is difficult to compare the R^2 values between the NE method and the other four models.

DISCUSSION

When using an explosion sphere to determine the flame speed, the thermal diffusion, hydrodynamic instabilities, and buoyancy can cause instabilities and may influence the flame propagation [21, 42]. Choosing the concentration close to stoichiometry ($\phi = 1.0$) will reduce instabilities. For some of the rich mixtures, small flame front instabilities can be seen in Fig. 3. These instabilities may cause small errors in the calculated LBV. Regarding the buoyancy effects, Ronney and Wachman [43] reported that buoyancy would not cause any significant errors in the radius measurements in the experiments with LBV values above 150 mm/s. As the measured LBV is above 200 mm/s in all experiments of the present study, the discrepancies due to buoyancy are considered as negligible.

Table 3. Summary of results for propane–air mixture burning at the initial temperature of 300 K and initial absolute pressure of 100 kPa

ϕ	Flame parameters	Stretch extrapolation model				
		LS	LC	N3P	NE	NQ
0.82	S_b^0, mm/s	2047.2	2000.4	2004.3	2004.5	1977.0
	L_b, mm	1.80	1.31	1.35	1.34	1.11
	S_u^0, mm/s	287.0	280.5	281.0	281.1	277.2
	R^2	0.999997	0.999998	0.999998	0.999998	0.995362
0.99	S_b^0, mm/s	2976.4	2932.3	2974.2	2 935.5	2905.7
	L_b, mm	1.39	1.08	1.38	1.10	0.94
	S_u^0, mm/s	378.8	373.1	378.5	373.6	369.8
	R^2	0.999999	0.999999	0.999999	0.999999	0.991300
1.20	S_b^0, mm/s	3139.5	3120.9	3138.5	3121.8	3108.0
	L_b, mm	0.84	0.72	0.84	0.72	0.65
	S_u^0, mm/s	396.0	393.7	395.9	393.8	392.1
	R^2	0.999999	0.999999	0.999999	0.999999	0.978764
1.43	S_b^0, mm/s	1926.5	1925.6	1924.2	1925.6	1896.2
	L_b, mm	−0.22	−0.23	−0.24	−0.23	−0.39
	S_u^0, mm/s	252.0	251.9	251.7	251.9	248.1
	R^2	0.999998	0.999998	0.999998	0.999998	0.563832

Pressure changes can also cause hydrodynamic instabilities. However, in the recorded pressure within the radius measurement range, no significant pressure increase was detected. Ignition-induced instabilities often propagate along with the flame development [44]. For this reason, the experiments with non-spherical flame propagation were rejected. By varying the spark gap in the interval 0.5–2.0 mm for different concentrations, the ignition-induced instabilities were reduced. Figure 3 shows that the flame exhibits spherical propagation in most experiments and has a smooth surface with relatively few wrinkles.

Figure 4a shows the unfiltered measured radii and the regression curves, except for the NE model. The light tone markers are all measured radii, and the black markers are the radii used in the regression study. The radii below 10 mm were automatically removed because of the relatively large change in the flame speed (Fig. 4b). Kelley et al. [44] reported a similar observation when investigating the critical radius necessary to sustain flame propagation. The flame propagates initially with a high velocity due to ignition, but decelerates as it propagates. At a certain flame radius, the flame speed starts to increase until it reaches a flame speed that approaches the LBV. For radii above 10 mm, the flame radius increased almost linearly in time for most of the experiments; therefore, this value was chosen as the initial minimum radius. More experimental points were removed for which the product of the Markstein number and the Karlovitz number was outside the recommended range of −0.05 to 0.15 proposed by Wu et al. [29], who demonstrated that the LBV measurement should be conducted within the mentioned range to minimize the extrapolation uncertainties:

$$\mathrm{Ma}_{\mathrm{linear}}\mathrm{Ka}_{\mathrm{mid}} = \frac{L_b}{\delta_L}\frac{\kappa\delta_L}{S_b} = \frac{2L_{b,\mathrm{linear}}}{r_{f,\mathrm{mid}}}$$

(δ_L is the laminar flame thickness). In Fig. 4a, all models fit equally well with the measured radii, which is expected based on the R^2 value in Tables 3 and 4. Based on the results in Tables 3 and 4, the models for extrapolating the laminar flame speed and burning velocity yield fairly similar results, which are almost independent of the model if used within the interval $-0.05 < \mathrm{Ma}\cdot\mathrm{Ka} < 0.15$.

Figure 5a shows the propane–air combustion results compared with previously published studies [22–26, 45]. The DMC results are also compared in Fig. 5b to the results of [19] and with the predictions by two reaction mechanisms [39, 40]. For comparison of the experimental results, only the LS model was used because it was this model that was used in the previous studies. It is worth mentioning that the variation in the LBV between the methods is significantly smaller (±5 mm/s at most) than the variation between the different studies (±30 mm/s on the average).

Table 4. Summary of results for DMC–air mixture burning at the initial temperature of 300 K and initial absolute pressure of 100 kPa

ϕ	Flame parameters	Stretch extrapolation model				
		LS	LC	N3P	NE	NQ
0.84	S_b^0, mm/s	1895.1	1804.6	1729.3	1814.8	1783.9
	L_b, mm	2.84	1.79	0.97	1.86	1.53
	S_u^0, mm/s	250.8	238.8	228.9	240.2	236.1
	R^2	0.999968	0.999987	0.999993	0.999984	0.991726
1.01	S_b^0, mm/s	2436.2	2383.8	2395.3	2388.3	2361.5
	L_b, mm	1.74	1.28	1.38	1.30	1.11
	S_u^0, mm/s	293.6	287.3	288.6	287.8	284.6
	R^2	0.999997	0.999998	0.999998	0.999998	0.994419
1.04	S_b^0, mm/s	2491.8	2446.3	2464.8	2450.0	2425.3
	L_b, mm	1.57	1.18	1.34	1.21	1.03
	S_u^0, mm/s	300.3	294.8	297.0	295.2	292.2
	R^2	0.999998	0.999998	0.999998	0.999998	0.993317
1.13	S_b^0, mm/s	2494.2	2474.8	2491.8	2475.9	2461.6
	L_b, mm	0.98	0.81	0.96	0.82	0.73
	S_u^0, mm/s	297.3	294.9	297.0	295.1	293.4
	R^2	0.999998	0.999998	0.999998	0.999998	0.988313
1.16	S_b^0, mm/s	2522.3	2497.8	2529.2	2499.4	2482.3
	L_b, mm	1.10	0.90	1.14	0.90	0.80
	S_u^0, mm/s	300.9	298.0	301.8	298.2	296.2
	R^2	0.999996	0.999996	0.999996	0.999996	0.962149
1.32	S_b^0, mm/s	2144.8	2141.5	2143.8	2141.6	2140.3
	L_b, mm	0.41	0.38	0.40	0.38	0.37
	S_u^0, mm/s	261.0	260.6	260.9	260.7	260.5
	R^2	0.999999	0.999999	0.999999	0.999999	0.910555

The propane results are compared well with the previously published data, which indicates that the experimental setup and method provide acceptable results. The experimental results for DMC in this study match reasonably well with the data reported in [19]. Although there are only a few overlapping points in Fig. 5, the trend from the two datasets shares the same curve profile.

The results of this study include LBV values at 300 ± 2 K with the equivalence ratios $\phi > 1$, which have not been reported previously. For the LBV at $\phi = 1.32$, the partial pressure in that experiment (8.5 kPa at 302 K) was close to the estimated DMC vapor pressure of 8.8 kPa in [46]. The small pressure difference may cause some uncertainties of the concentration in the experiment.

The reaction mechanism of Sun et al. [40] agrees with the experimental results better than that by Glaude et al. [39]. Both calculations predict a higher LBV value than the results for DMC from both experimental studies. It is uncertain what is the reason for this discrepancy. Meanwhile, the radiative heat loss can contribute to the discrepancy between simulations and experiments, according to Chen [16].

Figure 6 shows comparisons of the explosion pressure (a) and the rate of explosion pressure rise (b) for propane and DMC. DMC has the highest explosion pressure of 0.94 MPa, which is higher than that of propane. However, propane has the higher rate of explosion pressure rise of 43 MPa/s. The higher rate of explosion pressure rise for propane is consistent with the LBV value. In Fig. 6, there are more data points than in Fig. 5 because Fig. 6 also shows the LBV measurements earlier rejected due to pronounced non-sphericity of flame propagation.

In the case of a leak of DMC into a confined space, the vapor concentration is determined by the vapor–liquid equilibrium, if the leaked amount is sufficient.

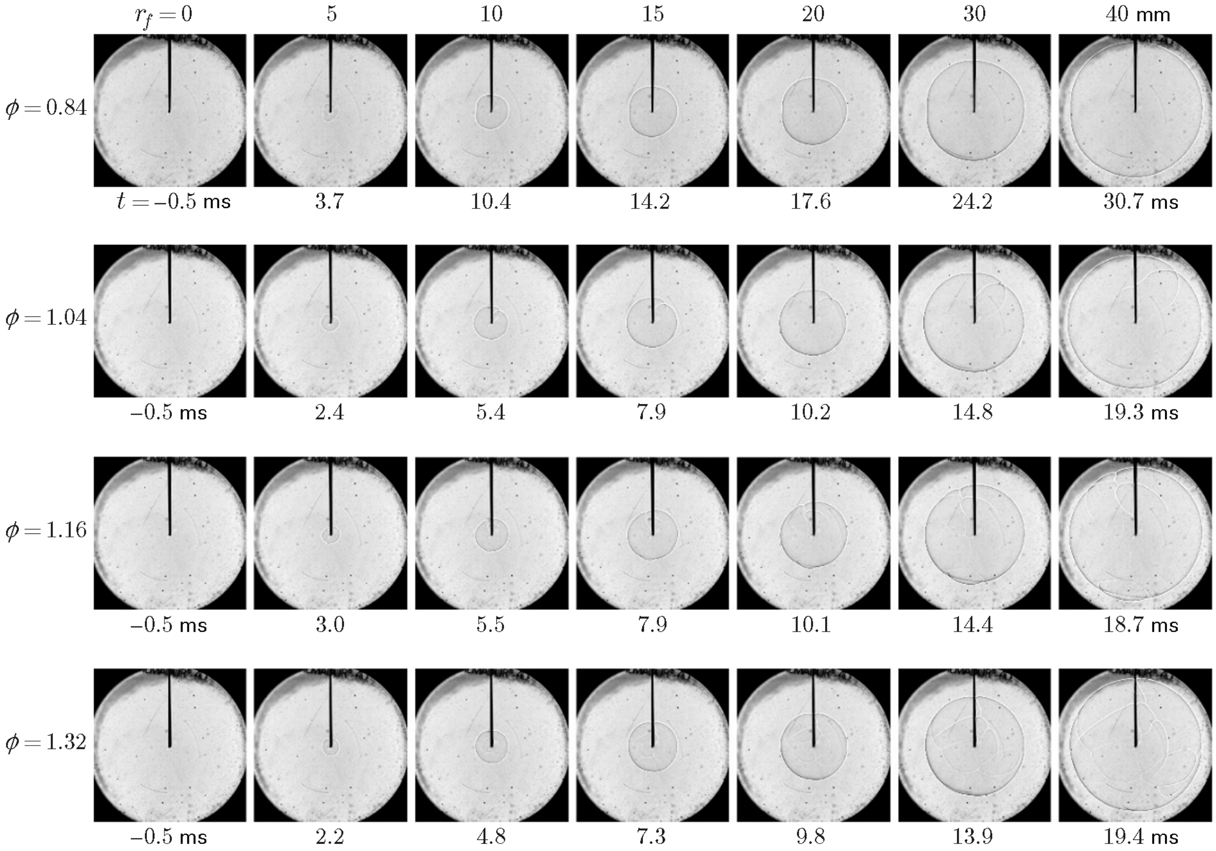

Fig. 3. Shadowgraph images of DMC combustion: the initial conditions are the temperature of 300 K and absolute pressure of 100 kPa.

At 1 atm and 300 K, the equilibrium vapor pressure for DMC corresponds to $\phi = 1.25$, which is above the stoichiometric value. At the same time, it means that the fuel–air mixture will never exceed the upper explosion limit under these conditions. An extra amount of DMC above the vapor–liquid equilibrium concentration induces vapor condensation, and the concentration of DMC in the gas phase is practically the same. The partial density of the DMC vapor at $\phi = 1.25$ under the above-mentioned conditions is 0.29 g/liter. The equilibrium explosion pressure at this concentration is 0.93 MPa, which is very close to the maximum explosion pressure recorded in this study. Also note that the ignition energy at $\phi = 1.25$ is close to its minimum value.

CONCLUSIONS

The laminar flame speed, Markstein length, and laminar burning velocity for propane and dimethyl carbonate at different concentrations were determined in a 20-liter explosion sphere at the initial temperature of 300 K and the initial absolute pressure of 100 kPa. If the product of the Markstein and Karlovitz numbers is within −0.05–0.15 for each experiment, then the results for the laminar flame speed are practically independent on the stretch extrapolation model used. The measured laminar burning velocities agree with the previously published data. The measurement procedure and the experimental setup provide consistent results and offer a suitable method for determining the laminar burning velocities.

For dimethyl carbonate, the highest laminar burning velocity of 300 mm/s was found at the fuel–air equivalence ratio of 1.04. This is slightly on the rich side, as expected. In this study of the laminar burning velocity, the concentration range for DMC is wider than that studied by Bardin et al. [19]. The laminar burning velocity measured near the saturated vapor pressure at 302 K is 261 mm/s.

The reaction mechanism of Sun et al. [40] yielded the laminar burning velocity closer to the experimental results than that of Glaude et al. [39]. Both reaction mechanisms overpredicted the laminar burning veloc-

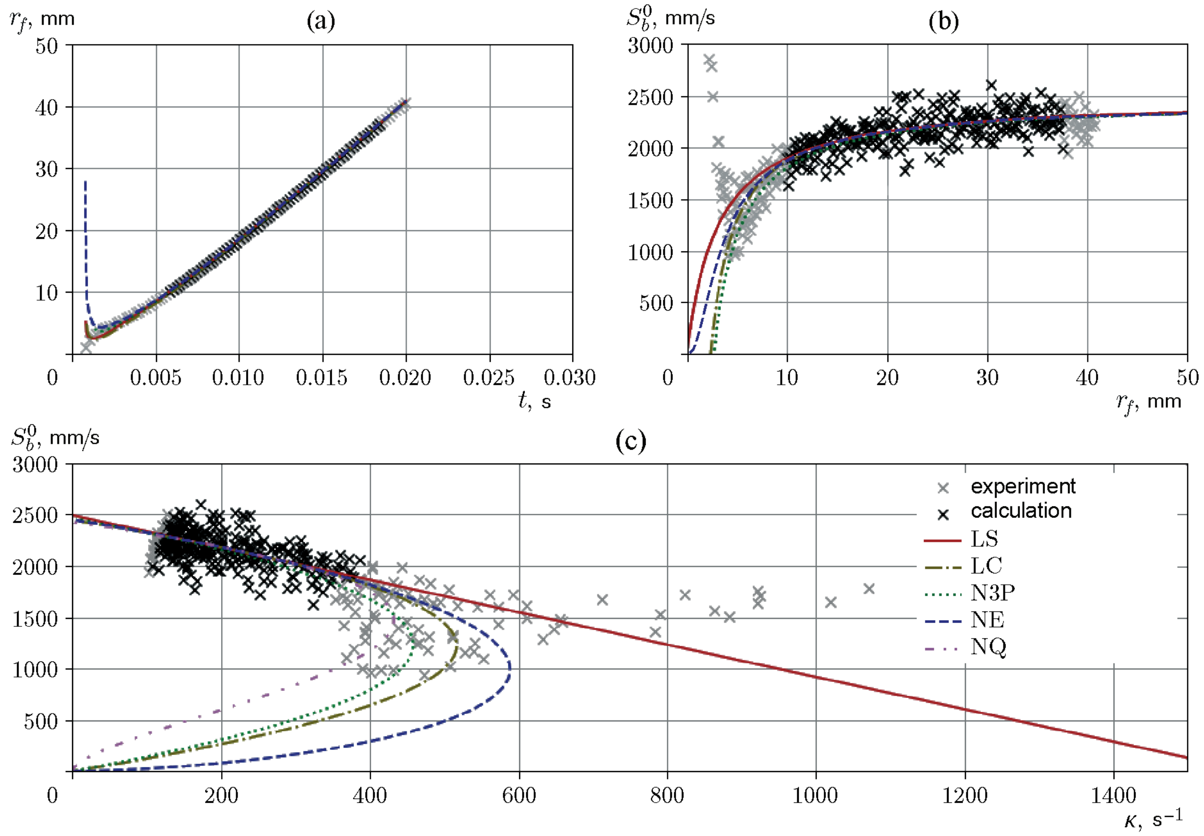

Fig. 4. Comparison of models used for extrapolation of LBV values: DMC, $\phi = 1.04$, the initial conditions are the temperature of 300 K and absolute pressure of 100 kPa.

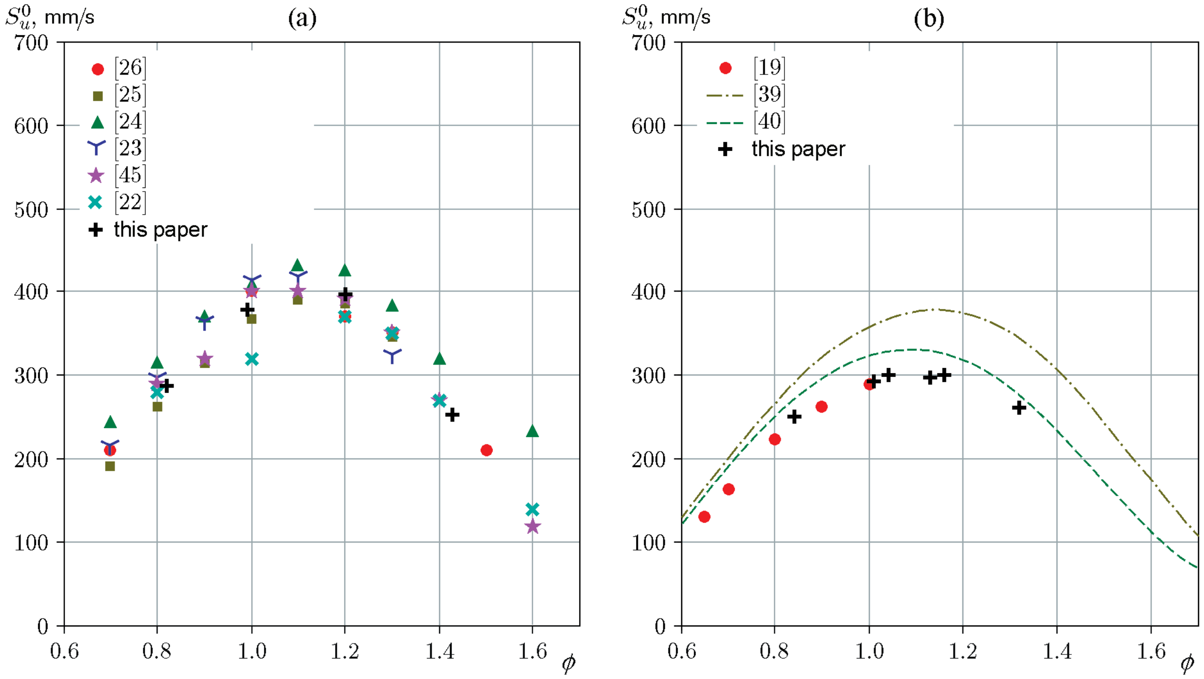

Fig. 5. Measured laminar burning velocity versus the equivalence ratio: (a) propane flame (comparison with previously reported results); (b) DMC flame (comparison with previously reported results and predictions with two reaction mechanisms); the initial conditions are the temperature of 300 K and absolute pressure of 100 kPa.

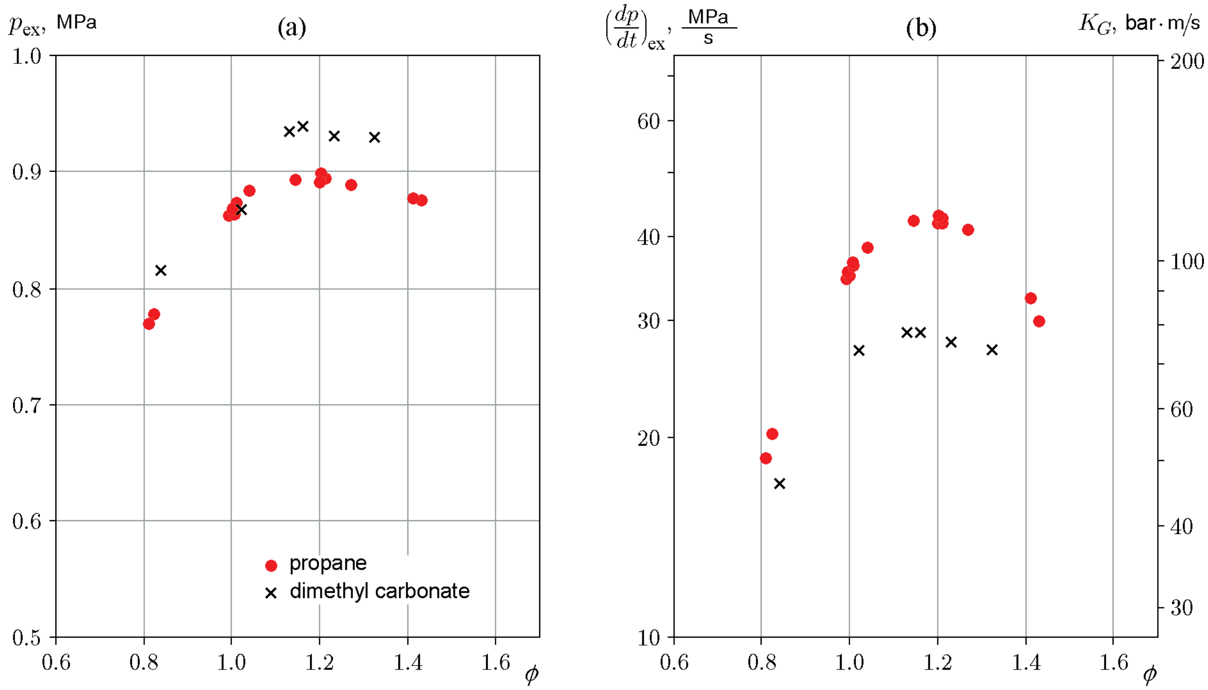

Fig. 6. Comparison of the explosion characteristics for propane and DMC: (a) explosion pressure; (b) rate of explosion pressure rise; K_G is the deflagration index; the initial conditions are the temperature of 300 K and absolute pressure of 100 kPa.

ities compared to the experimental results. This disagreement may be due to the radiative heat losses in the explosion sphere compared to the adiabatic conditions assumed in the theoretical calculation.

Dimethyl carbonate has the higher maximum explosion pressure of 0.94 MPa, and propane exhibits the higher rate of explosion pressure rise (43 MPa/s), which is consistent with the higher burning velocities in propane–air mixtures.

This work was performed at MoZEES, a Norwegian Centre for Environment-friendly Energy Research (FME), co-sponsored by the Research Council of Norway (project number 257653) and 40 partners from research, industry, and public sector.

Special thanks to Nabiha Chaumeix from CNRS-INSIS Laboratory ICARE for demonstrating the ICAREs experimental method and software for determining the laminar burning velocity. The development of the image and post-processing code was inspired by the helpful discussion with Nabiha Chaumeix.

REFERENCES

1. N.-S. Choi, Z. Chen, S. A. Freunberger, et al., “Challenges Facing Lithium Batteries and Electrical Double-Layer Capacitors,” Angew. Chem. Int. Ed. **51**, 9994–10024 (2012); DOI: 10.1002/anie.201201429.
2. What’s the Best Battery? (Battery Univ., 2017); http://batteryuniversity.com/learn/archive/whats_the_best_battery.
3. D. Lisbona and T. Snee, “A Review of Hazards Associated with Primary Lithium and Lithium-Ion Batteries,” Process Saf. Environ. Prot. **89** (6), 434–442 (2011); DOI: 10.1016/j.psep.2011.06.022.
4. P. G. Balakrishnan, R. Ramesh, and T. Prem Kumar, “Safety Mechanisms in Lithium-Ion Batteries,” J. Power Sources **155** (2), 401–414 (2006); DOI: 10.1016/j.jpowsour.2005.12.002.
5. S. Abada, G. Marlair, A. Lecocq, et al., “Safety Focused Modeling of Lithium-Ion Batteries: A Review,” J. Power Sources **306**, 178–192 (2016); DOI: 10.1016/j.jpowsour.2015.11.100.
6. Q. Wang, P. Ping, X. Zhao, et al., “Thermal Runaway Caused Fire and Explosion of Lithium Ion Battery,” J. Power Sources **208**, 210–224 (2012); DOI: 10.1016/j.jpowsour.2012.02.038.
7. C. Mikolajczak, M. Kahn, K. White, and R. T. Long, *Lithium-Ion Batteries Hazard and Use Assessment*, (Springer, Boston, 2011); DOI: 10.1007/978-1-4614-3486-3.
8. S. J. Harris, A. Timmons, and W. J. Pitz, “A Combustion Chemistry Analysis of Carbonate Solvents Used in Li-Ion Batteries,” J. Power Sources **193** (2), 855–858 (2009); DOI: 10.1016/j.jpowsour.2009.04.030.

9. C. C. Crafts, D. H. Doughty, J. McBreen, and E. P. Roth, "Advanced Technology Development Program for Lithium-Ion Batteries: Thermal Abuse Performance of 18650 Li-Ion Cells," Sandia Report No. 2004-1584 (Sandia Nat. Lab., 2004); DOI: 10.2172/918751.
10. P. Ribière, S. Grugeon, M. Morcrette, et al., "Investigation on the Fire-Induced Hazards of Li-Ion Battery Cells by Fire Calorimetry," Energy Envir. Sci. **5**, 5271–5280 (2012); DOI: 10.1039/C1EE02218K.
11. A. W. Golubkov, S. Scheikl, R. Planteu, et al., "Thermal Runaway of Commercial 18650 Li-Ion Batteries with LFP and NCA Cathodes—Impact of State of Charge and Overcharge," RSC Advances **5**, 57171–57186 (2015); DOI: 10.1039/C5RA05897J.
12. F. Colella et al., "Analysis of Combustion Hazards due to Catastrophic Failures in Lithium-Ion Battery Packs," in *Proc. of the 7th Int. Seminar Fire and Explosion Hazards* (Research Publ. Services, 2013), pp. 575–584; DOI: 10.3850/978-981-07-5936-0_09-02.
13. J. Johnsplass, *Lithium-Ion Battery Safety* (Univ. of South-Eastern Norway, 2017).
14. M. Henriksen, K. Vaagsaether, J. Lundberg, et al., "Explosion Characteristics for Li-Ion Battery Electrolytes at Elevated Temperatures," J. Hazard. Mater. **371**, 1–7 (2019); DOI: 10.1016/j.jhazmat.2019.02.108.
15. D. Bjerketvedt, J. R. Bakke, and K. Van Wingerden, "Gas Explosion Handbook," J. Hazard. Mater. **52** (1), 1–150 (1997).
16. Z. Chen, "On the Accuracy of Laminar Flame Speeds Measured from Outwardly Propagating Spherical Flames: Methane/Air at Normal Temperature and Pressure," Combust. Flame **162** (6), 2442–2453 (2015); DOI: 10.1016/j.combustflame.2015.02.012.
17. J. Huo, S. Yang, Z. Ren, et al., "Uncertainty Reduction in Laminar Flame Speed Extrapolation for Expanding Spherical Flames," Combust. Flame **189**, 155–162 (2018); DOI: 10.1016/j.combustflame.2017.10.032.
18. Ö. L. Gülder, "Correlations of Laminar Combustion Data for Alternative S. I. Engine Fuels," SAE Tech. Paper No. 841000, (1984); DOI: 10.4271/841000.
19. M. E. Bardin et al., "Laminar Burning Velocities of Dimethyl Carbonate with Air," Energy Fuels **27** (9), 5513–5517 (2013); DOI: 10.1021/ef401108a.
20. S. De Persis, N. Chaumeix, Y. Fernandes, et al., "Experimental and Theoretical Determination of DMC/Air Flame Velocities," in *11th Int. Conf. on Chemical Kinetics, Orleans, 2019*, Poster No. 30.
21. A. A. Konnov, A. Mohammad, V. R. Kishore, et al., "A Comprehensive Review of Measurements and Data Analysis of Laminar Burning Velocities for Various Fuel + Air Mixtures," Prog. Energy Combust. Sci. **68**, 197–267 (2018); DOI: 10.1016/j.pecs.2018.05.003.
22. L.-K. Tseng, M. A. Ismail, and G. M. Faeth, "Laminar Burning Velocities and Markstein Numbers of Hydrocarbon–Air Flames," Combust. Flame **95** (4), 410–426 (1993); DOI: 10.1016/0010-2180(93)90007-P.
23. G. Jomaas, X. L. Zheng, D. L. Zhu, and C. K. Law, "Experimental Determination of Counterflow Ignition Temperatures and Laminar Flame Speeds of C_2–C_3 Hydrocarbons at Atmospheric and Elevated Pressures," Proc. Combust. Inst. **30** (1), 193–200 (2005); DOI: 10.1016/j.proci.2004.08.228.
24. C. Tang, J. Zheng, Z. Huang, and J. Wang, "Study on Nitrogen Diluted Propane–Air Premixed Flames at Elevated Pressures and Temperatures," Energy Convers. Manage **51**, 288–295 (2010); DOI: 10.1016/j.enconman.2009.09.024.
25. W. Lowry, J. de Vries, M. Krejci, et al., "Laminar Flame Speed Measurements and Modeling of Pure Alkanes and Alkane Blends at Elevated Pressures," J. Eng. Gas Turbines Power **133** (9), ID 091501 (2011); DOI: 10.1115/1.4002809.
26. Q. Liu, Y. Zhang, F. Niu, and L. Li, "Study on the Flame Propagation and Gas Explosion in Propane/Air Mixtures," Fuel **140**, 677–684 (2015); DOI: 10.1016/j.fuel.2014.09.123.
27. M. Henriksen, K. Vaagsaether, A. V. Gaathaug, et al., "Laminar Burning Velocity Measurements for an Outwardly Propagating Flame of Dimethyl Carbonate and Air Mixtures," in *Proc. of the 9th Int. Seminar on Fire and Explosion Hazards, St Petersburg, Russia, 2019* (Peter the Great St. Petersburg Polytech. Univ. Press, 2019), Vol. 1, pp. 161–172; DOI: 10.18720/spbpu/2/k19-29.
28. G. S. Settles, *Schlieren and Shadowgraph Techniques: Visualizing Phenomena in Transparent Media* (Springer, Berlin–New York, 2001).
29. F. Wu, W. Liang, Z. Chen, et al., "Uncertainty in Stretch Extrapolation of Laminar Flame Speed from Expanding Spherical Flames," Proc. Combust. Inst. **35**, 663–670 (2015); DOI: 10.1016/j.proci.2014.05.065.
30. C. K. Law, *Combustion Physics* (Cambridge Univ. Press, 2006).
31. F. A. Williams, *Combustion Theory* (Chapman and Hall/CRC, Boulder, 2018).
32. G. H. Markstein, *Nonsteady Flame Propagation* (Elsevier Sci., Burlington, 2014).
33. Z. Chen, "On the Extraction of Laminar Flame Speed and Markstein Length from Outwardly Propagating Spherical Flames," Combust. Flame **158**, 291–300 (2011); DOI: 10.1016/j.combustflame.2010.09.001.
34. A. P. Kelley, J. K. Bechtold, and C. K. Law, "Premixed Flame Propagation in a Confining Vessel with Weak Pressure Rise," J. Fluid Mech. **691**, 26–51 (2012); DOI: 10.1017/jfm.2011.439.
35. A. P. Kelley and C. K. Law, "Nonlinear Effects in the Extraction of Laminar Flame Speeds from Expanding Spherical Flames," Combust. Flame **156**, 1844–1851 (2009); DOI: 10.1016/j.combustflame.2009.04.004.

36. Q. Liu, X. Chen, Y. Shen, and Y. Zhang, "Parameter Extraction from Spherically Expanding Flames Propagated in Hydrogen/Air Mixtures," Int. J. Hydrogen Energy **44** (2), 1227–1238 (2019); DOI: 10.1016/j.ijhydene.2018.11.004.
37. A. Savitzky and M. J. E. Golay, "Smoothing and Differentiation of Data by Simplified Least Squares Procedures," Anal. Chem. **36** (8), 1627–1639 (1964); DOI: 10.1021/ac60214a047.
38. D. G. Goodwin, H. K. Moffat, and R. L. Speth, "Cantera: An Object-Oriented Software Toolkit for Chemical Kinetics, Thermodynamics, and Transport Processes. Version 2.3.0," (2017); DOI: 10.5281/zenodo.170284.
39. P. A. Glaude, W. J. Pitz, and M. J. Thomson, "Chemical Kinetic Modeling of Dimethyl Carbonate in an Opposed-Flow Diffusion Flame," Proc. Combust. Inst. **30** (1), 1111–1118 (2005); DOI: 10.1016/j.proci.2004.08.096.
40. W. Sun, B. Yang, N. Hansen, et al., "An Experimental and Kinetic Modeling Study on Dimethyl Carbonate (DMC) Pyrolysis and Combustion," Combust. Flame **164**, 224–238 (2016); DOI: 10.1016/j.combustflame.2015.11.019.
41. G. P. Smith, D. M. Golden, M. Frenklach, et al., "GRI-Mech 3.0," http://www.me.berkeley.edu/gri_mech/.
42. F. N. Egolfopoulos et al., "Advances and Challenges in Laminar Flame Experiments and Implications for Combustion Chemistry," Prog. Energy Combust. Sci. **43**, 36–67 (2014); DOI: 10.1016/j.pecs.2014.04.004.
43. P. D. Ronney and H. Y. Wachman, "Effect of Gravity on Laminar Premixed Gas Combustion. I: Flammability Limits and Burning Velocities, Combust. Flame **62** (2), 107–119 (1985); DOI: 10.1016/0010-2180(85)90139-7.
44. A. P. Kelley, G. Jomaas, and C. K. Law, "Critical Radius for Sustained Propagation of Spark-Ignited Spherical Flames," Combust. Flame **156** (5), 1006–1013 (2009); DOI: 10.1016/j.combustflame.2008.12.005.
45. M. I. Hassan, K. T. Aung, O. C. Kwon, and G. M. Faeth, "Properties of Laminar Premixed Hydrocarbon/Air Flames at Various Pressures," J. Propul. Power **14** (4), 479–488 (1998); DOI: 10.2514/2.5304.
46. V. Pokorný, V. Štejfa, M. Fulem, et al., "Vapor Pressures and Thermophysical Properties of Dimethyl Carbonate, Diethyl Carbonate, and Dipropyl Carbonate," J. Chem. Eng. Data **62** (10), 3206–3215 (2017); DOI: 10.1021/acs.jced.7b00295.

Article C

Laminar Burning Velocity of Gases Vented from Failed Li-Ion Batteries

Published in the Journal of Power Sources, Volume 506, 2021,
doi: https://doi.org/10.1016/j.jpowsour.2021.230141

Journal of Power Sources 506 (2021) 230141

Contents lists available at ScienceDirect

Journal of Power Sources

journal homepage: www.elsevier.com/locate/jpowsour

Laminar burning velocity of gases vented from failed Li-ion batteries

M. Henriksen [a,*], K. Vaagsaether [a], J. Lundberg [a], S. Forseth [b], D. Bjerketvedt [a]

[a] Faculty of Technology, Natural Sciences and Maritime Sciences, University of South-Eastern Norway, Kjølnes Ring 56, Porsgrunn, 3901, Norway
[b] Norwegian Defence Research Establishment (FFI), Instituttveien 20, 2007, Kjeller, Norway

HIGHLIGHTS

- Different gas compositions vented from failed Li-ion batteries (LIBs) are investigated.
- Laminar burning velocities (LBVs) of multiple gases are determined experimentally.
- The obtained LBVs are compared with the LBVs predicted by reaction mechanisms.
- Ideal prediction models are identified based on the CO_2 content in gas mixtures.
- Generation of a simplified gas to resemble combustion properties of an actual LIB vent gas.

ARTICLE INFO

Keywords:
Li-ion explosion hazard
Combustion properties
Safety
Vented Li-ion gas
Laminar burning velocity
Reaction mechanisms

ABSTRACT

In the last decade, several fires and explosions caused by Li-ion batteries (LIBs) have been reported. This can be attributed to the thermal runaway and catastrophic failures of LIBs that release combustible gases, which when mixed with air can lead to explosions and fires. To address this explosion hazard, we determine the laminar burning velocity (LBV) of three gas compositions associated with Li-ion failure and a pseudo (simplified) gas in a 20-L explosion sphere at 300 K and 100 kPa. This simplified gas avoids toxic gases in experiments and represent the desired explosion characteristics. The LBVs in the case of gas compositions range from approximately 300 to 1050 mm s^{-1}. Additionally, four different reaction models are used to estimate the LBVs of these gas compositions. We compare the theoretical and experimental results to determine the prediction accuracy of the reaction models. All reaction models over- or under-predicted the LBV for the different gas compositions. A recommendation for choosing reaction models is given to predict LBV for various gas compositions. This study's results are intended as input to computational fluid dynamic simulations but can be used directly in safety engineering models.

1. 1. Introduction

The need for sustainable and emission-free energy has increased the demand for Li-ion batteries (LIBs) as leading energy storage units [1]. However, LIBs exhibit an inherent risk of catastrophic failures. Owing to the use of flammable organic electrolyte solvents and temperature-sensitive electrodes in Li-ion cells, a battery management system is required to ensure safe operation. A catastrophic failure or a thermal runaway may generate and release combustible gases and evaporate the electrolyte components. These combustible gases mixed with air can cause explosions and fires. Several severe accidents caused by failed LIBs have been reported in the last decade [2–6].

Numerous events, including heat exposure, mechanical abuse, overload, overcharge, under-discharge, and internal or external short circuits can lead to a catastrophic failure of an LIB. Any of these events can initiate self-heating that may result in thermal runaway [7]. Sufficient self-heating will cause the evaporation and decomposition of the electrolyte solvent, which increases the internal pressure. Consequently, the Li-ion cell may vent or rupture [5]. The gas released during venting or rupturing can be a mixture of hydrogen, carbon monoxide, carbon dioxide, and various hydrocarbons [8].

Since the early 2000s, several researchers have conducted experimental studies to explore the composition of gases released from failing LIBs. Certain studies focused on the toxic gases released during cell venting. For instance, Larsson et al. [9] and Nedjalkov et al. [10] reported a significant amount of a toxic substance, hydrogen fluoride.

---

[*] Corresponding author.
E-mail address: mathias.henriksen@usn.no (M. Henriksen).

https://doi.org/10.1016/j.jpowsour.2021.230141
Received 18 March 2021; Received in revised form 13 May 2021; Accepted 3 June 2021

Moreover, Nedjalkov et al. identified five additional substances that cause acute toxicity. This study focuses on the combustible gases released during thermal abuse testing of commercial LIBs in an inert atmosphere. Table 1 list a few examples of experimental studies [11–14] which fit the mention criteria. The species concentrations in Table 1 are normalized so that the sum of each gas composition equals 100%. The different gas mixtures in Table 1 indicate that the composition depends on the state of charge (SOC) and cell type or chemistry. For a more compressive list of gas releases from cell failure and thermal runaway, we suggested the following articles by Baird et al. [4], Wang et al. [11], and Fernandes et al. [12].

Laminar burning velocity (LBV) is a fundamental property of combustion and an important parameter in understanding the flame propagation, gas explosions, and combustion reaction mechanisms [17–19]. The LBV is used as a parameter in computational fluid dynamic (CFD) simulations to model turbulent combustion in large-scale explosions [20] and safety engineering models. Baird et al. [4] studied the explosive limits and the LBV of several gas compositions vented from failing LIBs, including the mixtures presented in Table 1. The combustion properties were calculated using the open-source tool Cantera [21] and the GRI-MECH 3.0 [22] reaction mechanism. The experimental results indicated that the LBV of the mixtures were in the range between 0.4 and 1.1 m s^{-1} [4].

In this study, we investigated the LBV of three potential gases released during an LIB venting. Experimentally determine LBV of gases released from LIBs has not been previously published; at least we found no such publications. The scope of this study was limited to the most common flammable species shown in Table 1. Therefore, the influence of fluorinated species and electrolyte solvents was neglected. However, fluorinated species can affect the LBV, and the explosion characteristics, as Gao et al. [23] showed in their study on explosion suppression of hydrogen explosions.

Based on the results reported by Baird et al. [4], we investigated the gas mixtures representing the upper and lower ranges of the LBV. The gas composition vented from a Lithium-nickel-cobalt aluminum (NCA) and Lithium-iron-phosphate (LFP) with a 100 SOC reported by Lammer et al. [13] and Golubkov et al. [16] (Table 1) were used as the basis for upper and lower LBVs gas compositions, hereafter referred to as the *high LBV Li-ion gas* and *low LBV Li-ion gas*, respectively. The third mixture was determined through several experiments conducted in a pressure vessel by heating commercial cells with cathode chemistry based on Lithium-iron-phosphate (LFP) with 100% SOC in an inert atmosphere. A gas chromatograph with a mass spectrometer detector analyzed the gas composition vented from LIBs, hereafter referred to as the *generic Li-ion gas*. These experiments were conducted by a research partner as part of the Norwegian Centre for Environment-friendly Energy Research, MoZEES [24].

In addition to the three different gas mixtures released from Li-ion batteries, we generated a pseudo or simplified gas, wherein the combustion properties were similar to that of the generic Li-ion gas composition. When studying an explosion in large-scale experiments, simplified gas has several advantages. Owing to the reduced number of species in the gas composition, less equipment is required when mixing the gases onsite and the cost of ordering large volumes of unique gas blends is reduced. Moreover, different combustion properties can be analyzed by adjusting only the ratio between species. Furthermore, the elimination of toxic species, such as carbon monoxide, can improve safety significantly. In this study, we generated a simplified gas mixture comprising hydrogen and methane, wherein their volume fractions were balanced to exhibit combustion properties similar to that of the generic Li-ion gas composition. Table 2 presents all four gas compositions studied experimentally and compared with theoretical calculations.

All experiments were performed in a 20-L explosion sphere [17,18] at 300 K and 100 kPa. The experimental results were compared with the theoretical calculations obtained using the open-source tool Cantera (version 2.4) [21]. Four different reaction mechanisms, namely the GRI-MECH 3.0 [22], the San Diego Mech [25], and two DMC combustion mechanisms reported by Glaude et al. [26] and Sun et al. [27] were used for the theoretical calculations. The results in this study are indented as input parameters for CFD simulations and safety engineering models.

Table 2
Gas compositions of the three potential gases vented from a failing Li-ion battery and the generated simplified gas.

Fuel mixture	H_2 [%]	CO [%]	CO_2 [%]	CH_4 [%]	C_2H_4 [%]	C_2H_6 [%]
High LBV Li-ion gas	42.8	37.1	10.0	7.1	3.0	[–]
Low LBV Li-ion gas	29.5	9.0	48.4	5.6	7.0	0.5
Generic Li-ion gas	34.9	25.0	20.1	15.0	5.0	[–]
Simplified gas	35.0	[–]	[–]	65.0	[–]	[–]

Table 1
Collection of normalized gas compositions vented from Li-ion batteries and cells during thermal abuse testing. The details are obtained from the existing literature [13–16].

REF.	Cell Type	SOC [%]	H_2 [%]	CO [%]	CO_2 [%]	CH_4 [%]	C_2H_2 [%]	C_2H_4 [%]	C_2H_6 [%]	C_3H_6 [%]	C_3H_8 [%]	C_4+ [%]
[13]	NCA-32A[c]	100	16.0	58.4	20.4	2.5	0.2	2.4	0.1	[–]	[–]	[–]
[13]	NCA-35E[c]	100	35.7	44.0	14.5	3.6	0.1	2.0	0.1	[–]	[–]	[–]
[13]	NCA-MJ1[c]	100	43.1	37.1	9.8	7.0	0.2	2.7	0.1	[–]	[–]	[–]
[14]	LCO	50	30.7	3.6	32.0	5.7	[–]	5.5	2.7	8.1	0.7	11.1
[14]	LCO	100	27.5	22.7	29.8	6.3	[–]	2.2	1.2	4.5	0.3	5.6
[14]	LCO	150	29.6	24.4	20.8	8.2	[–]	10.7	1.3	0.0	2.5	2.5
[15]	LCO/NMC	100	30.0	27.6	24.9	8.6	[–]	7.7	1.2	[–]	[–]	[–]
[15]	NMC	100	30.8	13.0	41.2	6.8	[–]	8.2	0.0	[–]	[–]	[–]
[15]	LFP	100	30.9	4.8	53.1	4.1	[–]	6.8	0.3	[–]	[–]	[–]
[16]	NCA	0[a]	1.3	1.4	95.7	1.3	[–]	0.3	0.0	[–]	[–]	[–]
[16]	NCA	50	17.5	39.9	33.8	5.2	[–]	3.2	0.4	[–]	[–]	[–]
[16]	NCA	100[b]	25.7	44.7	19.9	7.1	[–]	2.1	0.4	[–]	[–]	[–]
[16]	LFP	0	2.7	1.8	93.4	0.7	[–]	0.7	0.7	[–]	[–]	[–]
[16]	LFP	50	20.8	4.8	66.2	1.6	[–]	6.6	0	[–]	[–]	[–]
[16]	LFP	100	29.4	9.1	48.3	5.4	[–]	7.2	0.5	[–]	[–]	[–]

[a] The value is an average of five tests with identical chemistry and SOC.

[b] The value is an average of three tests with identical chemistry and SOC.

[c] The three gas compositions of the NCA cell type presented by Lammer et al. [13] are from different manufactures.

2. Materials and methods

Fig. 1 illustrates the experimental setup used in the study. A detailed description of the experimental setup, procedure, and determination of LBV is published previously [28,29]. The internal volume of the explosion sphere is 20 L, and a temperature-controlled heating jacket surrounding the vessel regulates the inner ambient temperature. While two pressure sensors recorded the explosion pressure, a separate pressure sensor was used to record the ambient pressure in the vessel during filling. Moreover, the separated fuel and air inlets reduced uncertainties in fuel–air concentrations. A single high-voltage spark ignited the fuel–air mixture. The flame propagation was recorded using a high-speed camera operating at 20,000 frames per second (fps) and the shadowgraph imaging technique [30]. We analyzed each image using an in-house image-processing algorithm generated in Python (v3.6) to obtain the temporal evolution of the flame radius.

The planar unstretched LBV ($S^0{}_u$) was calculated based on the temporal evolution of the flame radius. A detailed description of the procedure is published previously [28,31]. The laminar flame speed ($S^0{}_b$) and the Markstein length (L_b) is curve fitted to the implicit functions of radii ($r(t)$), which are the derivatives obtained from the most common stretch extrapolation models [17]. A previous study [31] reported that the derivatives obtained from these stretch extrapolation models generate remarkably similar LBV. In this study, we present the LBV obtained from the linear stretch model as it is commonly used in literature. The equations presented below are used to calculate the laminar flame speed, the Markstein length, and the LBV. The maximum explosion pressure and the rate of explosion pressure rise were calculated based on the recorded pressure.

$$r_f(t) = S_b^0 t - 2L_b \ln r_f + Cst \qquad 1$$

where, r_f, flame radius [m], $S^0{}_b$, laminar flame speed with respect to the burnt state [m s^{-1}], L_b, Markstein length with respect to the burnt state [m], Cst, integration constant [m]

$$S_u^0 = S_b^0 \frac{\rho_b}{\rho_u} \qquad 2$$

where, $S^0{}_u$, laminar burning velocity with respect to the unburnt state [m s^{-1}], $S^0{}_b$, laminar flame speed with respect to the burnt state [m s^{-1}], ρ_b, density with respect to the burnt state [kg m^{-3}], ρ_u, density with respect to the unburnt state [kg m^{-3}].

The Cantera module [21] comprises several routines and algorithms that aid in solving problems of thermodynamics, chemical kinetics, and transport processes. We used the *FreeFlame* algorithm that solves the governing equation of a steady laminar (planar) 1-D premixed adiabatic flame [32] to calculate the LBV. Furthermore, we used the thermodynamic solver *equilibrate,* which finds the composition with minimum Gibbs free energy at constant internal energy and volume, to calculate the constant-volume explosion pressure. Both calculations require a reaction model, which comprises the chemical kinetic, thermodynamic, and transport data of the included species and reactions, as input. The results obtained from four different reaction models were compared with the experimentally measured LBV.

The reaction models chosen in this study was GRI-Mech 3.0 [22], San Diego Mech [25], a reaction mechanism propose by Glaude et al. [26] and Sun et al. [27]. GRI-Mech 3.0, which is design for natural gas combustion, includes 53 species and 325 reactions. In the study by Baird et al. [4], GRI-Mech 3.0 was used exclusively to predict the combustion and explosion properties of gas vented from Li-ion cells. The San Diego reaction mechanism includes 57 species and 268 reactions and is design to suit a wide range of combustion processes. Both the reaction mechanism from Glaude et al. and Sun et al. (hereafter referred to as the Glaude model and Sun model, respectively) were designed to study DMC as an oxygenate additive in diesel combustion. The Glaude model contains 102 and 257 species, and the Sun model includes 802 and 1563 reactions. GRI-Mech 3.0 [22] and San Diego Mech [25] were chosen owing to their versatility in various combustion processes; whereas the Glaude model and the Sun model were selected because they include DMC. DMC is a commonly used electrolyte solvent that can be vented from failing LIBs [8,12].

The explosion characteristics of the simplified gas mixture were designed to resemble those of the generic Li-ion gas over a range of fuel–air equivalence ratios. Hydrogen (H_2) and methane (CH_4) were chosen as the simplified gas species owing to their high and low LBV and low and high constant volume explosion pressure, respectively. We determined the concentrations of H_2 and CH_4 in the simplified gas by matching its LBV and the explosion pressure to those of the generic Li-ion gas for a fuel–air equivalence ratio between 0.5 and 1.7. GRI-Mech 3.0 was used to calculate the combustion properties for both gas

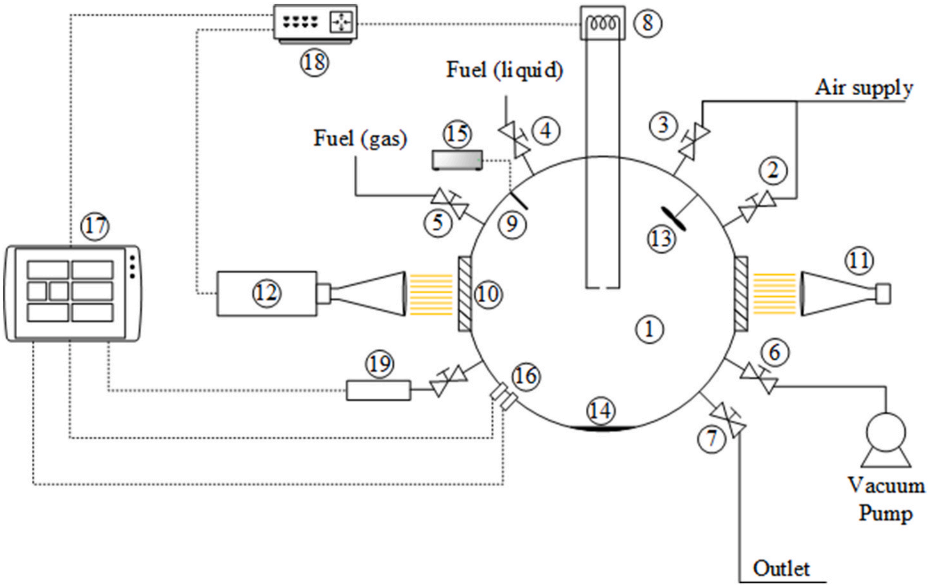

Fig. 1. Schematic of the experimental setup [28]. 1: explosion chamber; 2: oxidizer inlet; 3: flush inlet; 4: fuel (liquid) injection port; 5: fuel (gas) inlet; 6: vacuum port; 7: gas outlet; 8: ignition system; 9: thermocouple; 10: glass windows (100 mm); 11: LED light source; 12: high-speed camera; 13: stirrer; 14: heating plate; 15: ambient temperature display; 16: dual explosion pressure sensors; 17: data acquisition system; 18: control/trigger unit and 19: ambient pressure sensor.

mixtures. With a concentration of 35% and 65% of H_2 and CH_4, respectively, the simplified mixture matched the generic Li-ion gas reasonably. Fig. 2 depicts the calculated values of LBV and the closed volume explosion pressure in the generic Li-ion gas and the simplified mixture.

Further, the coefficient of determination (R^2) and the standard deviation of the error (SDE) were calculated to quantify the comparison of reaction mechanisms and the experimental result. These terms are commonly used in regression analysis to determine the “goodness of fit.” Table 3 summarizes the variables and equations used to calculate R^2 and SDE.

2.1. 3. Results

Table 5 summarizes the averaged results of the high LBV Li-ion gas mixture. As predicted, the highest recorded values exist on the fuel-rich side, wherein the fuel–air equivalence ratio (φ) > 1. The highest value of LBV recorded at φ = 1.4 is 1055 mm s^{-1}. Furthermore, the maximum laminar flame speed is 7153 mm s^{-1} at φ = 1.30; and the maximum explosion pressure and the maximum rate of explosion pressure rise are 0.78 MPa and 82.88 MPa s^{-1}, respectively, at φ = 1.20. However, the maximum explosion pressure is nearly identical for φ = 1.10 and φ = 1.20, with a difference of 0.03 kPa.

Table 6 summarizes the averaged results of the low LBV Li-ion gas mixture. The highest laminar burning velocity and laminar flame speed recorded at φ = 1.10 are 351 mm s^{-1} and 2266 mm s^{-1}, respectively. Additionally, the maximum explosion pressure and the maximum rate of explosion pressure rise measured at φ = 1.0 are 0.72 MPa and 25.34 MPa s^{-1}, respectively. Moreover, an average difference of 4 kPa is observed in the maximum explosion pressure between φ = 1.00 and φ = 1.10.

Table 3

Description of variables and equations used to calculate the coefficient of determination (R^2) and the standard deviation of the error (SDE).

Description	Variable and Equation
Experimental data value	Y
Mean experimental data value	$\overline{Y}$
Value calculated from reaction mechanism	$\widehat{Y}$
Number of data points	n
Sum of squared errors	$SSE = \sum_i (Y_i - \widehat{Y}_i)^2$
Sum of squared residuals	$SSR = \sum_i (\widehat{Y}_i - \overline{Y})^2$
Coefficient of determination	$R^2 = \frac{SSR}{SSE + SSR}$
Standard deviation of the error	$SDE = \sqrt{\left(\frac{SSE}{n-2}\right)}$

Table 7 summarizes the averaged results calculated for the generic Li-ion gas mixture. Herein, the highest laminar burning velocity (482 mm s^{-1}) is recorded slightly on the fuel-rich side (φ = 1.10), which concurs well with the preliminary calculation (Fig. 2). The highest laminar burning velocity and laminar flame speed recorded at φ = 1.10 are 484 mm s^{-1} and 3343 mm s^{-1}, respectively. Furthermore, the maximum explosion pressure and maximum rate of explosion pressure rise are 0.75 MPa and 35.81 MPa s^{-1}, respectively, at φ = 1.00.

Table 8 summarizes the averaged results of the simplified gas mixture, wherein the highest laminar burning velocity and laminar flame speed recorded at φ = 1.10 are 506 mm s^{-1} and 3751 mm s^{-1},

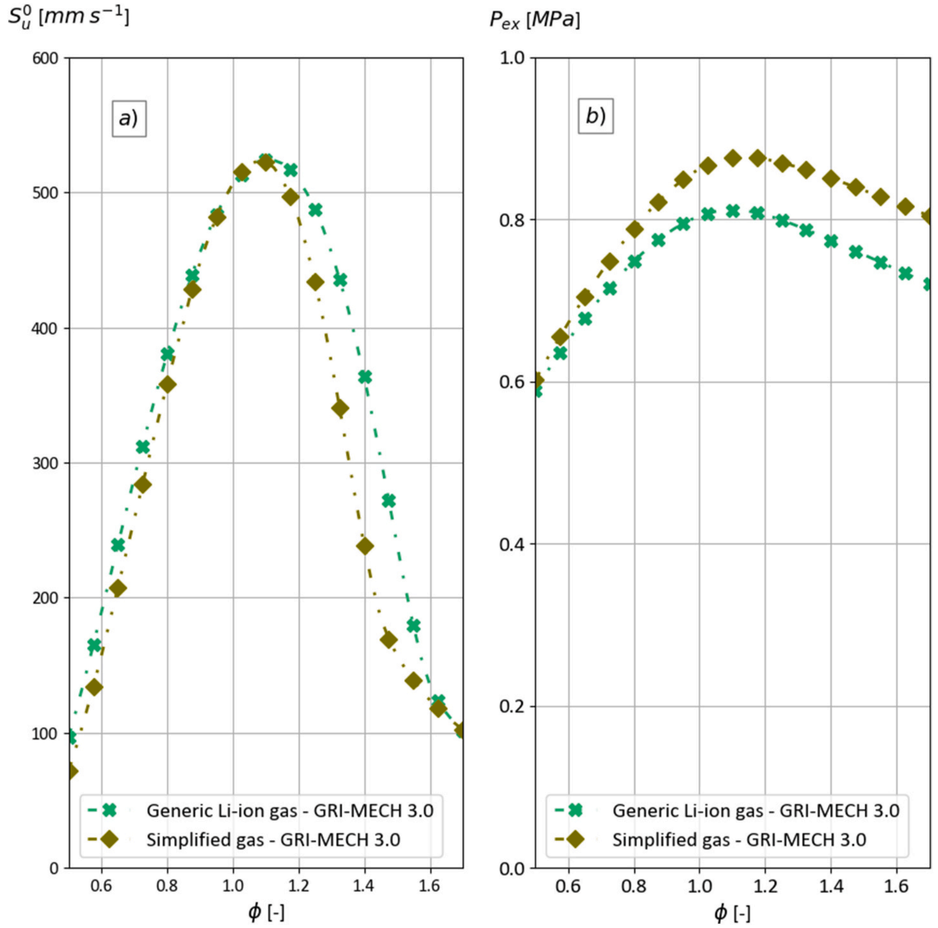

Fig. 2. Comparison of the calculated combustion properties of a generic Li-ion gas and the generated simplified gas. a): Comparison of the laminar burning velocity. b): Comparison of the explosion pressure.

Table 5

Laminar flame speed, Markstein length, laminar burning velocity, maximum explosion pressure, and maximum rate of explosion pressure rise measured for the high LBV Li-ion gas mixture at 300 K and 100 kPa absolute.

Fuel–air equivalence ratio	Laminar flame speed (S^{o}_{b}) [mm s^{-1}]	Markstein length (L_b) [mm]	Laminar burning velocity (S^{o}_{u}) [mm s^{-1}]	Maximum explosion pressure (P_{ex}) [MPa]	Maximum rate of explosion pressure rise $(dp/dt)_{ex}$ [MPa s^{-1}]
0.70	2939	−0.09	482	0.70	44.29
0.80	4071	0.21	627	0.74	59.81
0.90	5061	0.37	745	0.76	70.99
0.99	5965	0.46	852	0.77	77.15
1.10	6573	0.51	935	0.78	81.68
1.20	6984	0.52	1002	0.78	82.80
1.30	7152	0.52	1044	0.78	81.29
1.40	7101	0.53	1055	0.77	76.81

Table 6

Laminar flame speed, Markstein length, laminar burning velocity, maximum explosion pressure, and maximum rate of explosion pressure rise measured for the low LBV Li-ion gas mixture at 300 K and 100 kPa absolute.

Fuel–air equivalence ratio	Laminar flame speed (S^{o}_{b}) [mm s^{-1}]	Markstein length (L_b) [mm]	Laminar burning velocity (S^{o}_{u}) [mm s^{-1}]	Maximum explosion pressure (P_{ex}) [MPa]	Maximum rate of explosion pressure rise $(dp/dt)_{ex}$ [MPa s^{-1}]
0.80	1750	−0.31	292	0.67	21.26
0.90	2087	0.05	332	0.70	24.61
1.00	2256	0.12	347	0.71	25.10
1.10	2266	0.31	351	0.71	22.59
1.20	2087	0.44	333	0.69	18.18
1.30	1792	0.80	295	0.66	13.49

Table 7

Laminar flame speed, Markstein length, laminar burning velocity, maximum explosion pressure, and maximum rate of explosion pressure rise measured for the generic Li-ion gas mixture at 300 K and 100 kPa absolute.

Fuel–air equivalence ratio	Laminar flame speed (S^{o}_{b}) [mm s^{-1}]	Markstein length (L_b) [mm]	Laminar burning velocity (S^{o}_{u}) [mm s^{-1}]	Maximum explosion pressure (P_{ex}) [MPa]	Maximum rate of explosion pressure rise $(dp/dt)_{ex}$ [MPa s^{-1}]
0.70	1809	−0.36	306	0.66	22.00
0.80	2428	−0.09	384	0.70	29.40
0.90	2969	0.15	446	0.74	34.91
1.00	3308	0.31	479	0.75	35.79
1.10	3316	0.42	479	0.74	32.89
1.20	3051	0.61	451	0.74	27.66
1.30	2559	1.04	388	0.71	20.28
1.40	1900	2.19	295	0.68	11.69
1.50	1453	8.27	231	0.62	6.33
1.59	910	11.45	148	0.49	2.91

respectively. Additionally, the maximum explosion pressure recorded at $\varphi = 1.10$ (0.81 MPa) is only 1 kPa higher than that measured at $\varphi = 1.00$. The highest value of the maximum rate of explosion pressure rise recorded at $\varphi = 1.00$ is 39.66 MPa s^{-1}.

Table 9 presents the R^2 and SDE values determined using the experimental results and the theoretical calculations with the four reaction mechanisms using the equations in Table 3. The predictions of LBV by both GRI-Mech 3.0 and the Glaude model for the high LBV Li-ion concur well with the experimental results based on their calculated R^2 and SDE value. Moreover, the San Diego Mech and the Sun model obtained reasonable R^2 and SDE values, although they underestimate the LBV for $\varphi > 1.1$ (Fig. 3a).

Table 8

Laminar flame speed, Markstein length, laminar burning velocity, maximum explosion pressure, and maximum rate of explosion pressure rise calculated for the binary gas mixture at 300 K and 100 kPa absolute.

Fuel–air equivalence ratio	Laminar flame speed (S^{o}_{b}) [mm s^{-1}]	Markstein length (L_b) [mm]	Laminar burning velocity (S^{o}_{u}) [mm s^{-1}]	Maximum explosion pressure (P_{ex}) [MPa]	Maximum rate of explosion pressure rise $(dp/dt)_{ex}$ [MPa s^{-1}]
0.70	1623	−0.22	264	0.67	16.48
0.80	2450	−0.11	370	0.73	26.56
0.90	3223	0.27	455	0.78	35.05
1.00	3680	0.51	498	0.80	39.32
1.10	3751	0.55	506	0.81	37.60
1.20	3391	0.99	464	0.79	30.56
1.30	2636	1.80	369	0.76	19.26
1.38	1810	3.23	257	0.74	11.54
1.49	1194	8.58	174	0.62	5.35

Table 9

The calculated coefficient of determination (R^2) and standard deviation of the error (SDE) based on experimental laminar burning velocity (LBVs) and the LBVs predicted by the four different reaction mechanisms.

Fuel composition	GRI-Mech. 3.0	San Diego Mech	Glaude model	Sun model
	Coefficient of determination (R^2) [−]			
High LBV Li-ion gas	0.997	0.974	0.990	0.957
Low LBV Li-ion gas	0.547	0.720	0.585	0.970
Generic Li-ion gas	0.860	0.984	0.687	0.952
Simplified gas	0.990	0.972	0.772	0.950
	Standard deviation of the error (SDE) [mm s^{-1}]			
High LBV Li-ion gas	11.55	28.39	20.55	37.44
Low LBV Li-ion gas	60.96	20.42	38.93	4.50
Generic Li-ion gas	47.71	13.74	81.77	21.97
Simplified gas	12.09	19.94	78.89	26.15

Conversely, only the Sun model predicts LBVs that results in high R^2 and low SDE values for the low LBV Li-ion gas; the other three reaction mechanisms, particularly the GRI-Mech 3.0 and the Glaude model overestimate the LBV, as illustrated in Fig. 3b.

Furthermore, the LBV predictions of the San Diego Mech and Sun model concur well with the experimental results of the generic Li-ion gas. All reaction mechanisms predict the LBVs accurately when $\varphi < 1$; however, as φ increases, both the GRI-Mech 3.0 and Glaude model overpredict the LBV (Fig. 3c).

Finally, the LBV predictions of GRI-Mech 3.0 concur best with the experimental results of simplified gas based on the calculated R^2 and SDE values (Table 9). Additionally, both the San Diego Mech and Sun model predict the simplified mixture reasonably well, as presented in Table 9 and Fig. 3 d. However, the Glaude model overestimates the LBV in comparison with the experimental results when $\varphi > 0.9$.

2.2. 4. Discussion

3.1.1. 4.1 Experimental uncertainties and observations

Thermal diffusion, hydrodynamic instabilities, and buoyancy may influence the flame propagation, generating uncertainties in the measured LBV [17,18]. Although no hydrodynamic instabilities caused by pressure changes or buoyancy instabilities are observed in the

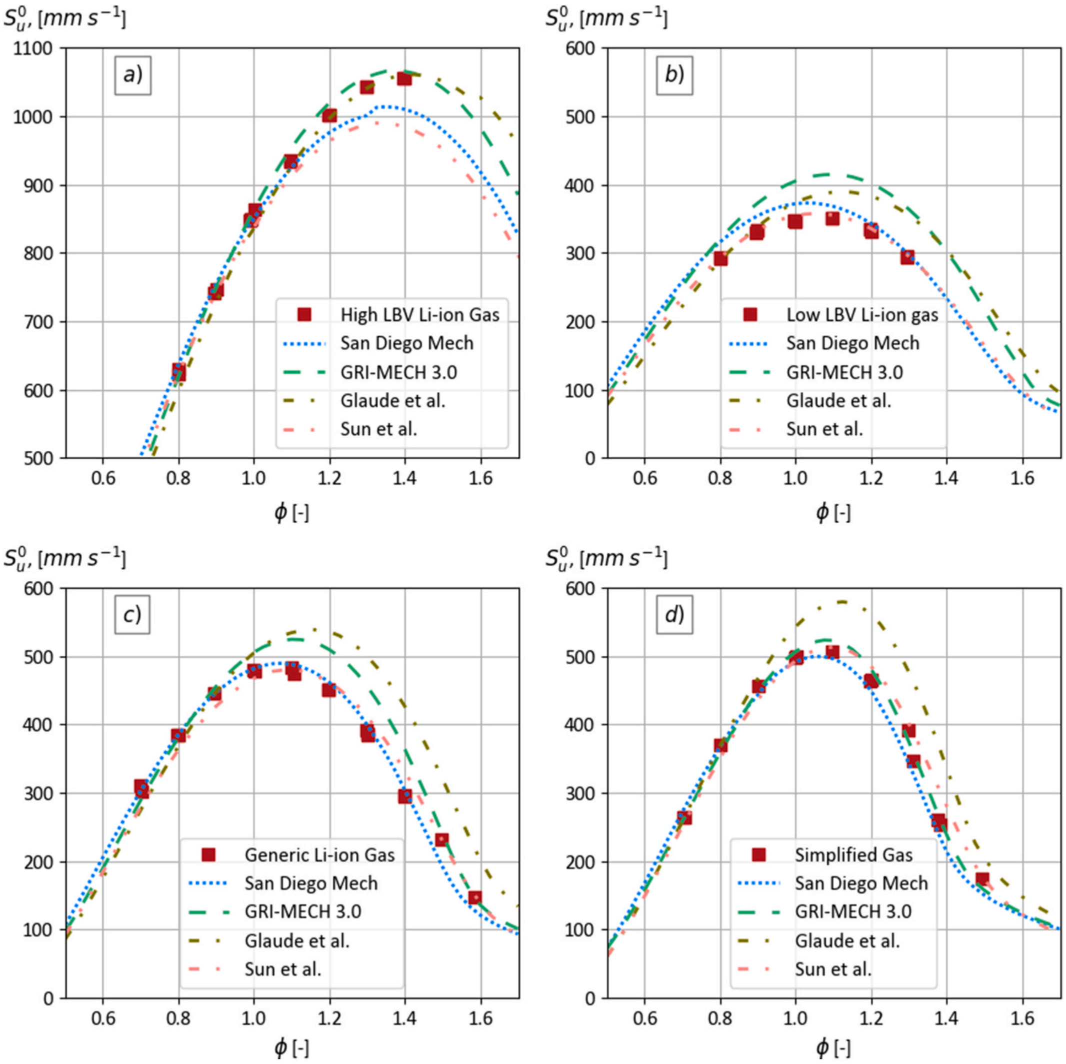

Fig. 3. Comparison of the predicted laminar burning velocity (LBV) using the four reaction mechanisms and the measured LBVs of a) the high LBV Li-ion gas mixture, b) the low LBV Li-ion gas mixture, c) the generic Li-ion gas mixture, and d) the simplified gas mixture.

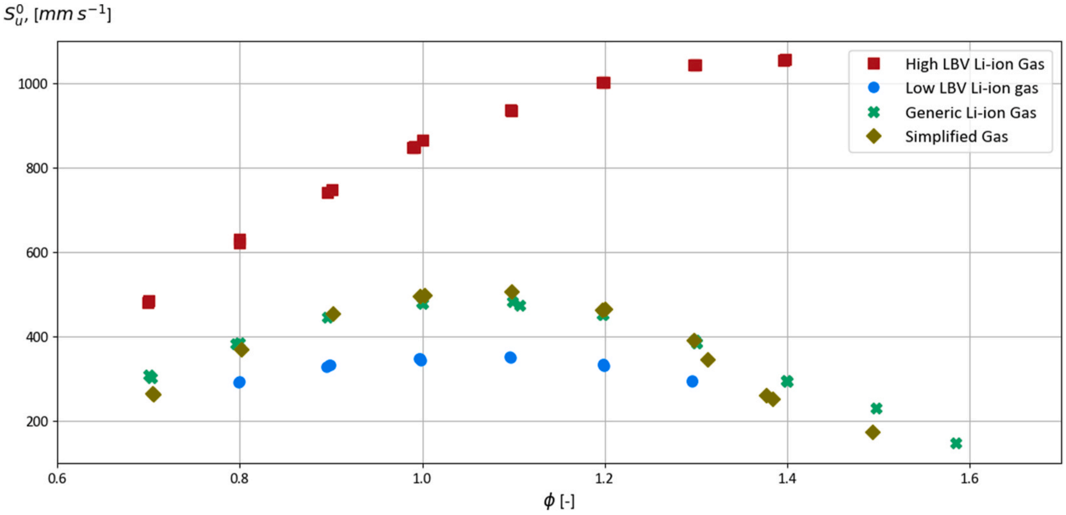

Fig. 4. Experimental laminar burning velocities obtained from four different gas compositions.

high-speed video of the experiments, minor front instabilities are observed in certain experiments on the far fuel-rich and fuel-lean sides. These can be attributed to thermal diffusion or ignition-induced instabilities. Moreover, the three mixtures with more than two species exhibited a higher tendency of front instabilities. Most of these front instabilities can be eliminated by adjusting the spark gap distance. However, the three gas compositions are significantly more sensitive to the spark gap distances than the simplified gas. To reduce the uncertainties, experiments with a flame front that does not propagate spherically are rejected. Moreover, parallel experiments are performed for nearly all concentrations to reduce the uncertainties in the experimental results further. However, only minor changes are observed in the LBV between two parallel experiments, as illustrated in Fig. 4.

The wide range of LBV observed between the gas compositions (Fig. 4) indicate that certain species influence the LBV significantly. The maximum LBV of the low LBV Li-ion gas is 351.4 mm s^{-1}, whereas that of the high LBV Li-ion gas is approximately three times higher at 1055.5 mm s^{-1}. Furthermore, pure H_2 has an LBV of approximately 2900 mm s^{-1} at a similar temperature and pressure [33,34]. The maximum LBV of a gas mixture with 5% H_2 and 95% CO is approximately 650 mm s^{-1} [35]. As the high LBV Li-ion gas comprises approximately 80% of H_2 and CO, a high LBV is expected. Additionally, CO_2 is an inert gas with a relatively high specific heat, which can reduce the amount of heat released from the combustible gas [36]. Consequently, an increase in the CO_2 concentration can lower the LBV. Therefore, as the low LBV Li-ion gas comprises approximately 50% CO_2, a low LBV is expected.

3.1.2. 4.2 LBV prediction accuracy of the reaction models

In this section, the LBV predictions of the four reaction models are compared to the experimentally obtained LBVs. A typical evaluation of reaction models is very compressive. The chemistry and reaction rates of gas mixtures must be analyzed [18,27]. In this study, however, we only perform a statistical analysis and compare the results with those reported in other similar studies to evaluate the LBV prediction accuracy of the reaction models.

A considerable discrepancy is observed in the prediction of the Glaude model in comparison with the experimental results. Except in the case of the experiment on the high LBV Li-ion gas, the Glaude model overestimates the LBV when $\varphi > 0.9$ in all other experiments. Additionally, previous studies have reported that the Glaude model deviates from experimentally obtained LBVs [27,31,37,38]. For instance, Bardin et al. [37] reported that the Glaude model over-predicts the LBV significantly in the case of methanol, ethanol, and DMC. Moreover, several studies [27,31,38] revealed similar results for the LBV of DMC. However, the Glaude model estimating the LBV of the high LBV Li-ion gas accurately (Fig. 3 and Table 9) could be attributed to the mixture composition, which primarily comprises H_2 and carbon monoxide (CO).

The GRI-Mech 3.0 model predicts the LBV for the high LBV Li-ion gas and simplified gas with the highest accuracy (Table 9 and Fig. 3). The high LBV Li-ion gas predominantly comprises H_2 and CO (approximately 80%), whereas the simplified gas comprises H_2 and CH_4 in the ratio of 35% and 65%, respectively. Although GRI-Mech 3.0 is developed for natural gas combustion, several experimental studies [35,39–41] reported that the model predicts the LBV for different syngas mixtures accurately. For instance, Wang et al. [35] reported that the GRI-Mech 3.0 predicts the LBV of gas mixtures comprising 95% CO and 5% H_2 with acceptable accuracy. Furthermore, the results of McLean et al. [41] on the LBV study of syngas mixture (50% CO and 50% H_2) are accurately predicted by the GRI-Mech 3.0 [22]. Both Rozenchan et al. [39] and Boushaki et al. [40] reported that the GRI-Mech 3.0 predicts the LBV for CH_4 accurately in several experiments under normal initial conditions. As the fuel composition of the high LBV Li-ion gas and the simplified gas are variations of the syngas and natural gas composition, respectively, the GRI-Mech 3.0 estimates the LBVs with an acceptable precision.

Conversely, the GRI-Mech 3.0 overestimates the LBVs of the low LBV Li-ion gas and the generic Li-ion gas. The discrepancy can be attributed to the higher CO_2 concentration as CO_2-rich mixtures exhibit higher heat loss owing to the thermal radiation. Typically, heat losses in a propagating flame reduce the propagation speed, which is not considered in the theoretical calculations, as it assumes adiabatic conditions. However, Yu et al. [42] studied the effect of thermal radiation on the LBV numerically and determined that the uncertainty is low, particularly for fuels diluted using species with strong radiative reabsorption properties. Thus, Yu et al. determined that the flame propagation speed increases when the fuel is diluted with up to 20% CO_2. Consequently, the increased radiative heat loss in the flame generated by the increased CO_2 is re-absorbed by the unburnt fuel. GRI-Mech 3.0 tends to over-predict the LBV as the CO_2 concentration increases in the fuel. Furthermore, Zahedi et al. [36] reported that the GRI-Mech 3.0 predicts slightly higher estimates of the LBV for 10% diluted CH_4 and 20% CO_2. Furthermore, the over-estimated LBVs in their study exists in a similar equivalence ratio range for the generic Li-ion gas with 20% CO_2.

Further, based on the R^2 values calculated using the San Diego Mech (Table 9), the model predictions concur well with the experimental results for all mixtures except the low LBV Li-ion mixture. Although the R^2 value is high for the high LBV Li-ion gas, Fig. 3 a) indicates that San Diego Mech under-estimates the LBV for $\varphi > 1.1$; the peak difference is 55 mm s^{-1} at $\varphi = 1.4$. By contrast, the peak difference between the LBV predicted by the San Diego Mech for the low LBV Li-ion gas and the experimentally obtained LBV is 25 mm s^{-1} with an R^2 value of 0.72. Additionally, the SDE (Table 9) determined indicates that the discrepancy between calculations and experimental results is large in the case of high LBV Li-ion gas than that of the low LBV Li-ion gas. Nilsson et al. [43] reported that the scatter between CH_4 LBV experiments is less than 20 mm s^{-1} based on the results observed over the last 15 years. Furthermore, the average deviance between the San Diego Mech predictions and the actual LBV of the low LBV Li-ion gas is 18 mm s^{-1}, which exists in the same range as the experimental uncertainty identified by Nilsson et al. Therefore, the San Diego Mech model designed to suit a broad range of combustion applications [25] ensures relatively reasonable predictions of the experimental LBV.

In comparison with the other reaction mechanisms, the Sun model is the most consistent with R^2 values, which are higher than 0.95 for all mixtures. However, similar to the San Diego model, the Sun model exhibits issues in predicting the LBV for high LBV Li-ion gas (Fig. 3a), wherein the largest deviance is 71 mm s^{-1} with average deviance of 27.4 mm s^{-1}. The reaction mechanism of the Sun model comprises 257 species and 1563 reactions, which renders this the most comprehensive model owing to the size. The second-largest reaction mechanism is the Glaude model with 102 species and 802 reactions. Typically, the computational time increases significantly owing to the detailed mechanism involved in the model despite higher prediction accuracy. Therefore, the Sun model requires 80 times longer computational time than the other reaction mechanisms.

An advantage of the Glaude and Sun models is that they contain the electrolyte solvent DMC. Although the studies in Table 1 do not report DMC or any other electrolyte solvent, a study by Roth et al. [8] reported 11.5% solvent in the vented gas from a failing LIB. Fernandes et al. [12] detected 42% DMC and 17% ethyl methyl carbonate (EMC) in the vented gas composition during overcharge abuse testing. These studies prove that electrolyte solvents, such as DMC can be present in the gases vented from an LIB. Furthermore, previous studies have reported that the Sun model predicts the LBV with high accuracy for pure DMC at normal conditions [31,38].

As shown, the different reaction models may yield different results when used to predict combustion properties intended for safety engineering models and as input to CFD. Although we identified certain discrepancies in LBV predictions, the uncertainties in models and CFD simulation can be substantially larger than the deviations between these reaction models.

3.1.3. 4.3 Ideal reaction mechanisms for different gas compositions

As indicated in Table 1, different SOC and chemistry can yield different gas compositions during an LIB failure. The experimental results (Fig. 3 and Table 9) verify that all reaction models over- or under-predict the LBV for the gas compositions listed in Table 2. Therefore, to predict the LBV accurately, we recommend selecting a reaction model based on the CO_2 concentration in the gas composition. Although the GRI-Mech 3.0 predicts the gas compositions with a low CO_2 concentration accurately, the LBV for gas compositions with 20% and higher CO_2 are over-predicted. Furthermore, both the San Diego Mech and Sun Model perform well in predicting the LBV for gas compositions with a CO_2 concentration above 20%. Based on the R^2 and SDE values (Table 9), we conclude that the San Diego Mech and Sun model perform better for gas composition with moderate and high concentrations of CO_2, respectively. Table 10 presents the method of choosing a reaction model to predict LBVs considering the CO_2 concentration in the gas compositions as a criterion. Fig. 5 illustrates the estimated LBVs for the different gas compositions (Tables 1 and 2) based on the details presented in Table 10. However, the criteria (Table 10) may be valid only for the gas compositions listed in Table 2. If a conservative estimation of LBVs is essential, GRI-Mech 3.0 can be considered as an ideal choice than the recommendations presented in Table 10.

The high and low LBV Li-ion gases are based upon cell type NCA-MJ1 [13] and one of the LFP batteries [16], respectively, with certain minor changes in the gas compositions. We remove the acetylene (C_2H_2) and ethane (C_2H_6) from the NCA-MJ1 owing to their low concentrations, and the other concentrations are adjusted accordingly. Fig. 5 illustrates a slight discrepancy between the NCA-MJ1 and the high LBV Li-ion gas owing to the lower H_2 concentration and the removed C_2H_2, which results in slightly lower LBV in the case of high LBV Li-ion gas. Conversely, the concentrations are reasonably identical ($\pm 0.2\%$) in the case of the compositions of low LBV Li-ion gas and the LFP, resulting in identical estimations of LBV (Fig. 5).

3.1.4. 4.4 Challenges in generating a simplified Li-ion gas

The simplified gas is generated based on the combustion properties calculated using the GRI-Mech 3.0. As presented in Fig. 3c) and Table 9, the GRI-Mech 3.0 do not predict the LBV for the generic Li-ion gas accurately. Based on these results, we conclude that both reaction mechanisms should have been used in the preliminary calculations; while the San Diego Mech is ideal for the generic Li-ion gas calculation, the GRI-Mech 3.0 can be used for the calculations of the simplified gas. These two mechanisms can predict the LBV with enhanced accuracy (Fig. 6).

However, despite the increase in the LBV prediction accuracy, the specie composition of the simplified gas will remain the same. This implies that if the LBV in simplified gas is lowered by reducing the H_2 concentration, the explosion pressure increases owing to the increase in CH_4, which further increases the discrepancy in closed volume explosion pressure. Moreover, the simplified gas can resemble the generic Li-ion gas to a certain extent using only two species. If a higher level of resemblance is required, a third inert component, such as CO_2 must be added. Additionally, the discrepancy between the calculated and the experimentally obtained explosion pressures can be attributed to the heat losses in the explosion sphere.

Table 10
Recommendation for choosing a reaction mechanism to predict laminar burning velocities of the gases vented from Li-ion batteries based on the carbon dioxide (CO_2) concentration in gas compositions.

Reaction mechanism	CO_2 concentration	Gas mixture
GRI-Mech 3.0	Less than 15%	Simplified, High LBV
San Diego Mech	Between 15% and 40%	Generic
Sun model	Above 40%	Low LBV

The simplified gas generated resembles the generic Li-ion gas only in terms of combustion properties. In actual experiments, gas dispersion and mixing with air are essential factors. For instance, the flow in the gravity current relies on the density difference [44]. The simplified gas and the generic Li-ion gas have a density of 0.45 kg m^{-3} and 0.86 kg m^{-3}, respectively, at 300 K and 100 kPa. As the simplified gas is lighter than the generic Li-ion gas, the dispersion will differ. However, the temperature of the gas released from a failing Li-ion battery is expected to be higher than 300 K. An increase in temperature reduces the density of the vented gas. Consequently, the combustion properties of the gas are altered. Therefore, matching both density and combustion properties of a vented Li-ion gas requires the knowledge of release temperature and species composition. Based on the results of this study, a non-toxic "pseudo" or "simplified" gas that reproduces the required properties can be designed using theoretical calculations.

4.0 5. Conclusions

To evaluate the explosion hazards related to gas vented from failed LIBs, we determined the Markstein length, laminar flame speed, LBV, maximum explosion pressure, and maximum rate of explosion pressure rise for various concentrations of three gas compositions and one pseudo (simplified) Li-ion gas. The high LBV Li-ion gas exhibited the highest measured LBV of 1055 mm s^{-1} owing to the high content of hydrogen and carbon monoxide. Conversely, the low LBV Li-ion gas comprised more than 50% carbon dioxide, which significantly decreased the LBV; the maximum measured LBV for the low LBV Li-ion gas was 351 mm s^{-1}. The experimental results are considered novel and can be used in risk assessments of battery installations.

The measured LBV was compared with the predictions of four reaction mechanisms, namely the GRI-Mech 3.0, San Diego Mech, Glaude model, and Sun model. Among these, the Sun model exhibited the highest coefficient of determination (R^2) based on the measured LBVs. However, in comparison with the other models, the highest discrepancy in the LBV prediction of high LBV Li-ion gas was observed in the Sun model, wherein the value was under-predicted by 71 mm s^{-1}. The GRI-Mech 3.0 predicted the LBV with the highest accuracy for gas compositions with low CO_2 content. However, when the CO_2 content was more than 20%, the GRI-Mech 3.0 over-predicted the LBV. Furthermore, the Sun model and San Diego Mech exhibited the most accurate predictions of the LBV when the CO_2 concentrations were moderate and high, respectively. Therefore, based on the CO_2 concentration in a Li-ion gas release, the ideal reaction mechanism can be selected to predict LBVs.

The simplified gas composition was designed with combustion properties similar to that of a generic Li-ion gas. To reduce the number of species and eliminate toxic species, such as carbon monoxide, the simplified gas comprised 65% hydrogen and 35% methane. The initial calculations indicated that the LBV was nearly identical when applying the GRI-Mech 3.0 reaction model. However, the experimentally determined LBV was slightly higher in the simplified gas than that of the original generic Li-ion gas. Although, altering the simplified specie composition would not improve the combustion property resembles. This is because matching both explosion pressure and LBV was challenging based on only hydrogen and methane. However, introducing a third inert species, such as carbon dioxide, will result in nearly equal numerical results in terms of explosion pressure and LBV. Thus, a simplified gas composition can be generated conveniently using tools (Cantera) to reproduce the combustion properties of a gas vented from failed Li-ion batteries. The elimination of toxic species in the combustible gas composition, such as carbon monoxide, can improve the safety of experiments significantly.

5.0. Glossary

Laminar burning velocity is one of the most fundamental properties in premixed combustion is the and gives an insight into the distinctive

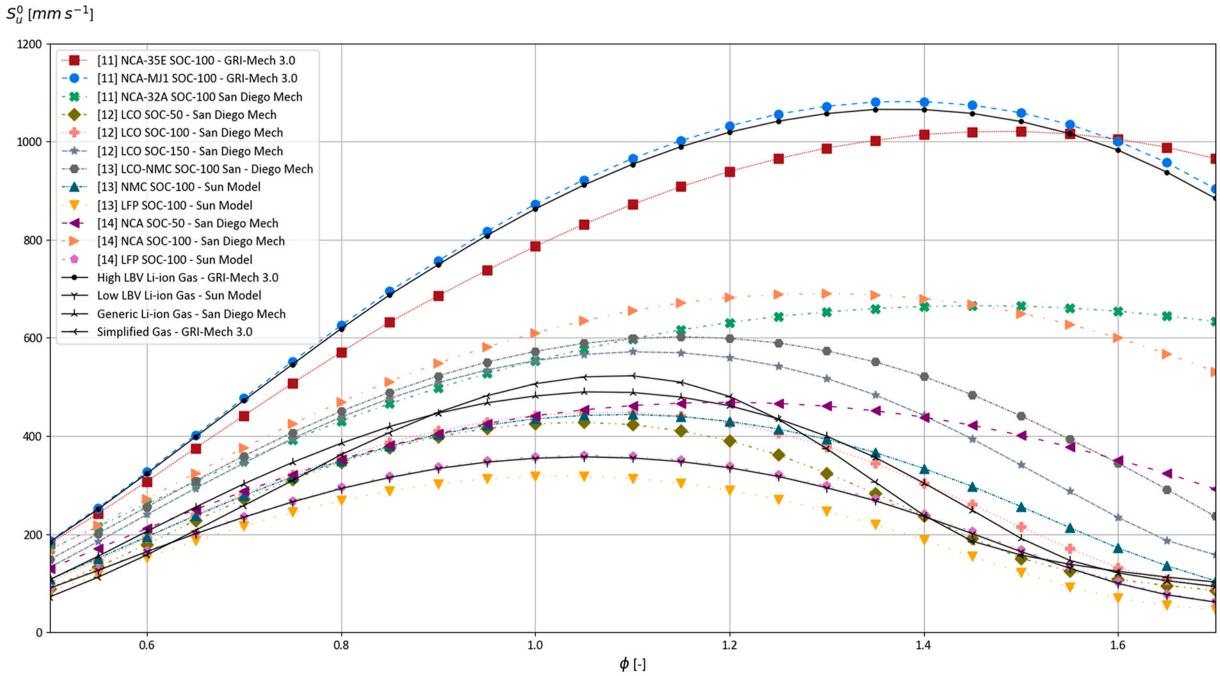

Fig. 5. Calculated laminar burning velocity for a collection of normalized gas compositions vented from Li-ion batteries during thermal abuse testing [11–14].

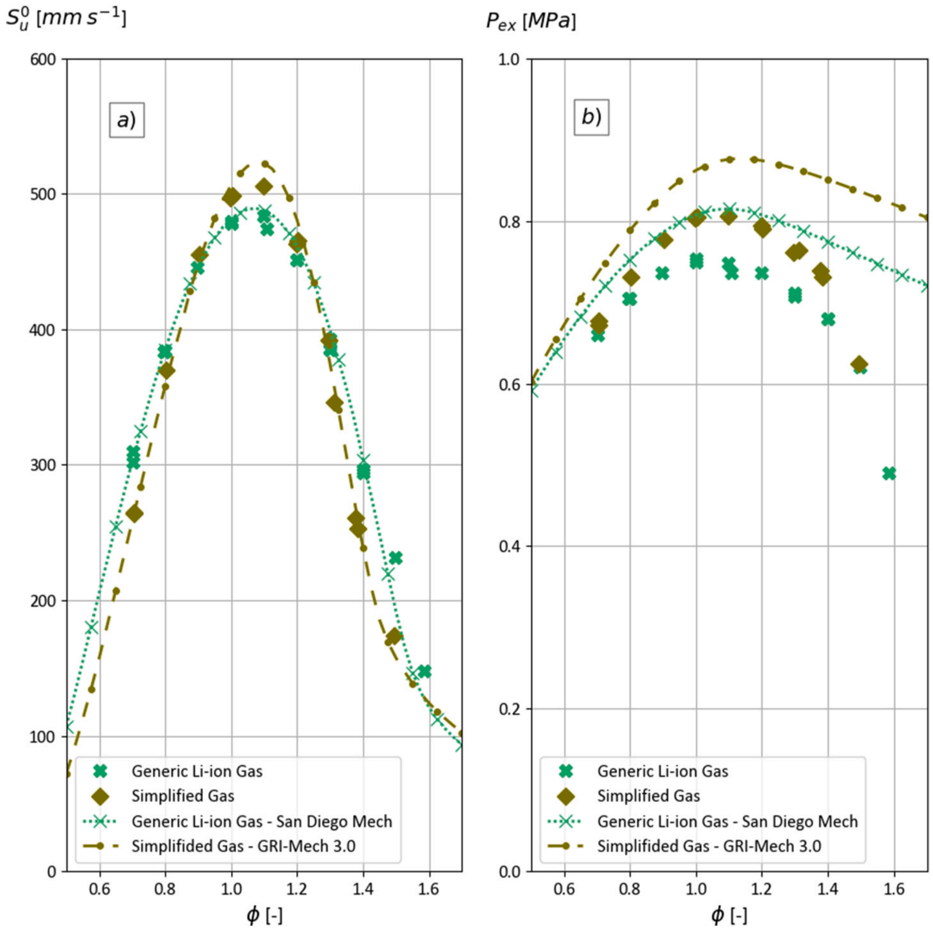

Fig. 6. Comparison of the generic Li-ion gas and the simplified gas based on experimental results, a) comparison of the laminar burning velocity, b) comparison of the close volume explosion pressure.

property of reactivity, exothermicity and in a given diffusive medium. It is defined as a planar/unstretched, adiabatic, one-dimensional velocity relative to the unburnt reactants [45].

Markstein length is a coefficient on which the effect of flame stretch/curvature has on the flame speed.

CRediT authorship contribution statement

M. Henriksen: Conceptualization, Methodology, Formal analysis, Writing – original draft, Writing – review & editing. **K. Vaagsaether:** Conceptualization, Methodology, Formal analysis, Writing – review & editing, Supervision, Funding acquisition. **J. Lundberg:** Conceptualization, Methodology, Formal analysis, Writing – review & editing, Supervision, Funding acquisition. **S. Forseth:** Formal analysis, Conceptualization, Writing – review & editing, Supervision, Funding acquisition. **D. Bjerketvedt:** Conceptualization, Methodology, Formal analysis, Writing – review & editing, Supervision, Funding acquisition.

Declaration of competing interest

The authors declare that they have no known competing financial interests or personal relationships that could have appeared to influence the work reported in this paper.

Acknowledgment

This work was performed within MoZEES, a Norwegian Centre for Environment-friendly Energy Research (FME). This work was supported by the Research Council of Norway [project number 257653]; and co-sponsored by 40 partners from the research industry and public sector.

References

[1] A. Mayyas, D. Steward, M. Mann, The case for recycling: overview and challenges in the material supply chain for automotive li-ion batteries, Sustain. Mater. Technol. 19 (2019), e00087, https://doi.org/10.1016/j.susmat.2018.e00087.

[2] D. Lisbona, T. Snee, A review of hazards associated with primary lithium and lithium-ion batteries, Process Saf. Environ. Protect. 89 (2011) 434–442, https://doi.org/10.1016/j.psep.2011.06.022.

[3] P.G. Balakrishnan, R. Ramesh, T. Prem Kumar, Safety mechanisms in lithium-ion batteries, J. Power Sources 155 (2006) 401–414, https://doi.org/10.1016/j.jpowsour.2005.12.002.

[4] A.R. Baird, E.J. Archibald, K.C. Marr, O.A. Ezekoye, Explosion hazards from lithium-ion battery vent gas, J. Power Sources 446 (2020) 227257, https://doi.org/10.1016/j.jpowsour.2019.227257.

[5] C. Mikolajczak, M. Kahn, K. White, R.T. Long, Lithium-Ion Batteries Hazard and Use Assessment, Springer US, Boston, MA, 2011, https://doi.org/10.1007/978-1-4614-3486-3.

[6] Q. Wang, P. Ping, X. Zhao, G. Chu, J. Sun, C. Chen, Thermal runaway caused fire and explosion of lithium ion battery, J. Power Sources 208 (2012) 210–224, https://doi.org/10.1016/j.jpowsour.2012.02.038.

[7] T. Lian, P.J.S. Vie, M. Gilljam, S. Forseth, Changes in thermal stability of cyclic aged commercial lithium-ion cells, ECS Trans 89 (2019) 73–81, https://doi.org/10.1149/08901.0073ecst.

[8] E.P. Roth, C.C. Crafts, D.H. Doughty, James McBreen, Advanced technology development program for lithium-ion batteries : thermal abuse performance of 18650 Li-ion cells. https://doi.org/10.2172/918751, 2004.

[9] F. Larsson, P. Andersson, P. Blomqvist, B.-E. Mellander, Toxic fluoride gas emissions from lithium-ion battery fires, Sci. Rep. 7 (2017), https://doi.org/10.1038/s41598-017-09784-z.

[10] A. Nedjalkov, J. Meyer, M. Köhring, A. Doering, M. Angelmahr, S. Dahle, A. Sander, A. Fischer, W. Schade, Toxic gas emissions from damaged lithium ion batteries—analysis and safety enhancement solution, Batteries 2 (2016) 5, https://doi.org/10.3390/batteries2010005.

[11] Q. Wang, B. Mao, S.I. Stoliarov, J. Sun, A review of lithium ion battery failure mechanisms and fire prevention strategies, Prog. Energy Combust. Sci. 73 (2019) 95–131, https://doi.org/10.1016/j.pecs.2019.03.002.

[12] Y. Fernandes, A. Bry, S. de Persis, Identification and quantification of gases emitted during abuse tests by overcharge of a commercial Li-ion battery, J. Power Sources 389 (2018) 106–119, https://doi.org/10.1016/j.jpowsour.2018.03.034.

[13] M. Lammer, A. Königseder, V. Hacker, Holistic methodology for characterisation of the thermally induced failure of commercially available 18650 lithium ion cells, RSC Adv. 7 (2017) 24425–24429, https://doi.org/10.1039/C7RA02635H.

[14] V. Somandepalli, K. Marr, Q. Horn, Quantification of combustion hazards of thermal runaway failures in lithium-ion batteries, SAE Int. J. Altern. Powertrains. 3 (2014) 98–104, https://doi.org/10.4271/2014-01-1857.

[15] A.W. Golubkov, D. Fuchs, J. Wagner, H. Wiltsche, C. Stangl, G. Fauler, G. Voitic, A. Thaler, V. Hacker, Thermal-runaway experiments on consumer Li-ion batteries with metal-oxide and olivin-type cathodes, RSC Adv. 4 (2014) 3633–3642, https://doi.org/10.1039/C3RA45748F.

[16] A.W. Golubkov, S. Scheikl, R. Planteu, G. Voitic, H. Wiltsche, C. Stangl, G. Fauler, A. Thaler, V. Hacker, Thermal runaway of commercial 18650 Li-ion batteries with LFP and NCA cathodes – impact of state of charge and overcharge, RSC Adv. 5 (2015) 57171–57186, https://doi.org/10.1039/C5RA05897J.

[17] A.A. Konnov, A. Mohammad, V.R. Kishore, N.I. Kim, C. Prathap, S. Kumar, A comprehensive review of measurements and data analysis of laminar burning velocities for various fuel+air mixtures, Prog. Energy Combust. Sci. 68 (2018) 197–267, https://doi.org/10.1016/j.pecs.2018.05.003.

[18] F.N. Egolfopoulos, N. Hansen, Y. Ju, K. Kohse-Höinghaus, C.K. Law, F. Qi, Advances and challenges in laminar flame experiments and implications for combustion chemistry, Prog. Energy Combust. Sci. 43 (2014) 36–67, https://doi.org/10.1016/j.pecs.2014.04.004.

[19] D. Bjerketvedt, J.R. Bakke, K. Van Wingerden, Gas explosion handbook, J. Hazard Mater. 52 (1997) 1–150.

[20] O.R. Hansen, P. Hinze, D. Engel, S. Davis, Using computational fluid dynamics (CFD) for blast wave predictions, J. Loss Prev. Process. Ind. 23 (2010) 885–906, https://doi.org/10.1016/j.jlp.2010.07.005.

[21] D.G. Goodwin, H.K. Moffat, R.L. Speth, Cantera: an object-oriented software toolkit for chemical kinetics, thermodynamics, and transport processes, Version 2.4, https://doi.org/10.5281/zenodo.170284, 2017.

[22] G.P. Smith, D.M. Golden, M. Frenklach, N.W. Moriarty, B. Eiteneer, M. Goldenberg, C.T. Bowman, R.K. Hanson, S. Song, W.C.G. Jr, V.V. Lissianski, Z. Qin, GRI-MECH 3.0. http://combustion.berkeley.edu/gri-mech/version30/text30.html#cite, 1999. (Accessed 18 March 2018).

[23] M. Gao, M. Bi, L. Ye, Y. Li, H. Jiang, M. Yang, C. Yan, W. Gao, Suppression of hydrogen-air explosions by hydrofluorocarbons, Process Saf. Environ. Protect. 145 (2021) 378–387, https://doi.org/10.1016/j.psep.2020.08.036.

[24] MOZEES, MOZEES, mobil. Zero emiss. Energy syst. https://www.mozees.no/, 2017. (Accessed 20 August 2019).

[25] UCSD, Chemical-Kinetic Mechanisms for Combustion Applications", San Diego Mechanism Web Page, Mechanical and Aerospace Engineering (Combustion Research), University of California at San Diego, San Diego Mech, 2016. http://combustion.ucsd.edu.

[26] P.A. Glaude, W.J. Pitz, M.J. Thomson, Chemical kinetic modeling of dimethyl carbonate in an opposed-flow diffusion flame, Proc. Combust. Inst. 30 (2005) 1111–1118, https://doi.org/10.1016/j.proci.2004.08.096.

[27] W. Sun, B. Yang, N. Hansen, C.K. Westbrook, F. Zhang, G. Wang, K. Moshammer, C. K. Law, An experimental and kinetic modeling study on dimethyl carbonate (DMC) pyrolysis and combustion, Combust. Flame 164 (2016) 224–238, https://doi.org/10.1016/j.combustflame.2015.11.019.

[28] M. Henriksen, K. Vaagsaether, A.V. Gaathaug, J. Lundberg, S. Forseth, D. Bjerketvedt, Laminar burning velocity measurements for an outwardly propagating flame of dimethyl carbonate and air mixtures, in: Proc. Ninth Int. Semin. Fire Explos. Hazards, St. Petersburg Polytechnic University Press, St. Petersburg, 2019, pp. 161–172, https://doi.org/10.18720/spbpu/2/k19-29.

[29] M. Henriksen, D. Bjerketvedt, K. Vaagsaether, A.V. Gaathaug, T. Skjold, P. Middha, Accidental hydrogen release in a gas chromatograph laboratory: a case study, Int. J. Hydrogen Energy 42 (2017) 7651–7656, https://doi.org/10.1016/j.ijhydene.2016.05.299.

[30] G.S. Settles, Schlieren and Shadowgraph Techniques: Visualizing Phenomena in Transparent Media, Springer, Berlin ; New York, 2001.

[31] M. Henriksen, A.V. Gaathaug, K. Vaagsaether, J. Lundberg, S. Forseth, D. Bjerketvedt, Laminar burning velocity of the dimethyl carbonate-air mixture formed by the Li-ion electrolyte solvent, Combust. Explos. Shock Waves 56 (2020) 383–393, https://doi.org/10.1134/S0010508220040024.

[32] J. Johnsplass, Lithium-ion Battery Safety, University of South-Eastern Norway, 2017.

[33] M. Kuznetsov, S. Kobelt, J. Grune, T. Jordan, Flammability limits and laminar flame speed of hydrogen–air mixtures at sub-atmospheric pressures, Int. J. Hydrogen Energy 37 (2012) 17580–17588, https://doi.org/10.1016/j.ijhydene.2012.05.049.

[34] G. Dayma, New insights into the peculiar behavior of laminar burning velocities of hydrogen–air flames according to pressure and equivalence ratio, Combust. Flame (2014) 7.

[35] Z.H. Wang, W.B. Weng, Y. He, Z.S. Li, K.F. Cen, Effect of H2/CO ratio and N2/CO2 dilution rate on laminar burning velocity of syngas investigated by direct measurement and simulation, Fuel 141 (2015) 285–292, https://doi.org/10.1016/j.fuel.2014.10.040.

[36] P. Zahedi, K. Yousefi, Effects of pressure and carbon dioxide, hydrogen and nitrogen concentration on laminar burning velocities and NO formation of methane-air mixtures, J. Mech. Sci. Technol. 28 (2014) 377–386, https://doi.org/10.1007/s12206-013-0970-5.

[37] M.E. Bardin, E.V. Ivanov, E.J.K. Nilsson, V.A. Vinokurov, A.A. Konnov, Laminar burning velocities of dimethyl carbonate with air, Energy Fuels 27 (2013) 5513–5517, https://doi.org/10.1021/ef401108a.

[38] S. de Persis, N. Chaumeix, Y. Fernandes, A. Bry, A. Comandini, Experimental and theoretical determination of DMC/air flame velocities, in: 11th Int. Conf. Chem. Kinet., Orleans, 2019. Poster, https://icck2019.sciencesconf.org/data/pages/ICCK_Proc_final.pdf. (Accessed 13 August 2019).

[39] G. Rozenchan, D.L. Zhu, C.K. Law, S.D. Tse, Outward propagation, burning velocities, and chemical effects of methane flames up to 60 ATM, Proc. Combust. Inst. 29 (2002) 1461–1470, https://doi.org/10.1016/S1540-7489(02)80179-1.

[40] T. Boushaki, Y. Dhué, L. Selle, B. Ferret, T. Poinsot, Effects of hydrogen and steam addition on laminar burning velocity of methane–air premixed flame: experimental and numerical analysis, Int. J. Hydrogen Energy 37 (2012) 9412–9422, https://doi.org/10.1016/j.ijhydene.2012.03.037.

[41] I.C. McLean, D.B. Smith, S.C. Taylor, The use of carbon monoxide/hydrogen burning velocities to examine the rate of the CO+OH reaction, Symp. Int. Combust. 25 (1994) 749–757, https://doi.org/10.1016/S0082-0784(06)80707-1.

[42] H. Yu, W. Han, J. Santner, X. Gou, C.H. Sohn, Y. Ju, Z. Chen, Radiation-induced uncertainty in laminar flame speed measured from propagating spherical flames, Combust. Flame 161 (2014) 2815–2824, https://doi.org/10.1016/j.combustflame.2014.05.012.

[43] E.J.K. Nilsson, A. van Sprang, J. Larfeldt, A.A. Konnov, The comparative and combined effects of hydrogen addition on the laminar burning velocities of methane and its blends with ethane and propane, Fuel 189 (2017) 369–376, https://doi.org/10.1016/j.fuel.2016.10.103.

[44] O.K. Sommersel, D. Bjerketvedt, K. Vaagsaether, T.K. Fannelop, Experiments with release and ignition of hydrogen gas in a 3m long channel, Int. J. Hydrogen Energy 34 (2009) 5869–5874, https://doi.org/10.1016/j.ijhydene.2009.02.058.

[45] C.K. Law, Combustion Physics, Cambridge University Press, Cambridge ; New York, 2006.

Article D

Simulation of a Premixed Explosion of Gas Vented During Li-Ion Battery Failure

Submitted to the Fire Safety Journal, on the 07 of April 2021.

SIMULATION OF A PREMIXED EXPLOSION OF GAS VENTED DURING LI-ION BATTERY FAILURE

Mathias Henriksen [a,*], Knut Vaagsaether [a], Joachim Lundberg [a], Sissel Forseth [b], Dag Bjerketvedt [a]

[a] Faculty of Technology, Natural Sciences and Maritime Sciences, University of South-Eastern Norway, Kjølnes Ring 56, Porsgrunn, 3901, Norway
[b] Norwegian Defence Research Establishment (FFI), Oslo, Norway
***Corresponding author email:** mathias.henriksen@usn.no*

ABSTRACT

Several fires and explosions caused by Lithium-ion batteries (LIBs) have been reported in the last decades. If a LIB is thermally, electrically, or mechanically abused, it can cause a catastrophic failure of the LIB. Flammable gases such as hydrogen, carbon monoxide, and methane can be released from the LIB during a catastrophic failure. When these gases mix with air, they form a combustible mixture, which may cause explosions and fires. This study presents a computational fluid dynamic (CFD) method for simulating an explosion from gases vented from failing LIBs using only open-source software. The code *mech2Foam* was used to generate the required CFD input parameters for a Li-ion vent gas composition, which was then used in several CFD simulations of an explosion in a 1-meter rectangular channel. The simulation results were compared with experimental results as a validation of the method and the CFD model. The CFD simulation results agreed well with the experimentally measured flame front position and the maximum explosion pressure. However, discrepancies between experiments and simulations were observed in the temporal pressure and flame front velocity evolution.

Keywords: Li-ion battery safety, Open-Source Software, OpenFOAM, Explosion simulation, premixed combustion

1. INTRODUCTION

Lithium-ion batteries (LIBs) are the leading energy-storing system for sustainable and emission-free energy. In a Li-ion cell, there is a combination of high energetic materials and flammable electrolyte solvent. This combination can cause a catastrophic failure of the LIB [1]. However, the probability of a single Li-ion cell failure is considered very low. Still, a single cell failure could have severe consequences for large LIB applications such as grid storage, electric vehicles, and ferries with several thousand cells. The heat released during a single cell failure can lead to cell-to-cell propagation and cause more and more cells to release toxic and flammable gas [2].

Several fires and explosions caused by LIBs have been reported in the last decades [3–5]. In April 2019, a LIB energy storage system (BESS) caught fire, likely from a single cell failure. Several hours after the fire had started, an explosion occurred inside the BESS. The BESS was severely damaged, and several firefighters were injured [6]. In July 2019, a parked electrical car caused an explosion in a private garage in Montreal, Canada. The strength of the explosion was enough to throw the garage door across the street and create a hole in the garage ceiling [7]. In October 2019, a hybrid car ferry in Norway caught fire. The cooling system for the LIB is suspected to be the cause of the fire. After the fire was extinguished, an explosion occurred in the switchboard room next to the battery room. The explosion occurred due to accumulated flammable gases vented from the damaged LIB [8].

Various events can cause a catastrophic failure of a LIB. Over-charge, over-discharge, short-circuit, cell deformation, cell puncture, heat exposure are some of the possible events that can lead to LIB failure [9,10]. During LIB failure, gases such as hydrogen (H_2), carbon monoxide (CO), carbon dioxide (CO_2), and methane (CH_4), and electrolyte solvents ((dimethyl carbonate (DMC), ethyl methyl carbonate (EMC)) can be vented [11–16]. When these gases mix with air, a combustible mixture forms that may lead to an explosion in confined and partly confined rooms/geometries [17].

Previous experimental and numerical studies have shown that gases vented from LIBs pose an explosion hazard. Somandepalli et al. [16] studied the explosion characteristics in a 20-liter explosion sphere for lithium Cobalt Oxide (LCO) cells with different states of charge (SOC). The study showed that the explosion characteristics were similar to that of hydrocarbons such as methane and propane. Baird et al. [4] estimated the lower explosive limit, explosion pressure, rate of explosion pressure rise, and the laminar burning velocity (LBV) numerically for various gas compositions vented from LIBs. The study showed that LIBs with lithium Nickel Cobalt Aluminium (NCA) cathode chemistry had a higher LBV than typical hydrocarbons, with an LBV range between 0.6 m/s to 1.1 m/s. Similar studies on the explosion characteristics and LBVs of electrolyte solvents have been published by Henriksen et al. and Johnsplass et al. [18–20].

In the last 20 years, computational fluid dynamics (CFD) simulations have been essential for risk and consequence analysis. CFD tools such as FLACS, OpenFOAM, and ANSYS Fluent have been widely used to model explosions, blast waves, and gas dispersion [21–24]. However, most CFD studies related to the LIB hazards focus on thermal analysis of a single cell or cell to cell propagation. For example, Kim et al. [25] developed a 3-dimensional finite volume method for studying the thermal runaway (TR) in cylindrical cells subjected to thermal abuse, which showed the spatial temperature distribution during cell failure. Similar CFD studies of single-cell failure have been published by Zhao et al.[26] and Kim et al. [27]. In a study by Srinivasan et al. [28], CFD and thermal modeling investigated cell to cell propagation in a multi-cell battery module. The study identified that the organic solvents vented can play a significant role in the complex process of cell-to-cell propagation.

Although the single-cell and cell-to-cell CFD analysis can explain a thermal event and TR process, the consequence of an explosion from the vented gases is not directly addressed. In a report by DNV [29], the explosion risk related to LIBs installation in the maritime sector was thoroughly examined. Their study used the commercial CFD software FLACS [30] to model the gas dispersion and explosion of a pseudo-Li-ion vent gas composition. DNV reported an explosion pressure between 90 kPa (gauge) and 270 kPa (gauge) in a partly confined geometry, with various Li-ion vent gas release profiles.

The value of CFD simulation results is dependent on the prediction accuracy of the CFD method. Therefore, the focus of this study is to develop and evaluate the prediction accuracy of a CFD method for simulating explosions from gases vented from LIBs for safety and consequence analysis. The CFD method is based upon the XiFoam model/solver in the open-source CFD toolbox OpenFOAM [31,32]. An essential parameter in this model is the species combustion, transport, and thermodynamic properties. As previous studies have shown, the gas composition released from a failing LIB can vary in types of species and concentration. Therefore, a code (*mech2Foam*) was developed to generate the required combustion, transport, and thermodynamic properties for any gas composition. The effect of gas dispersion and partly premixed combustion were excluded to limit the scope of the study. However, gas dispersion and partly premixed gas clouds should be addressed for CFD studies of a real scenario of an explosion from gases vented from a LIB.

The *mech2Foam* code was validated by comparing the results to numerical calculations using a reaction mechanism/chemical kinetics model. For evaluating the prediction accuracy of the XiFoam simulations, the maximum pressure, the temporal evolution of the pressure, flame front position, and flame front velocity were qualitative compared with experimental results of premixed gas explosions in a 1-meter explosion channel. Finally, the initial conditions of the CFD simulations and experiments were typical atmospheric conditions at 293 K and 101.3 kPa (absolute).

2. MATERIALS AND METHOD

2.1. Experimental Setup

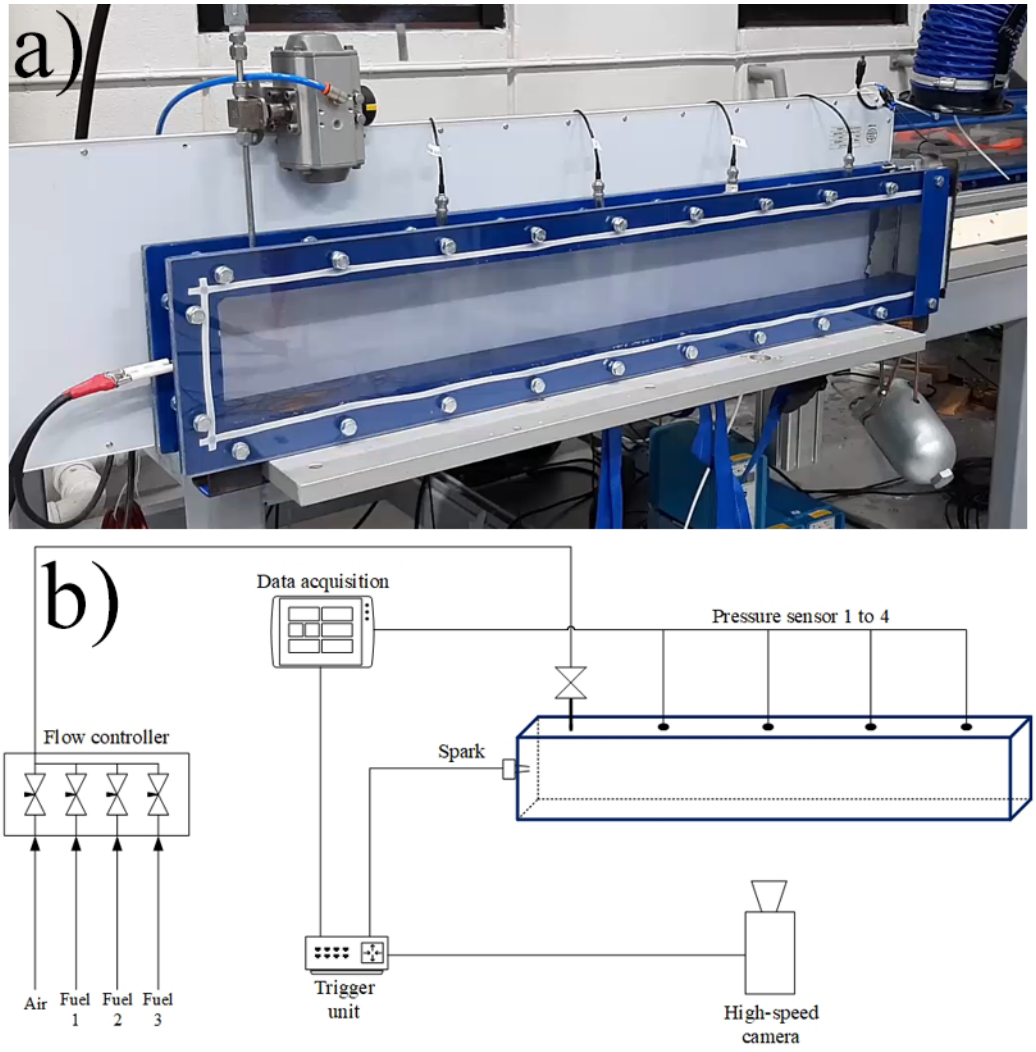

Figure 1. Photo and schematic illustration of the experimental setup. (a): Photo of the 1-meter explosion channel; (b): Schematic illustration of the experimental setup.

Figure 1 shows a photo of the 1-meter explosion channel and a schematic illustration of the experimental setup. The channel's inner length, width, and height are 1000.0 mm, 65.0 mm, and 116.5 mm, respectively. At the top of the channel, 50 mm from the closed end, is the inlet for premixed fuel and air. Four calibrated rotameters control the volume flow of fuel and air into the channel. The channel volume was exchanged eight times to ensure a homogeneous mixture. There is a porous lid in the channel's open-end during filling to avoid gravity currents and stratification. After filling the channel with premixed fuel and air, a pneumatic controlled valve stops the flow.

The ignition is delay by one minute to reduce convective flow in the channel. After the one-minute delay, the porous lid is released, immediately followed by ignition. The ignition has a duration of 0.02 s, which gives two sparks produced by an AC transformer with an output voltage of 10 kV and a current of 20 mA. Four Kistler 7001 pressure transducers mounted on the top of the channel record the explosion pressure. The first pressure transducer is located 250 mm from the closed end of the channel, with an equal interval of 200 mm between the three following pressure transducers. A Photron SA-1 high-speed camera records the flame propagation with a frame rate between 2000 and 5000 frames per second (fps).

A research partner determined the vented Li-ion gas composition used in this study, how is part of the Norwegian Centre for Environment-friendly Energy Research MoZEES [33]. The gas composition shown in Table 1 was determined by analyzing the vented gas from thermally abused commercial cells with cell chemistry based upon lithium-iron-phosphate (LFP) with 100% SOC. A previous study has shown that the LBV of the Generic Li-ion gas composition is in the same range as many other cell chemistries at 100% SOC [34]. A gas supplier supplied the gas bottle of the Generic Li-ion gas composition with concentrations shown in Table 1.

Table 1. The gas composition of the Generic Li-ion gas in volume percentage.

Name of fuel mixture	**H_2 [%]**	**CO [%]**	**CO_2 [%]**	**CH_4 [%]**	**C_2H_4 [%]**
Generic Li-ion gas	34.9	25.0	20.1	15.0	5.0

2.2. CFD model and computational mesh

The CFD simulations were performed using the XiFoam solver/model, a combustion solver for premixed and partly premixed gas explosions, part of the OpenFOAM CFD toolbox's official release [31,32]. The combustion model in XiFoam is based upon a formulation of the laminar-flamelet approach proposed by Weller et al. [35]. In this approach, the combustion is represented by a transport equation of regress variable b. Whereas $b = 1$ is unburnt, and $b = 0$ is burnt. Below is the transport equation of regress variable b.

$$\frac{\partial}{\partial t}(\rho b) + \nabla.(\rho \boldsymbol{U} b) + \nabla.(\rho D \nabla b) = -\rho_u S_u \Xi |\nabla b| \qquad \text{Eq. 1}$$

where: b – reaction regress variable [-], ρ – density [kg/m^3], $\boldsymbol{U}$ – velocity vector [m/s], D – diffusion coefficient [m^2/s], S_u – laminar burning velocity [m/s], Ξ – turbulent and laminar flame speed ratio.

In the source term of Eq. 1, the LBV (S_u) is calculated from the Gülder equation [36]. As a flame propagates, turbulence and instabilities will stretch and wrinkle the flame front. The flame surface area will change and affects the flame propagation speed. The turbulent and laminar flame speed ratio (Ξ) is a function of the turbulence intensity. Ξ models the contribution which the subgrid turbulence has on the LBV. An in-depth explanation of the combustion model can be found in Wellers et al.'s publication [35].

For the Large Eddy Simulation (LES) approach, XiFoam solves the Navier-Stokes conservation equations for mass, momentum, and energy for an unsteady compressible and reactive flow. A first-order forward Euler scheme was used for the time integration. For the gradient and Laplacian/diffusion terms, the second-order linear scheme was used. Furthermore, for the divergence/convective terms, a combination of the first-order upwind scheme and the second-order limited linear and linear scheme was used to obtain stability and robustness. The discretized equations are solved using the PIMPLE algorithm, a combination of PISO (Pressure Implicit with Splitting Operators) and SIMPLE (Semi-Implicit Method for Pressure-Linked Equations). Nicoud and Ducros's [37] model WALE was used to evaluate the sub-grid turbulence. The WALE model is based on the square of the velocity gradient tensor and has a near-wall scaling function without requiring a dynamic procedure. Moreover, the model is suited for complex geometries and flow that experience laminar to turbulent transition.

The computer-aided design (CAD) geometry was drawn in Onshape, the online CAD tool [38], under the free subscription. From the CAD file, the computational mesh was generated using blockMesh and snappyHexMesh. BlockMesh and snappyHexMesh are two mesh utility tools that are part of the OpenFOAM toolbox. BlockMesh was used to generate the background mesh with a homogeneous cell size within the channel. Near the channel's open end, the cell size expands linearly to twice the initial cell size, creating a rectangular frustum shape with a 500 mm length. SnappyHexMesh was used to snap the background mesh to the CAD geometry and refine the cell sizes. After refinement, the computational channel was equal to the experimental channel inner dimensions. The wall refinement in the computational domain had three layers with a cell size that was half the background mesh's initial cell size. Four different background meshes with a cell of 2, 4, 8, and 16 mm were compared. Figure 2 shows the geometry (a) and three angles of the computational mesh (b,c,d). The mesh shown in Figure 2 was generated from the background mesh with an initial cell size of 4 mm and had 426 026 cells after refinement.

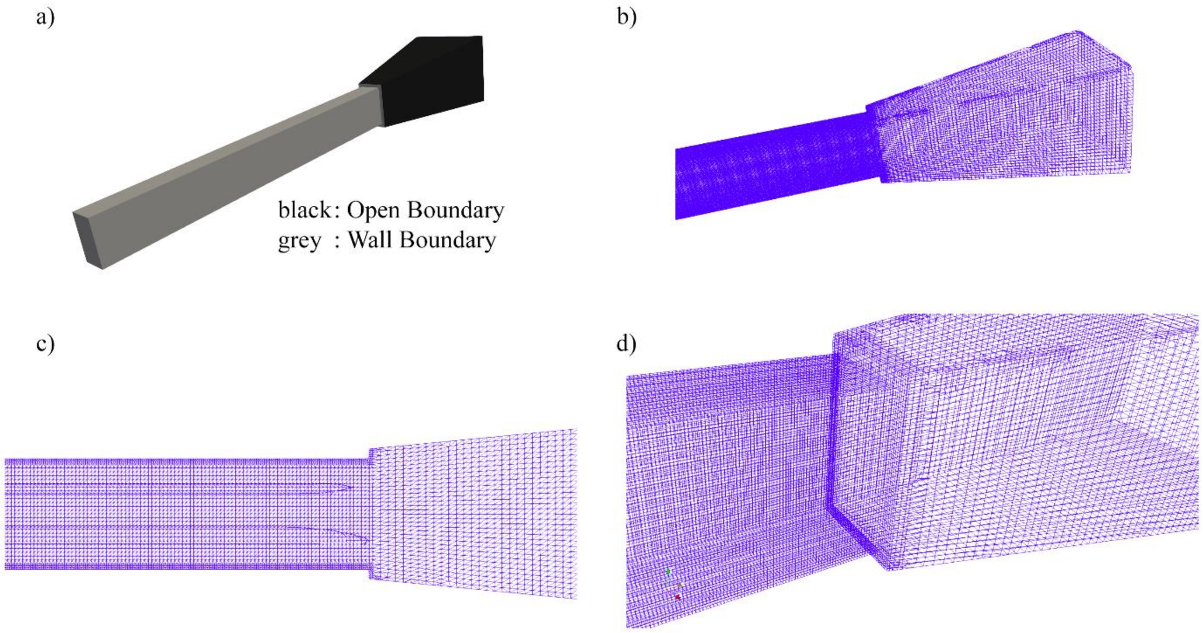

Figure 2. The geometry and the computational mesh. a): Side view of the entire CAD geometry with boundary conditions; b): Side front view of the computational mesh; c): Horizontal cross-section view of the computational mesh; d): Close-up of the transition between the channel and open geometry in the computational mesh.

The boundary condition for the mesh was divided into two domains; typical wall boundary conditions (the grey part of Figure 2a)) were set on the channel walls, whereas typical open boundary conditions (black part of Figure 2a)) were set on the boundaries outside the channel. Inside the channel, the species were premixed fuel and air. Outside of the channel, only air. The atmospheric conditions for the simulations were set to 293 K and 101.3 kPa (absolute). Table 2 lists all the wall and open boundary conditions used for each variable in the simulations.

Table 2. List of variables with the applied wall and open boundary conditions.

Variable	**Wall boundary**	**Open boundary**
Temperature (T)	fixed wall temperature (293 K)	zero gradient outlet fixed value inlet (T = 293)
Temperature unburnt (T_u)	fixed wall temperature (293 K)	zero gradient outlet fixed value inlet (T_u) = 293)
Pressure (p)	zero gradients at the wall	a constant total pressure, dynamic + static pressure equals 101.3 kPa.
Velocity (U)	zero velocity at the wall (noSlip)	zero gradient outlet; inlet value based on flux normal to the boundary surface
LBV (S_u)	zero gradients at the wall	zero gradients at the boundary surface
Turbulent, LBV ratio (Xi)	zero gradients at the wall	zero gradients at the boundary surface
regress variable (b)	zero gradients at the wall	zero gradients at the boundary surface
Fuel mixture fraction (ft)	zero gradient at wall	zero gradient outlet fixed value inlet (ft = 0)
Turbulent viscosity (nut)	calculated based on the turbulent kinetic energy	calculated based on the turbulent properties
Turbulent thermal diffusivity (alphat)	calculated based on the turbulent viscosity for compressible flow	calculated based on the turbulent viscosity

We referred to the OpenFOAM user guide [31] for a more comprehensive explanation of the boundary conditions and the discretization schemes. The base case for the CFD simulations is also found in the supplementary materials.

2.1. mech2Foam

For an inhomogeneous combustion simulation with XiFoam, the three species, fuel, oxidant, and burntProducts require coefficients for the transport, combustion, and thermodynamic models. The thermodynamic properties heat capacity (C_P), enthalpy (H), and entropy (S) can be calculated by the NASA polynomials [39], whereas the dynamic viscosity (transport property) can be calculated by the Sutherland Equation [40]. Furthermore, the LBV can be calculated by the Gülder equation

[36]. The model/equation coefficient for the NASA polynomials, Sutherland equation, and Gülder equation were determined using the developed mech2Foam code. The fuel species model coefficients were calculated from the gas composition in Table 1, whereas the oxidant species model coefficients were calculated for typical air (21 vol% O_2 and 79 vol% N_2). The San Diego reaction mechanism [41] was chosen as the reaction mechanism used in *mech2Foam*. A study by Henriksen et al. [34] has shown that the San Diego reaction mechanism accurately predicts the LBV for the Generic Li-ion gas composition in Table 1.

For a detailed description of *mech2Foam* and the complete code, we referred to *mech2Foam - Generating transport, combustion, and thermodynamic properties for the CFD solver XiFoam* (Henriksen and Bjerketvedt [42])

3. RESULTS

3.1. Output from *mech2Foam*

Table 3 shows the NASA polynomial and Sutherland coefficients for the fuel, oxidant, and burntProducts created with *mech2Foam*. As a code verification, the thermodynamic output (C_p, H, and S) of the generated NASA polynomial coefficients was compared with values calculated using the open-source Python module Cantera [43]. For all three species, the coefficient of determination (R^2) was practically one, and the standard deviation of the error (SDE) was approximately zero. Furthermore, the R^2 and the SDE values indicate that the thermodynamic output from Cantera and the newly generated NASA polynomial coefficients are essentially identical. Comparing the dynamic viscosity from Cantera and the fitted Sutherland coefficients gave a maximum SDE and minimum R^2 of $1.547 \cdot 10^{-6}$ Pa·s and 0.997, respectively. The Sutherland coefficients are fitted and, therefore, not identical to the Cantera calculated viscosity.

Table 3. NASA polynomial and Sutherland coefficients for oxidant, fuel, and the burntProducts generated by mech2Foam

NASA Polynomial Coefficients		
oxidant	fuel	burntProducts

NASA coefficients (high)	NASA coefficients (low)	NASA coefficients (high)	NASA coefficients (low)	NASA coefficients (high)	NASA coefficients (low)
3.0014	3.4003	2.7103	3.1162	3.0830	3.3331
1.4870E-03	4.8320E-04	4.9372E-03	2.2932E-03	2.0433E-03	1.8360E-03
-6.0827E-07	-1.0630E-06	-2.0779E-06	3.9069E-06	-7.3569E-07	-2.3696E-06
1.2376E-10	2.4237E-09	4.3680E-10	-5.3380E-09	1.2695E-10	2.9921E-09
-9.8862E-15	-1.2503E-12	-3.5960E-14	1.9922E-12	-8.4267E-15	-1.2824E-12
-957.6	-1029.9	-18030.7	-18071.4	-13405.8	-13469.1
5.8698	3.8889	4.5660	2.8315	5.2440	3.9041

Sutherland Coefficients

A_s	T_s	A_s	T_s	A_s	T_s
1.7943E-06	336.8612	1.6151E-06	377.9981	1.8322E-06	435.4540

Table 4 shows the Gülder coefficients generated by *mech2Foam*, used to estimate LBVs for the Generic Li-ion gas composition at different ϕ, temperatures, and pressures. Figure 3 shows that the Gülder equation fits well with the numerically calculated LBVs used in the regression. The lowest R^2 for the three fitted LBVs curves was 0.98, where the LBV was a function of pressure (Figure 3 c)).

Table 4. The fitted Gülder coefficients for the Generic Li-ion gas in Table 1 and air generated by mech2Foam

Gülder Coefficients

ω	0.5039	η	-0.1455
ξ	4.5231	α	1.8735
β	-0.3738	f	2.3

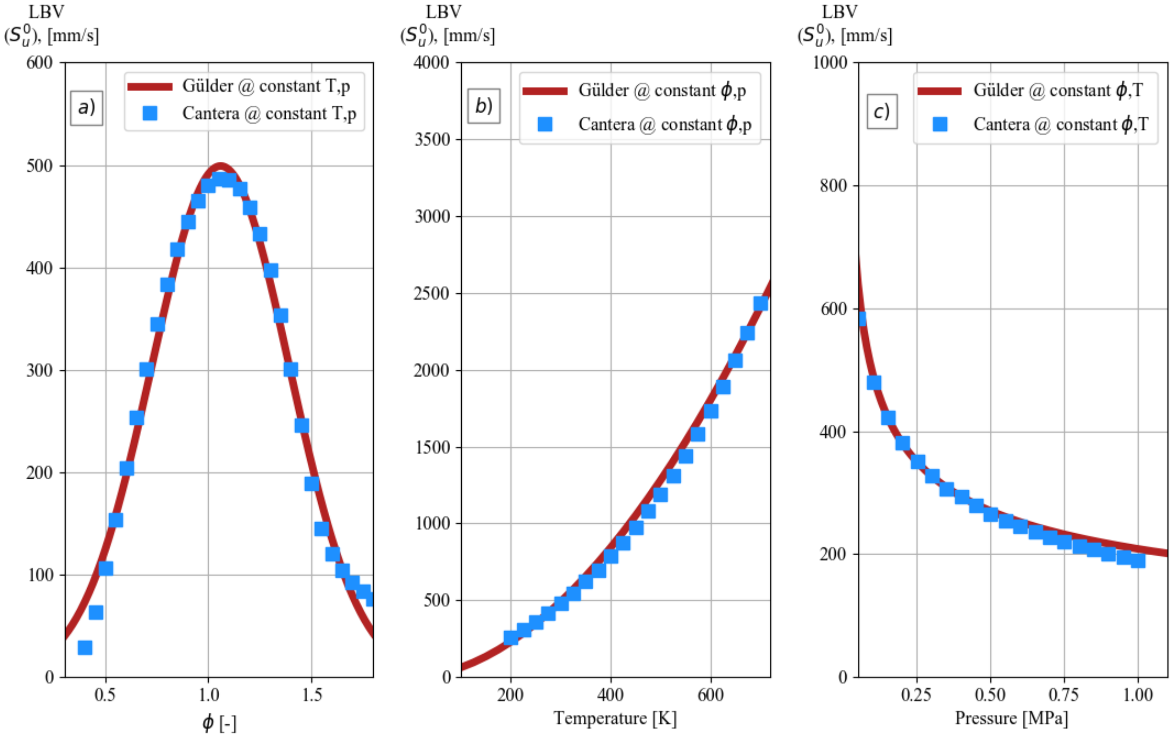

Figure 3. Comparison of the LBVs calculated using the Gülder equation and numerical calculation in Cantera, using the San Diego reaction mechanism. a): The LBV as a function of ϕ, at constant temperature and pressure; b): The LBV as a function of temperature, at constant ϕ and pressure; c): The LBV as a function of pressure, at constant ϕ and temperature.

3.2. Mesh Sensitivity

Figure 4 compares the temporal evolution of the pressure, flame front position, and flame front velocity for the four different background meshes. There are discrepancies in minimum and maximum values between the cases, but the profiles are very similar. Between the 2 mm and the 4 mm case, the maximum pressure difference is 0.24 kPa. Based on the comparison in Figure 4, the 4 mm case gave an acceptable accuracy compared to the 2 mm case. Furthermore, for large geometries such as BESS or large battery applications, a cell size of 4 mm is favorable over 2 mm regarding the computational time and requirements. Therefore, the computational grid generated from the background mesh with a cell size of 4 mm, was chosen for all following simulation cases.

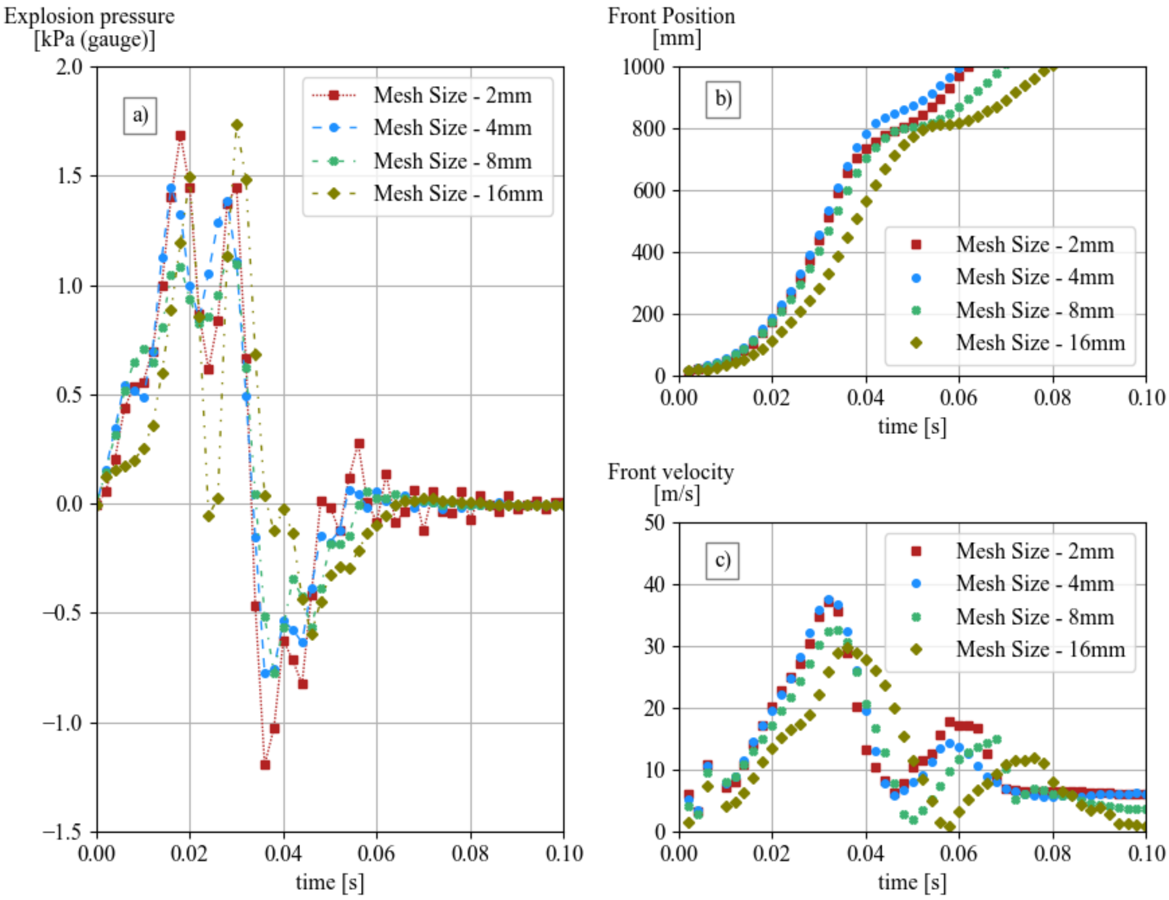

Figure 4. Comparison of four different background meshes with 2, 4, 8, and 16 mm in cell size. (a): Temporal evolution of the explosion pressure, at pressure transducer one; (b): Temporal evolution of the flame front for variable b at 0.5; (c): Temporal evolution of the flame front velocity.

3.3. Experimental and Simulation results

The maximum explosion pressure for all experiments and simulation cases are shown in Figure 5. Only the first two pressure peaks in the experiments were used when evaluating the maximum explosion pressure. In all experiments and simulation cases, the maximum explosion pressure was measured at pressure sensor 1, the sensor closest to the ignition source. For the experiments, the maximum explosion pressure was 1.36 kPa (gauge), at ϕ equal to 1.08; whereas, the maximum explosion pressure for the simulation was 1.45 kPa (gauge), at ϕ equal to 1.0.

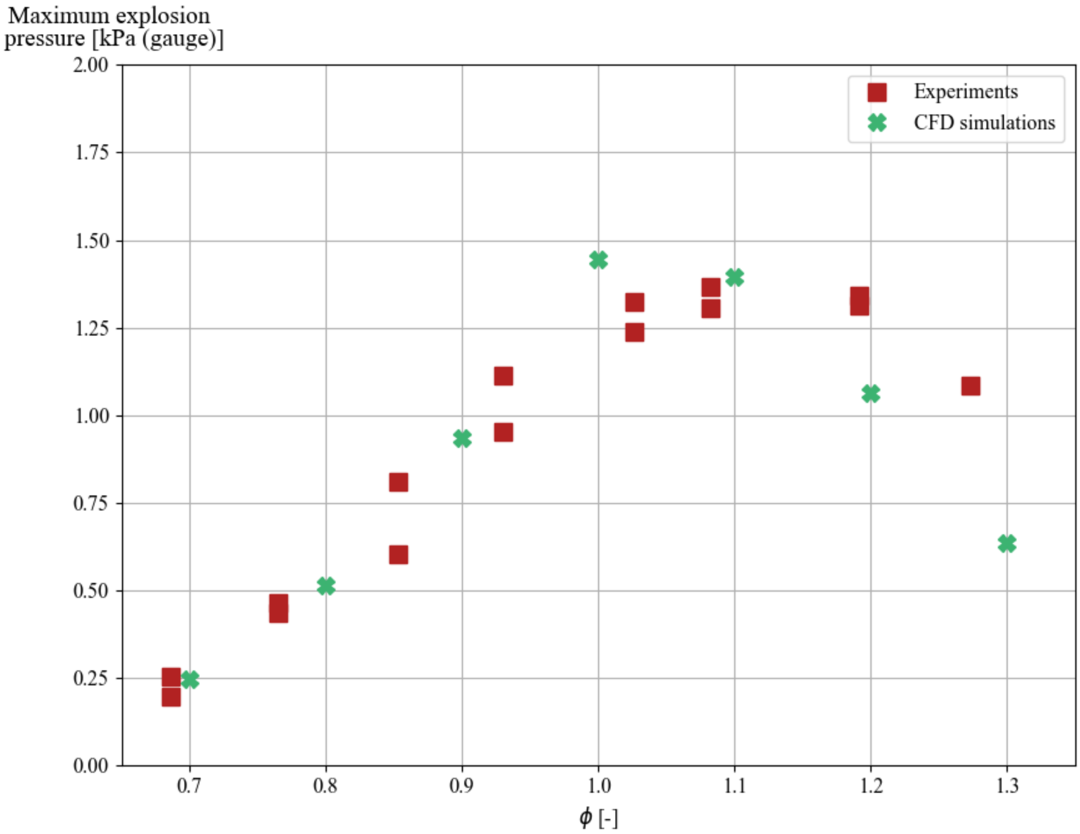

Figure 5. The maximum explosion pressure, all measured at pressure sensor 1, for the 1-meter explosion channel experiments and numerical simulations.

Figure 6 shows a side-by-side comparison of the flame propagation in an experiment (left) and a CFD simulation (right) with a ϕ of 1.2. In the simulation images, an isosurface of regress variable b equal to 0.5 was used to visualize the flame surface. The explosion pressure measured at pressure sensor one is shown on both sides in Figure 6, with the experimental pressure on the left and the simulated pressure on the right. Moreover, the images in Figure 6 shows that the initial flame propagation is similar in the simulation and the experiment. However, there are some minor differences in the pressure. The first and second pressure peaks are reached slightly earlier in the simulation compared to the experiments. There is also a higher peak pressure in the experiment than predicted in the simulations, as Figure 5 also shows. The pressure decline rate, which occurs after the second pressure peak, is higher in the experimental case. This higher rate of pressure decline, and the flame reaching the top and bottom channel walls earlier in the experiments (at times 40ms, 44ms, and 48), results in an earlier onset of the tulip flame shape. Although there are some differences between the simulation and the experiment, the overall propagation is in good agreement. For the unfiltered experimental results, we refer to, *Experimental data of gas explosions in a 1-meter open-ended channel* (Henriksen and Bjerketvedt [44]).

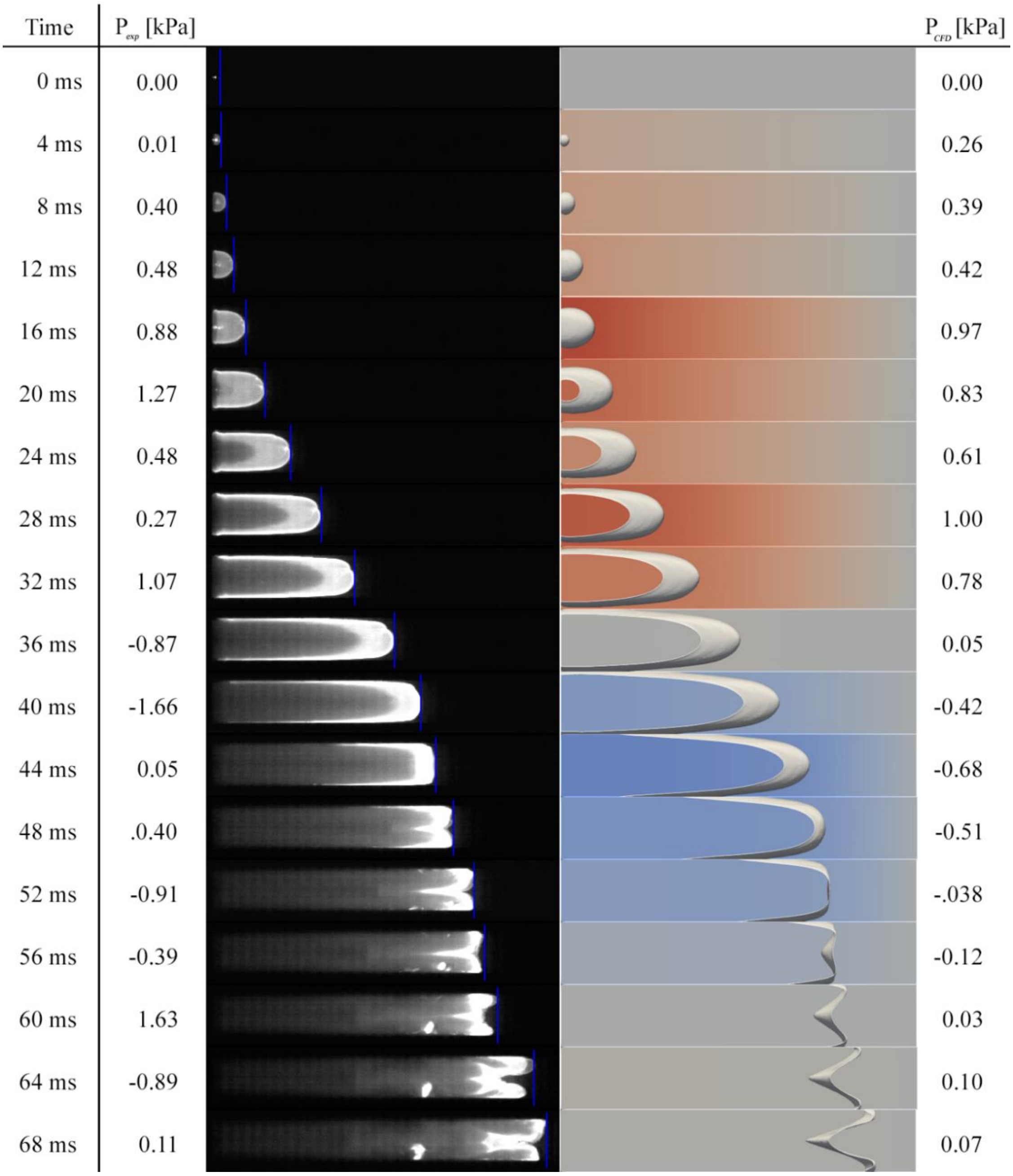

Time	P_{exp} [kPa]	P_{CFD} [kPa]
0 ms	0.00	0.00
4 ms	0.01	0.26
8 ms	0.40	0.39
12 ms	0.48	0.42
16 ms	0.88	0.97
20 ms	1.27	0.83
24 ms	0.48	0.61
28 ms	0.27	1.00
32 ms	1.07	0.78
36 ms	-0.87	0.05
40 ms	-1.66	-0.42
44 ms	0.05	-0.68
48 ms	.0.40	-0.51
52 ms	-0.91	-.038
56 ms	-0.39	-0.12
60 ms	1.63	0.03
64 ms	-0.89	0.10
68 ms	0.11	0.07

Figure 6. Series of images from the high-speed video and CFD simulation showing the flame propagation with a time interval of 0.004 seconds. Left: High-speed images of the flame propagation with a fuel-air equivalence ratio of 1.19. Right: Isosurface images from CFD simulation of variable b at 0.5 for fuel-air equivalence ratio of 1.2.

4. DISCUSSION

4.1. Accuracy of the generated CFD input parameter

The sums of the mole-fraction-weighted NASA polynomial coefficients (hereafter referred to as weighted NASA polynomial) in Table 3 gave nearly identical thermodynamic values as those calculated from the reaction mechanism. However, different common reference temperatures (the reference temperature shared by the higher and lower NASA polynomials) for different species in the reaction mechanism can affect the accuracy of the weighted NASA polynomial. For example, there are seven different common reference temperatures in the San Diego reaction mechanism, ranging from 1000 K to 1392 K. It is uncertain how much different common reference temperatures will affect the accuracy of the weighted NASA polynomial because there is usually some overlap between the lower and higher NASA polynomials. For gas mixtures with different common reference temperatures, the weighted NASA polynomial coefficients should be validated.

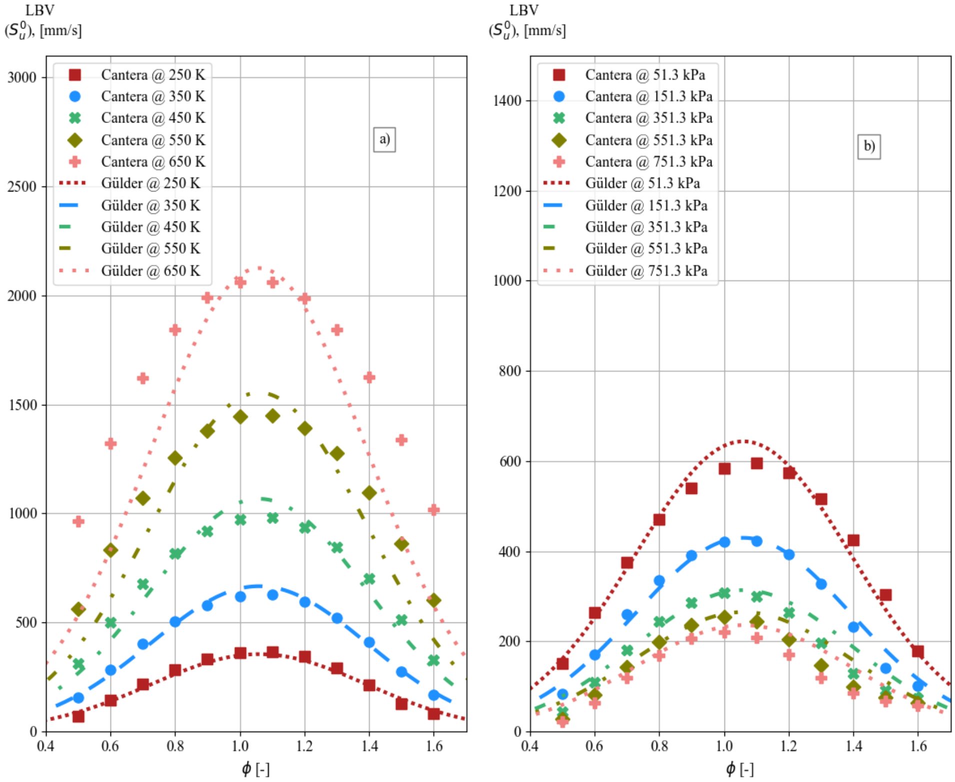

Figure 7 Comparison of the LBVs obtained from the Gülder equation and numerical calculation. a): LBV at constant pressure of 101.3 kPa (absolute); b): LBV at constant temperature of 300 K.

Although Figure 3 and Table 4 show that the generated Gülder coefficients fit well with the regression data, the accuracy is lower when used outside of this range. This reduction in accuracy between LBVs from Cantera calculations and the Gülder equation can be seen in Figure 7. Figure 7 a) show that as the temperature increases, the Gülder equation under predicts the LBVs on the lean and rich side. At 650 K, the *SDE* is 338 mm/s, and R^2 is 0.66. Figure 7 b) shows that the Gülder equation slightly overestimates the LBVs as the pressure increases. At constant pressure of 751.3 kPa (absolute), the *SDE* and R^2 were 35 mm/s and 0.70, respectively. The expected temperature and pressure range in a simulation should be considered when using the Gülder equation for LBV estimations.

4.2. CFD simulations

Figure 4 a) shows that the temporal evolution of the pressure for the 2, 4, and 8 mm cases have similar profiles. However, the explosion pressure peaks and crest values differ. These differences may indicate that there is mesh dependency for the maximum and minimum explosion pressure. The cell size used in the simulation will affect the gradient of regress variable b (flame thickness). It is reasonable to assume that the pressure peak and crest values will increase for steeper gradients of variable b (smaller flame thickness).

The maximum explosion pressure for the 16 mm and the 2 mm background mesh cases is similar, despite having very different cell sizes. In order to have comparable simulation cases, the minimum value of variable b after ignition should be close to identical. The strength and duration of the ignition determine the minimum value of variable b. However, for the 16 mm simulation case, the ignition's strength, duration, and size had to be increased in order to match the minimum value of variable b in the other cases. For an open-ended channel, the strength, size, and duration of the numerical ignition can affect the simulated pressure, and thus resulting in a relatively high-pressure peak, as in the 16 mm case.

Figure 5 shows that the CFD simulation predicts the maximum explosion pressure with minor differences compared to experimental results. Although the maximum explosion pressure is essential for safety engineering purposes, more parameters should be analyzed when validating a

CFD model. In the following, the simulated explosion pressure, flame front position, and flame front velocity versus time are compared with experiments at similar ϕ.

In Figure 8, the temporal evolution of the pressure is compared for three different cases, A, B, and C. In all cases, the CFD simulations estimated the initial pressure development (to 0.06 s for case A and 0.035 s for cases B and C) with only minor deviations compared to the experiments. However, there is an apparent discrepancy in the pressure profile after the initial pressure development in all cases. In the experiments, the minimum pressure crests were larger than in the CFD simulations. Furthermore, the pressure also began to oscillate, which was not predicted by the simulations. Plotting the temporal evolution of the flame front position for the three cases shows that the flame thickness starts to grow simultaneously as the onset for pressure discrepancy. This growth in the simulated flame thickness is a possible explanation for the smoothing of the pressure oscillations.

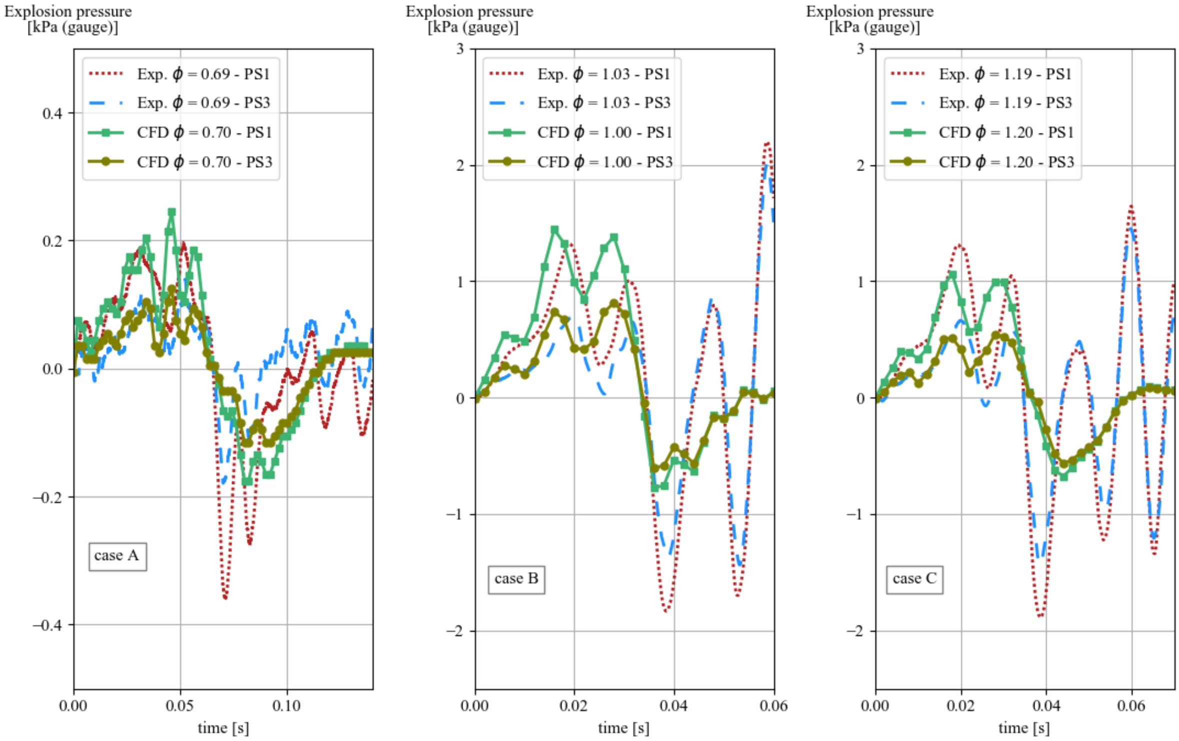

Figure 8. Comparison of the CFD simulated and the experimental measured temporal evolution of the pressure for the three cases A, B, and C, with different fuel-air equivalence ratios.

The simulated and experimental temporal evolution of the flame front position for cases A, B, and C, are shown in Figure 9. For cases, A and C, the simulated flame front position agrees with the experimental results. However, for case B, there is a more considerable discrepancy between the experiment and the simulation. There is a difference of 0.03 in the ϕ between the compared simulation and experiment for case B, which may explain some of the flame front position discrepancies for this particular case.

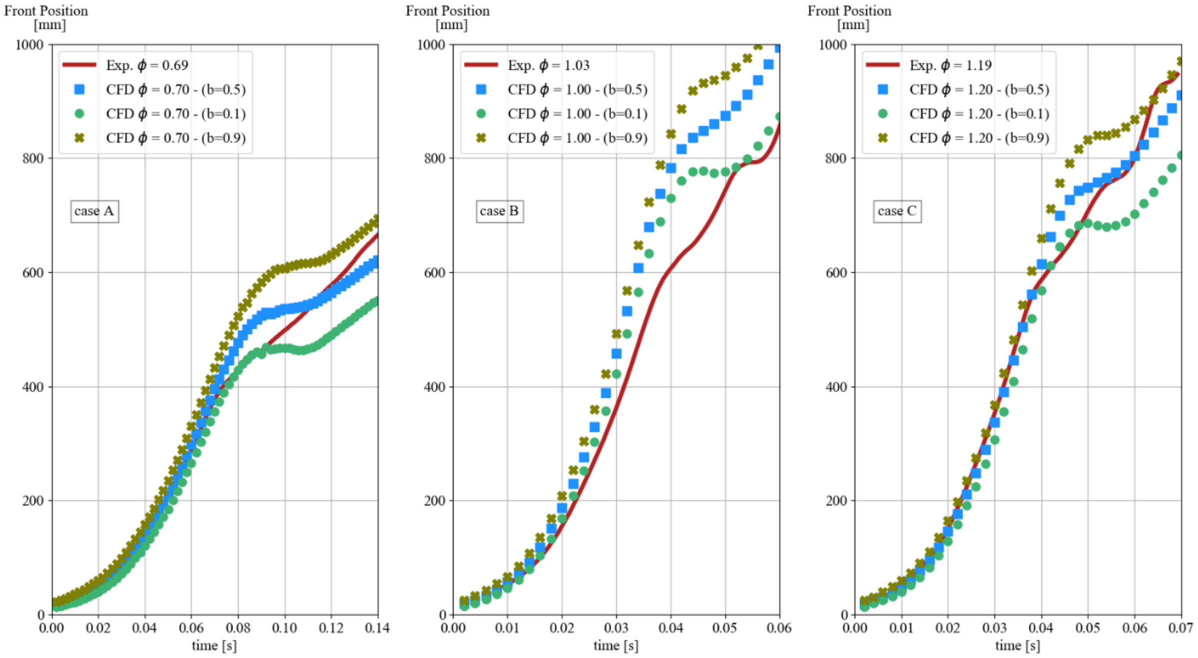

Figure 9. Comparison of the CFD simulated and the experimental measured temporal evolution of the flame front position for the three cases A, B, and C, with different fuel-air equivalence ratios.

As discussed, when the pressure starts to decline in the channel, the flame thickness (distance from 0.1 to 0.9 in regress variable *b*) significantly increases in the simulation, as seen in Figure 9. In cases A, B, and C, the maximum flame thickness is 152 mm, 177 mm, and 166 mm, respectively. Compared to the thickness of an actual flame, the maximum modeled flame thickness is over several hundred times larger. The substantial difference in flame thickness between simulation and experiments may affect the accuracy of the simulation. A broader flame may smooth and dampen the pressure response in the simulations.

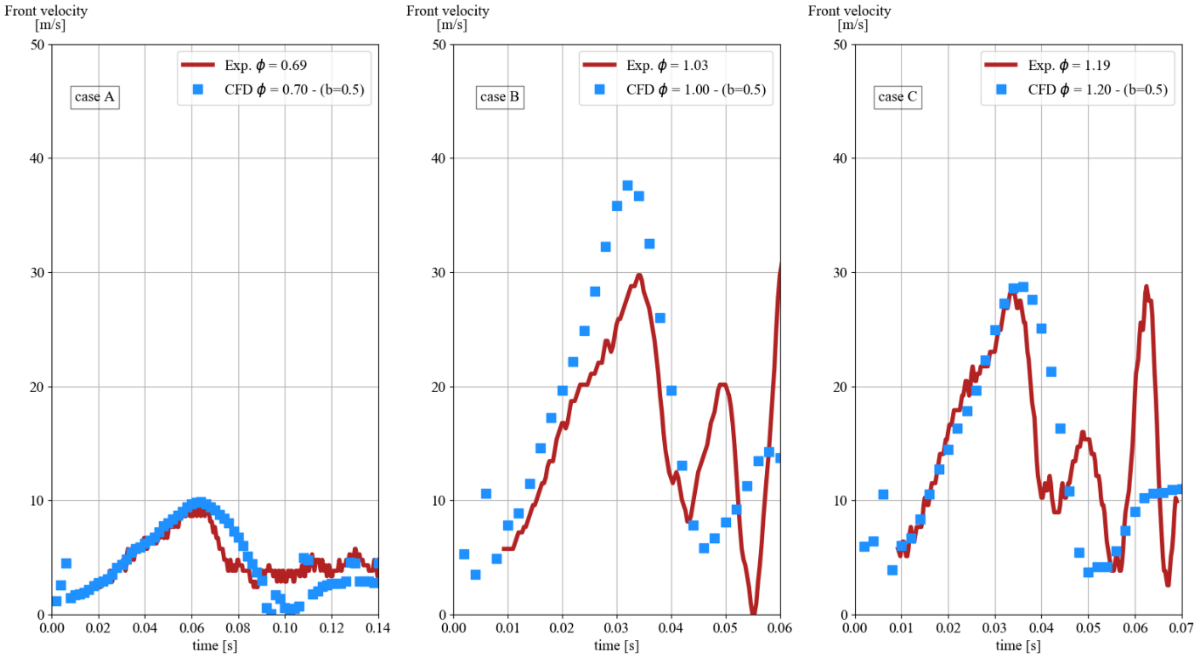

Figure 10. Comparison of the CFD simulated and the experimental measured temporal evolution of the flame front velocity for the three cases A, B, and C, with different fuel-air equivalence ratios.

Figure 10 shows a comparison of the temporal evolution of the flame front velocity. For cases, A and C, the first peak in flame front velocity is predicted with only a minor discrepancy compared to the experimental results. In Figure 10, case B shows a higher peak in flame front velocity than in the experiment, with a maximum difference of 8 m/s. The higher peak in flame front velocity in case B is consistent with the difference in the flame front position in Figure 9. Like the pressure comparison, the initial velocity peak is predicated with a relatively low discrepancy; however, the later occurring oscillations are not predicted. These oscillations may not be captured due to the grid cell size chosen. Although the 2 mm mesh case in Figure 4 shows no sign of oscillations in the flame front velocity or pressure. Therefore, it is uncertain whether the pressure and flame front velocity oscillations would be predicted with a finer mesh. Furthermore, for large geometries than the explosion channel in this study, a cell size under 2 mm would require significant computational effort.

If the combustion model (regress variable *b*) is the cause of the discrepancy in the simulation results, a slightly finer mesh would not significantly improve the simulation results. Since first-order schemes were used in discretizing the time and some of the convective terms, it may have influenced the accuracy of the simulation results. Improving both the mesh quality and discretization scheme may yield a more accurate prediction of the temporal evolution of pressure and flame front velocity. However, based on the results in Figure 5 and Figure 9, the XiFoam solver/model predicts the maximum explosion pressure and the flame front position with acceptable accuracy for safety engineering and consequence analysis. Moreover, there is good agreement between the simulation and experiment results of the initial pressure peaks and initial flame front velocity development shown in Figure 8 and Figure 10, respectively. Finally, further investigation of the prediction accuracy of the XiFoam combustion model can be performed by improving mesh quality, discretization schemes, and model parameters, but it is beyond this study's scope.

5. CONCLUSION

This study presents a CFD method for simulating explosions of gases vented from failed LIBs. The required transport, combustion, and thermodynamic model coefficients for the XiFoam CFD combustion model/solver were determined by the code *mech2Foam*. Furthermore, the code *mech2Foam* generates the required parameters for homogeneous and inhomogeneous combustion. Although *mech2Foam* is designed for XiFoam, any CFD model that can utilize the same input parameters could use the method. Finally, the prediction accuracy of the CFD method was evaluated by comparing simulation and experiments of premixed explosions in an open-ended channel from a gas composition vented from a failed LIB.

The CFD simulations predicted the maximum explosion pressure and flame front position with only minor discrepancies compared to the experimental results. Simulation results for the pressure and flame front velocities also agreed with the experimental results in the initial stages of the flame propagation. However, pressure and flame front velocity oscillations, which occurred as the flame approached the channel opening, were not accurately predicted. A maximum explosion pressure of 1.36 kPa (gauge) and 1.45 kPa (gauge) was recorded in the channel for the experiments and simulations, respectively.

A complete and open method for generating CFD input parameters and modeling an explosion from a gas release from a LIB has been presented. The method is intended for evaluating the risk and consequences related to LIB applications and installations.

6. ACKNOWLEDGEMENT

This work was performed within MoZEES, a Norwegian Centre for Environment-friendly Energy Research (FME), co-sponsored by the Research Council of Norway (project number 257653) and 40 partners from research, industry and public sector.

7. REFERENCES

[1] P.G. Balakrishnan, R. Ramesh, T. Prem Kumar, Safety mechanisms in lithium-ion batteries, Journal of Power Sources. 155 (2006) 401–414. https://doi.org/10.1016/j.jpowsour.2005.12.002.

[2] D.P. Finegan, E. Darcy, M. Keyser, B. Tjaden, T.M.M. Heenan, R. Jervis, J.J. Bailey, N.T. Vo, O.V. Magdysyuk, M. Drakopoulos, M. Di Michiel, A. Rack, G. Hinds, D.J.L. Brett, P.R. Shearing, Identifying the Cause of Rupture of Li-Ion Batteries during Thermal Runaway, Advanced Science. 5 (2018) 1700369. https://doi.org/10.1002/advs.201700369.

[3] S. Abada, G. Marlair, A. Lecocq, M. Petit, V. Sauvant-Moynot, F. Huet, Safety focused modeling of lithium-ion batteries: A review, Journal of Power Sources. 306 (2016) 178–192. https://doi.org/10.1016/j.jpowsour.2015.11.100.

[4] A.R. Baird, E.J. Archibald, K.C. Marr, O.A. Ezekoye, Explosion hazards from lithium-ion battery vent gas, Journal of Power Sources. 446 (2020) 227257. https://doi.org/10.1016/j.jpowsour.2019.227257.

[5] L. Kong, C. Li, J. Jiang, M. Pecht, Li-Ion Battery Fire Hazards and Safety Strategies, Energies. 11 (2018) 2191. https://doi.org/10.3390/en11092191.

[6] D. Hill, McMicken Battery Energy Storage System Event Technical Analysis and Recommendations, DNV-GL, 2020. https://www.aps.com/-/media/APS/APSCOM-PDFs/About/Our-Company/Newsroom/McMickenFinalTechnicalReport.ashx?la=en&hash=50335FB5098D9858BFD276C40FA54FCE.

[7] A. Reid, Exploding Kona EV in Montreal prompts investigation from Hyundai, Exploding Kona EV in Montreal Prompts Investigation from Hyundai. (2019). https://driving.ca/hyundai/auto-news/news/exploding-kona-ev-in-montreal-prompts-investigation-from-hyundai.

[8] Corvus Energy, Fire onboard the car-ferry Ytterøyningen: Preliminary investigation results, Fire Onboard the Car-Ferry Ytterøyningen: Preliminary Investigation Results. (2020). https://corvusenergy.com/fire-onboard-the-car-ferry-ytteroyningen-preliminary-investigation-results/.

[9] C. Mikolajczak, M. Kahn, K. White, R.T. Long, Lithium-Ion Batteries Hazard and Use Assessment, Springer US, Boston, MA, 2011. https://doi.org/10.1007/978-1-4614-3486-3.

[10] Q. Wang, B. Mao, S.I. Stoliarov, J. Sun, A review of lithium ion battery failure mechanisms and fire prevention strategies, Progress in Energy and Combustion Science. 73 (2019) 95–131. https://doi.org/10.1016/j.pecs.2019.03.002.

[11] Y. Fernandes, A. Bry, S. de Persis, Identification and quantification of gases emitted during abuse tests by overcharge of a commercial Li-ion battery, Journal of Power Sources. 389 (2018) 106–119. https://doi.org/10.1016/j.jpowsour.2018.03.034.

[12] A.W. Golubkov, S. Scheikl, R. Planteu, G. Voitic, H. Wiltsche, C. Stangl, G. Fauler, A. Thaler, V. Hacker, Thermal runaway of commercial 18650 Li-ion batteries with LFP and NCA cathodes – impact of state of charge and overcharge, RSC Advances. 5 (2015) 57171–57186. https://doi.org/10.1039/C5RA05897J.

[13] A.W. Golubkov, D. Fuchs, J. Wagner, H. Wiltsche, C. Stangl, G. Fauler, G. Voitic, A. Thaler, V. Hacker, Thermal-runaway experiments on consumer Li-ion batteries with metal-oxide and olivin-type cathodes, RSC Adv. 4 (2014) 3633–3642. https://doi.org/10.1039/C3RA45748F.

[14] M. Lammer, A. Königseder, V. Hacker, Holistic methodology for characterisation of the thermally induced failure of commercially available 18650 lithium ion cells, RSC Advances. 7 (2017) 24425–24429. https://doi.org/10.1039/C7RA02635H.

[15] E.P. Roth, C.C. Crafts, D.H. Doughty, James. McBreen, Advanced technology development program for lithium-ion batteries : thermal abuse performance of 18650 Li-ion cells., 2004. https://doi.org/10.2172/918751.

[16] V. Somandepalli, K. Marr, Q. Horn, Quantification of Combustion Hazards of Thermal Runaway Failures in Lithium-Ion Batteries, SAE International Journal of Alternative Powertrains. 3 (2014) 98–104. https://doi.org/10.4271/2014-01-1857.

[17] D. Bjerketvedt, J.R. Bakke, K. Van Wingerden, Gas explosion handbook, Journal of Hazardous Materials. 52 (1997) 1–150.

[18] M. Henriksen, A.V. Gaathaug, K. Vaagsaether, J. Lundberg, S. Forseth, D. Bjerketvedt, Laminar Burning Velocity of the Dimethyl Carbonate-Air Mixture Formed by the Li-Ion Electrolyte Solvent, Combustion, Explosion, and Shock Waves. 56 (2020) 383–393. https://doi.org/10.1134/S0010508220040024.

[19] M. Henriksen, K. Vaagsaether, J. Lundberg, S. Forseth, D. Bjerketvedt, Explosion characteristics for Li-ion battery electrolytes at elevated temperatures, Journal of Hazardous Materials. 371 (2019) 1–7. https://doi.org/10.1016/j.jhazmat.2019.02.108.

[20] J. Johnsplass, M. Henriksen, K. Vaagsaether, J. Lundberg, D. Bjerketvedt, Simulation of burning velocities in gases vented from thermal run-a-way lithium ion batteries, in: 2017: pp. 157–161. https://doi.org/10.3384/ecp17138157.

[21] R. Shen, Z. Jiao, T. Parker, Y. Sun, Q. Wang, Recent application of Computational Fluid Dynamics (CFD) in process safety and loss prevention: A review, Journal of Loss Prevention in the Process Industries. 67 (2020) 104252. https://doi.org/10.1016/j.jlp.2020.104252.

[22] O.R. Hansen, P. Hinze, D. Engel, S. Davis, Using computational fluid dynamics (CFD) for blast wave predictions, Journal of Loss Prevention in the Process Industries. 23 (2010) 885–906. https://doi.org/10.1016/j.jlp.2010.07.005.

[23] D. Makarov, F. Verbecke, V. Molkov, O. Roe, M. Skotenne, A. Kotchourko, A. Lelyakin, J. Yanez, O. Hansen, P. Middha, S. Ledin, D. Baraldi, M. Heitsch, A. Efimenko, A. Gavrikov, An inter-comparison exercise on CFD model capabilities to predict a hydrogen explosion in a simulated vehicle refuelling environment, International Journal of Hydrogen Energy. (2009) 15.

[24] P. Middha, O.R. Hansen, CFD simulation study to investigate the risk from hydrogen vehicles in tunnels, International Journal of Hydrogen Energy. 34 (2009) 5875–5886. https://doi.org/10.1016/j.ijhydene.2009.02.004.

[25] G.-H. Kim, A. Pesaran, R. Spotnitz, A three-dimensional thermal abuse model for lithium-ion cells, Journal of Power Sources. 170 (2007) 476–489. https://doi.org/10.1016/j.jpowsour.2007.04.018.

[26] W. Zhao, G. Luo, C.-Y. Wang, Modeling Nail Penetration Process in Large-Format Li-Ion Cells, J. Electrochem. Soc. 162 (2015) A207–A217. https://doi.org/10.1149/2.1071501jes.

[27] J. Kim, A. Mallarapu, D.P. Finegan, S. Santhanagopalan, Modeling cell venting and gas-phase reactions in 18650 lithium ion batteries during thermal runaway, Journal of Power Sources. 489 (2021) 229496. https://doi.org/10.1016/j.jpowsour.2021.229496.

[28] R. Srinivasan, M.E. Thomas, M.B. Airola, B.G. Carkhuff, L.J. Frizzell-Makowski, H. Alkandry, J.G. Reuster, H.N. Oguz, P.W. Green, J. La Favors, L.J. Currano, P.A. Demirev, Preventing Cell-to-Cell Propagation of Thermal Runaway in Lithium-Ion Batteries, J. Electrochem. Soc. 167 (2020) 020559. https://doi.org/10.1149/1945-7111/ab6ff0.

[29] H. Helgesen, Technical Reference for Li-ion Battery Explosion Risk and Fire Suppression, DNV GL, Norway, 2019.

[30] GexCon, FLACS -CFD, Explosion & Dispersion Modelling Software. (2021). https://www.gexcon.com/products-services/flacs-software/.

[31] CFD Direct, OpenFOAM v7 User Guide, OpenFOAM v7 User Guide. (2021). https://cfd.direct/openfoam/user-guide-v7/.

[32] H.G. Weller, G. Tabor, H. Jasak, C. Fureby, A tensorial approach to computational continuum mechanics using object-oriented techniques, Comput. Phys. 12 (1998) 620. https://doi.org/10.1063/1.168744.

[33] MOZEES, MOZEES, Mobility Zero Emission Energy Systems. (2017). https://www.mozees.no/ (accessed August 20, 2019).

[34] M. Henriksen, K. Vaagsaether, J. Lundberg, S. Forseth, D. Bjerketvedt, Laminar burning velocity of gases vented from failed Li-ion batteries, Journal of Power Sources. 506 (2021) 230141. https://doi.org/10.1016/j.jpowsour.2021.230141.

[35] H.G. Weller, G. Tabor, A.D. Gosman, C. Fureby, Application of a flame-wrinkling les combustion model to a turbulent mixing layer, Symposium (International) on Combustion. 27 (1998) 899–907. https://doi.org/10.1016/S0082-0784(98)80487-6.

[36] Ö.L. Gülder, Correlations of Laminar Combustion Data for Alternative S.I. Engine Fuels, in: 1984. https://doi.org/10.4271/841000.

[37] F. Nicoud, F. Ducros, Subgrid-Scale Stress Modelling Based on the Square of the Velocity Gradient Tensor, Flow, Turbulence and Combustion. 62 (1999) 18.

[38] Onshape, Onshape. (2014). https://www.onshape.com/en/.

[39] B.J. McBride, S. Gordon, M.A. Reno, Coefficients for Calculating Thermodynamic and Transport Properties of Individual Species, NASA, 1993. https://ntrs.nasa.gov/api/citations/19940013151/downloads/19940013151.pdf.

[40] W. Sutherland, LII. *The viscosity of gases and molecular force*, The London, Edinburgh, and Dublin Philosophical Magazine and Journal of Science. 36 (1893) 507–531. https://doi.org/10.1080/14786449308620508.

[41] UCSD, “Chemical-Kinetic Mechanisms for Combustion Applications”, San Diego Mechanism web page, Mechanical and Aerospace Engineering (Combustion Research), University of California at San Diego, The San Diego Mechanism. (2016). http://combustion.ucsd.edu.

[42] M. Henriksen, D. Bjerketvedt, mech2Foam - Generating transport, combustion, and thermodynamic properties for the CFD solver XiFoam, University of South-Eastern Norway, 2021. https://doi.org/10.23642/USN.13721134.V3.

[43] D.G. Goodwin, H.K. Moffat, R.L. Speth, Cantera: An Object-Oriented Software Toolkit For Chemical Kinetics, Thermodynamics, And Transport Processes, Zenodo, 2017. https://doi.org/10.5281/zenodo.170284.

[44] M. Henriksen, D. Bjerketvedt, Experimental data of gas explosions in a 1-meter open-ended channel, (2021) 1706040587 Bytes. https://doi.org/10.23642/USN.13796108.V2.

Article E

Numerical Study of Premixed Gas Explosion in a 1-meter Channel Partly Filled with 18650 Cell-like Cylinders with Experiments

Submitted to the Journal of Loss Prevention in the Process Industries on the 19 of August 2021.

Numerical Study of Premixed Gas Explosion in a 1-meter Channel Partly Filled with 18650 Cell-like Cylinders with Experiments

Henriksen, M.[1], Vaagsaether K.[1] , Lundberg, J.[1] , Forseth S.[2], Bjerketvedt D.[1]
[1] Faculty of Technology, Natural Sciences and Maritime Sciences, University of South-Eastern Norway, Kjølnes Ring 56, Porsgrunn, 3901, Norway
[2] Norwegian Defence Research Establishment (FFI), Oslo, Norway
***Corresponding author email:** mathias.henriksen@usn.no*

ABSTRACT

Abused and defective Li-ion cells can cause a catastrophic failure of a Li-ion battery (LIB), leading to severe fires and explosions. In recent years, several numerical and experimental studies have been conducted on the explosion hazard related to the vented combustible gases from failed Li-ion cells. Experimentally quantifying fundamental properties for failing LIBs is essential for understanding safety issues; however, it can be costly, time-consuming, and can be partly incomplete. Computational fluid dynamic (CFD) simulations have been an essential tool for studying the risk and consequences in the process industry. In this study, the prediction accuracy of the open-source CFD combustion model/solver XiFoam was evaluated by comparing numerical simulations and experiments of premixed gas explosions in a 1-meter explosion channel partly filled with 18650 cell-like cylinders. The prediction accuracy was determined by calculating the mean geometric bias and variance for the temporal pressure evolution, maximum pressure peak, positive impulse, spatial flame front velocity for two different channel geometries, in addition to two gas compositions at several fuel-air equivalence ratios. From this method, the XiFoam model/solver gave an overall acceptable model performance for both geometries and gas composition.

Keywords: Li-ion battery safety, Open-Source Software, OpenFOAM, Explosion simulation, premixed combustion

1. INTRODUCTION

Over the last decade, several fires and explosions have been caused by failing Li-ion batteries (LIBs). For example, in Texas, USA, in April 2017, a train car carrying discarded LIBs for recycling caused an explosion, which shattered windows 350 feet from the incident [1]. In April 2019, a Li-ion battery energy storage system (BESS) caught fire in Arizona, USA. Three hours after the fire suppressant had extinguished the fire, firefighters entered the BESS, shortly after an explosion occurred. The BESS was severely damaged, and several firefighters were injured [2]. Similarly, in September 2020, there was a fire in 20 MWh BESS in Liverpool, UK. The BESS was already well alight when the firefighters arrived, and residents in the vicinity reported hearing an explosion [3,4]. In April 2021, a fire occurred in a solar panel installation with 25 MWh of lithium-iron-phosphate (LFP) LIB on the rooftop of a shopping mall in Beijing, China. While the firefighters tried to extinguish the fire, an explosion occurred. The explosion led to the death of two firefighters. Due to limiting accidental information, the definite cause of the explosion is not known [5].

If Li-ion cells are over-charged, over-discharged, short-circuited, deformed, punctured, or exposed to heat, there is a possibility for a catastrophic failure [6–8]. A failing LIB can release gases such as hydrogen (H_2), carbon monoxide (CO), carbon dioxide (CO_2), methane (CH_4), electrolyte solvents, and toxic species [7,9–15]. When combustible gases mix with air, they can cause explosions and fires [16].

In recent years, researchers have experimentally and numerically investigated the explosion hazard abused LIBs pose by determining the released gas composition, gas release rates, and combustion properties of the gas vented [7,9,17–22]. Fernandes et al. [9] determined the gas composition and total amount of released gas from commercial Li-ion cells abused by overcharge. The study showed that the abused cells mainly released electrolyte solvent, along with hydrogen and other hydrocarbons. Henriksen et al. [18,19] experimentally determined the explosion characteristics of several Li-ion electrolyte solvents and the laminar burning velocity (LBV) for the solvent dimethyl carbonate (DMC). The Li-ion electrolyte solvents had similar explosion characteristics as propane, whereas DMC had a slightly lower LBV than propane.

Moreover, Baird et al. [20] numerically estimated the lower explosive limit, explosion pressure, rate of explosion pressure rise, and the LBV for various vented Li-ion gas compositions found in the literature. The study showed that LBV ranged from 0.3 m/s to 1.1 m/s, depending on the state of charge (SOC) and cell chemistry. Kennedy et al. [22] studied the release rates, total volume released, and gas composition from a single cell to an array of five and ten cells. The study showed that the venting speed, the total amount of gas released, and cell to cell propagation increased as the SOC increased. For a more compressive literature study, we suggest the articles by Fernandes et al. [9], Wang et al. [7], and Baird et al. [20].

Experimentally quantifying fundamental properties for failing LIBs is essential for understanding safety issues; however, it can be costly and time-consuming and can be partly incomplete. Computational fluid dynamics (CFD) simulations have become essential for evaluating explosion consequences and risks, especially in the process industry [23–26]. Using CFD tools such as FLACS, OpenFOAM, and ANSYS Fluent to predicting explosion pressures, blast loads (impulse), and gas dispersion can significantly improve the safety of a design. Most CFD simulations related to LIBs are on single-cell failure, single-cell thermal runaway characterization, and cell-to-cell propagation [27–29]. In a report by DNV GL [30], the LIB explosion hazard was investigated by CFD simulations of gas dispersion and gas explosions in maritime LIB installations. DNV GL reported explosion pressures between 90 kPa (gauge) and 270 kPa (gauge) in a partly confined geometry depending on the Li-ion gas release profile.

The benefits from simulations are heavily dependent on the prediction accuracy of the CFD models. Therefore, this study explores the prediction accuracy of the XiFoam combustion model/solver in the open-source CFD toolbox OpenFOAM [29,30]. More specifically, we analyze prediction accuracy of the temporal evolution of the pressure, maximum pressure peak, positive impulse, and the spatial evolution of the flame front for two gas compositions in a 1-meter-long explosion channel, partly filled with 18650 cell-like cylinders. In addition, two different channel geometries were studied by varying the location of an identical set of 40 18650 cell-like cylinders. The prediction accuracy with an early-onset for turbulent flame propagation was investigated with the cylinders close to the ignitions source. Whereas with the cylinders in the center, i.e., further away from the ignition source, the prediction accuracy with an initial laminar flame propagation stage could be examined.

Finally, in addition to two gas compositions and the two geometries, the CFD simulations were compared at three different fuel-air equivalence ratios (ϕ) 0.8, 1.0, and 1.2, resulting in a total of 12 simulation cases. The numerical and experimental condition was typical atmospheric conditions, 293 K and 101.3 kPa (absolute).

2. MATERIALS AND METHODS

2.1. Experimental Setup

The explosion channel's length, width, and height are 1000.0 mm, 65.0 mm, and 116.5 mm, respectively. Two different channel setups were analyzed. The channel setup referred to as the inner channel geometry had 40 18650 cell-like cylinders near the closed end of the channel, whereas the channel setup referred to as the center channel geometry had 40 18650 cell-like cylinders approximately in the center of the channel. Each cylinder has a diameter of 18 mm and a length of 650 mm, the same dimensions as a 18650 Li-ion cell. Furthermore, the distance between the cells in the vertical and horizontal direction is 4.6 mm (±0.1 mm), creating a 0.5 void ratio and maximum blockage ratio of 0.77 in the obstructed part of the channel. For the inner channel geometry, the center of the first column of cylinders was 40 mm from the closed end of the channel. The center of the first column of cells was 400 mm from the closed end of the channel for the center channel geometry. Figure 1 a) shows a photo of the explosion channel with the center channel geometry, and Figure 1 b) shows a schematic illustration of the experimental setup with dimensions.

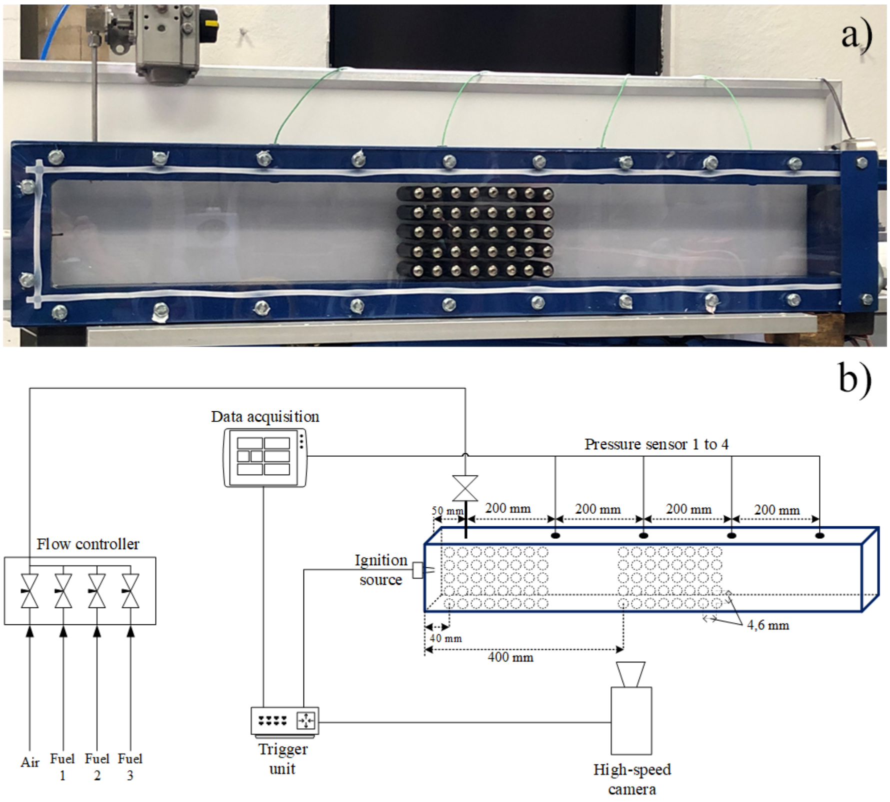

Figure 1. Photo and schematic illustration of the 1-meter explosion channel. a): Photo of explosion channel with the Li-ion 18650 cell-like cylinders in the center of the channel; b): Schematic illustration of the experimental setup with dimensions.

The premixed fuel-air inlet is located 50 mm from the closed end of the channel. With a porous lid attached to the open end of the channel, the channel's volume was exchanged eight times to ensure a homogenous mixture. After filling, there was a one-minute delay before ignition to reduce convective flow. Moreover, the ignition duration was 0.02 s, which gives two sparks generated from an AC transformer with an output voltage of 10 kV and a current of 20 mA. At the top of the channel, four Kistler pressure transducers spaced 250, 450, 650, and 850 mm from the closed end of the channel recorded the explosion pressure. A Photron SA-1 high-speed camera records the flame propagation with frame rates ranging from 10 000 and 22 500 frames per second, depending on the flame propagation speed.

The gas compositions shown in Table 1 are taken from a previously published study by Henriksen et al. [21]. The High LBV Li-ion gas composition has a relatively high LBV compared to other published Li-ion vent gas compositions [20,21], and the Simplified Li-ion gas composition is a pseudo/simplified Li-ion vent gas, which has an LBV in the same range as several different types of LIBs [21]. The High LBV Li-ion gas was supplied from a premixed gas bottle prepared by a supplier, whereas two separate gas bottles supplied the hydrogen and methane for the Simplified Li-ion gas. Furthermore, the ϕ and the fuel ratio in the Simplified Li-ion gas were controlled by adjusting separate rotameters for the fuel and air. All the gas bottles had a purity above 99.95%.

Table 1. The gas compositions analyzed numerically and experimentally in this study in volume percentage.

Name of fuel mixture	H_2 [%]	CO [%]	CO_2 [%]	CH_4 [%]	C_2H_4 [%]
High LBV Li-ion gas	42.8	37.1	10.0	7.1	3.0
Simplified Li-ion gas	35.0	[-]	[-]	65.0	[-]

The flame front position and velocity were determined using an in-house developed image processing code from the high-speed video. The pressure data, flame front position, and velocity were post-processed by a Savitzky-Golay filter [31] before further analysis.

2.2. CFD Simulation

The XiFoam model/solver, part of the OpenFOAM toolbox's [32,33] official release, was used for all simulations. In XiFoam, the flame is modeled as a laminar flamelet, which assumes that the turbulent premixed flame comprises a group of laminar flamelets [34]. With the laminar flamelet approach, a regress variable (b) can express the flame propagation. Eq. 1 shows the transport equation for regress variable b implemented in the XiFoam model.

$$\frac{\partial}{\partial t}(\rho b) + \nabla.(\rho \boldsymbol{U} b) + \nabla.(\rho D \nabla b) = -\rho_u S_u \Xi |\nabla b| \qquad \textit{Eq. 1}$$

Where: b – reaction regress variable [-], ρ – density [kg/m^3], $\boldsymbol{U}$ – velocity vector [m/s], D – diffusion coefficient [m^2/s], S_u – laminar burning velocity (LBV) [m/s], Ξ – turbulent and laminar flame speed ratio [-].

The LBV (S_u) in the source term in Eq. 1 is calculated from the Gülder equation [35]. Ξ models the contribution which the subgrid turbulence has on the flame speed. Eq. 2 shows the transport equation for Ξ. Additional information about the XiFoam combustion model can be found in the original publications by Weller et al. [36,37].

$$\frac{\partial \Xi}{\partial t} + \widehat{U}_s \cdot \nabla \Xi = \mathrm{G}\Xi - \mathrm{R}(\Xi - 1) + (\sigma_s - \sigma_t)\Xi \qquad \textit{Eq. 2}$$

Where: Ξ is the subgrid wrinkling factor; U_s is the surface filter velocity; G is the turbulence generation rate; R is the turbulence removal rate; σ_s is the surface-filtered strain rate; σ_t is the resolved strain rate

To determine the discretized schemes and model parameters to apply for all simulations, we simulated the High LBV Li-ion gas at ϕ equal to 1.0 with the center channel geometry and compared the results to an experiment with similar conditions (case 38). For the comparison, the focus was on the flame propagation and explosion pressure in pressure sensor 1 (PS1). This comparison led to the following discretized schemes and models presented.

The time integration was discretized using the second-order Crank-Nicolson scheme with a ratio of 0.6 forward Euler and 0.4 Crank-Nicolson. For the gradient and Laplacian/diffusion terms, the second-order linear scheme was used. Furthermore, the three different second-order schemes, linear, linear-upwind, and limited-linear, were used for the divergence schemes. The discretized equations are solved using the PIMPLE algorithm, a combination of PISO (Pressure Implicit with Splitting Operators) and SIMPLE (Semi-Implicit Method for Pressure-Linked Equations).

Large-eddy simulation (LES) was chosen as the turbulence approach, using the subgrid model proposed by Akira Yoshizawa [38] for compressible turbulent shear flows. The Van-Driest dampening function was used for wall turbulence treatment, with the A^+ coefficient and ΔC equal 26 and 0.158, respectively.

The combustion, transport, and thermodynamic properties were generated using the *mech2Foam* code [39]. *mech2Foam* generates the NASA polynomial [40], Sutherland [41], and Gülder coefficients using a specified reaction mechanism. A study by Henriksen et al. [21] has demonstrated that the GRI-Mech 3.0 reaction mechanism accurately predicts the LBV for the two gas compositions in Table 1, and therefore use in this study.

Two computer-aided design (CAD) geometries were drawn, with the exact dimensions as the experimental channel geometries. The initial cell size is set by the background mesh generated in the utility blochMesh, with the initial cell size in the channel of 4 mm in all directions. At the open end of the channel, the cell size expands linearly in all directions to 8 mm, creating a rectangular frustum with a length of 500 mm outside the rectangular channel, as illustrated in Figure 2 a). Using the snappyHexMesh utility in OpenFOAM, the background mesh is snapped to the CAD drawing and refined to three layers with half the initial cell size at the channel walls. At the cylinder/cell walls, the first three layers have a fourth of the initial cell size, followed by an additional three layers with half the initial cell size, as shown in Figure 2 c). The total amount of cells for the inner and center channel geometry was 944 849 and 945 843, respectively.

Figure 2 a) shows that the boundaries are divided into two domains, wall boundaries and open boundaries. Typical wall boundary conditions (grey part of Figure 2 a)) were set on the channel walls, and typical open boundary conditions (black part of Figure 2 a)) were set on the boundaries outside the channel. A volume outside the channel was included in the computational domain to reduce errors caused by the outlet boundary conditions. Inside the channel, the species were premixed fuel and air, and outside of the channel, there was only air. The atmospheric conditions for the simulations were 293 K and 101.3 kPa (absolute), similar to the overall experimental conditions. Table 2 lists all the wall and open boundary conditions used for each variable in the simulations.

Table 2. List of variables with the applied wall and open boundary conditions.

Variable	**Wall boundary**	**Open boundary**
Temperature (T)	Adiabatic walls (zero gradient) (293 K)	zero gradient outlet fixed value inlet (T = 293)
Temperature unburnt (T_u)	Adiabatic walls (zero gradient) (293 K)	zero gradient outlet fixed value inlet (T_u) = 293)
Pressure (p)	zero gradient at the wall	a constant total pressure, dynamic + static pressure equals 101.3 kPa.
Velocity (U)	zero velocity at the wall (noSlip)	zero gradient outlet; inlet value based on flux normal to the boundary surface
LBV (S_u)	zero gradient at the wall	zero gradient at the boundary surface
Subgrid turbulent kinetic energy (k)	zero gradient at the wall	zero gradient at the boundary surface
Turbulent, LBV ratio (Xi)	zero gradient at the wall	zero gradient at the boundary surface
regress variable (b)	zero gradient at the wall	zero gradient at the boundary surface
Fuel mixture fraction (ft)	zero gradient at wall	zero gradient outlet fixed value inlet (ft = 0)
Turbulent viscosity (nut)	calculated based on the turbulent kinetic energy	calculated based on the turbulent properties
Turbulent thermal diffusivity (alphat)	calculated based on the turbulent viscosity for compressible flow	calculated based on the turbulent viscosity

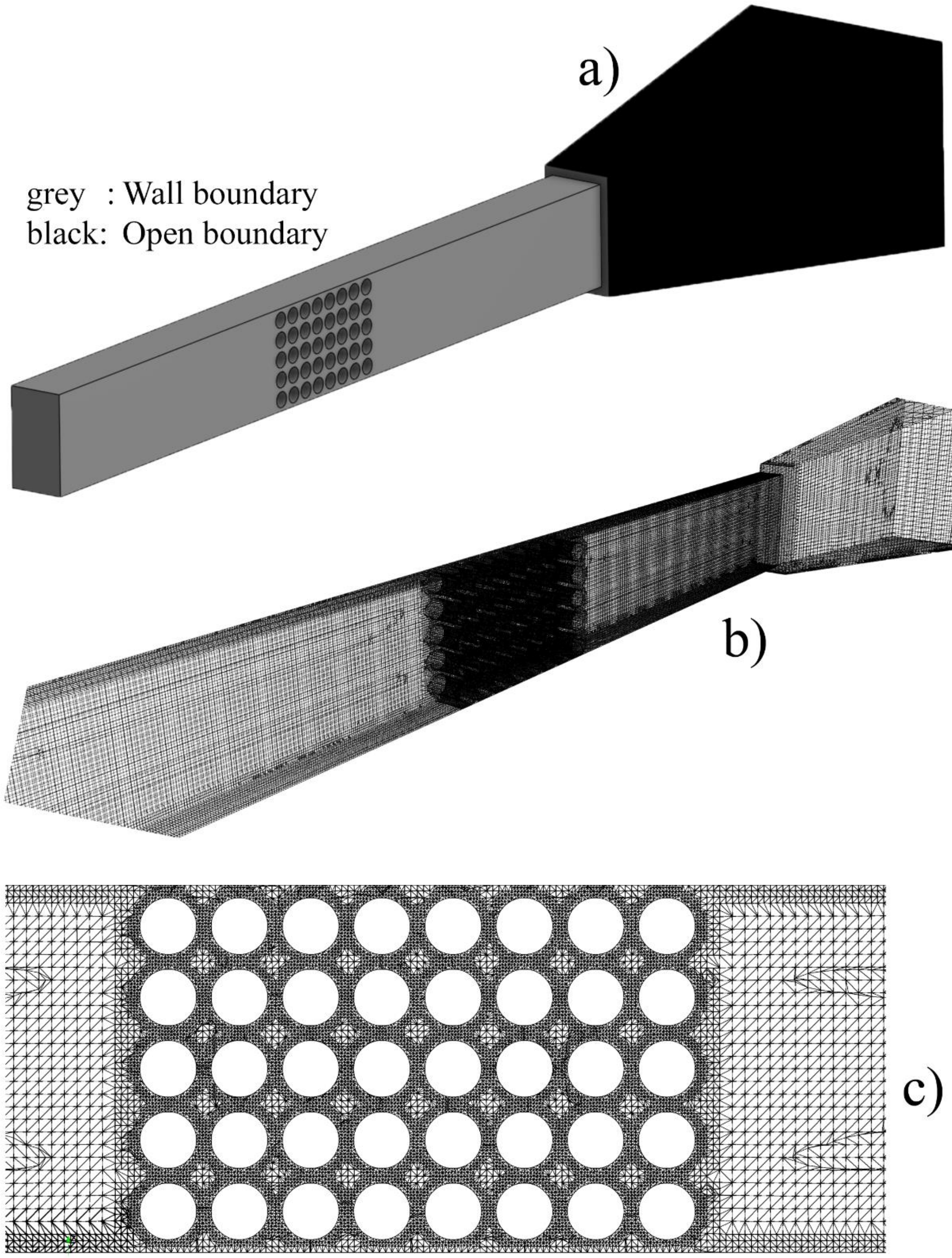

Figure 2. Images of the geometry and computational mesh used in numerical simulations. a) Side view of the entire CAD geometry with boundary conditions. b) Side view of the computational mesh. c) Horizontal cross-section view of the computational mesh cell geometry

Finally, we referred to the OpenFOAM user guide to further explain the boundary conditions and discretization schemes [32]. The CFD base case is given in the supplementary materials.

In Table 3, all the experimental cases are listed, with gas composition, ϕ, channel geometry, and the corresponding CFD simulation case name.

Table 3. List of all experiments with the corresponding CFD simulations.

Experiment Case Number	Gas Composition	Fuel-Air Equivalence ratio (ϕ)	Channel Geometry	CFD Case Name
Case 01.	High LBV Li-ion gas	0.79	Inner	High CFD 0.8 Inner
Case 02.	High LBV Li-ion gas	0.89	Inner	None
Case 03.	High LBV Li-ion gas	1.00	Inner	High CFD 1.0 Inner
Case 04.	High LBV Li-ion gas	1.09	Inner	None
Case 05.	High LBV Li-ion gas	1.18	Inner	High CFD 1.2 Inner
Case 06.	High LBV Li-ion gas	1.18	Inner	High CFD 1.2 Inner
Case 07.	High LBV Li-ion gas	1.29	Inner	None
Case 08.	High LBV Li-ion gas	1.29	Inner	None
Case 09.	High LBV Li-ion gas	1.38	Inner	None
Case 10.	High LBV Li-ion gas	1.38	Inner	None
Case 11.	High LBV Li-ion gas	1.47	Inner	None
Case 12.	High LBV Li-ion gas	1.47	Inner	None
Case 13.	Simplified Li-ion gas	0.69	Inner	None
Case 14.	Simplified Li-ion gas	0.69	Inner	None
Case 15.	Simplified Li-ion gas	0.79	Inner	Simple CFD 0.8 Inner
Case 16.	Simplified Li-ion gas	0.79	Inner	Simple CFD 0.8 Inner
Case 17.	Simplified Li-ion gas	0.90	Inner	None
Case 18.	Simplified Li-ion gas	0.90	Inner	None
Case 19.	Simplified Li-ion gas	0.90	Inner	None
Case 20.	Simplified Li-ion gas	0.97	Inner	Simple CFD 1.0 Inner
Case 21	Simplified Li-ion gas	0.97	Inner	Simple CFD 1.0 Inner
Case 22.	Simplified Li-ion gas	1.01	Inner	Simple CFD 1.0 Inner
Case 23.	Simplified Li-ion gas	1.01	Inner	Simple CFD 1.0 Inner
Case 24.	Simplified Li-ion gas	1.08	Inner	None
Case 25.	Simplified Li-ion gas	1.10	Inner	None
Case 26.	Simplified Li-ion gas	1.10	Inner	None
Case 27.	Simplified Li-ion gas	1.19	Inner	Simple CFD 1.2 Inner
Case 28.	Simplified Li-ion gas	1.19	Inner	Simple CFD 1.2 Inner
Case 29.	Simplified Li-ion gas	1.26	Inner	None
Case 30.	Simplified Li-ion gas	1.29	Inner	None
Case 31.	Simplified Li-ion gas	1.37	Inner	None
Case 32.	Simplified Li-ion gas	1.39	Inner	None
Case 33.	High LBV Li-ion gas	0.79	Center	High CFD 0.8 Center
Case 34.	High LBV Li-ion gas	0.89	Center	None
Case 35.	High LBV Li-ion gas	0.89	Center	None
Case 36.	High LBV Li-ion gas	0.97	Center	High CFD 1.0 Center
Case 37.	High LBV Li-ion gas	0.98	Center	High CFD 1.0 Center
Case 38.	High LBV Li-ion gas	0.98	Center	High CFD 1.0 Center
Case 39.	High LBV Li-ion gas	1.08	Center	None
Case 40.	High LBV Li-ion gas	1.09	Center	None
Case 41.	High LBV Li-ion gas	1.09	Center	None
Case 42.	High LBV Li-ion gas	1.18	Center	High CFD 1.2 Center
Case 43.	High LBV Li-ion gas	1.18	Center	High CFD 1.2 Center
Case 44.	High LBV Li-ion gas	1.29	Center	None
Case 45.	High LBV Li-ion gas	1.29	Center	None
Case 46.	High LBV Li-ion gas	1.38	Center	None
Case 47.	High LBV Li-ion gas	1.38	Center	None
Case 48.	High LBV Li-ion gas	1.47	Center	None
Case 49.	High LBV Li-ion gas	1.47	Center	None
Case 50.	Simplified Li-ion gas	0.69	Center	None
Case 51.	Simplified Li-ion gas	0.69	Center	None
Case 52.	Simplified Li-ion gas	0.79	Center	Simple CFD 0.8 Center
Case 53.	Simplified Li-ion gas	0.79	Center	Simple CFD 0.8 Center
Case 54.	Simplified Li-ion gas	0.79	Center	Simple CFD 0.8 Center
Case 55.	Simplified Li-ion gas	0.90	Center	None
Case 56.	Simplified Li-ion gas	0.90	Center	None
Case 57.	Simplified Li-ion gas	1.01	Center	Simple CFD 1.0 Center
Case 58.	Simplified Li-ion gas	1.01	Center	Simple CFD 1.0 Center
Case 59.	Simplified Li-ion gas	1.10	Center	None
Case 60.	Simplified Li-ion gas	1.10	Center	None
Case 61.	Simplified Li-ion gas	1.10	Center	None
Case 62.	Simplified Li-ion gas	1.19	Center	Simple CFD 1.2 Center
Case 63.	Simplified Li-ion gas	1.19	Center	None
Case 64.	Simplified Li-ion gas	1.19	Center	None
Case 65.	Simplified Li-ion gas	1.26	Center	None
Case 66.	Simplified Li-ion gas	1.26	Center	None
Case 67.	Simplified Li-ion gas	1.26	Center	None
Case 68.	Simplified Li-ion gas	1.37	Center	None
Case 69.	Simplified Li-ion gas	1.37	Center	None
Case 70.	Simplified Li-ion gas	1.37	Center	None

3. RESULTS

The model parameters and discretization schemes used for all simulations were determined by comparing the experimental Case 38 and the High CFD 1.0 center simulation case. Figure 3 compares the recorded pressure from the four pressure sensors (PS) for these two cases. The simulated explosion pressure at PS1 was used as one of the target parameters in the optimization, and therefore has the lowest deviation of the four pressure sensors. PS4 had the highest difference in the maximum pressure peak of 117 kPa and a relative deviation of 61%.

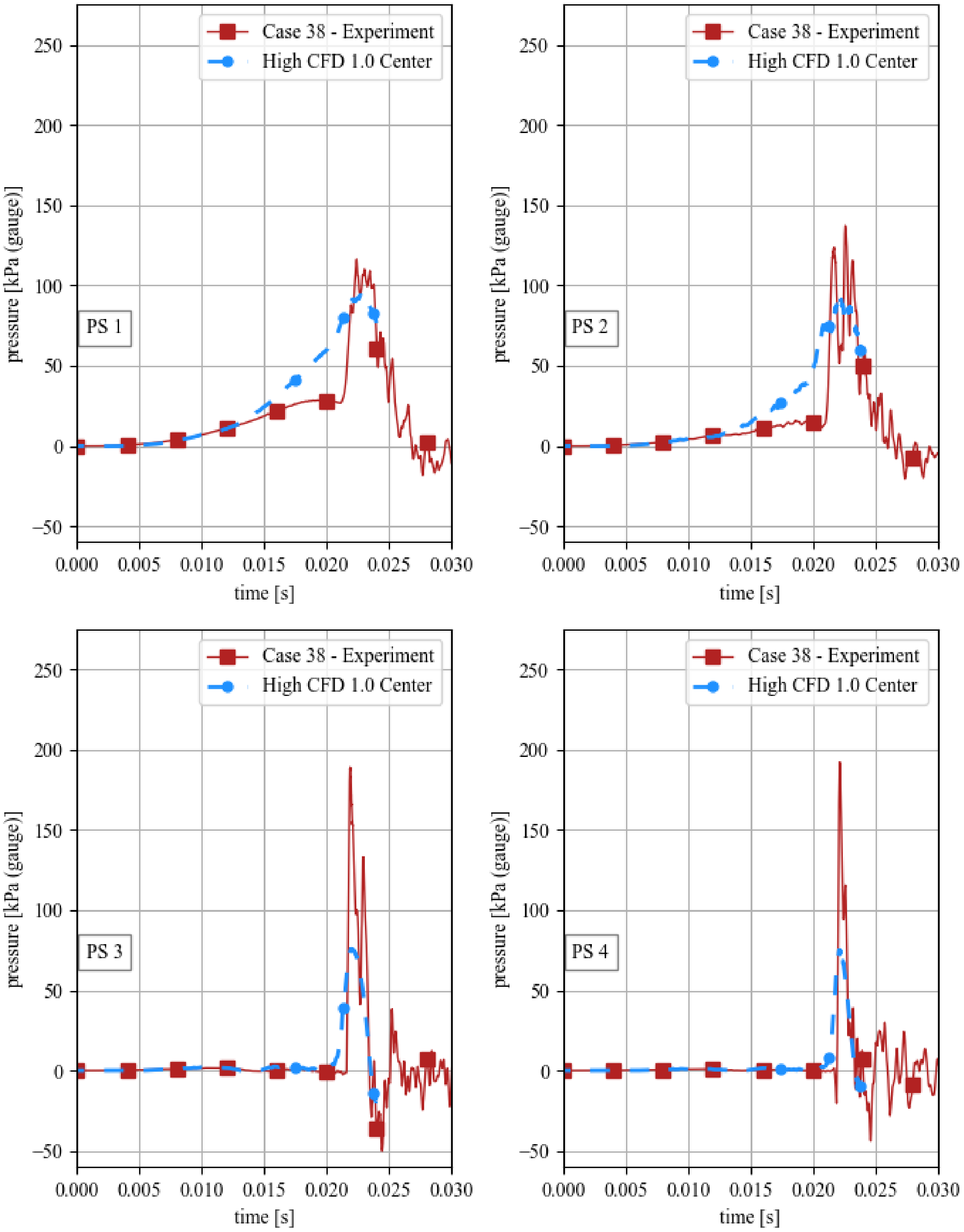

Figure 3. Comparison of the temporal evolution of the pressure for the four pressure sensors (PS1, PS2, PS3, and PS4) for Case 38 and the simulated case High CFD 1.0 center.

Figure 4 shows the comparison of Case 38 and the simulation case High CFD 1.0 center for the temporal flame front position and flame front velocity and the spatial flame front velocity. The flame front position in Figure 4 a) shows a good agreement between the simulated and experimental results. Figure 4 b) and c) shows that the simulated flame acceleration is under-predicted after the flame reaches the cylinders.

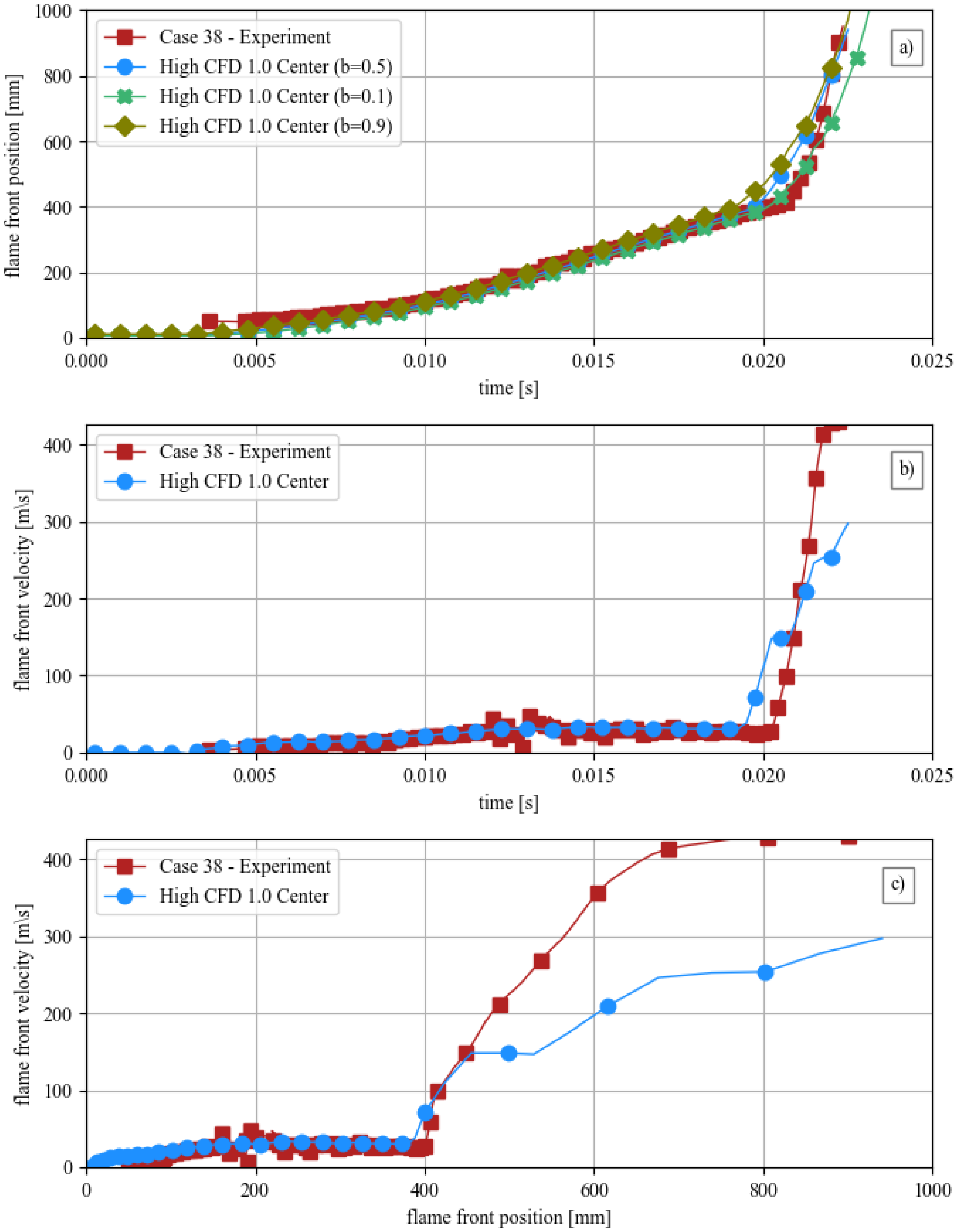

Figure 4. Comparison of experimental Case 38 and the simulation case High CFD 1.0 center. a): Comparison of the temporal evolution of the flame front position; b): Comparison of the temporal evolution of the flame front velocity; c): Comparison of the spatial evolution of the flame front velocity.

Figure 5 shows the numerical and experimental maximum pressure peaks for each pressure sensor recorded in the inner channel geometry for the High LBV Li-ion gas and the Simplified Li-ion gas. The highest maximum pressure for the High LBV Li-ion gas was 156 kPa (gauge), recorded at PS3 in case 10 (ϕ = 1.38). In the numerical simulations, the highest maximum pressure of 89 kPa (gauge) was in the High CFD 1.2 Inner case. Furthermore, the average absolute deviation between the experimental and simulated maximum pressures for the High LBV Li-ion gas is 38 kPa, with a maximum absolute deviation of 64 kPa for case 05 (at PS4).

For the Simplified Li-ion gas experiments, the highest maximum pressure peak was 56 kPa (gauge) (at PS1) in case 26 (ϕ = 1.10). The highest simulated maximum pressure was 77 kPa (gauge) (at PS2) in the Simple CFD 1.0 Inner case. Finally, the average absolute deviation between the experiments and simulations for the Simplified Li-ion gas was 14 kPa, with a maximum deviation of 28 kPa for case 21 (at PS2).

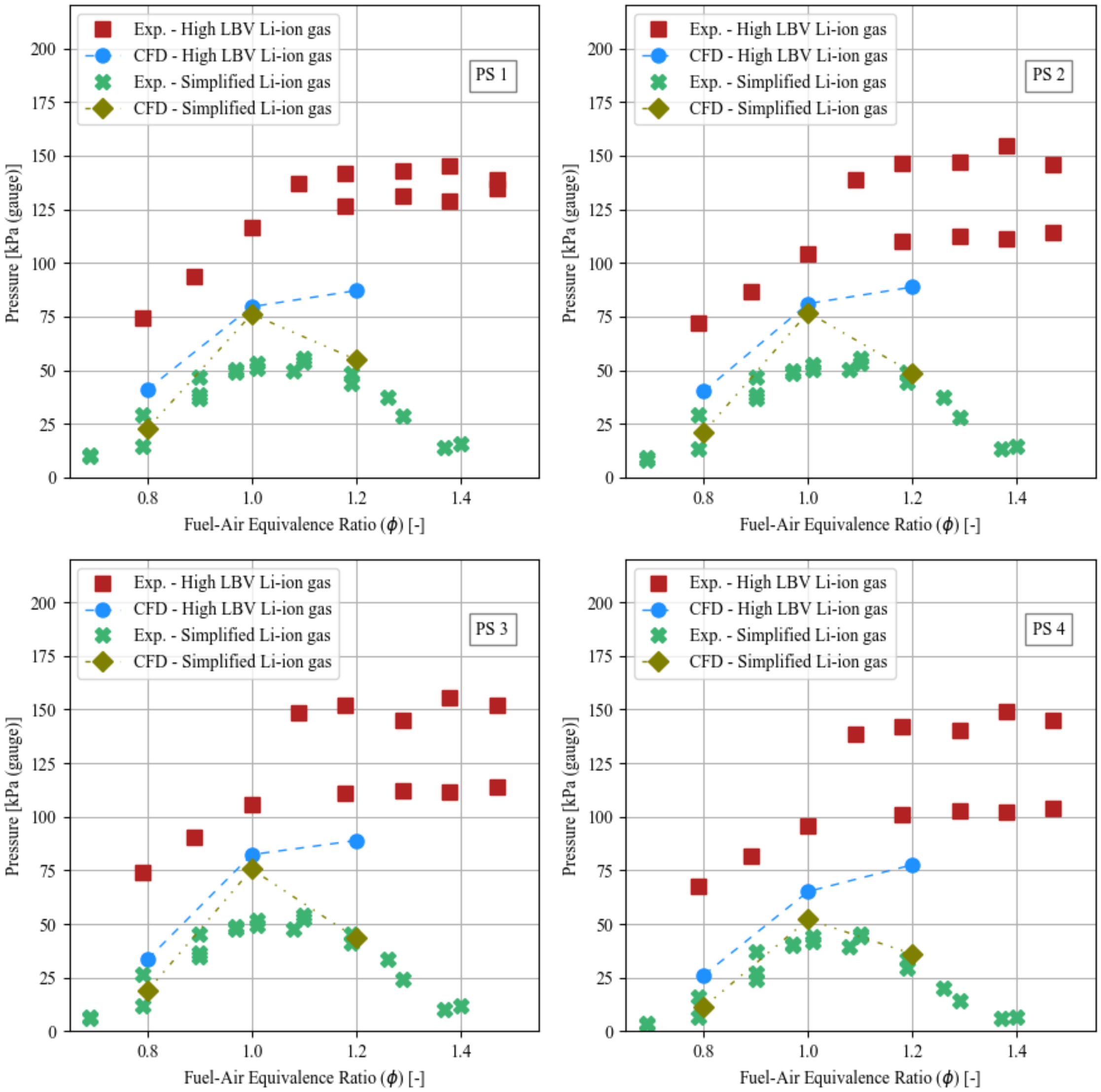

Figure 5. The maximum pressure peak for each pressure sensor for the inner channel geometry High LBV Li-ion gas and the Simplified Li-ion gas experiments and numerical simulations.

Figure 6 shows the simulated and experimental maximum pressure peaks from the center channel geometry for each pressure sensor. For the High LBV Li-ion gas, the highest experimental maximum pressure of 223 kPa (gauge) was measured at PS3 for case 41 ($\phi = 1.09$), and the highest simulated maximum pressure of 94 kPa (gauge) was measured at PS1 for the High CFD 1.2 Center case. Moreover, the average absolute deviance between the experimental and numerical results was 64 kPa, with a maximum absolute deviation of 137 kPa for case 43 (at PS3).

The highest maximum pressure peaks for the Simplified Li-ion gas were 55 kPa (gauge) measured at PS1 in case 58 ($\phi = 1.01$) and 119 kPa (gauge) at PS1 in simulation case Simple CFD 1.0 Center. The average absolute deviation was 50 kPa, and the maximum absolute deviation was 97 kPa PS1 for case 62.

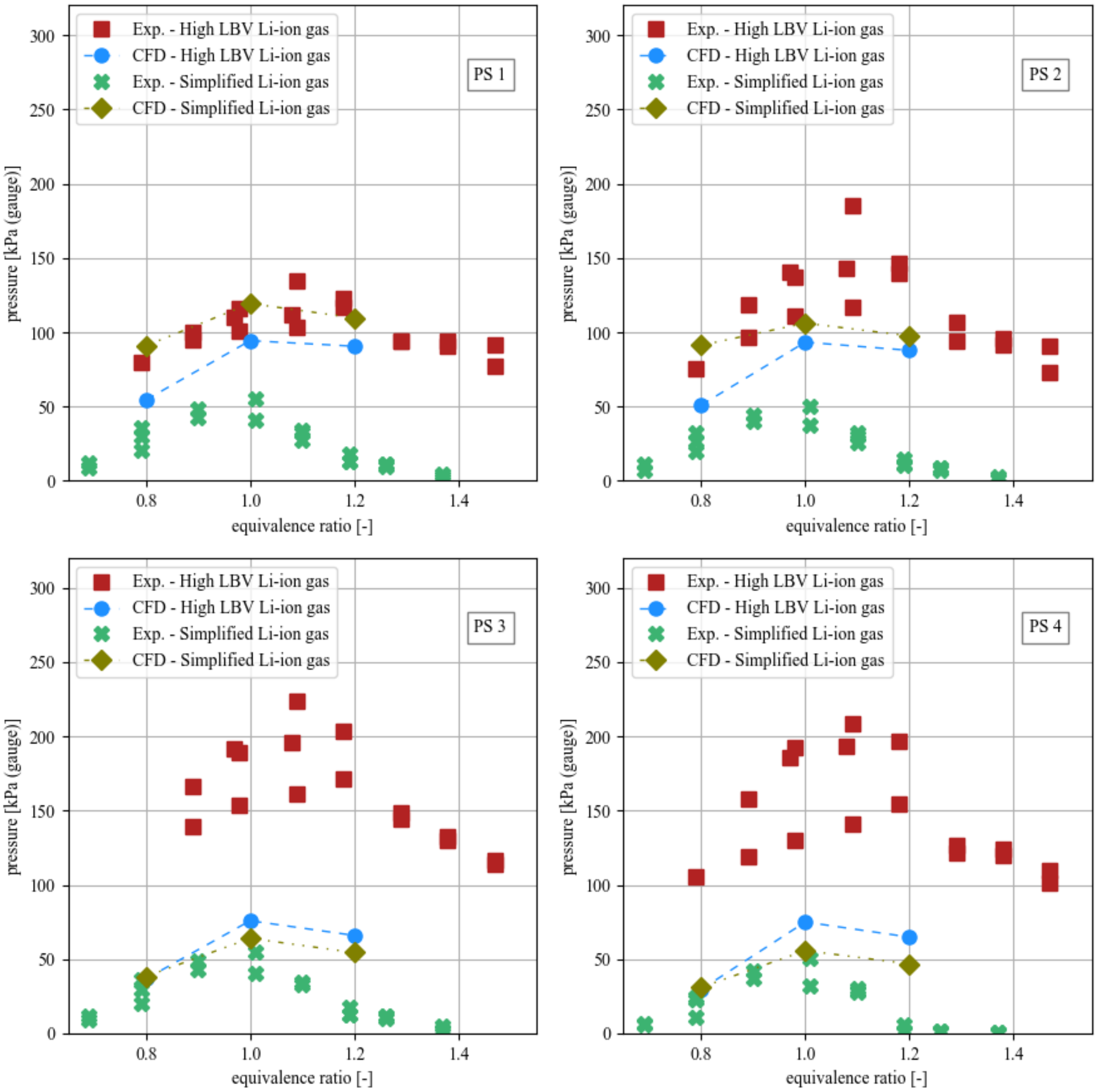

Figure 6. The maximum pressure peak for each pressure sensor for the center channel geometry High LBV Li-ion gas and the Simplified Li-ion gas experiments and numerical simulations.

Figure 7 shows the positive impulses for each pressure sensor for the inner channel geometry experiments and simulations. The positive impulse was calculated by numerically integrating the maximum pressure peak, with the upper and lower integral limits set to one-tenth of the maximum pressure. All maximum values for the experimental and simulated positive impulses were recorded on the first pressure sensor (PS1) for both gas compositions.

The maximum experimental positive impulse was 188 kPa·ms and 160 kPa·ms for the High LBV Li-ion gas (case 11, $\phi = 1.47$) and the Simplified Li-ion gas (case 26, $\phi = 1.10$) in the inner channel geometry, respectively. In the simulations, the maximum positive impulse was 313 kPa·ms (High CFD 1.2 Inner) and 280 kPa·ms (Simple CFD 1.0 Inner) for the High LBV Li-ion gas and the Simplified Li-ion gas, respectively. The absolute average deviation between simulation and experimental positive impulse results for the High LBV Li-ion gas was 100 kPa·ms, whereas 82 kPa·ms for the Simplified Li-ion gas. Furthermore, the maximum absolute deviation was 171 kPa·ms (case 06, at PS2) and 144 kPa·ms (case 20, at PS1) for the High LBV Li-ion gas and Simplified Li-ion gas, respectively.

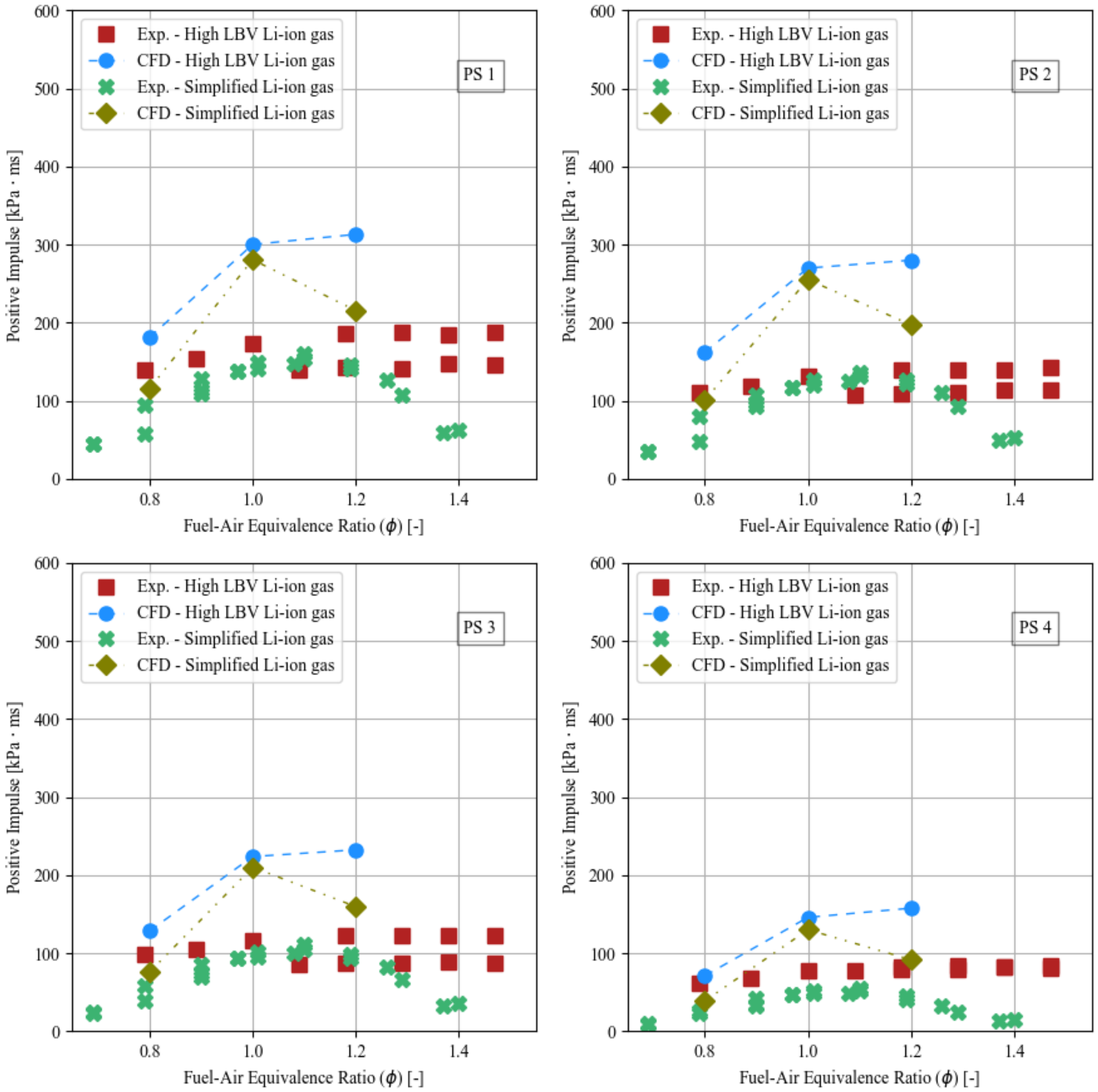

Figure 7. The positive impulse for each pressure sensor for the inner channel geometry High LBV Li-ion gas and the Simplified Li-ion gas experiments and numerical simulations.

Figure 8 shows the experimental and numerically positive impulses for each pressure sensor for all center channel geometry cases. All maximum positive impulses were recorded on the first pressure sensor (PS1) for both gas compositions in the experiments and numerical simulations, like the inner channel geometry cases. For the High LBV Li-ion gas, the experimental maximum positive impulse was 591 kPa·ms (case 42, $\phi = 1.18$), whereas in the simulation, 666 kPa·ms for case High CFD 1.2 Center. The absolute average deviation between the simulation and experiments for the High LBV Li-ion gas was 100 kPa·ms, with a maximum absolute deviation of 243 kPa·ms for case 36 (at PS2).

For the Simplified Li-ion gas, the experimental maximum positive impulse was 324 kPa·ms (case 58, ϕ = 1.01). In the simulation, the maximum positive impulse was 743 kPa·ms measured in the Simple CFD 1.0 Center case. Moreover, the absolute average deviation between the experimental and numerical positive impulse is 206 kPa·ms, with a maximum absolute deviation of 532 kPa·ms in case 62 (at PS1).

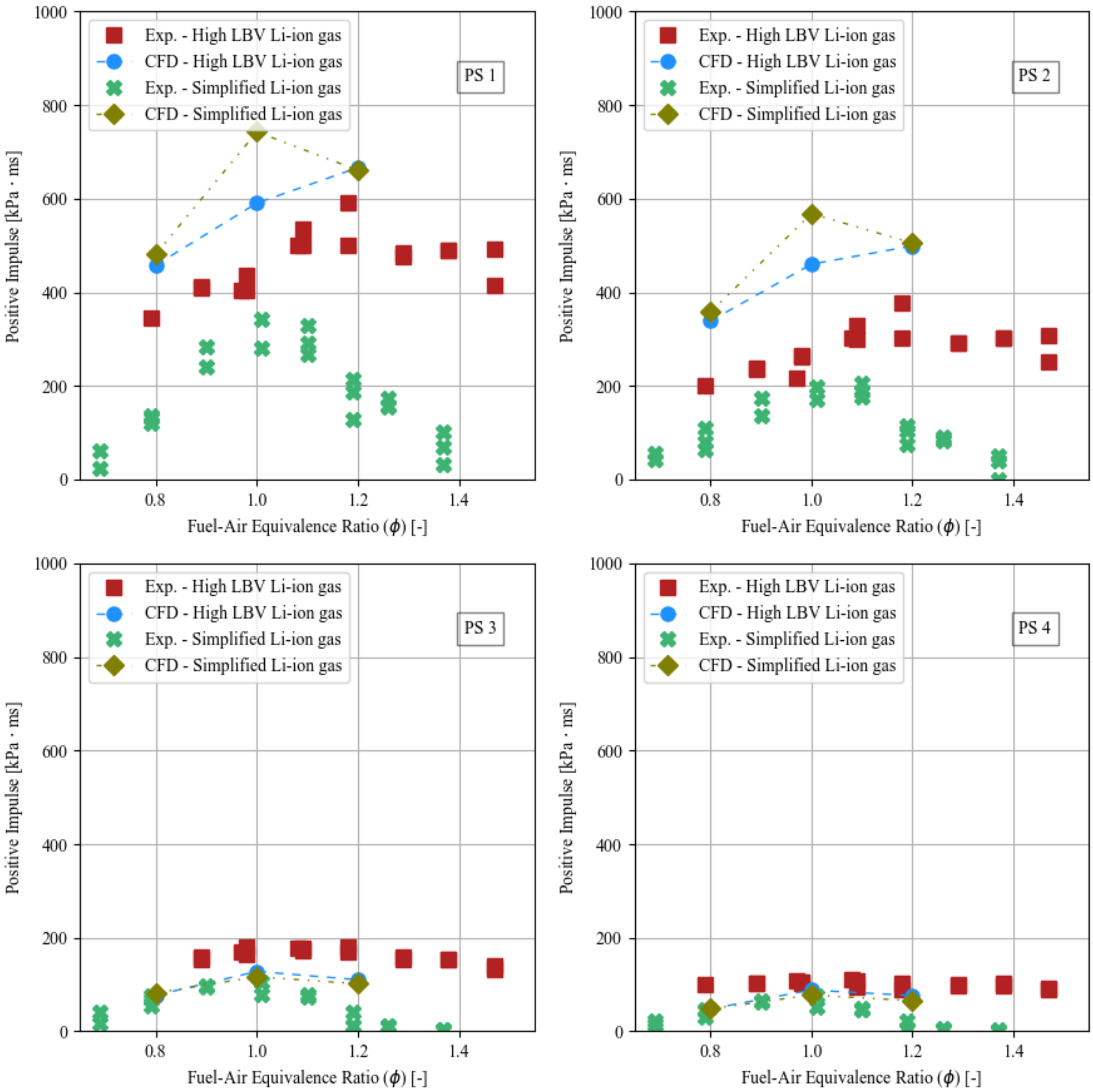

Figure 8. The positive impulse for each pressure sensor for the center channel geometry High LBV Li-ion gas and the Simplified Li-ion gas experiments and numerical simulations.

Further quantification of the model performance was done by calculating the statistical quantities, mean geometric variance (VG), and mean geometric bias (MG) for the temporal pressure evolution, maximum pressure, positive impulse, and spatial evolution of the flame front velocity. Table 4 presents the criteria used to assess the model performance, taken from the model evaluation protocol for the HySEA project [42], which is based upon the MEGGE protocol [43].

Table 4. Criteria for evaluating model performance for a specific variable from the model evaluation protocol for the HySEA project [42].

The scale of Model Performance	**MG and VG Limits**	
Excellent	$0.7 < MG < 1.3$ $VG < 1.6$	[Solid vertical lines] [Solid horizontal line]
Acceptable	$0.5 < MG < 2.0$ $VG < 3.3$	[Dashed vertical lines] [Dashed horizontal line]
Poor	$0.5 > MG > 2.0$ $VG > 3.3$	

Figure 9 shows the MG and VG values for the inner channel geometry High LBV Li-ion gas and Simplified Li-ion gas cases. The calculated VG and MG values for the temporal pressure evolution are within the limit for excellent model performance, as shown in Figure 9 a). For the MG and VG values in Figure 9 b) (maximum pressure peak), only case 42 had an MG value slightly above the limit for excellent model performance. The MG and VG values shown in Figure 9 a) and b) indicate that the XiFoam model predicted the maximum pressure peaks and temporal pressure evolution accurately for both gas compositions in the inner channel geometry. For several cases, the MG values for the positive impulse were outside the acceptable limit. The spatial flame front velocity MG and VG values were within the acceptable limits for all, except case 15.

The overall XiFoam model performance was evaluated by equally weighting the arithmetic mean MG and VG values of the temporal pressure evolution, maximum pressure peaks, positive impulse, and spatial evolution of the flame front velocity. For the inner channel geometry, the overall average MG and VG were 0.96 and 1.26 for the High LBV Li-ion gas, respectively, whereas the overall average MG and VG for the Simplified Li-ion gas were 0.89 and 1.36, respectively. Both the overall averaged MG and VG for the two gas compositions are within the acceptable performance criteria.

Figure 10 shows the MG and VG values for the center channel geometry cases. The MG and VG values for the temporal pressure evolution and the maximum pressure are all within the acceptable criteria for both gas compositions. The positive impulse MG and VG values for the High LBV Li-ion cases are all within the excellent performance criterion. However, for the Simplified Li-ion gas, only case 57 is within the MG acceptable criterion. This poor model performance is reflected in the predicted positive impulse of the Simplified Li-ion gas in Figure 8. For all cases, the spatial evolution of the flame front velocity MG and VG values are within the acceptable criteria for both gas compositions, with seven out of ten within the excellent criteria.

The overall averaged MG and VG values were 1.10 and 1.14 for the High LBV Li-ion gas, respectively. For the Simplified Li-ion gas, the overall average MG and VG values were 0.80 1.86, respectively. Furthermore, the overall average MG and VG values were within the excellent performance criteria for the High LBV Li-ion gas. For the Simplified Li-ion gas, the overall average MG and VG were within acceptable model performance criteria.

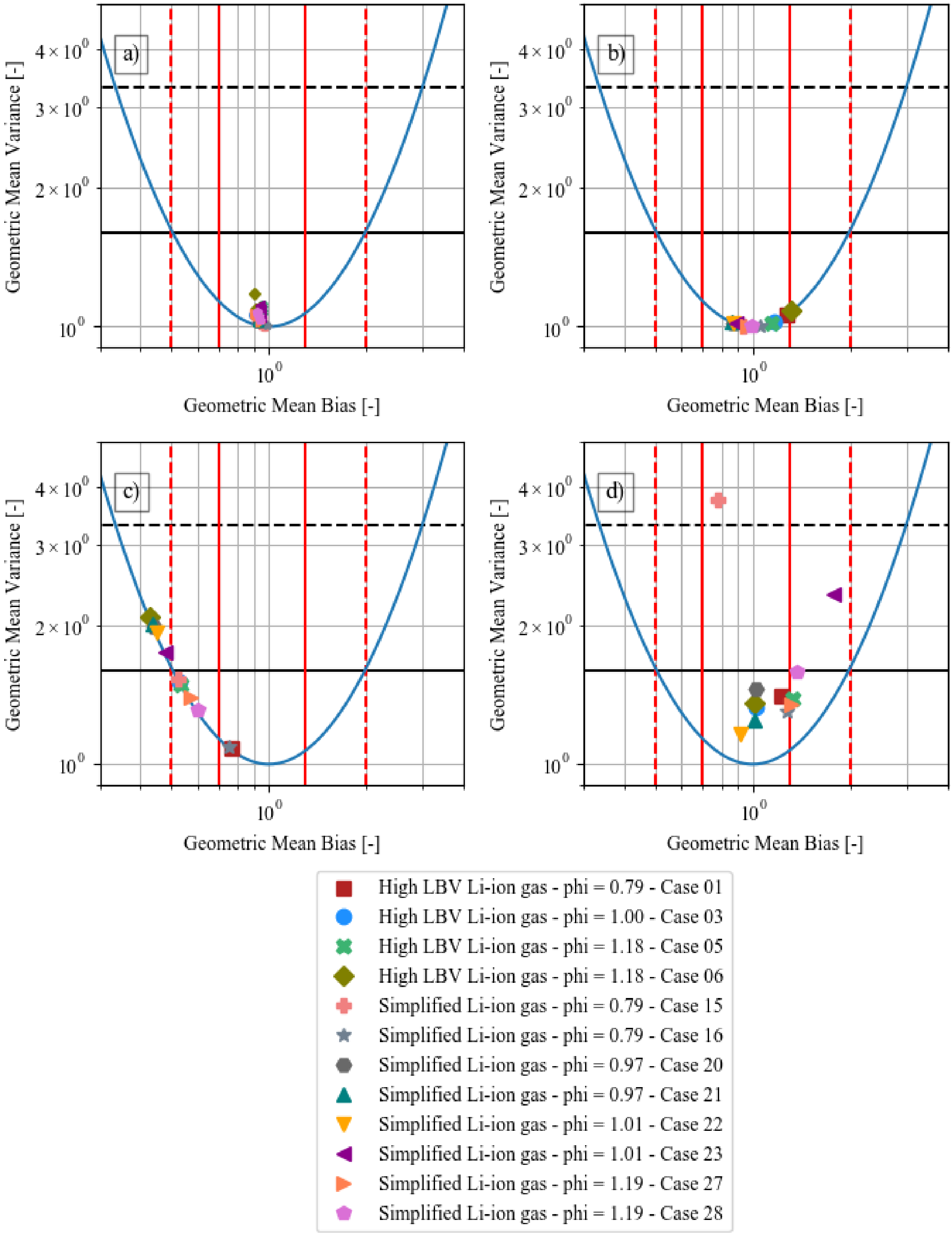

Figure 9. The mean geometric bias and the mean geometric variance for the High LBV Li-ion gas and the Simplified Li-ion gas in the inner channel geometry; a) Temporal pressure evolution; b) Maximum pressure; c) Positive impulse; d) Spatial evolution of the flame front velocity

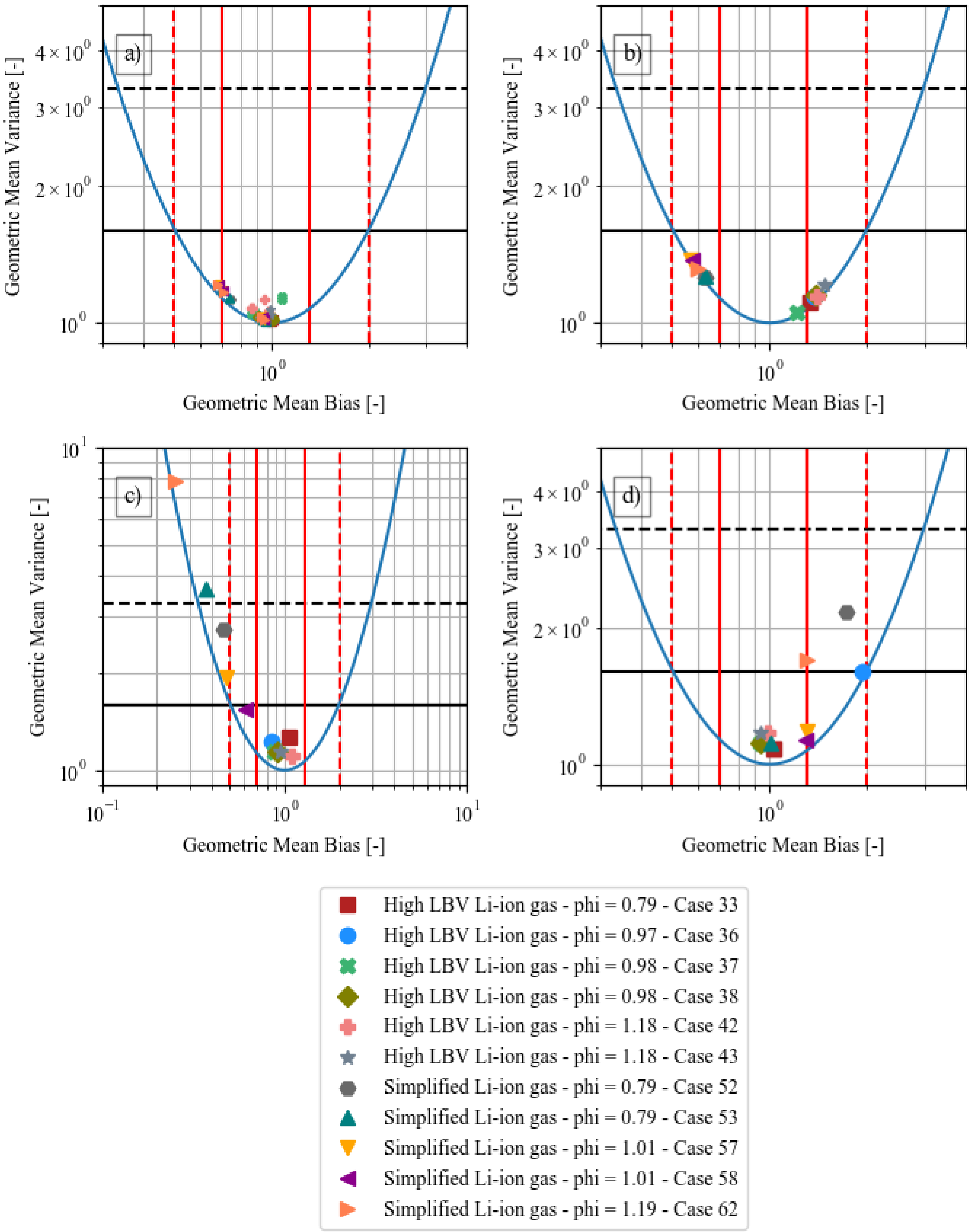

Figure 10. The mean geometric bias and the mean geometric variance for the High LBV Li-ion gas and the Simplified Li-ion gas in the center channel geometry; a) Temporal pressure evolution; b) Maximum pressure; c) Positive impulse; d) Spatial evolution of the flame front velocity

For the unfiltered experimental results, we refer to the dataset *Experiments of Premixed Gas Explosion in a 1-meter Channel Partly Filled with 18650 Cell Geometry* (Henriksen and Bjerketvedt [44]).

4. DISCUSSION

4.1. Variance in the experimental results

Figure 5 and Figure 6 shows that parallel experiments can give significantly different maximum pressures peaks. These differences in the results are especially noticeable for the center channel geometry High LBV Li-ion gas experiments at pressure sensors 2, 3, and 4. The differences in the maximum pressure peaks can be as high as 60 to 70 kPa, which is in the same range as the more significant deviations between the simulation and experimental results. Although minor differences were noticed in the flame front velocity and surface in parallel experiments, no phenomena or measured parameter could be attributed to the experiments with an increased or reduced maximum pressure peak. It is common to compare simulated and experimental maximum pressure peaks results [23,25]; however, it may not be an ideal comparable parameter due to potential variance between parallel experiments as observed in this study.

4.2. Model Performance

Based on the overall average MG and VG values, the XiFoam model performed acceptable for the Simplified Li-ion gas and performed excellently for the High LBV Li-ion gas for both channel geometries. XiFoam had the highest model performance for the High LBV Li-ion gas in the center channel geometry, which is expected since the model parameters were adjusted to this configuration at a ϕ equal to 1.0. However, the model showed discrepancies in predict the maximum pressure peaks recorded at PS3 and PS4, as seen in Figure 6. In the simulations, the flame thickness grows as it propagates through the geometry. This increase in flame thickness probably dampens the maximum pressure peaks caused by the rapid increase in flame acceleration when the flame passes through the cylinders. Although the model does not predict the maximum pressure peaks at these sensors, the positive impulse is predicated with less deviation.

The XiFoam model performance for the Simplified Li-ion gas was lower than for the High LBV Li-ion gas, based on the MG and VG values. Although the overall average model performance for the center channel geometry Simplified Li-ion gas cases were within the acceptable criteria, only one case was within acceptable performance criteria for positive impulse, as seen in Figure 10 c). Additionally, there is a significant discrepancy between the simulated and experimental flame front position before the flame reaches the cylinders for these cases. This discrepancy reveals that the flame accelerates more rapidly in the initial stages in the simulation compared to the experiments. The higher flame acceleration leads to the higher maximum pressure peaks, as seen in Figure 6 a) and b) for the Simplified Li-ion gas. Conversely, the experimental and simulated flame acceleration is in the same range for the inner channel geometry Simplified Li-ion gas cases, resulting in better model performance.

4.3. Model Parameters and Discretization

There are many different model parameters and discretization schemes to adjust and choose from in the OpenFOAM toolbox. Our focus was on the XiFoam combustion parameters and the discretization of time and divergence terms to limit the number of parameters and settings. However, other model parameters or discretization schemes could also significantly impact the simulation performance than those chosen in this study.

The Xi (Ξ) variable in Eq. 1 and Eq. 2 is the ratio between laminar and turbulent burning velocity. Xi, cannot be lower than one and will thus only increase or not affect the propagation velocity. For the center channel geometry, the initial flame acceleration was slightly higher in most simulation cases compared to the experiments. This discrepancy in flame acceleration was especially noticeable for the Simplified Li-ion gas cases. In the combustion property file, three variables can be adjusted to affect the value of Xi, *XiCoef*, *XiShapeCoef*, and *uPrimeCoef*. Using the Xi transport model, only changes to the *uPrimeCoef* significantly altered flame acceleration. *uPrimeCoef* is multiplied with the turbulent kinetic energy (k) used to evaluate the Xi value. Initially, the *uPrimeCoef* coefficient was set to 0.6, which has given good results in previous simulations and fitted reasonably well for the High CFD 1.0 Center validation case. However, for the center channel geometry Simplified Li-ion gas simulation cases, a lower value of the *uPrimeCoef* coefficient would have reduced flame acceleration and thus lower maximum pressure peaks. For example, altering the *uPrimeCoef* coefficient to 0.1 in the Simple CFD 1.0 Center simulation case will result in a maximum pressure peak of 25 kPa (gauge). Changes to *uPrimeCoef* could lead to an odd-shaped flame surface compared to experiments and previous simulations, as depicted in Figure 11 c). The odd-shaped flame surface can cause significant changes to the predicted flame front position and velocity.

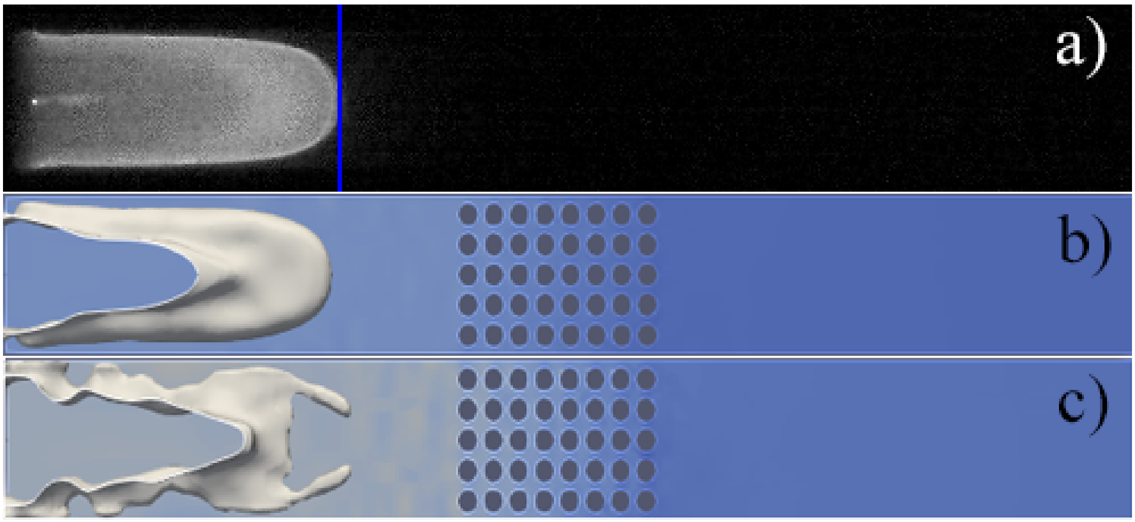

Figure 11. Examples of images of the experimental and simulated flame propagation in the center channel geometry. a): Image from the high-speed video; b): Typical numerical flame surface (isosurface of the regress variable b at 0.5); c) Odd-shaped flame surface due to changes in the numerical schemes or combustion parameters (isosurface regress variable b at 0.5)

Different discretization schemes were tested to analyze if they had any significant effect on the solution. Discretizing time using first-order forward Euler resulted in numerically stable simulations, with little to no effect when changing the discretization schemes for the divergence terms. However, changing the time discretization scheme to second-order backward Euler or Crank-Nicolson significantly impacted the flame propagation. Using the second-order backward scheme would lead to convergence errors. Using the Crank-Nicolson scheme, the intended simulation time was achieved (for most cases) with a Crank-Nicolson coefficient between 0.1 and 0.6. The larger Crank-Nicolson coefficient usually increased the flame acceleration and thus the maximum pressure peak. For example, by increasing the coefficient to 0.6 for the High CFD 1.0 Center simulation case, the maximum pressure peak was 450 kPa (gauge), 300 kPa higher than for the simulation case using a coefficient of 0.4. Although a higher coefficient increased the flame acceleration, it could also lead to similar odd-shaped flames, as shown in Figure 11 c). Numerical instabilities probably cause the odd-shaped flame surfaces. Thus, a linearUpwind discretization scheme was used to minimize the numerical instability and retain second-order accuracy for most divergence terms.

Finally, by adjusting the value of *uPrimeCoef* and the Crank-Nicolson coefficient in post-analysis for each simulation case, it is possible to predict the desired target parameter fairly accurately, whether it be flame acceleration or maximum pressure peak, or positive impulse. However, accurately predicting all three of these parameters in the same simulation with the XiFoam model is proven to be challenging.

4.4. Final Observations

In the simulations, the pressure peaks are broader than in most experiments, making it impossible to predict both the maximum pressure peak and the positive impulse with extreme precision. In the simulations, the flame thickness is initially thin with the thickness of a few cells, but as it propagates, it broadens and can grow to a thickness larger than 200 mm. However, the flame thickness of an actual flame is at least a hundred times thinner than this. Since the numerical flame thickness is large, the total heat of combustion is released over a larger volume than the actual experimental flame, and thus generating a broader pressure peak. A possible solution for this issue in the XiFoam model could be to reduce the cell size; unfortunately, this could not be investigated further due to limited computational resources.

For the experimental center channel geometry Simplified Li-ion gas cases, only the cases with a ϕ below 1.19 (case 50 to 61) would propagate through the cylinders without quenching. Most cases would completely quench within the cylinders in the experiments with ϕ 1.19 and above (case 62 to 70). However, a few experiments (case 63, 67, 68, and 69) eventually propagated through, although the time from no visible flame to visible flame in the high-speed video was on average 0.21 s. By contrast, the average time for the flame to reach the cylinders after ignition for these cases was 0.05 s. A common occurrence for cases 63, 67, 68, and 69, the first visible flame after "quenching," was always in the top part of the channel.

Case 62, which had a ϕ of 1.19, propagated past the cylinders similar to those experimental cases with a ϕ below 1.19. For case 62, the flame was partly quenched while propagated in the center of the cylinders. However, the flame continued to propagate without quenching in the top and bottom of the channel. Since case 62 propagated through the cylinders, similarly to the experiments with ϕ below 1.19, it was the only experimental case compared to the Simple CFD 1.2 Center simulation case.

Conversely, all the center channel geometry High LBV Li-ion gas cases propagated through without any indication of quenching. The LBV for the High LBV Li-ion gas is more than twice that of the Simplified Li-ion gas at similar ϕ [21], which is an essential parameter for this phenomenon. The quenching may be caused by a highly turbulent flow, which may be violating the XiFoam laminar flamelet assumption. Further investigation is needed to explain this phenomenon more deeply, which is beyond the scope of this study.

5. CONCLUSION

This study examined the XiFoam model performance, a combustion solver part of the open-source CFD toolbox OpenFOAM. The XiFoam model performance was evaluated by comparing numerical simulations and experiments of premixed gas explosions in a 1-meter explosion channel partly filled with 18650 cell-like cylinders. In addition to comparing two geometries with different locations of the 40 18650 cell-like cylinders, two gas compositions with significantly different LBV at several ϕ were compared. The model performance was based on the prediction accuracy of the temporal pressure evolution, maximum pressure peak, positive impulse, and spatial evolution of the flame front velocity.

Based upon the overall average MG and VG values and the model performance criteria in Table 4, the XiFoam had an overall acceptable model performance. XiFoam had the highest prediction accuracy for the center channel geometry High LBV Li-ion gas cases; however, this was expected since one of these cases was used to determine the combustion model parameters and discretization schemes. XiFoam had the lowest prediction accuracy for the center channel geometry Simplified Li-ion gas cases. The lower prediction accuracy was mainly due to an over-predicted flame acceleration in the initial laminar flame propagation stage.

Adjusting the combustion parameter *uPrimeCoef* and the Crank-Nicolson coefficient for the time discretization would significantly change the flame propagation and thus the simulation results. By adjusting these parameters in post-analysis for each simulation, one can increase the prediction accuracy significantly. However, predicting with high precision the maximum pressure peak and positive impulse in the same simulation is difficult with the XiFoam combustion model.

ACKNOWLEDGEMENT

This work was performed within MoZEES, a Norwegian Centre for Environment-friendly Energy Research (FME), co-sponsored by the Research Council of Norway (project number 257653) and 40 partners from research, industry and public sector.

REFERENCES

[1] Sophia Beausoleil, Lithium batteries causes train car explosion in NE Houston, KPRC, Click2Houston. (2017). https://www.click2houston.com/news/2017/04/24/lithium-batteries-causes-train-car-explosion-in-ne-houston/.

[2] D. Hill, McMicken Battery Energy Storage System Event Technical Analysis and Recommendations, DNV-GL, 2020. https://www.aps.com/-/media/APS/APSCOM-PDFs/About/Our-Company/Newsroom/McMickenFinalTechnicalReport.ashx?la=en&hash=50335FB5098D9858BFD276C40FA54FCE.

[3] Andy Colthorpe, Fire at 20MW UK battery storage plant in Liverpool, Energy Storage News. (2020). https://www.energy-storage.news/news/fire-at-20mw-uk-battery-storage-plant-in-liverpool.

[4] Ben Turner, Live updates as fire rips through Carnegie Road electrical unit, Liverpool Echo. (2020). https://www.liverpoolecho.co.uk/news/liverpool-news/live-updates-fire-rips-through-18934842.

[5] CTIF - International Association of Fire and Rescue Services, Accident analysis of the Beijing lithium battery explosion which killed two firefighters, (2021). https://www.ctif.org/news/accident-analysis-beijing-lithium-battery-explosion-which-killed-two-firefighters.

[6] C. Mikolajczak, M. Kahn, K. White, R.T. Long, Lithium-Ion Batteries Hazard and Use Assessment, Springer US, Boston, MA, 2011. https://doi.org/10.1007/978-1-4614-3486-3.

[7] Q. Wang, B. Mao, S.I. Stoliarov, J. Sun, A review of lithium ion battery failure mechanisms and fire prevention strategies, Progress in Energy and Combustion Science. 73 (2019) 95–131. https://doi.org/10.1016/j.pecs.2019.03.002.

[8] T. Lian, P.J.S. Vie, M. Gilljam, S. Forseth, Changes in Thermal Stability of Cyclic Aged Commercial Lithium-Ion Cells, ECS Transactions. 89 (2019) 73–81. https://doi.org/10.1149/08901.0073ecst.

[9] Y. Fernandes, A. Bry, S. de Persis, Identification and quantification of gases emitted during abuse tests by overcharge of a commercial Li-ion battery, Journal of Power Sources. 389 (2018) 106–119. https://doi.org/10.1016/j.jpowsour.2018.03.034.

[10] A.W. Golubkov, S. Scheikl, R. Planteu, G. Voitic, H. Wiltsche, C. Stangl, G. Fauler, A. Thaler, V. Hacker, Thermal runaway of commercial 18650 Li-ion batteries with LFP and NCA cathodes – impact of state of charge and overcharge, RSC Advances. 5 (2015) 57171–57186. https://doi.org/10.1039/C5RA05897J.

[11] A.W. Golubkov, D. Fuchs, J. Wagner, H. Wiltsche, C. Stangl, G. Fauler, G. Voitic, A. Thaler, V. Hacker, Thermal-runaway experiments on consumer Li-ion batteries with metal-oxide and olivin-type cathodes, RSC Adv. 4 (2014) 3633–3642. https://doi.org/10.1039/C3RA45748F.

[12] M. Lammer, A. Königseder, V. Hacker, Holistic methodology for characterisation of the thermally induced failure of commercially available 18650 lithium ion cells, RSC Advances. 7 (2017) 24425–24429. https://doi.org/10.1039/C7RA02635H.

[13] E.P. Roth, C.C. Crafts, D.H. Doughty, James. McBreen, Advanced technology development program for lithium-ion batteries : thermal abuse performance of 18650 Li-ion cells., 2004. https://doi.org/10.2172/918751.

[14] V. Somandepalli, K. Marr, Q. Horn, Quantification of Combustion Hazards of Thermal Runaway Failures in Lithium-Ion Batteries, SAE International Journal of Alternative Powertrains. 3 (2014) 98–104. https://doi.org/10.4271/2014-01-1857.

[15] A. Nedjalkov, J. Meyer, M. Köhring, A. Doering, M. Angelmahr, S. Dahle, A. Sander, A. Fischer, W. Schade, Toxic Gas Emissions from Damaged Lithium Ion Batteries—Analysis

and Safety Enhancement Solution, Batteries. 2 (2016) 5. https://doi.org/10.3390/batteries2010005.

[16] D. Bjerketvedt, J.R. Bakke, K. Van Wingerden, Gas explosion handbook, Journal of Hazardous Materials. 52 (1997) 1–150.

[17] J. Johnsplass, M. Henriksen, K. Vaagsaether, J. Lundberg, D. Bjerketvedt, Simulation of burning velocities in gases vented from thermal run-a-way lithium ion batteries, in: 2017: pp. 157–161. https://doi.org/10.3384/ecp17138157.

[18] M. Henriksen, K. Vaagsaether, J. Lundberg, S. Forseth, D. Bjerketvedt, Explosion characteristics for Li-ion battery electrolytes at elevated temperatures, Journal of Hazardous Materials. 371 (2019) 1–7. https://doi.org/10.1016/j.jhazmat.2019.02.108.

[19] M. Henriksen, A.V. Gaathaug, K. Vaagsaether, J. Lundberg, S. Forseth, D. Bjerketvedt, Laminar Burning Velocity of the Dimethyl Carbonate-Air Mixture Formed by the Li-Ion Electrolyte Solvent, Combustion, Explosion, and Shock Waves. 56 (2020) 383–393. https://doi.org/10.1134/S0010508220040024.

[20] A.R. Baird, E.J. Archibald, K.C. Marr, O.A. Ezekoye, Explosion hazards from lithium-ion battery vent gas, Journal of Power Sources. 446 (2020) 227257. https://doi.org/10.1016/j.jpowsour.2019.227257.

[21] M. Henriksen, K. Vaagsaether, J. Lundberg, S. Forseth, D. Bjerketvedt, Laminar burning velocity of gases vented from failed Li-ion batteries, Journal of Power Sources. 506 (2021) 230141. https://doi.org/10.1016/j.jpowsour.2021.230141.

[22] R.W. Kennedy, K.C. Marr, O.A. Ezekoye, Gas release rates and properties from Lithium Cobalt Oxide lithium ion battery arrays, Journal of Power Sources. 487 (2021) 229388. https://doi.org/10.1016/j.jpowsour.2020.229388.

[23] R. Shen, Z. Jiao, T. Parker, Y. Sun, Q. Wang, Recent application of Computational Fluid Dynamics (CFD) in process safety and loss prevention: A review, Journal of Loss Prevention in the Process Industries. 67 (2020) 104252. https://doi.org/10.1016/j.jlp.2020.104252.

[24] O.R. Hansen, P. Hinze, D. Engel, S. Davis, Using computational fluid dynamics (CFD) for blast wave predictions, Journal of Loss Prevention in the Process Industries. 23 (2010) 885–906. https://doi.org/10.1016/j.jlp.2010.07.005.

[25] P.A. Diakow, J.K. Thomas, E. Vivanco, Comparison of large-scale vented deflagration tests to CFD simulations for partially congested enclosures, Journal of Loss Prevention in the Process Industries. 56 (2018) 147–154. https://doi.org/10.1016/j.jlp.2018.07.012.

[26] O.R. Hansen, P. Middha, CFD-based risk assessment for hydrogen applications, Proc. Safety Prog. 27 (2008) 29–34. https://doi.org/10.1002/prs.10213.

[27] J. Kim, A. Mallarapu, D.P. Finegan, S. Santhanagopalan, Modeling cell venting and gas-phase reactions in 18650 lithium ion batteries during thermal runaway, Journal of Power Sources. 489 (2021) 229496. https://doi.org/10.1016/j.jpowsour.2021.229496.

[28] G.-H. Kim, A. Pesaran, R. Spotnitz, A three-dimensional thermal abuse model for lithium-ion cells, Journal of Power Sources. 170 (2007) 476–489. https://doi.org/10.1016/j.jpowsour.2007.04.018.

[29] R. Srinivasan, M.E. Thomas, M.B. Airola, B.G. Carkhuff, L.J. Frizzell-Makowski, H. Alkandry, J.G. Reuster, H.N. Oguz, P.W. Green, J. La Favors, L.J. Currano, P.A. Demirev, Preventing Cell-to-Cell Propagation of Thermal Runaway in Lithium-Ion Batteries, J. Electrochem. Soc. 167 (2020) 020559. https://doi.org/10.1149/1945-7111/ab6ff0.

[30] H. Helgesen, Technical Reference for Li-ion Battery Explosion Risk and Fire Suppression, DNV GL, Norway, 2019.

[31] A. Savitzky, M.J.E. Golay, Smoothing and Differentiation of Data by Simplified Least Squares Procedures., Analytical Chemistry. 36 (1964) 1627–1639. https://doi.org/10.1021/ac60214a047.

[32] CFD Direct, OpenFOAM v7 User Guide, OpenFOAM v7 User Guide. (2021). https://cfd.direct/openfoam/user-guide-v7/.

[33] H.G. Weller, G. Tabor, H. Jasak, C. Fureby, A tensorial approach to computational continuum mechanics using object-oriented techniques, Comput. Phys. 12 (1998) 620. https://doi.org/10.1063/1.168744.

[34] N. Peters, Laminar flamelet concepts in turbulent combustion, Symposium (International) on Combustion. 21 (1988) 1231–1250. https://doi.org/10.1016/S0082-0784(88)80355-2.

[35] Ö.L. Gülder, Correlations of Laminar Combustion Data for Alternative S.I. Engine Fuels, in: 1984. https://doi.org/10.4271/841000.

[36] H.G. Weller, C.J. Marooney, A.D. Gosman, A new spectral method for calculation of the time-varying area of a laminar flame in homogeneous turbulence, Symposium (International) on Combustion. 23 (1991) 629–636. https://doi.org/10.1016/S0082-0784(06)80310-3.

[37] H.G. Weller, G. Tabor, A.D. Gosman, C. Fureby, Application of a flame-wrinkling les combustion model to a turbulent mixing layer, Symposium (International) on Combustion. 27 (1998) 899–907. https://doi.org/10.1016/S0082-0784(98)80487-6.

[38] A. Yoshizawa, Statistical theory for compressible turbulent shear flows, with the application to subgrid modeling, Phys. Fluids. 29 (1986) 2152. https://doi.org/10.1063/1.865552.

[39] M. Henriksen, D. Bjerketvedt, mech2Foam - Generating transport, combustion, and thermodynamic properties for the CFD solver XiFoam, University of South-Eastern Norway, 2021. https://doi.org/10.23642/USN.13721134.V3.

[40] B.J. McBride, S. Gordon, M.A. Reno, Coefficients for Calculating Thermodynamic and Transport Properties of Individual Species, NASA, 1993. https://ntrs.nasa.gov/api/citations/19940013151/downloads/19940013151.pdf.

[41] W. Sutherland, LII. *The viscosity of gases and molecular force*, The London, Edinburgh, and Dublin Philosophical Magazine and Journal of Science. 36 (1893) 507–531. https://doi.org/10.1080/14786449308620508.

[42] H. Hisken, S. Lakshmipathy, G. Atanga, T. Skjold, Model evaluation protocol for HySEA, Gexcon AS, 2020.

[43] Model Evaluation Group Gas Explosion, Gas Explosion Model Evaluation Protocol, 1996.

[44] M. Henriksen, D. Bjerketvedt, Experiments of Premixed Gas Explosion in a 1-meter Channel Partly Filled with 18650 Cell Geometry, (2021) 7976511794 Bytes. https://doi.org/10.23642/USN.15134442.V1.

Supplementary Data A – mech2Foam documentation

mech2Foam - Generating transport, combustion, and thermodynamic properties for the CFD solver XiFoam

Version 4 Posted on Figshare on the 17.08.2021. University of South-Eastern Norway. Software. https://doi.org/10.23642/usn.13721134.v4

mech2Foam

mech2Foam is a code that generates the required combustion, thermodynamic, and transported properties model coefficients for a computational fluid dynamic (CFD) simulation with the model/solver XiFoam part of the open-source toolbox OpenFOAM [1], [2]. The code is written in the open-source programming language Python version 3.6 [3], and the output files are suited and tested for OpenFOAM version 7. Although the code is written for the CFD solver XiFoam, other CFD software that uses the same input parameters can utilize *mech2Foam*. This document explains how *mech2Foam* generates combustion, thermodynamic, and transported properties model coefficients. The thermodynamic and transport properties are in the *Generating thermophysicalProperties file* section, whereas the combustion properties section documents the generation of the Gülder model/equation coefficient.

Generating thermophysicalProperties file

The *thermophysicalProperties* file in the XiFoam case folder contains the transport and thermodynamic properties (model coefficients) and defines how these properties are modeled. There is one mixture specific and three specie specific parameters needed for simulating inhomogeneous combustion. The global mixture parameter is the stoichiometric air-fuel mass ratio. Furthermore, the mole weight, NASA polynomial coefficients, and Sutherland coefficients are the three specie specific parameters. These parameters are calculated using the open-source package Cantera version 2.4 [4] and a reaction mechanism/chemical kinetics. As input parameters to *mech2Foam*, the fuel and oxidizer composition, the initial pressure (p), temperature (T), and a reaction mechanism are needed.

The thermodynamic parameters can be evaluated directly for the oxidant and the fuel since all species and concentrations are input values. For the combustion products, the species are not input parameters and must therefore be calculated. Using the inbuilt equilibrate function in Cantera, the burnt product species and concentrations can be determined. The fuel and air mixture is equilibrated at constant pressure and enthalpy to determine the burnt product species at initial input (T,p) conditions. Species with a mole fraction below 0.001 are removed to reduce the number of species in the product gas. The species concentration is then normalized before the parameters can be calculated. The function *calculate_burnt_product_gas_composition* in the script *calculateThermoProperties.py* calculates the stoichiometric air-fuel mass ratio.

For the thermodynamic model Janaf in OpenFOAM, the NASA polynomials [5] are used to calculate the heat capacity (C_p), enthalpy (h), and entropy (s). The NASA polynomials are functions of temperature, with seven polynomial coefficients. There are two temperature ranges separated by the minimum, shared/common, and maximum reference temperature. The NASA polynomial equations are shown below.

$$\frac{C_p(T)}{R_u} = a_0 + a_1 T + a_2 T^2 + a_3 T^3 + a_4 T^4 \qquad \text{Eq. 1}$$

$$\frac{h(T)}{R_u} = a_0 T + \frac{a_1 T^2}{2} + \frac{a_2 T^3}{3} + \frac{a_3 T^4}{4} + \frac{a_4 T^5}{5} + a_5 \qquad \text{Eq. 2}$$

$$\frac{s(T)}{R_u} = a_0 \ln T + a_1 T + \frac{a_2 T^2}{2} + \frac{a_3 T^3}{3} + \frac{a_4 T^4}{4} + a_6 \qquad \text{Eq. 3}$$

where: C_p – specific heat capacity at constant pressure, [J/(mol·K)]; R_u – Universal gas constant, [J/(mol·K)]; h – enthalpy, [J/mol]; s – entropy, [J/(mol·K)]; T – temperature, [K], a_0 – polynomial coefficient velocity vector [J/(mol·K)];], a_1 – polynomial coefficient, [J/(mol·K^2)]; a_2 – polynomial coefficient, [J/(mol·K^3)]; a_3 – polynomial coefficient, [J/(mol·K^4)]; a_4 – polynomial coefficient, [J/(mol·K^5)]; a_5 – polynomial coefficient, [J/(mol)]; a_6 – polynomial coefficient, [J/(mol·K)]

As mentioned previously, one of the required inputs to *mech2Foam* is a reaction mechanism/chemical kinetics model. The NASA polynomials (Eq. 1 to Eq. 3) are the most common thermodynamic model used in these reaction mechanisms. Each species in the reaction mechanism has its own set of NASA polynomial coefficients. In mech2Foam, mole weighted NASA polynomial coefficients are calculated from the species-specific NASA polynomial coefficient using Eq. 4. The function *calculate_NASApolynomial_coefficients_for_mixture*, calculates the mole weighted NASA polynomial coefficients used in XiFoam.

$$\overline{a_\iota} = \sum_{i=0}^{k} a_{i,k} X_k \qquad \text{Eq. 4}$$

where: $\bar{a}_i$ – mole weighted NASA polynomial coefficient of index i; $a_{i,k}$ – NASA polynomial coefficient of index i and specie k; X – mole fraction of specie k; i – polynomial coefficient index; k – species.

Different species may have different reference temperatures, which can cause deviations in thermodynamic properties in some temperature regions. For different reference temperatures in a mixture, the species with the highest mole fraction will determine the mixture's reference temperatures. Suppose a mixture contains species with different reference temperatures. In that case, it will be documented in the support documentation written alongside the *thermophysicalProperties* file. If the minimum reference temperature exceeds 200 K, it is adjusted to 200 K to avoid warnings during OpenFOAM simulations.

The Sutherland equation is the chosen transport model in this case. The dynamic gas viscosity is calculated from the Sutherland equation below (Eq. 5) [6].

$$\mu = \frac{A_s\sqrt{T}}{1+\frac{T_s}{T}} \qquad \text{Eq. 5}$$

where: μ – dynamic gas viscosity, [Pa·s]; A_S – Sutherland coefficient; T_S – Sutherland Coefficient; T – temperature [K]

In the Sutherland equation, two constants need to be curve fitted (A_s and T_s). The mixture-specific Sutherland coefficients are fitted to the dynamic viscosities gathered from a Cantera Solution object generated using the reaction mechanism, initial conditions, and the three species compositions (fuel, oxidizer, and burntProducts). The temperature range for the viscosity is set to the minimum and maximum NASA polynomial reference temperatures. The Sutherland coefficients are calculated in the *calculate_sutherland_coefficients_for_gas_mixture* function.

Combustion properties– Gülder coefficient

One of the laminar burning velocity (LBV) models in OpenFOAM is the Gülder correlations model [7] shown in Eq. 6.

$$S_L(\phi,T,p) = \omega\phi^{\eta}e^{\xi(\phi-1.075)}\cdot\left(\frac{T}{T_{ref}}\right)^{\alpha}\cdot\left(\frac{p}{p_{ref}}\right)^{\beta}\cdot\left(1-X_f\cdot f\right) \qquad \text{Eq. 6}$$

where: S_L – laminar burning velocity, [m/s]; ϕ – fuel-air equivalence ratio, [-]; T – temperature, [K]; p – pressure, [Pa]; ω – Gülder coefficient; η – Gülder coefficient; ξ – Gülder coefficient; T_{ref} – Reference temperature; α – Gülder coefficient; p_{ref} – reference pressure; β – Gülder coefficient, X_f – mole fraction of inert [-]; f – Gülder coefficient

Five coefficients in the Gülder equation needs to be estimated, which is ω, η, ξ, α, and β. The coefficient f is set to 2.3, independent of the gas composition. X_f is the mole fraction of inert that is not part of the fuel and oxidizer mixture. The Gülder coefficients are fitted in three steps, Eq. 7 to Eq. 9. In the Cantera package, the routine *FreeFlame* was used to calculate the LBVs used in the fitting procedure. The *FreeFlame* routine solves the governing equation for a 1-D premixed, steady, laminar/planar, adiabatic flame. The reference pressure and temperature values are 101.3 kPa and 300 Kelvin, respectively.

$$S_L(\phi) = \omega\phi^{\eta} e^{\xi(\phi-1.075)} \qquad \text{Eq. 7}$$

$$S_L(T) = S_L(\phi = 1, T_{ref}, p_{ref}) \cdot \left(\frac{T}{T_{ref}}\right)^{\alpha} \qquad \text{Eq. 8}$$

$$S_L(p) = S_L(\phi = 1, T_{ref}, p_{ref}) \cdot \left(\frac{p}{p_{ref}}\right)^{\beta} \qquad \text{Eq. 9}$$

where: S_L – laminar burning velocity, [m/s]; ϕ – fuel-air equivalence ratio, [-]; T – temperature, [K]; p – pressure, [Pa]; ω – Gülder coefficient; η – Gülder coefficient; ξ – Gülder coefficient; T_{ref} – Reference temperature; α – Gülder coefficient; p_{ref} – reference pressure; β – Gülder coefficient.

References

[1] H. G. Weller, G. Tabor, H. Jasak, and C. Fureby, "A tensorial approach to computational continuum mechanics using object-oriented techniques," *Comput. Phys.*, vol. 12, no. 6, p. 620, 1998, doi: 10.1063/1.168744.

[2] CFD Direct, "OpenFOAM v7 User Guide," *OpenFOAM v7 User Guide*, Jul. 30, 2021. https://cfd.direct/openfoam/user-guide-v7/

[3] *Python*. [Online]. Available: https://www.python.org/

[4] D. G. Goodwin, H. K. Moffat, and R. L. Speth, *Cantera: An Object-Oriented Software Toolkit For Chemical Kinetics, Thermodynamics, And Transport Processes*. Zenodo, 2017. doi: 10.5281/zenodo.170284.

[5] B. J. McBride, S. Gordon, and M. A. Reno, "Coefficients for Calculating Thermodynamic and Transport Properties of Individual Species," NASA, Technical NASA TM-4513, Oct. 1993. [Online]. Available: https://ntrs.nasa.gov/api/citations/19940013151/downloads/19940013151.pdf

[6] W. Sutherland, "LII. *The viscosity of gases and molecular force*," *The London, Edinburgh, and Dublin Philosophical Magazine and Journal of Science*, vol. 36, no. 223, pp. 507–531, Dec. 1893, doi: 10.1080/14786449308620508.

[7] Ö. L. Gülder, "Correlations of Laminar Combustion Data for Alternative S.I. Engine Fuels," presented at the West Coast International Meeting and Exposition, Aug. 1984. doi: 10.4271/841000.

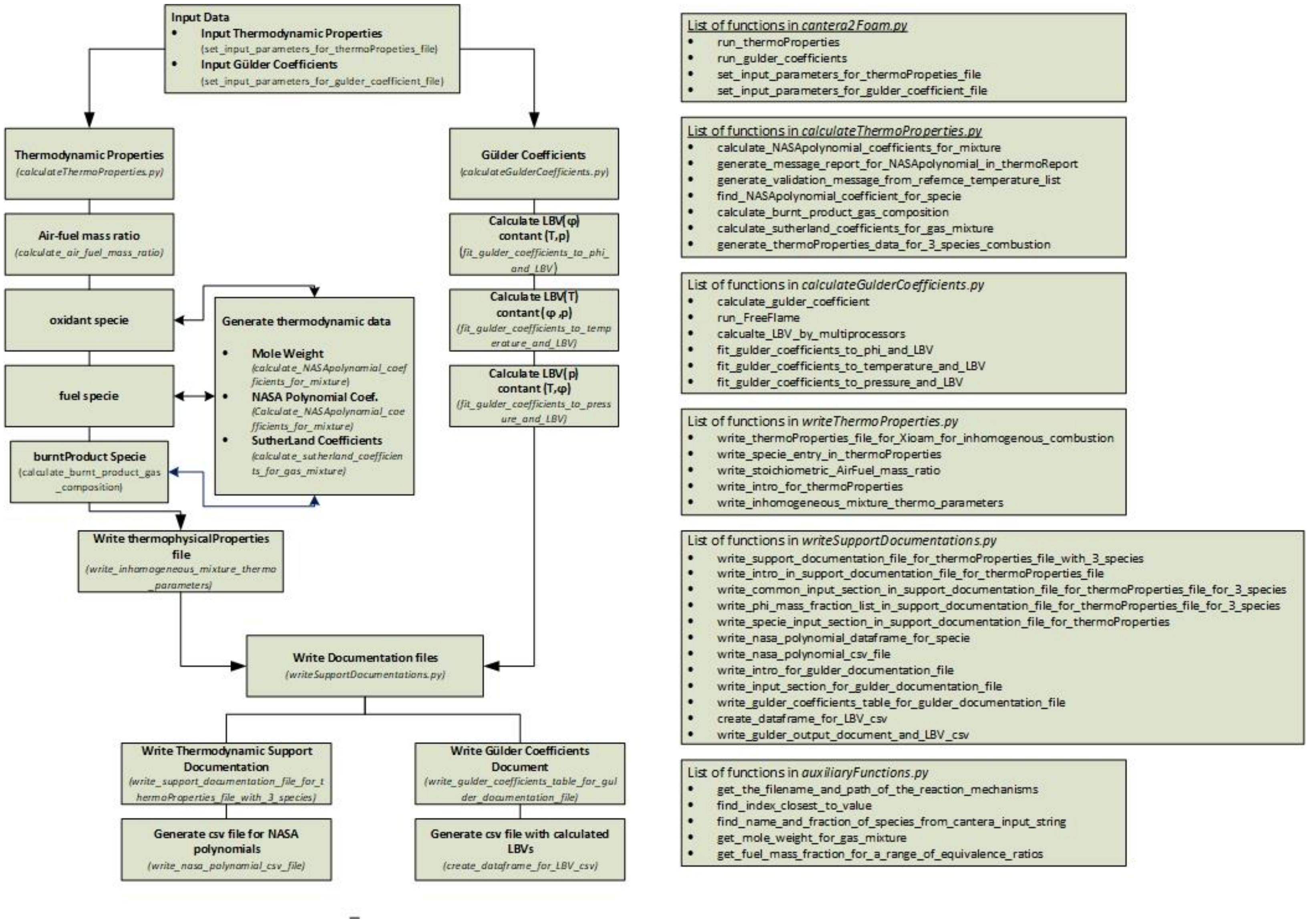

Figure 1. A diagram that illustrates the structure of the mech2Foam code and all the scripts and underlying functions.

Errata

1. **Page XI and XII, Abbreviations:**
   LEL - Lower Explosive Limit, to, “LFL - Lower Flammability Limit”
   UEL - Upper Explosive Limit, to, “UFL - Upper Flammability Limit”

2. **Page XII and XIII, Nomenclature:**
   KG - Deflagration Index – from, bar·m3·s-1, to, “bar·m·s-1”
   l - Markstein Length - from M to “m”.
   ex – from, maximum explosion pressure in an experiment, to, “explosion pressure in an experiment”
   max – from, maximum explosion pressure in a series of experiments, to, “maximum pressure in a series of experiments”

3. **Page 6, section 2.1:**
   A primary lithium cell or lithium-metal cell is a non-rechargeable battery that is “disposable” after use.

4. **Page 37, Figure 21:**
   Updated the dimension 4.6 mm to 22.6 on the schematic illustration of the experimental setup.

5. **Page 38, Figure 23:**
   Updated Y-axis name from Maximum explosion pressure, to, “explosion pressure”

Doctoral dissertation no. 109
2021

—

A study of premixed combustion of gas vented from failed Li-ion batteries

Dissertation for the degree of Ph.D

—

Mathias Henriksen

—

ISBN: 978-82-7206-631-3 (print)
ISBN: 978-82-7206-632-0 (online)

usn.no